# erosion, wear, and interfaces with corrosion

STP 567

AMERICAN SOCIETY FOR TESTING AND MATERIALS

# EROSION, WEAR, AND INTERFACES WITH CORROSION

A symposium
presented at the
Seventy-sixth Annual Meeting
AMERICAN SOCIETY FOR
TESTING AND MATERIALS
Philadelphia, Pa. 24-29 June 1973

ASTM SPECIAL TECHNICAL PUBLICATION 567
A. Thiruvengadam, symposium chairman

04-567000-29

AMERICAN SOCIETY FOR TESTING AND MATERIALS
1916 Race Street, Philadelphia, Pa. 19103

Library of Congress Catalog Card Number: 74-83948

NOTE

The Society is not responsible, as a body,
for the statements and opinions
advanced in this publication.

Printed in Philadelphia, Pa.
December 1974

Second Printing, Baltimore, Md.
May 1982

# Foreword

The symposium on Erosion, Wear, and Interfaces with Corrosion was presented at the Seventy-sixth Annual Meeting of the American Society for Testing and Materials held in Philadelphia, Pa., 24-29 June 1973. Committee G-2 on Erosion and Wear sponsored the symposium. A. Thiruvengadam, The Catholic University of America, presided as symposium chairman.

# Related
# ASTM Publications

Evaluation of Wear Testing, STP 446 (1969)
(04-446000-23)

Characterization and Determination of Erosion Resistance, STP 474 (1970)
(04-474000-29)

Localized Corrosion—Cause of Metal Failure, STP 516 (1972) (04-516000-27)

# Contents

# Introduction

This symposium was the fourth on the subject of erosion to be sponsored by ASTM, the first three having been held in 1961, 1966, and 1969, respectively. These symposia have contributed to the establishment of a common forum for scientists and engineers working in the areas of cavitation and impingement erosion and wear of materials. Specifically, attention was focused on understanding the interfaces of these problems with corrosion. D. H. Kallas, through his many years of experience in the field of marine corrosion-erosion problems, was able to set the theme of the symposium in his introductory papers. Erosion-corrosion problems were dealt with in detail in several papers presented, and metallographic studies of the basic mechanism of material deformation and fracture were also reported.

A new model for rain erosion phenomena was presented. Also, erosion of nonmetallics received considerable attention. The effects of fatigue, dynamic recovery, and failure mechanisms of some rain erosion-resistant coatings were discussed. Solid particle erosion of glassy materials was presented, as well as the wear characteristics of plasma-deposited aluminum bronze. Many new findings that could be used in practical applications were highlighted during the discussions that followed the presentation of each paper, and these also are recorded in this volume.

It was highly encouraging to note the international response to this symposium, which has contributed greatly to the promotion of knowledge in the area of erosion and wear of materials in corrosive environments.

*A. Thiruvengadam*

Professor of Mechanical Engineering,
The Catholic University of America,
Washington, D. C. 20017.

# Erosion, Wear, and Interfaces with Corrosion

*D. H. Kallas*[1]

# Corrosion, Wear, and Erosion—An Ancient Art and a Modern Science

**REFERENCE:** Kallas, D. H., "Corrosion, Wear, and Erosion—An Ancient Art and a Modern Science," *Erosion, Wear, and Interfaces with Corrosion, ASTM STP 567*, American Society for Testing and Materials, 1974, pp. 5–17.

**ABSTRACT:** A thorough historical review of corrosion, erosion, and wear is given along with a study of the state of the art with a view to how the interdisciplining approach is attempting to unify opinions on the mechanism of damage. This is followed by some thoughts on areas for future research and development. The paper concludes by speculating on how the knowledge gained can impact on our material resources, the environment, and the quality of life.

**KEY WORDS:** corrosion, erosion, wear, mechanical properties, electrochemical corrosion, damage

The destructive agents which cause deterioration of engineering materials can be roughly classified into mechanical and chemical modes. Our technology abounds with examples of material failure caused by one or the other agent. For example, mechanical destruction is the end point of a process of elastic or plastic deformation. Common examples are failure of a propeller shaft, the breaking of a winch cable, the collapsing of a ring stiffener of a submarine hull. Although these gross failures remove valuable components from systems and cause significant economic and human problems in terms of downtime and possible injury, the failed material is frequently recoverable in terms of repair or rework. In more subtle situations the mechanical destruction is gradual such as the wear in bearings and engine parts or gouging or roughening of propellers and hydrofoils. Such processes are generally defined as erosion or wear phenomena, derived from the Latin—*erodere*—to gnaw out. Materials also

[1] Technical director, Bradford Computer & Systems, Inc., Rockville Division, Rockville, Md. 20852.

can be gradually destroyed by the chemical action of the environment, by an irreversible conversion to a new substance having markedly different properties from the original such as the rusting of steel to produce iron oxide, the dissolution of zinc anodes in galvanically protecting a ship ballast tank, the oxidation of rubber by ozone to produce embrittlement by altering the polymer chain structure, or the biodegradation of fabrics by fungi and molds. The physicochemical destruction of materials (most frequently by liquid or gases) is termed corrosion, again from the Latin—*corrodere*—to gnaw away.

The interaction of corrosion with erosion and wear processes combines in many subtle ways to affect the rate of destruction of materials. This elusive mechanical-chemical interface has challenged the minds of many for decades and only within the past generation are we able to understand the interplay between these agents as they affect the behavior of materials in dynamic environments of the ocean, Arctic, space, and various atmospheres. The focus of this volume is to understand the mechanisms operating at the interface between erosion and corrosion of materials in order to be able to design systems exposed to the combined, often synergistic, interaction of corrosion processes with erosion and wear processes. Many examples of corrosion-mechanical interaction have been investigated. Some will be reviewed in historical perspective, which give insight into scope, differentiation, and severity of these combined, superimposed processes. Cavitation erosion on propellers is a classical example of the destructive interaction of mechanical implosion of vapor bubbles with the corrosive environment of the sea. Other examples of impingement phenomena are: the destructive action of raindrops on aircraft wings and radomes; the steam erosion of turbine blades; the sand, dirt, and ice abrasion of skirt systems on surface effect vehicles; and the impingement of micrometeorites on space vehicles. Wear, caused by rubbing, sliding, or rolling contact materials on each other in liquid or gaseous environments produce galling, fretting, and surface cracking, actions which are accelerated by the corrosive influence.

I would like to amplify the subject of my remarks from four aspects:

1. Historical review of corrosion and erosion as independent phenomena.
2. State of the art on how the interdisciplinary approach is attempting to unify what were formerly divergent views on the mechanism of destruction.
3. The areas of research and development that should be pursued in the future.
4. Speculation on how the knowledge gained will impact on the quality of life for generations to come.

## Historical Review

My long-term association in the cavitation-erosion field during my 30-year stint with the U. S. Naval Applied Science Laboratory and the U. S. Naval Ship Research and Development Center has afforded me the happy experience of participating with many key investigators in the resolution of controversies arising from the influence of corrosion on cavitation-erosion damage of materials. Much progress has been made in understanding the contribution of chemical processes acting in concert with mechanical forces causing damage to materials.

From ancient times, steel armor and weapons were polished, bronzed, and embossed with noble metals not only to improve appearance but to prevent corrosion. The Greek historian Herodotus (5th century BC) and the Roman nationalist Pliny the Elder (1st century BC) both mention the adoption of tin for the protection of iron against corrosion—the forerunner of cladding, plating, and hot dip fused metal coatings. Alchemists throughout the centuries made inadvertent contributions through their futile attempts to convert base metals into noble metals, that is, into metals having outstanding corrosion-resistant properties.

By the dawn of the industrial revolution in the 18th century, the accumulated requirements of rapidly developing industries gave impetus to scientific inquiry into corrosion, erosion, and wear.

Without attempting a critical review of every important investigation, it will suffice for purposes of this paper to touch on highlights of scientific discoveries leading up to the serious study of interaction of corrosion with erosion and wear phenomena. The recognition of cavitation phenomena, which strangely enough preceded the serious corrosion inquiry, is attributed to Euler in 1794. However, the term "cavitation" was coined later by Froude in 1895 during an investigation of a British destroyer which failed to meet its design speed[*1*].[2] Lord Rayleigh in 1917[*2*] postulated that for a symmetrical cavity and incompressible fluid, the bubble collapse pressure approaches infinity. Later, this concept was modified by others who recognized that cavities do not collapse symmetrically and that real fluids are contaminated with compressible gases[*3–9*].

We are all familiar with the asymmetric bubble collapse photographs of Ellis and Naude[*3*] and Benjamin and Ellis[*10*] which showed the existence of jets and led to jet impact theories further developed by Eisenberg[*11*], Tulin[*12*], and others. The historical development of the nature

[2] The italic numbers in brackets refer to the list of references appended to this paper.

and mechanism of cavitation damage was amply reviewed by Eisenberg et al[*14,15*] for example, as well as many others; and erosion by liquid impingement by Heymann[*16*] and many others too numerous to mention here.

Turning to corrosion phenomena, the earliest scientific contribution is credited to Lomonsov[*17*] in 1756, who showed tthat heated metals increase their weight only in air and not in a vacuum. Lavoisier[*18*] in 1773 repeated these experiments and proved that the oxidation of a metal is the chemical union of the metal with oxygen from the air. In 1790 Keir[*19*] described in detail the passivation of steel in nitric acid. Hall (1819) established the fact that iron does not rust in the absence of oxygen. Cathodic protection dates back to 1824 when Sir Humphrey Davy[*20*] proposed an electrochemical method using zinc or steel protectors for halting corrosion of hulls sheathed with impure copper. Unfortunately, his experiments were ultimately abandoned when it was discovered that the antifouling properties of copper ceased when its corrosion was stopped. De La Rive[*21*] (1830), in his work on zinc in sulphuric acid, developed the concept of the electrochemical nature of corrosion. In 1833, Faraday[*22*] established the relationship between the quantity of electricity passing through a solution and the amount of metal deposited or gases liberated at the electrodes. In 1847, Adie[*23*] showed the existence of a corrosion current on iron surfaces having a difference of accessibility to oxygen in a flowing stream. The establishment of the "Periodic Law" by Mendeleev in 1869 was significant in evaluating and classifying corrosion characteristics of different metals.

Edison[*24*] recognized the corrosion problem confronting the steel ship industry, and designed a cathodic protection system in 1890 using a trailing graphite anode. Whitney[*25*] (1903) proposed an electrochemical explanation for the corrosion of iron in water, which was substantiated by other investigators such as Evans[*26*] in England.

Hoar[*27*] in 1931 and Mears and Brown[*28*] in 1938 advanced the theory of cathodic protection by establishing criteria for achieving complete corrosion protection. From that time many investigators have studied the role of polarization and current distribution in cathodic protection[*29–32*]. In recent years, some excellent books have been published on corrosion and cathodic protection which embody the discoveries and advances to date[*33–42*].

The science of wear has a similar long history which matured side by side with corrosion and erosion technology. Suffice it to say that since the dawn of the nuclear and space age in the 1940's, the phenomenon of wear and its sister fields of friction and lubrication has resulted in the

establishment of an international journal devoted entirely to these subject matters.

The progress toward clarifying the mechanisms of elusive chemical/mechanical interactions responsible for the rate and severity of this material degradation is briefly reviewed in the following.

## State of the Art: Corrosion Interface With Erosion and Wear

In my personal experience with cavitation damage phenomena, I have observed and participated in the controversies which seem to rage perennially as to whether the mechanism of damage to a material is chemical corrosion or mechanical erosion or both. To this end, Fottinger[*43*] damaged glass venturi tubes with cavitation in cold water. The general conclusion today is that the basic damage is mechanical in nature, and failure by fatigue for ductile materials predominates at least the initial stages of erosion. Thus several researchers began to correlate material properties with damage behavior; namely, Kerr[*44*] Mousson[*45*], Nowotny[*46*], and Rheingans[*47*], and Leith[*48*]. They tend to agree on the mechanism that a material undergoes, that is, plastic deformation, under the impacts of bubble collapse, depending on its hardness or yield properties or some other physical parameter, which results in fatigue and erosion. What they do not agree on is the material parameter governing the resistance to erosion. Even today this dispute still continues. Properties such as yield strength, ultimate strength, ultimate elongation, Brinell hardness, and modulus of elasticity have been suggested as the controlling parameter, besides some other exotic combinations of these properties. Thiruvengadam[*49*] proposed strain energy to fracture as the parameter that provides the highest degree of correlation of material response to cavitation attack. This definition of erosion strength is gaining wide acceptance as the best means of correlating materials, but it is still far short of being a universal solution.

However, there are still those who believe that corrosion has a large part in the damage mechanism. The belief that the mechanisms is primarily electrochemical in nature—damage being caused by galvanic corrosion as a result of non-uniform stresses in the metal, oxygen concentration cells, or ion-concentration cells—is referenced by Wheeler[*50*] and Petracchi[*51*].

Ramsay[*52*], besides being the first to notice cavitation on propellers, first suggested that cavitation erosion was not mechanical but electrolytic corrosion occurring at the strain-hardened indentations caused by bubble collapse. In 1919, Parsons and Cook[*53*] found that in seawater, when

iron was eroded, iron hydroxide was produced, whereas in alcohol, pure iron particles were found. He said nevertheless that the mechanism was mostly mechanical but that the results of his own tests did not eliminate the corrosive influence. Beeching[*54*] found definite indications of corrosion during accelerated cavitation and concluded that the corrosion attack accelerates the mechanical erosion. Evans[*55*], like many others, believed that cavitation erosion is at most a conjoint action of mechanical-chemical effects. The normally protective oxide film on the material is continuously torn off by collapsing bubbles, so the chemical attack continues unabated at the same rapid rate. This is closest to the present thinking by many observers of the extent of corrosion in the damage process. Eisenberg et al[*14*] emphasize that many theories on corrosion are not in conflict with the mechanical model of cavitation. The main point to remember is the intensity of cavitation damage in which these phenomena take place. Since the mechanical intensity of erosion is supposedly much greater than the intensity of corrosion, the proposed corrosion theories might only account for a small percentage of total damage. Eisenberg also points out that the conjoint action of mechanical and electrochemical effects, with an accelerated attack rate, is common in corrosion fatigue, stress-corrosion cracking, jet impingement, velocity corrosion, sand abrasion, fretting corrosion, and wire drawing, for instance.

Another school of thought centers around the idea of thermogalvanic effects. Krenn[*56*] believes that high momentary temperatures attributed to the collapsing bubbles and the compression of the contained gas, or high temperatures associated with instantaneous stressing of the metal at the point of bubble collapse, cause the flow of corrosive current. Both Foltyn[*57*] and Nechleba[*58*], however, use a more rational approach, saying that the bubbles cause local heating that in turn creates a temperature gradient between the heated area and the surrounding metal which then causes an electric current to flow.

Both Wheeler[*50*] and Petracchi[*51*] propose a theory of strain-produced anodic corrosion. They believe that the strained portions of a metal, similar to corrosion fatigue, are electrochemically unstable and anodic areas are created. The anodic areas next to the undisturbed metal will have electrolytic corrosion if in contact with an electrolyte, and corrosion will continue until polarization prevents further flow of current or until the anodic areas are etched away. Thus they conclude that an annealed specimen subjected to repeat plastic deformation with the formation of associated strain centers will act as a cold-worked material. For iron that is cold-worked, the solution rate is much greater than for annealed iron.

Petracchi further explains in the cavitation process the liquid detaches

and then impinges on the surface, creating vacuum pockets with their associated liberation of gases. Thus there is a system of microcells with local corrosion set up by the turbulent action of the cavitation. He concludes that cavitation is not initially destructive because of mechanical stresses, but only from the stresses that arise in connection with corrosion.

Ffield, Mosher, and O'Neil[*59*] note that many materials such as bronzes in water form a protective film that under cavitation influence would rupture, exposing bare metal. Corrosion would proceed at a high rate owing to the favorable cathode-anode area relationships. However, this theory can be put into perspective by the explanations advanced by Preiser and Tytell[*60*]. They postulate three zones of cavitation erosion: cavitation deformation or fracture; cavitation fatigue; and cavitation corrosion, depending on the intensity of cavitation. In the first zone, with intensities found in most accelerated laboratory test apparatus, there would be no corrosion effects as the ratio of cavitation to corrosion intensity is so high, and thus the time scale of corrosion is too short. For the second zone, the forces are below the yield strength of many materials tested, unlike forces in the first zone where there was much plastic deformation. Owing to the lower cavitation intensities, the time scale of corrosion is longer and thus corrosion could exhibit some influence on damage. It is in this zone that Preiser and Tytell conducted their experiments on rotating propellers. For the last case the cavitation forces are assumed to destroy only the material protective films and to remove any corrosive products. Thus the film rupture scheme of Ffield et al is in the third zone, and, as such, is lower in magnitude than many actual experimental and field intensities.

Another interesting hypothesis is put forth by Shal'nev[*61*], called the "interfacial potential fluctuations theory." His observations of cast iron in seawater lead to the theory that the rapid movement of the liquid vapor interface across the surface of the metal during cavitation results in momentary electrode potentials capable of causing corrosion hundreds to thousands of times stronger than that caused by an unbroken contact between the metal and electrolyte.

Besides these theories, similar theories related to high temperatures produced in cavitation, as in the thermogalvanic theory, have been proposed but only to explain some concurrent chemical activity. Also, cathodic protection experiments were conducted by Plesset[*67*], Preiser and Tytell[*60*], and Wheeler[*50*] among others, which conclusively showed that this protection substantially reduced the corrosion influence in the overall attack.

Leith and Thompson[*63*], studying the action of corrosion on accelerated cavitation of diesel cylinder liners and hydraulic turbines on a mag-

netostriction apparatus, demonstrated how both corrosion and erosion are affected by various metal properties and liquid characteristics. Lichtman et al[*65*], likewise using a magnetostriction device plus a piezoelectric apparatus and a rotating disk apparatus, studied damage as the pressure and velocity varied. They also studied numerous ships and concluded that cavity collapse is the prime cause of damage only on the propellers. Damage to the struts, rudders, and other appendages was due to corrosion aggravated by mechanical scour. Also, they concluded that the lowest-velocity laboratory test was higher than the service velocities of naval ships and thus the damage to be seen in the field was corrosion primarily accelerated by turbulence from the cavitation region.

Waring et al[*66*] studied in detail the effect of corrosion on SAE 1020 medium steel and 1100-F aluminum using a vibratory device, polarization measurements, and the pulsing technique of Plesset[*67*]. Briefly, the pulsing technique applies cavitation in an intermittent manner. For the remaining interval, the material is immersed in seawater. For corrosion-sensitive materials only did the damage rate increase in this manner. Waring's findings showed that aluminum was unaffected by seawater in any type of test, but that steel had three times the damage rate in seawater than in distilled water. This was attributed to the deterioration of the mechanical properties in a corrosive environment.

Thus the general opinion to date is that cavitation erosion is a mechanical process and can be accelerated by corrosion or any other parameter such as temperature or pressure. It is believed that the main effect of corrosion is in weakening the properties of a material and rendering it more susceptible to erosion. The only area in which corrosion is believed to exert a strong influence is at low intensities of cavitation, as in Eisenberg et al[*14*], Petracchi[*51*], Wheeler[*50*], Lichtman and Weingram[*68*] and Thiruvengadam[*69*].

McGuiness[*70*], in developing a cavitation erosion-corrosion modeling law, concluded that for corrosion-sensitive systems, such as steels in seawater, the present modeling law of Thiruvengadam[*62*] is altered, with greater damage associated with the corrosive systems. The percent changes in the modeling law for such systems increase with increasing erosion intensity.

## Future Research and Development

It is apparent from this review that much progress has been made toward understanding the interaction of chemical and mechanical forces on the destruction of materials. From this knowledge comes means and methods of preventing such damage from occurring, through the use of

resistant materials, overlays and protective coatings, cathodic and anodic protection, and inhibitors. Schemes for gas cushioning by air injection or electrolytic gas generation have been proposed and used successfully. Methods of design to control input parameters leading to cavitation are being explored but are not fully developed.

I believe that fruitful endeavor will come from investigating the nature of the fatigue process in corrosive environments for correlation with repetitive cycling phenomena of cavitation and wear.

Development of modeling technique would be valuable to designers where cavitation intensities and damage rates could be predicted or avoided before full-size systems are built.

Further research is needed on the mechanism of resistance and adhesion of plastic and elastomeric coatings under cavitation influence in hostile environments.

Research on the metallurgical aspects of resistance to erosion and wear may lead to more resistant metallic overlay or inlay materials. The behavior of brittle materials such as glasses, concrete, and ceramics under the influence of combined chemical and mechanical agents needs more intensive study. Auxiliary protection techniques such as air injection, gas evolution, and cathodic protection must be refined for practical application to a wide variety of dynamic systems, especially where erosion and wear occur at low intensities. It is necessary to plan and conduct service trials to acquire quantitative field observations for evaluation and improvement of protection methods. Vigorous attempts should continue, through research at high erosion rates, to harness forces of cavitation for such useful applications as in mining, tunnelling, drilling, and cleaning.

## Impact on Quality of Life

There is no question that corrosion, erosion, and wear represent a major drain on resources, create pollution and environmental problems, and hold back the progress of society. As we resolve the problems posed by these influences on materials, we can expect a major impetus toward improving the quality of life.

Let us speculate for a moment on the impact of corrosion, erosion, and wear on our everyday life. It has been estimated by Tomashov, Uhlig, and others that 10 percent of the world output of metal is lost by corrosion alone. When this is combined with mechanical destruction, the percentage probably doubles. At this rate, and considering the world production of steel to be about 250 million tons annually, the amount of steel destroyed yearly would total between 25 and 50 million tons. Aside from the economic and manpower loss, which is staggering, the amount of raw

materials alone that would be conserved if this waste could be stopped is astronomical. For example, the production of one ton of steel requires 8 tons of air, 165 tons of water, 1/3 ton of steel scrap, 2/3 ton of coal, 1/5 ton of limestone, and $1\frac{1}{5}$ ton of iron ore.

In addition, 10 tons of polluting carbon monoxide gas, which is converted photochemically to $CO_2$, are generated for every ton of steel produced.

The reduction of these gas pollutants and residual contaminated process waters would have a large impact on the quality of the environment in the air we breathe, the water we drink, and the nature of the landscape around us.

Of equal importance, aside from stopping the destructive waste of materials, is the harnessing of the energies of erosion and impingement and the protection of high-performance systems from malfunction. I can see the day in the not too distant future where the labors of all men will be more meaningful in terms of production of durable goods. We will be able to transport ourselves over vast distances, at high speeds in all environments, without mishap. Hydrofoil ships will traverse oceans at speeds exceeding 100 knots. We will be able to span the distance of remote space with materials resistant to micrometeorite penetration. We will be able to water-blast and paint our ships underwater so as not to contaminate the atmosphere. We will be able to traverse in comfort the hostile terrain of the Arctic and the desert at high speeds in air cushion vehicles. Our automobiles and machines will require little or no maintenance, replacement, or repair.

A growing awareness of the importance of materials and crucial properties, such as those to which this volume is addressed, is finding its way into our national materials policy. In recognizing the impact of materials, Congress passed the National Resource Act of 1970 and established a national commission. This commission, known as the National Commission on Materials Policy, has initiated planning and recommendations intended to lead to legislation establishing a national posture on materials. This policy will deal with the conservation of resources, the more effective utilization of materials, and minimization of the impact on our environment caused by the deterioration and recycling of materials.

These developments are more than high-sounding goals and aspirations; they represent impending major actions on the part of the federal government and the materials community which will result in the improvement of the quality of life for ourselves and our children. Certainly the aspects of corrosion, erosion, and wear as related to materials must take a high priority in the list of major problems to be solved in response to this

emerging national policy. Probably for the first time in history the materials community has been faced by an array of technical problems of great social significance, and we are asked to think about them not only as scientists but as concerned citizens. I hope this challenge will inspire each and every one of us with the enthusiasm, desire, and dedication to function as a team in making a significant contribution.

I, myself, feel optimistic that the materials community can offer much, particularly those of us who specialize in corrosion, erosion, and wear. I am confident that we have much to contribute; I believe we are highly motivated; I am convinced that we are team-oriented; I know we are socially concerned. . . . What do you think?

## References


[1] Thornycroft, Sir John and Barnaby, S. W., *Minutes of Proceedings of the Civil Engineers*, Vol. 122, 1895, pp. 51–103.

[2] Rayleigh, Lord, *Philosophical Magazine*, London, Vol. 34, 1917, pp. 94–98.

[3] Naude, C. F. and Ellis, A. T., *Transactions*, American Society of Mechanical Engineers, *Journal of Basic Engineering*, Vol. 83, Series D., 1961, p. 648.

[4] Hammitt, F. G., "Impact and Cavitation Erosion and Material Mechanical Properties," Report No. 03371-1-T, Cavitation and Multiphase Flow Laboratory, University of Michigan, Ann Arbor, Nov. 1969.

[5] Plesset, M. S. and Chapman, R. B., "Collapse of an Initially Spherical Vapor Cavity in the Neighborhood of a Solid Boundary," Report 85-49, California Institute of Technology, Division of Engineering and Applied Science, Pasadena, Calif., June 1970.

[6] Ackeret, J. and De Haller, P., *Schweizer Archiv für angewandte Wissenschaft und Technik*, Vol. 4, 1938, pp. 293–294.

[7] Ackeret, J., *Technische Mechanik und Thermodynamik*, Vol. 1, 1930.

[8] Ivany, R. D. and Hammitt, F. G., *Transactions*, American Society of Mechanical Engineers, *Journal of Basic Engineering*, Series D, Vol. 87, No. 4, 1965, pp. 977–985.

[9] Hickling, R. and Plesset, M. S., *Physics of Fluids*, Vol. 7, 1964, pp. 7–140.

[10] Benjamin, T. B. and Ellis, A. T., *Philosophical Transactions of the Royal Society of London*, Series A, Vol. 260, No. 1110, 28 July 1966, pp. 221–240.

[11] Eisenberg, Phillip, "On the Mechanism and Prevention of Cavitation," David Taylor Model Basin Report 712, Washington, D. C., 1950; see also *Forschungshefte fur Schiffstechnik*, No. 3, 1953, and No. 5, 1954.

[12] Tulin, M. P., "On the Creation of Ultra-Jets," *L. I. Sedov 60th Anniversary Volume, Problems of Hydrodynamics and Continuum Mechanics*, Moscow, 1969.

[13] Johnson, V. E., Jr. and Hsieh, T., "The Influence of the Trajectories of Entrained Gas Nuclei on Cavitation Inception," Sixth Symposium on Naval Hydrodynamics, Office of Naval Research, Washington, D. C., 30 Sept.-3 Oct. 1966; also Technical Report No. 707-1, HYDRONAUTICS, Inc., Laurel, Md., 1967.

[14] Eisenberg, P. E., Preiser, H. S., and Thiruvengadam, A., *Transactions*, Society of Naval Architects and Marine Engineers, Vol. 73, 1965, pp. 241–286.

[15] Eisenberg, Phillip, *Characterization and Determination of Erosion Resistance, ASTM STP 474*, American Society for Testing Materials, 1970, pp. 3–28.

[16] Heymann, F. J., "Erosion by Cavitation, Liquid Impingement—A Review," Engineering Report E-1460, Development Engineering Department, Westinghouse Electric Corporation, Lester, Pa., March 1968.
[17] Menshutkin, B. N., *The Biography of M. V. Lomonosov*, Publication of the Academy of Sciences, USSR, 1947.
[18] Partington, J. R., *A History of Chemistry*, Vol. 3, Biographical Sketch of A. L. Lavoisier, MacMillan and Co., Ltd., London, 1962, pp. 363–495.
[19] Kier, J., *Philosophical Transactions*, 1790, pp. 80, 359.
[20] Davy, Sir Humphrey, *Philosophical Transactions of the Royal Society of London*, 1824–1825, pp. 114–115.
[21] Partington, J. R., *A History of Chemistry*, Vol. 4, Biographical Sketch of A. A. De La Rive, MacMillan and Co., Ltd., London, 1964, pp. 133–135.
[22] Faraday, M., The Correlation of the Physical Forces," a lecture at the Royal Institution, reprinted in the *Harvard Classics*, Vol. 30, Collier, N. Y., 1910, pp. 75–88.
[23] Adie, R., *Philosophical Magazine*, Vol. 31, 1947, pp. 350–356.
[24] Edison, T. A., *Method and Apparatus for Protecting Ships' Bottoms*, British Patent No. 13971, Sept. 1890.
[25] Whitney, W. R., *Journal of the American Chemical Society*, Vol. 25, 1903, p. 304.
[26] Evans, U. R., *Metallic Corrosion, Passivity and Protection*, Arnold Publishing Company, London, 1937.
[27] Hoar, T. P., *Journal Transactions of Electroplaters Technical Society*, Vol. 14, 1937, p. 33.
[28] Mears, R. B. and Brown, R. H., *Transactions of the Electrochemical Society*, Vol. 75, 1938, p. 519.
[29] Schuldiner, S., "Cathodic Protection of Ships' Hulls—A Critical Review," NRL Report 3616, Naval Research Laboratory, Jan. 1950.
[30] Waldron, L. J., Nelson, E. E., and Peterson, M. H., "Major Factors in the Cathodic Protection of Steel in Sea Water," NRL Report 4596, Naval Research Laboratory, 19 Aug. 1956.
[31] Stern, M. and Geary, A. L., *Journal of Electrochemical Society*, Vol. 104, No. 1, Jan. 1957, p. 36.
[32] Stern, Milton, *Corrosion*, Vol. 14, Nov. 1957, p. 440t.
[33] Uhlig, H. H., *Corrosion Handbook*, Wiley, New York, 1948.
[34] Uhlig, H. H., *Corrosion and Corrosion Control*, Wiley, New York, 1963.
[35] Speller, F. N., *Corrosion, Causes and Prevention*, McGraw-Hill, New York, 1951.
[36] LaQue, F. L. and Copson, H. R., *Corrosion Resistance of Metals and Alloys*, Rheinhold, N. Y., 1963.
[37] Rodgers, T. H., *The Marine Corrosion Handbook*, McGraw-Hill, N. Y., 1960.
[38] Tomashov, N. D., *Theory of Corrosion and Protection of Metals*, published in Russian by the Academy of Sciences, USSR, 1959, translated and edited by B. H. Tytell, I. Geld, and H. S. Preiser, MacMillan, N. Y.
[39] Greathouse, G. A. and Wessel, C. J., *Deterioration of Materials, Causes and Prevention Techniques*, Rheinhold, New York, 1954.
[40] Morgan, J. H., *Cathodic Protection, Its Theory and Practice in the Prevention of Corrosion*, Leonard Hill Ltd., London, 1959.
[41] Schreir, L. L., Ed., *Corrosion*, Vols. I and II, Wiley, New York, 1963.
[42] Evans, U. R., *An Introduction to Metallic Corrosion*, Edward Arnold Ltd., London, 1955.
[43] Fottinger, H., "Studies of Cavitation and Erosion in Turbines, Turbopumps and Propellers," (in German), Hydraulische Probleme, Lecture, Gottingen, VDI Verlag, Berlin, 1926, pp. 107–110.

[44] Kerr, L. S., *Transactions*, American Society of Mechanical Engineers, Vol. 59, 1937, pp. 373–397.
[45] Mousson, J. M., *Transactions*, American Society of Mechanical Engineers, Vol. 59, 1937, pp. 399–408.
[46] Nowotny, Hans, "Werkstoffzerstorung durch Kavitation," *Zeitschift des Vereins der Deutschen Ingenieure*, Berlin, 1942 (reprinted by Edwards Brothers, Inc., Ann Arbor, Mich., 1946).
[47] Rheingans, W. J., *Transactions, American Society of Mechanical Engineers*, Vol. 72, No. 5, June 1950, pp. 705–719.
[48] Leith, W. G., *The Engineering Journal*, March 1959.
[49] Thiruvengadam, A., "Prediction of Cavitation Damage," Ph.D. thesis, Department of Hydraulic Engineering, Indian Institute of Science, Bangalore, India, 1961.
[50] Wheeler, W. H., "Indentation of Metals by Cavitation," *Journal of Basic Engineering*, Paper No. 59-Hyd-15, ASME Hydraulic Conference, American Society of Mechanical Engineers, 13–15 April 1959.
[51] Petracchi, G., *La Metallurgia Italiana*, Vol. 41, No. 1, Jan.-Feb. 1949, pp. 1–6.
[52] Ramsay, W., *Engineering*, Vol. 93, 1912, pp. 687–690.
[53] Parsons, C. A. and Cook, S. S., *Engineering*, Vol. 107, 1919, pp. 515–519.
[54] Beeching, R., *Transactions*, Institute of Engineers and Shipbuilders in Scotland, Vol. 85, 1942, pp. 210–238.
[55] Evans, U. R., *Engineering*, Vol. 155, 1943, p. 454.
[56] Krenn, H., *Maschinenbau und Warmewirtschaft*, 1948, pp. 81–87.
[57] Foltyn, V., *Strojirenstvi*, Czecholovakia, Vol. 2, No. 9, Sept. 1952, pp. 402–408.
[58] Nechleba, Miroslav, *Maschinenbautechnik*, Vol. 2, Feb. 1955, pp. 81–88.
[59] Ffield, P., Mosher, L. M., and O'Neil, A. J., "Some Aspects of Propeller Deterioration and Its Prevention," Society of Naval and Marine Engineers, New England Section, May 1956.
[60] Preiser, H. S. and Tytell, B. H., *Corrosion*, Vol. 7, 1961, pp. 535t–549t.
[61] Shal'nev, K. K., (in Russian) *Koklady Akademii Nauk*, USSR, Vol. 95, No. 2, 1954, pp. 229–232.
[62] Thiruvengadam, A., "On the Selection of Modeling Materials to Scale Long Term Erosion Behavior of Prototype Systems," Proceedings of the Third International Conference on Rain Erosion and Allied Phenomena, Royal Aircraft Establishment, Farborough, England, 1970.
[63] Leith, W. C. and Thompson, A. L., *Transactions*, American Society of Mechanical Engineers, *Journal of Basic Engineering*, Vol. 82, Series D, 1960, pp. 805–807.
[64] Lichtman, J. Z., Kallas, D. H., Chatten, C. K., and Cochran, E. P., Jr., *Transactions*, American Society of Mechanical Engineers, Vol. 80, 1958, pp. 1325–41.
[65] Lichtman, J. Z., Kallas, D. H., and Rufolo, A., *Handbook on Corrosion Testing and Evaluation*, W. H. Ailor, Ed., Wiley, New York, 1971, pp. 453–472.
[66] Waring, S., Preiser, H. S., and Thiruvengadam, A., *Journal of Ship Research*, Vol. 9, Dec. 1965.
[67] Plesset, M. S., *Transactions*, American Society of Mechanical Engineers, *Journal of Basic Engineering*, Vol. 85, Series D, 1963, pp. 360–364.
[68] Lichtman, J. Z. and Weingram, E. R., *Symposium on Cavitation Research Facilities and Techniques*, J. W. Holl and G. M. Wood, Eds., American Society of Mechanical Engineers, 1964, pp. 185–196.
[69] Thiruvengadam, A., *Applied Mechanics Reviews*, American Society of Mechanical Engineers, March 1971, pp. 245–253.
[70] McGuinness, Terence, "Cavitation Erosion-Corrosion Modeling in An Ocean Environment," Ph.D. thesis, The Catholic University, Washington, D. C., 1972.

*J. M. A. Van der Horst* [1] *and C. R. Sloan* [2]

# Erosion-Corrosion of Finned Heat Exchanger Tubes

**REFERENCE:** Van der Horst, J. M. A. and Sloan, C. R., "Erosion-Corrosion of Finned Heat Exchanger Tubes," *Erosion, Wear, and Interfaces with Corrosion, ASTM STP 567*, American Society for Testing and Materials, 1974, pp. 18–29.

**ABSTRACT:** Converted reformer gas on the shell side of a heat exchanger was cooled by water on the tube side. In addition to hydrogen and nitrogen, the gas contained substantial quantities of $CO_2$ and water vapor. The tubes were integral finned of C-steel. Condensate from the gas stream filled the space between fins, while $CO_2$ from the stream dissolved into the water. Maximum gas velocity was of the order of 150 ft/s.

In the areas of highest gas velocity the fins had disappeared completely. In more or less stagnant gas areas the fins were corroded but still present, attack in intermediate areas ranging between the two extremes. The difference in corrosive attack between various areas clearly demonstrates the relatively modest effect of pure corrosion under these circumstances. On the other hand, the maximum velocity is about half the threshold velocity cited in the literature for steel. The synergistic effect of corrosion and erosion is therefore unmistakable. It may be assumed that impact of water droplets continuously removes the corrosion layer and thus accelerates the process.

The corrosive effect of $CO_2$ at ambient temperatures is often belittled, but should not be, especially when assisted by high-velocity gas.

Incidentally, the use of finned tubing in an environment producing condensate is absurd since condensation removes any heat-transfer advantage of the fins. Recalculation in fact showed that the fins were unnecessary.

**KEY WORDS:** erosion, corrosion, carbon steels, velocity, carbon dioxide, temperature

The case concerns a converted gas cooler in an ammonia plant. The gas arrives from the carbon monoxide converter where carbon monoxide and

[1] President, Surface Research Inc., Olean, N. Y. 14760.
[2] Senior process engineer, H. E. Wiese, Inc., Baton Rouge, La.

water are catalytically reacted to form carbon dioxide and hydrogen. The arriving gas consists essentially of hydrogen, nitrogen, carbon dioxide, and water. The function of the converted gas cooler is to remove most of the water as liquid by cooling.

The incoming gas (Fig. 1) has a temperature of 127°C (260°F) at

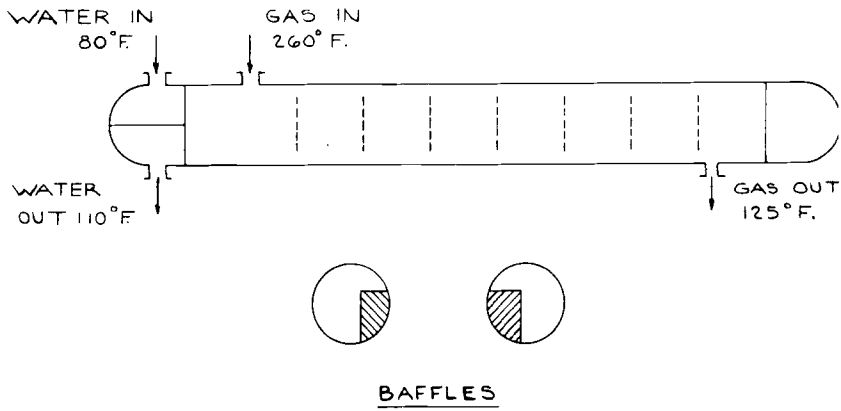


FIG. 1—*Sketch of heat exchanger.*

$1.65 \times 10^9$ N/m² (252 psi) and the exit gas has a temperature of 50°C (125°F) at a pressure of $1.63 \times 10^9$ N/m² (249 psi). Incoming gas contains 13.2 mol percent water, outgoing gas 0.7 mol percent. Cooling water temperatures are 25°C (80°F) and 40°C (110°F), respectively, at a flow of 442 liter/s (7000 gal/min). Cooling water is on the tube side and gas on the shell side. Carbon dioxide partial pressure is $2.69 \times 10^8$ N/m² (41 psi).

The cooler was originally designed with admiralty brass integral finned tubing. Since in an ammonia plant one is never quite sure that cooling water is completely ammonia-free, and since admiralty brass is subject to stress corrosion cracking (SCC) in ammoniacal atmospheres, plant management decided at an annual turnaround to replace the brass tubing by integrally finned carbon steel tubing.

The original design with finned tubing was rather irrational. Gas is cooled much more efficiently by finned tubing, provided it is indeed gas. At 127°C (260°F) and $1.65 \times 10^9$ N/m² (252 psi), however, the incoming gas already contains moisture. This moisture inevitably lodges between the fins, which in this case are only 1 mm (0.040 in.) apart. As a result the advantage of the fins is practically completely lost.

The replacement with carbon steel tubing was not successful. When the cooler was next opened, the fins on the tubes had disappeared completely in the direct line of the gas stream, were severely attacked on both sides of this line, and only remained relatively intact in stagnant corners. The gas stream is interrupted by numerous baffles, which steer it in a zigzag motion through the tube bundle. By direct line of the gas stream is meant the line connecting the center of the opening in one baffle with the center of the opening in the next baffle. Attack is diminished progressively from entry to exit.

Incidentally, recalculation of the heat-transfer duty determined that for a requirement of $3.02 \times 10^6$ kcal/h ($12 \times 10^6$ Btu/h), finned tubes with liquid water can transmit $3.73 \times 10^6$ kcal/h ($14.8 \times 10^6$ Btu/h) while plain tubes of Type 304 stainless steel with the same wall thickness can transmit $6.30 \times 10^6$ kcal/h ($25 \times 10^6$ Btu/h).

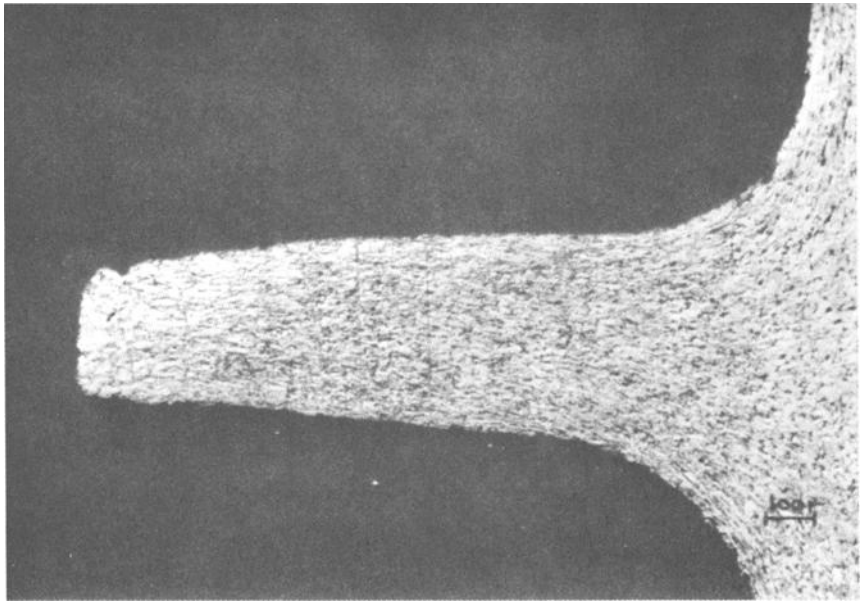

FIG. 2—*Undamaged fin (×65).*

Figure 2 (×65) shows a fin in the original state, Fig. 3 (×65) a fin with an advanced stage of attack, and Fig. 4 (×65) a fin which has virtually disappeared. Figure 5 (×65) is a cross section of a fin which

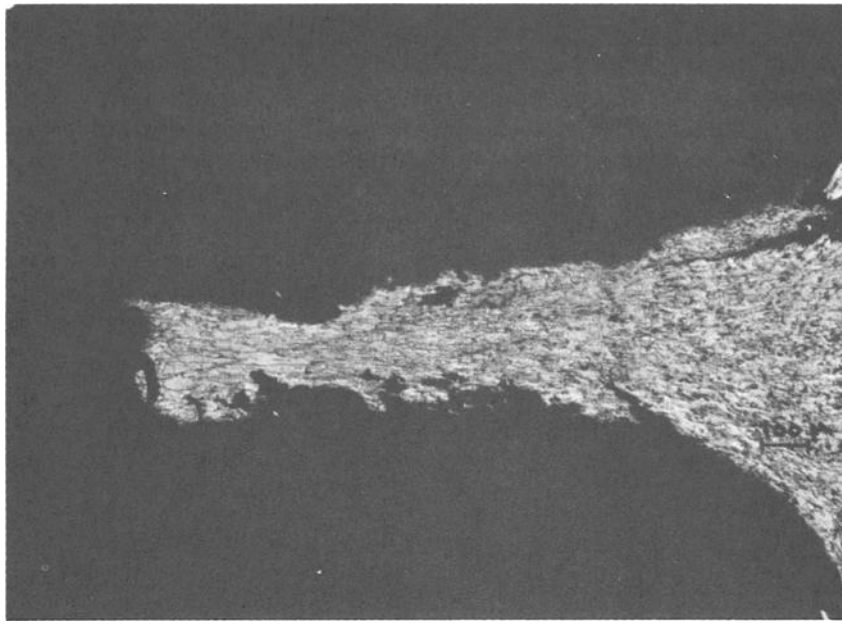

FIG. 3—*Fin attacked by corrosion (×65).*

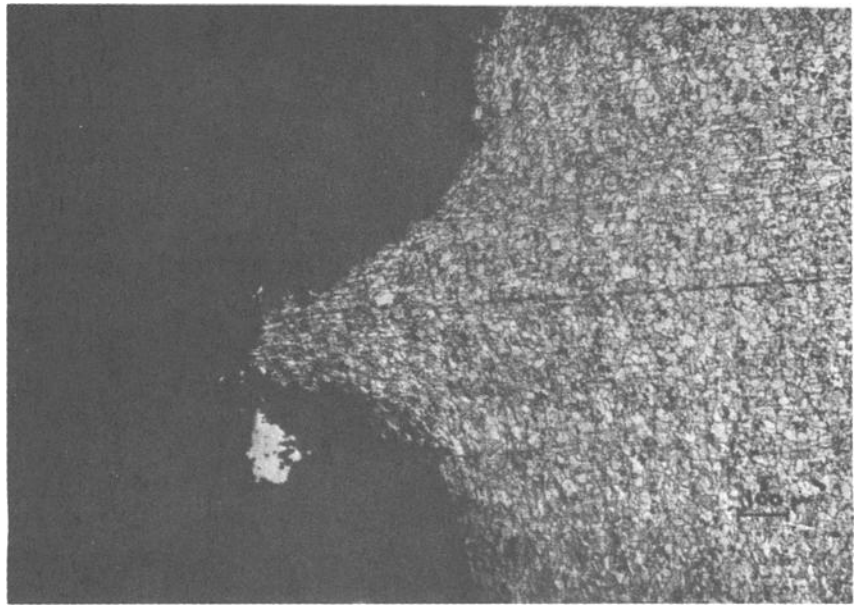

FIG. 4—*Fin removed by corrosion (×65).*

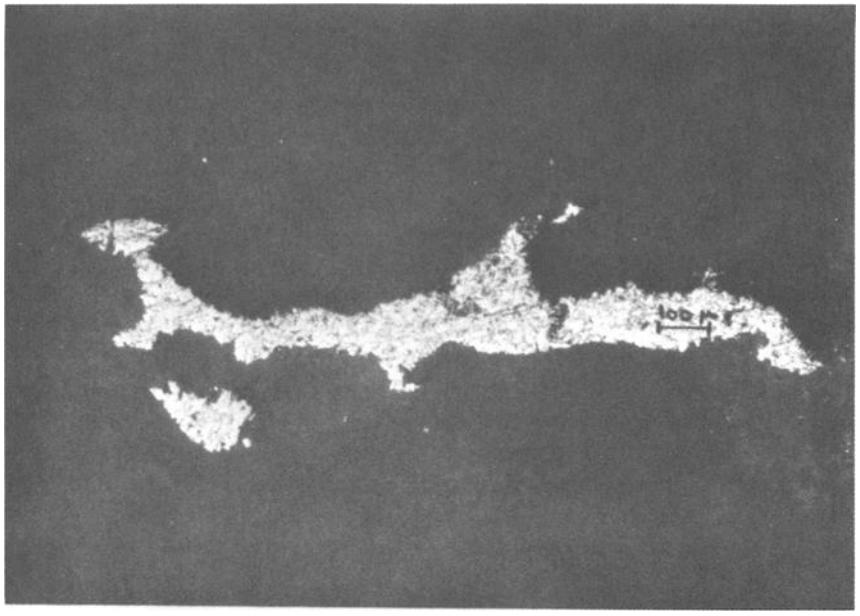

FIG. 5—*Cross section of severely corroded fin detached from tube* (×65).

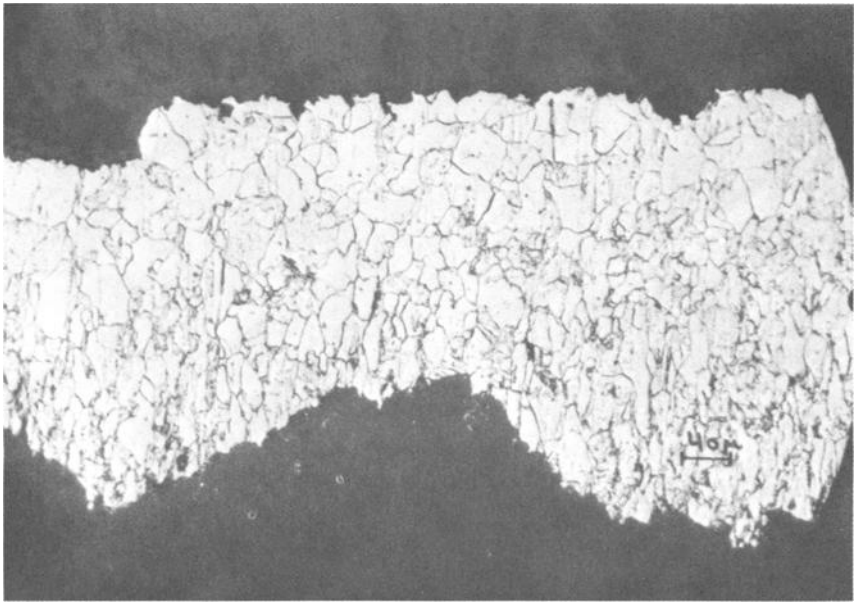

FIG. 6—*Longitudinal section of fin* (×162).

had become detached from the tube by attack. Figure 6 (×162) represents a longitudinal section of a severely attacked fin, the location of which is shown in Fig. 7. In general, the fin side facing the gas stream was often more severely attacked than the opposite side.

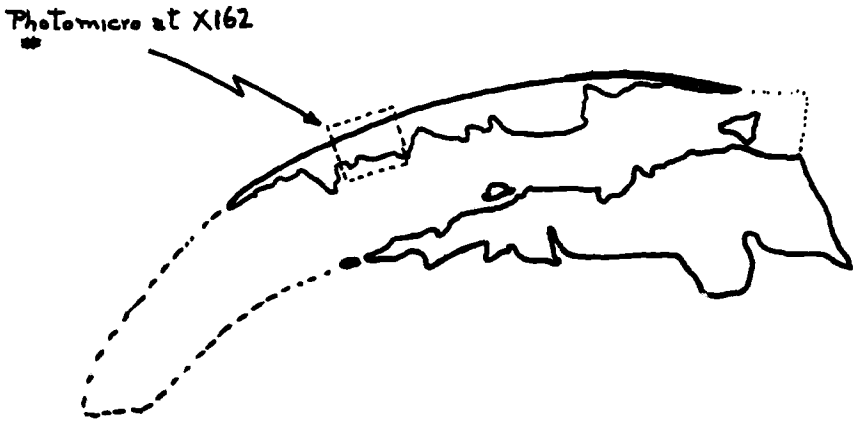


FIG. 7—*Location of specimen shown in Fig. 6. Broken segments of low carbon steel tubing fins, longitudinal (circumferential) view.*

Figure 8 (×330) and Fig. 9 (×720) are nital etched (2 percent nital—10 s) cross sections of attacked fins. Although there seems to be some tendency for the attack to follow grain boundaries as well as preferred attack of some crystals, no strong case can be made for this.

Finally, in order to investigate the type of corrosive attack, scanning electron micrographs (SEMs) were made of the surface. In all of the SEMs it is very clear (Fig. 10, ×100) that the surface is entirely covered with a corrosion product. In some of them (Fig. 11, ×3000) the rhombohedral crystals of ferrous carbonate can immediately be recognized.

## Temperature

In a variety of experiments, various investigators have found a maximum corrosion rate at a certain temperature [*1–3*].[3] Shulmeister [*4*] found 40 to 70°C (104 to 158°F) for aluminum, cast iron, and steel in various aqueous media. In short, a maximum rate at a certain temperature seems

[3] The italic numbers in brackets refer to the list of references appended to this paper.

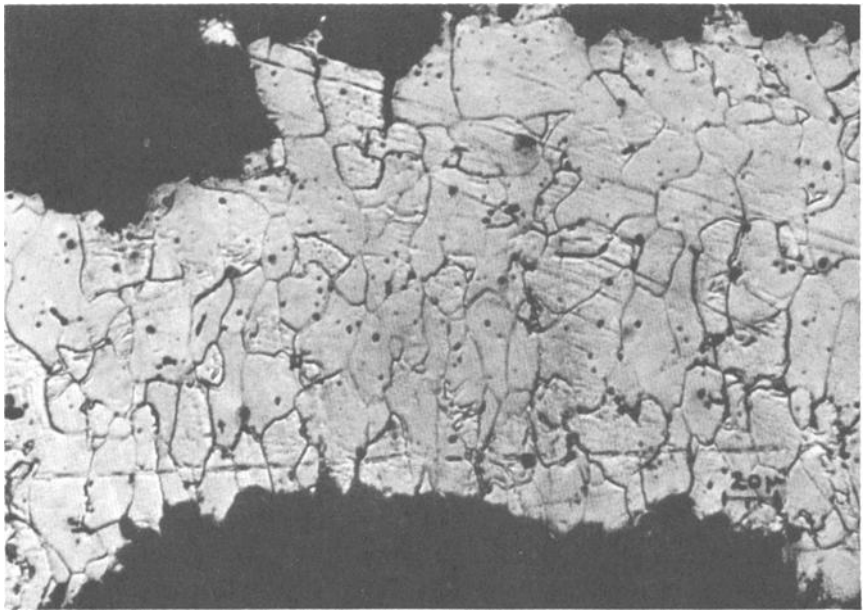


FIG. 8—*Cross section of corroded fin, nital etched (×330).*

to be characteristic for erosion processes. However, when corrosion accompanies erosion, the situation changes. Practically all corrosion processes in a liquid environment intensify as the temperature increases. Therefore, when corrosion is a major factor in the erosion-corrosion process, an increase in temperature will increase the rate of destruction and, as a result, processes at higher pressures containing corrosive drops of water become more destructive.

In the present case the influence of temperature is obvious. Destruction is greatest at gas entry and lowest at gas exit. Since carbon dioxide content in the gas stream remains unchanged and liquid water in the stream progressively increases, the severity of attack must be due to the temperature gradient, which is the only declining factor from entry to exit of the heat exchanger.

## Corrosion

Carbonic acid, a solution of carbon dioxide in water, is corrosive to carbon steel[*5*]. At moderate temperatures, velocities, and pressures, this

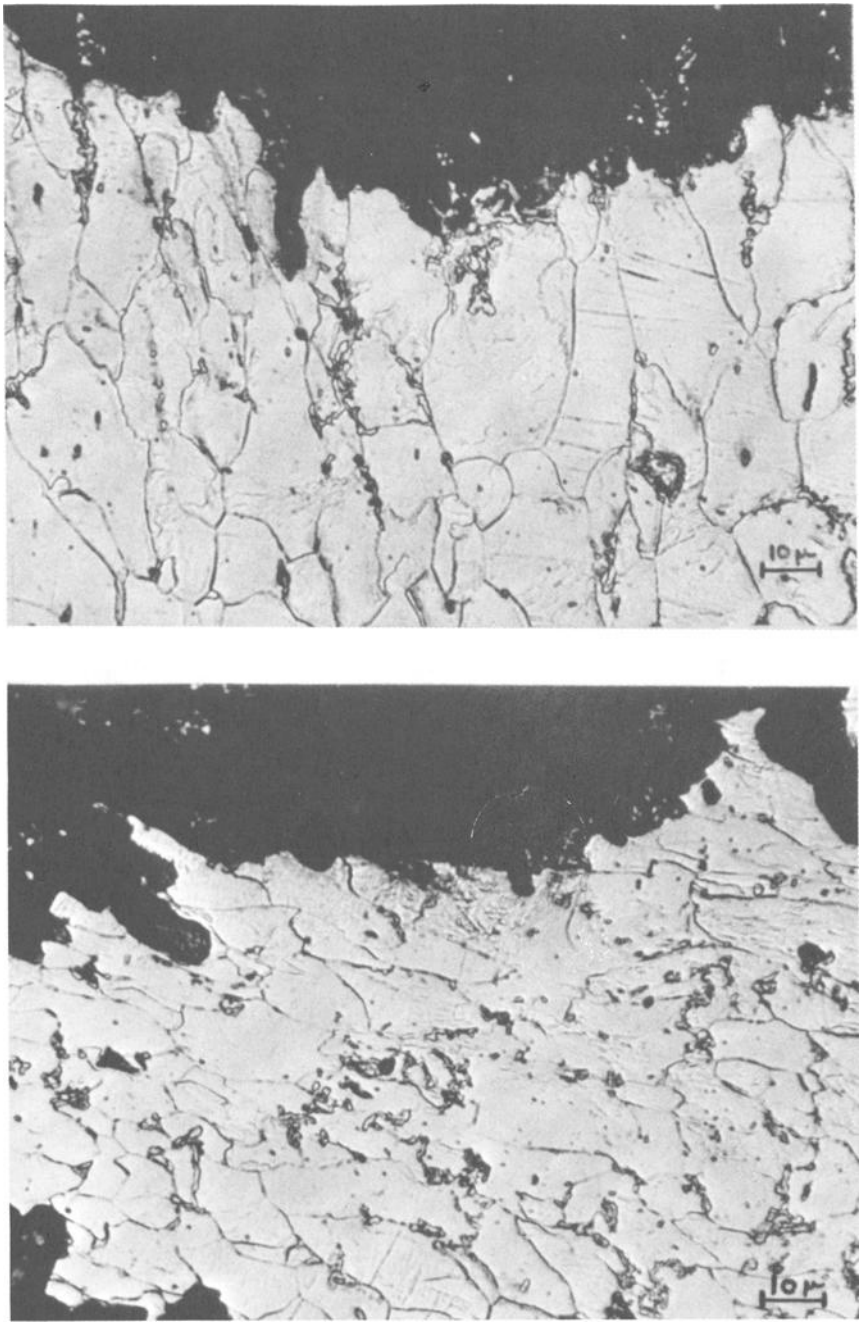

FIG. 9—*Two views of corroded fin surface, nital etched (×720).*

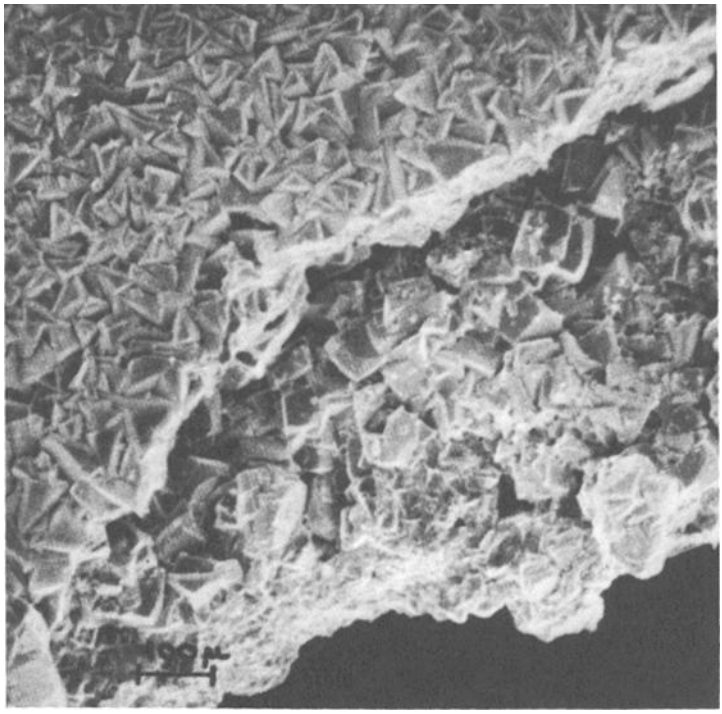

FIG. 10—*SEM of corroded fin surface (×100).*

type of corrosion is self-arresting, since the corrosion product (in the absence of oxygen) is ferrous carbonate, which has very limited solubility in water [0.0067 g/100 $cm^3$ at 25°C (77°F)]. Only at much higher partial pressures of carbon dioxide will ferrous bicarbonate be formed[6], which has a higher solubility in water and therefore allows more rapid corrosion. Moreover, at the temperatures involved in this case the kinetics of the reaction are rather slow.

This is demonstrated by the fact that, in the present case, finned-tube areas exposed to low gas velocities only showed very superficial attack. Since these areas are exposed to the same environment of carbon dioxide dissolved in water, their low corrosion rate should approximately represent what happens under stagnant conditions. The high rate of attack of the fins exposed to high gas velocities must therefore be due to a factor other than the chemical corrosion process.

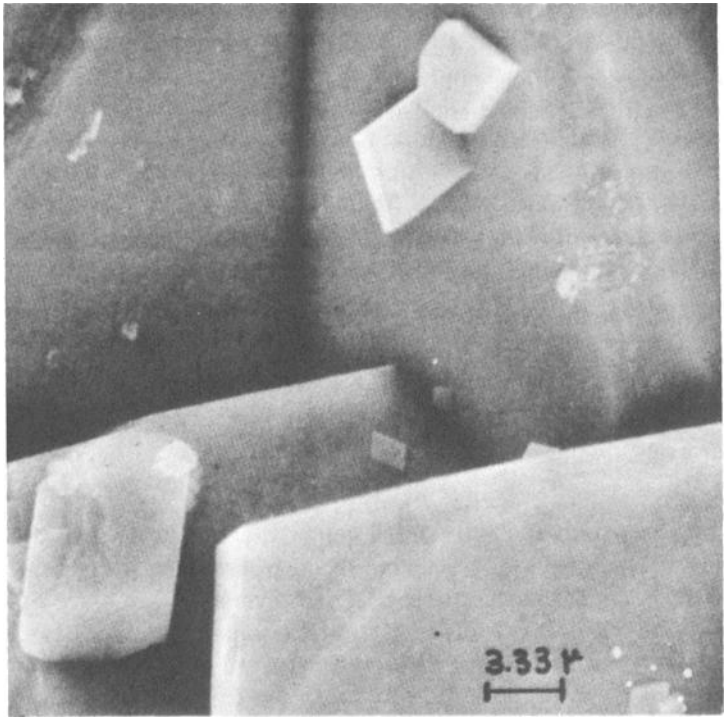


FIG. 11—*SEM of rhombohedral ferrous carbonate crystals (×3000).*

## Gas Velocity

Total gas flow is 825.8 liters/s (1750 $ft^3$/min). The opening between the tubes, not counting the space between the fins, is 529 $cm^2$ (82 $in.^2$), giving a velocity of approximately 15.24 m/s (50 ft/s). The line-of-sight area between tubes from one baffle opening to the next is approximately 161 $cm^2$ (25 $in.^2$), giving an absolute maximum velocity of approximately 51.81 m/s (170 ft/s). Actual velocities should therefore range from a maximum somewhere below 51.81 m/s (170 ft/s) to close to zero in the remote corners of each compartment between baffles.

We can therefore assume a maximum gas velocity of 45.72 m/s (150 ft/s) at the centerline connecting the openings in the baffles, which is about half the threshold value cited by Thiruvengadam [7] for pure impact erosion of carbon steel. In other words, the velocity of the gas containing drops of water is insufficient to cause massive destruction as found.

## Synergism of Velocity and Corrosion

The synergistic effect of gas velocity and corrosion by carbon dioxide is not unknown. Winkler and Nemeth[*8*] have described the effect. It is also known from so-called condensate gas wells containing carbon dioxide with gas[*9*]. With a temperature above 71°C (160°F) and a carbon dioxide partial pressure above $9.85 \times 10^7$ N/m$^2$ (15 psi), such wells are considered to be quite corrosive [0.9 mm per year = 36 mpy (mils per year)]. Usually corrosion is reduced to a low level by alloying with 9 percent nickel or eliminated by alloying with 12 percent chromium.

The velocity effect in condensate gas wells is illustrated by the virtual absence of attack in the case of a gas flow of 1.31 m/s (4.3 ft/s) at $2.62 \times 10^{10}$ N/m$^2$ (4000 psi), while at 5.88 m/s (19.3 ft/s) and $1.31 \times 10^{10}$ N/m$^2$ (2000 psi) attack is excessive. Furthermore, severe corrosion occurs at any points of turbulence as well as a few inches beyond pipe joints[*10*].

In the present case, both initial temperature, carbon dioxide partial pressure and gas velocity are higher than is usual for condensate wells. It may be assumed that the process of metal attack takes place by impact removal of the larger crystals of ferrous carbonate, opening new sites for attack. At the same time, the continuous renewal of liquid surface films in the high-velocity area provides for maximum carbon dioxide content on the metal-liquid interface, thus promoting the corrosion process.

## Conclusion

Extensive metal attack can occur in the presence of both erosion and corrosion, where either one of these effects taken individually would cause only insignificant or no damage.

## References

[*1*] Hobbs, J. M. and Rachman, D., in *Characterization and Determination of Erosion Resistance, ASTM STP 474*, American Society for Testing and Materials, 1970, p. 29.

[*2*] Shalnev, K. K., Varga, J. J., and Sebestyen, G., in *Erosion by Cavitation or Impingement, ASTM STP 408*, American Society for Testing and Materials, 1967, p. 220.

[*3*] Young, S. G. and Johnston, J. R., in *Symposium on Erosion and Cavitation, ASTM STP 307*, American Society for Testing and Materials, 1961, p. 186.

[*4*] Schulmeister, R., in *Erosion by Cavitation or Impingement, ASTM STP 408*, American Society for Testing and Materials, 1967, p. 109.

[5] Evans, U. R., *Corrosion and Oxidation of Metals*, Edward Arnold Ltd., London, 1967, pp. 160–164.
[6] Grover, K. C. and Mayar, M. R., *Agra University Journal of Research*, Vol. 6, Part 1, 1957, pp. 35–38.
[7] Thiruvengadam, A., in *Erosion by Cavitation or Impingement, ASTM STP 408*, American Society for Testing and Materials, 1961, p. 22.
[8] Winkler, G. and Nemeth, M., "The Effect of Contaminations in Carbon Dioxide on the Corrosion Caused by the Gas," *41st Corrosion Week, Manifestation European Federation of Corrosion*, 1968, pp. 788–791.
[9] Carlson, H. A., *Industrial and Engineering Chemistry*, Vol. 41, 1949, p. 644.
[10] Reynolds, R., private communication.

*Terence McGuinness* [1] *and A. Thiruvengadam* [2]

# Cavitation Erosion—Corrosion Modeling

**REFERENCE:** McGuinness, Terence and Thiruvengadam, A., "**Cavitation Erosion–Corrosion Modeling,**" *Erosion, Wear, and Interfaces with Corrosion, ASTM STP 567,* American Society for Testing and Materials, 1974, pp. 30–55.

**ABSTRACT:** Due to the increased occurrence of cavitation erosion in hydrodynamic systems operating in an ocean environment, there is a need to study the role of corrosion on the process of cavitation erosion. Previously, for noncorrosive systems, correlation of experimental data with the theory of erosion resulted in a time-scale modeling law of erosion. The changes in this scaling law due to corrosion were then investigated. A high-frequency, 20 kHz, piezoelectric vibratory apparatus was employed to generate erosion time history data for HY-130, HY-80, SAE 1020 steels, and Al 5086 H117 at several different erosion intensities in sea and distilled water. Results indicated that the relative erosion rate curves for materials susceptible to corrosion were different, and that the changes due to corrosivity increased with increasing erosion intensities. By coupling changes in corrosivity with maximum erosion rate increases, and times to the maximum rates, it is possible to make prototype performance predictions for either seawater or distilled water conditions. Qualitative relationships were found between the relative erosion rates and galvanic potentials of tested materials. A mechanism was proposed to account for the corrosive influence on erosion based on hydrogen-generated micropit destruction of a material surface that accelerates cavitation erosion.

**KEY WORDS:** cavitation erosion, corrosion, modeling, erosion, vibration, galvanic corrosion, Weibull density functions, parameters, high-strength steels, aluminum, erosion strength, erosion intensity

For many high-speed systems operating in the marine environment, a designer must cope with the combined problems of cavitation erosion and corrosion of materials. Erosion causes extensive damage to hydraulic

[1] Formerly graduate student, The Catholic University of America; presently, senior engineer and head, Advanced Studies Department, ManTech of N. J. Corp., Rockville, Md. 20852.

[2] Professor of mechanical engineering and director, Institute of Ocean Science and Engineering, The Catholic University of America, Washington, D. C. 20017.

systems such as ship propellers[*1*],[3] hydrofoils[*2*], and pumps[*3*] among others. Corrosion can also destroy many susceptible materials[*4*]. Coupling the two mechanisms, even the most resistant materials can be severely damaged.

Figure 1 shows the engineering aspects of cavitation erosion involved

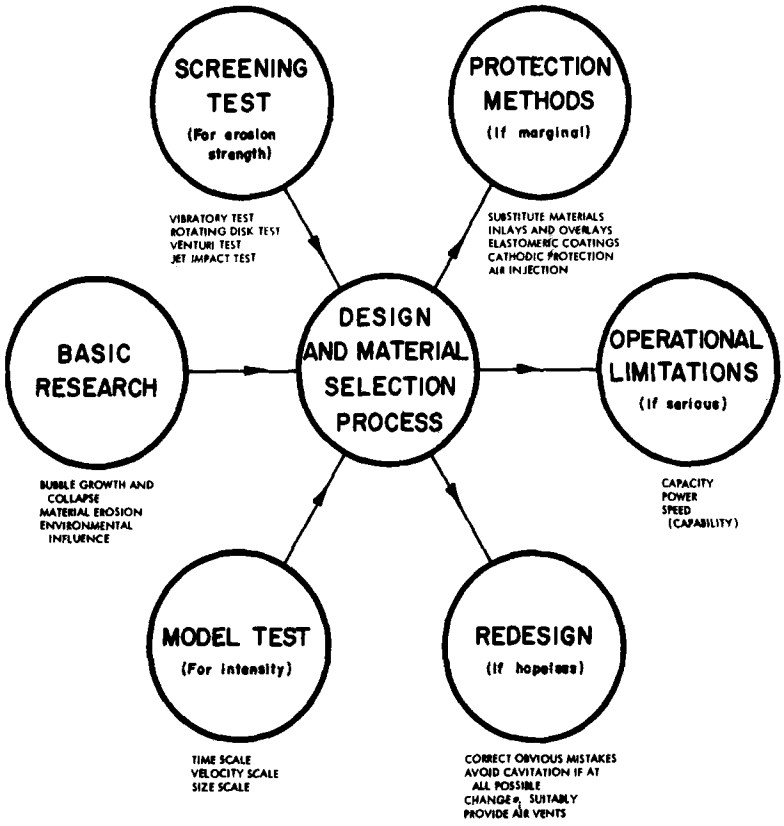


FIG. 1—*Engineering aspects of cavitation erosion.*

[3] The italic numbers in brackets refer to the list of references appended to this paper.

in design and material selection[5]. Our investigation concentrated on three of the aspects, namely, model testing (in particular the time-scale modeling); basic research on material erosion and the environmental influence of corrosion; and finally screening tests, employing the ASTM standard vibratory apparatus[6] in both sea and distilled water.

Previously, Thiruvengadam[7] suggested model scaling laws for non-corrosive systems, based on model testing to aid in predicting prototype performance. The basis of the time-scale model law is the relation between the relative erosion rates and relative exposure periods for several materials. The purpose of our program was to see how corrosive environment affects this relation and to explore the reasons for these effects.

As shown in Fig. 2, cavitation erosion is known to be time dependent

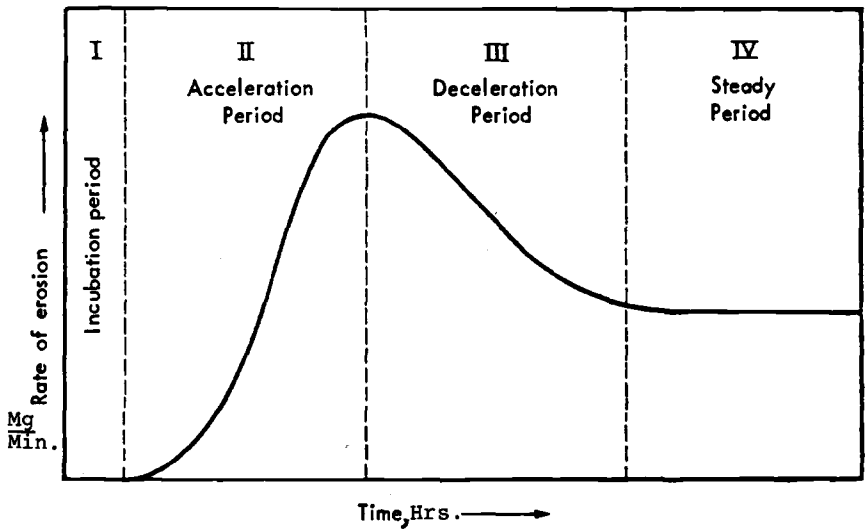


FIG. 2—*Rate of erosion versus time.*

from previous investigations[8–10]. Four distinct periods are described, namely, incubation, acceleration, deceleration, and steady state. Both Heymann[11] and Thiruvengadam[12] have proposed theories of erosion to explain the time-dependent nature of erosion. Experimental data[13,14] have shown a correlation with the theory for noncorrosive systems. Essentially, it was found that over a wide range of materials tested, there existed a definite relationship between the relative erosion rate and relative exposure time in a quantitative manner regardless of erosion intensity tested. This conclusion led to the possibility of testing a "weak" material at a

high erosion intensity in the laboratory to stimulate the erosion behavior of a "resistant" material in the field at a lower erosion intensity. This time-scale modeling procedure is outlined in Fig. 3.

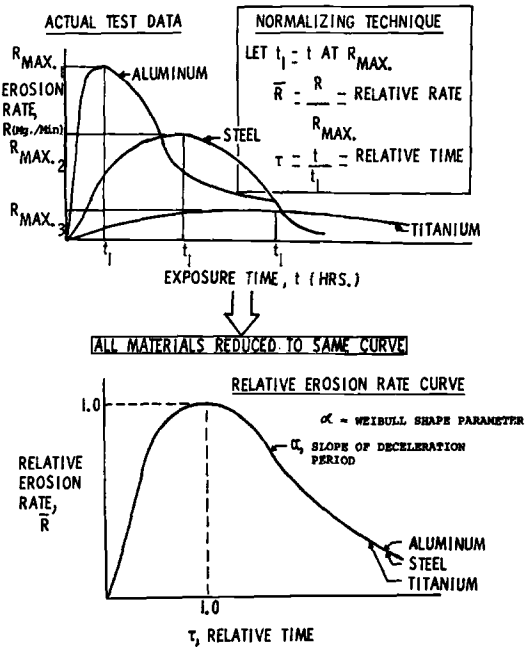


FIG. 3—*Basis of time-scale modeling.*

There have only been a few studies involved in determining the influence of a corrosive environment on the time-scale erosion modeling law. The main drawback to any testing has been the much longer time scale for corrosive damage versus erosive damage. However, in previous accelerated velocity corrosion testing, the corrosion rate has been accelerated by several orders of magnitude. For instance, in tests with carbon steel, Tuthill and Schillmoller[*15*] found that the corrosion rate increased from 5 to 300 mils per year (1 mil = $10^{-3}$ in.) by changing the velocity from zero to 120 ft/s. In jet impingement testing[*16*], the maximum depth of attack was quite substantial for many materials[*17*] in a short time span. Thus, there is evidence that the time scale of corrosion could be accelerated under certain conditions to model erosion along with corrosion in the laboratory.

The present research directs itself to a systematic investigation of the influence of corrosion on the erosion time-scale model law. Several mechanisms have been considered concerning the role of corrosion on erosion[*18–29*]. However, the previous studies did not examine the corrosive influence directly when the time scale could be controlled.

## Experimental Apparatus and Procedures

The test apparatus for the combined erosion and corrosion studies consisted mainly of two instruments, a piezoelectric vibratory unit and a potentiostat, seen schematically in Figs. 4 and 5. The new ASTM standard vibratory appartus[*6*] permitted variations in erosion intensity, liquid mediums, and test material. The potentiostat was used for measuring the test materials' galvanic potentials to compare them with other materials' potentials in our test program. According to LaQue[*30*], it is very important to ascertain potentials for a particular area, in this case, for the erosion specimen area. In the erosion test procedure, only the surface of the specimen was subject to cavitation and corrosion. Then for any corresponding galvanic potential reading, the tested area should be limited to the specimen surface, as seen by the Teflon-ringed insert in Fig. 5.

The materials tested were: HY-130, HY-80, and SAE 1020 steels and Al 5086 H117; along with limited testing of 90/10 and 70/30 copper-

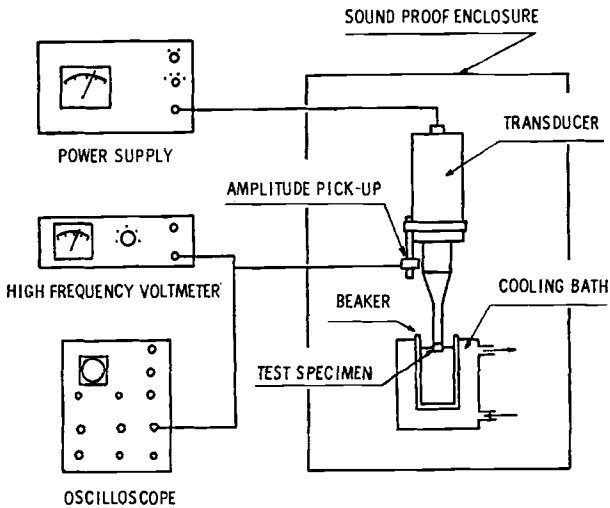


FIG. 4—*Schematic of vibratory cavitation erosion apparatus.*

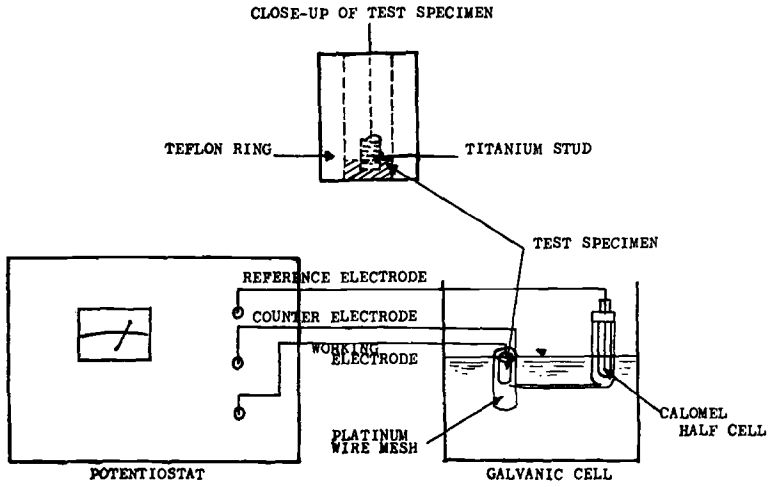


FIG. 5—*Schematic of potentiostat apparatus.*

nickel. The steels were chosen for their widespread use in marine systems, high erosion strength, and susceptibility to corrosion. The aluminum, selected expressly for its immunity to the marine environment, was chosen also for its low erosion strength. The cupro-nickels, with erosion strengths between aluminum and the steels, possessed good corrosion resistance. Thus, the test materials' erosion strengths and corrosion resistances varied over a wide range.

The erosion test procedure subjected the test materials to several vibrational amplitudes, measured in mils (ranging from 2.5 to 1.0 mils), which could be correlated with corresponding erosion intensities[*28*] in both sea and distilled water at a constant frequency of 20 kHz and 72°F (22°C) in a container of fixed dimensions. A low-form, 800-ml, 4-in.-diameter glass beaker contained 600 ml of test liquid. Glass was used to avoid any galvanic coupling action of the specimen with a metallic container. The specimen was machined to a diameter of 0.625 ± 0.002 in. and the surface mechanically polished with a number 320 emery paper. Upon eroding the material for a prescribed time interval, the specimen was weighed with an analytical balance accurate to ±0.1 mg and its weight loss recorded. Several specimens (at least three per material per test liquid) at given vibration amplitudes were eroded until a reasonably steady-state value for the weight loss rate was obtained. ASTM standard procedures[*6*] were employed in collecting these data. Figures 6 and 7 show the rate of erosion as a function of exposure period at various amplitudes of

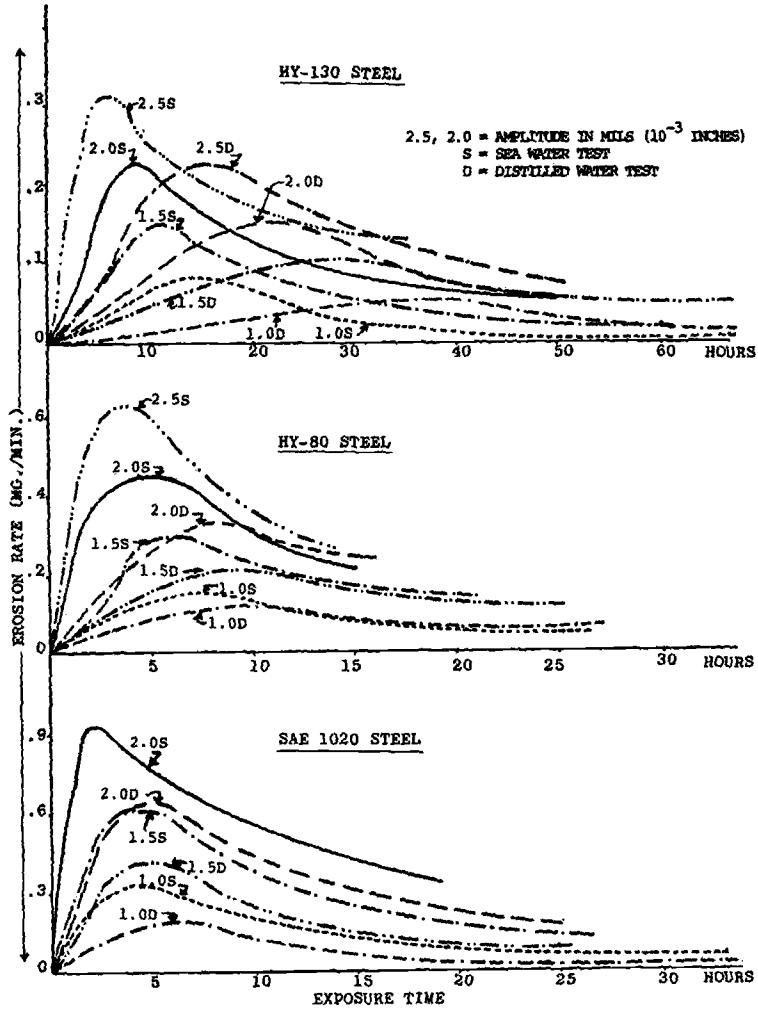


FIG. 6—*Erosion rate curve for HY-130, HY-80, and SAE 1020 steels.*

vibration both in distilled and synthetic seawater for the six materials tested.

The exposure time varied significantly from material to material depending upon its erosion strength. For example, Al 5086 H117 at a 2.0-mil vibrational amplitude, in either test liquid, approximated a steady erosion rate in 2.5 h. Test intervals were as short as 5 min in this case. For HY-130 steel at a 1.0-mil amplitude in distilled water, test intervals were as long as 13 h. The reason for the various intervals is due to the confine-

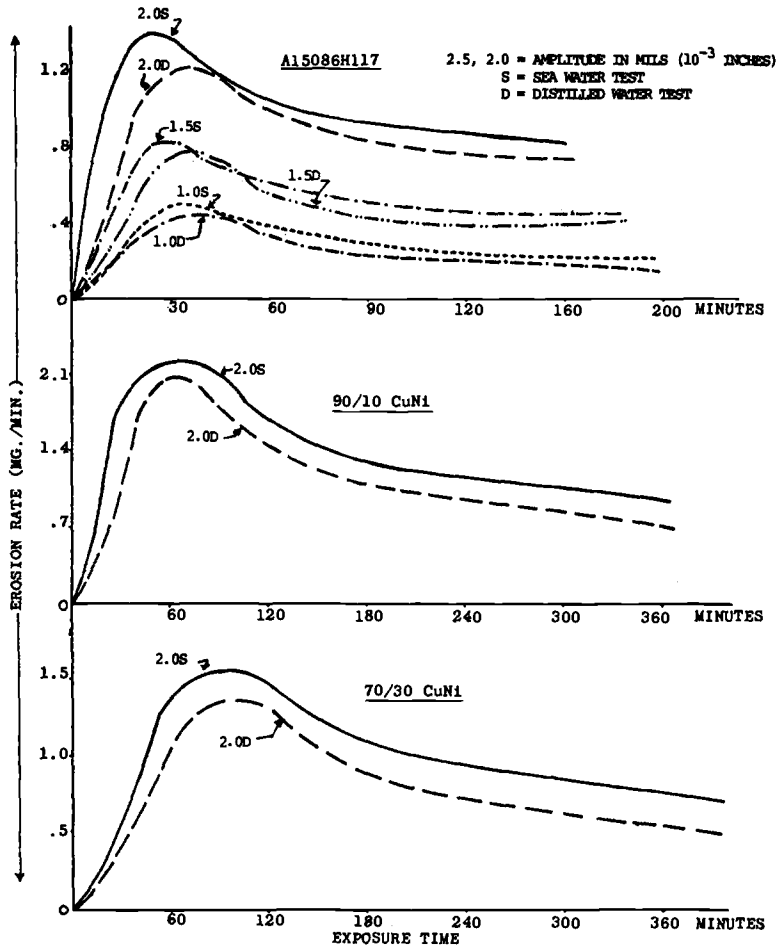


FIG. 7—*Erosion rate curve for Al 5086 H117, 90/10 copper-nickel, and 70/30 copper-nickel.*

ment of the beaker containing the test liquid. There is an inherent problem that the liquid used will become contaminated with eroded or corroded material from the specimen. It is possible that chemical changes in the fluid could affect its corrosivity relative to the test material. It was shown by Waring et al[*28*], that contamination of corrosive products affects the relationship between the erosion rate and amplitude of vibration due to changes in the conductivity of the electrolyte[*31*].

The synthetic seawater was formulated according to the ASTM Specification for Substitute Ocean Water (D 1141-52); see Table 1.

TABLE 1—*Chemical composition of synthetic seawater*[a]

| Compound | Concentration, g per liter |
|---|---|
| NaCl | 24.53 |
| MgCl | 5.20 |
| $Na_2SO_4$ | 4.09 |
| $CaCl_2$ | 1.16 |
| KCl | 0.695 |
| $NaHCO_3$ | 0.201 |
| KBr | 0.101 |
| $H_3BO_3$ | 0.027 |
| $SrCl_2$ | 0.025 |
| NaF | 0.003 |
| $Ba(NO_3)_2$ | 0.0000994 |
| $Mn(NO_3)_2$ | 0.0000340 |
| $Cu(NO_3)_2$ | 0.0000308 |
| $Zn(NO_3)_2$ | 0.0000096 |
| $Pb(NO_3)_2$ | 0.0000066 |
| $AgNO_3$ | 0.00000049 |

[a] ASTM D 1141-52, Substitute Ocean Water.

The galvanic potentials for the erosion specimens were measured with the potentiostat using a calomel half cell as the reference electrode. Figure 8 plots the potentials into a galvanic series which correlates to previously published series[*15*].

## Results and Discussions

As shown in Figs. 6 and 7, the range of maximum erosion rates varied from 2 mg/min for a copper-nickel alloy to 0.2 mg/min for HY-130 steel, with both materials tested at a vibrational amplitude of 2 mils in synthetic seawater. Similarly, the exposure periods needed to reach a steady-state erosion rate varied from 2½ h for most of the Al 5087 H117 tests to 115 h for the 1.0-mil, distilled water HY-130 steel tests. Both distilled water and synthetic seawater were used as test liquids. Four different amplitudes of vibration were considered (Fig. 6). The importance of testing the materials for extended periods of exposure, particularly in a corrosive medium, is brought forth clearly in Fig. 6 for the case of HY-130 steel. At a vibrational amplitude of 2.5 mils in synthetic seawater, the maximum erosion rate is reached in 7 h, whereas in distilled water, at a 1.0-mil amplitude, the maximum erosion rate is reached in 40 h.

In our investigations, we were concerned primarily with the ability to predict the erosion potential of materials in a corrosive environment. The theory of erosion[*12*] has shown that the relative intensity of erosion, $\bar{I}$,

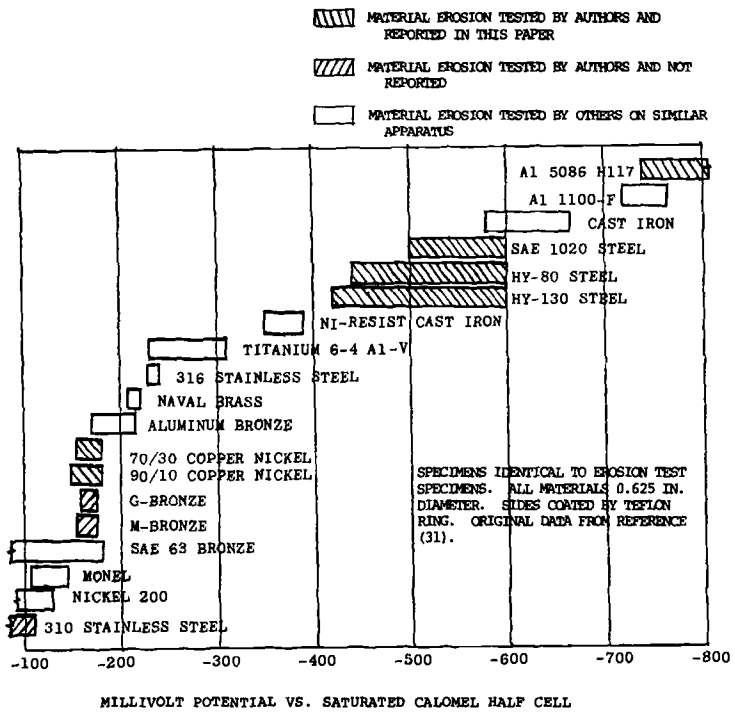


FIG. 8—*Galvanic series in synthetic seawater for laboratory tested materials.*

intensity divided by the maximum intensity (related to the maximum erosion rate), $\bar{I} = I_e/I_{max}$, depends upon an efficiency factor, $\eta$, which is a measure of a material's ability to absorb energy. The efficiency factor is time dependent. This is based on the assumption that when a particle of material erodes, it behaves as a fatigue specimen. One statistical distribution of the probability of fatigue failure after a number of cycles, is known as the Weibull distribution. The time dependent erosion rate can be described using this distribution with the slope of the deceleration section of the curve being defined by $\alpha = dR/dt$ where $R$ = erosion rate; see Fig. 3. For certain values of $\alpha$, the Weibull shape parameter, a number of well-known distributions can be generated, such as the exponential distribution for $\alpha = 1$; Rayleigh distribution for $\alpha = 2$, and normal distribution for $\alpha = 3.57$. As $\alpha$ decreases, the attenuation of the curve goes to zero. The family of Weibull curves in Fig. 9 shows the time dependency of erosion as a function of $\alpha$. In order to evaluate the influence of corrosion on the shape parameter, we replotted most of the erosion data shown in Figs. 10 and 11. The value of the shape parameter decreases as the erosion

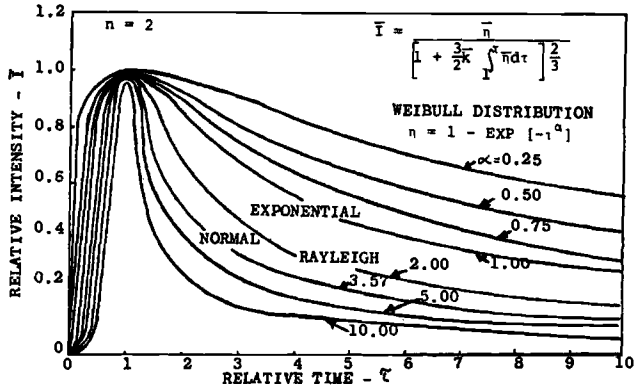


FIG. 9—*Family of erosion history curves for* n = 2.

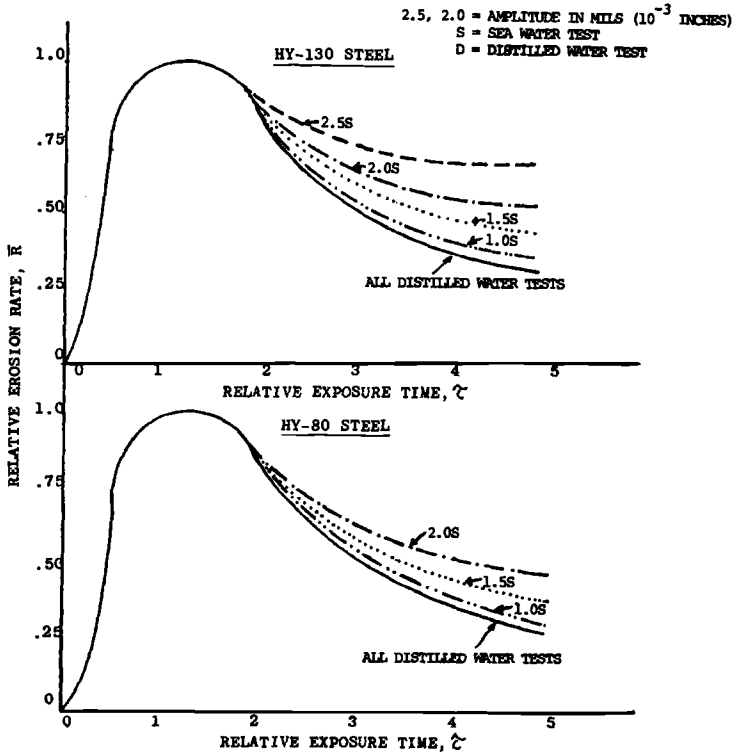


FIG. 10—*Normalized erosion rate curves for HY-130 and HY-80 steels.*

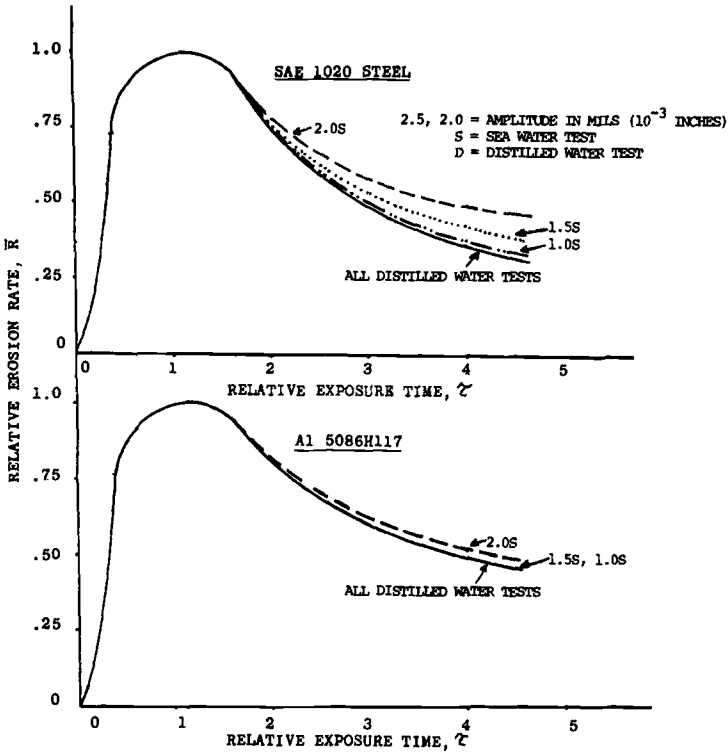


FIG. 11—*Normalized erosion rate curves for SAE 1020 steel and Al 5086 H117.*

rate increases, thus deceleration is less at higher intensities. There seems to be a general qualitative trend relating the galvanic potential to the shape parameter in seawater as illustrated in Fig. 12. It appears that the more prone a material is to corrosion, the larger the change in the shape parameter. As a natural consequence, the difference between the relative erosion rates in seawater and in distilled water is found to be greater for corrosion-prone materials as compared to materials that are not susceptible to corrosion in seawater. Thus, a material's corrosion resistance appears to be a significant factor in erosion rate data.

An exception to the general qualitative trend is Al 5086 H117. It is noted that this material was designed to have good corrosion resistance in seawater when not coupled to another material more noble than itself. The galvanic potential is one measure of an alloy's corrosivity. In the case of the aluminum, such a measure is somewhat meaningless. However, for the other five materials reported on herein plus analysis of results from seven other materials tested in similar conditions but not included herein,

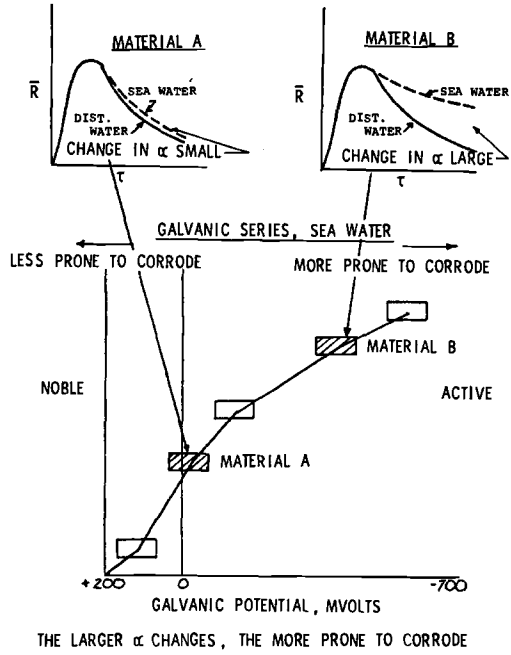


FIG. 12—*Relationship between curve slope changes and the galvanic series.*

the trend just mentioned holds true. If Al 5086 H117 was tested while galvanically coupled to a more noble material and thus exhibited its true corrosivity or galvanic potential, it is believed that this aluminum also would show changes in its relative erosion rates.

As discussed previously, the maximum rate of erosion and the time to reach the maximum rate (called the characteristic time), depends upon the intensity of erosion and, as shown in Figs. 13 and 14, upon the amplitude of vibration. The maximum erosion rate increases as the 1.5 power of the amplitude of vibration both in seawater and in distilled water. (Previously, in noncorrosive testing[*13*,*14*,*28*], the steady-state erosion rate had been found to increase as the amplitude squared. Since then, there has been some questions on the validity of the steady-state rate[*11*]. The maximum erosion rate is more easily discernible and more important for prototype predictions.) The characteristic time decreases linearly with increasing amplitude; and it decreases more rapidly in synthetic seawater as compared to the decrease in distilled water as a function of a material's corrosivity or galvanic potential.

Another interesting result is obtained by recalling the basic equation from the theory of erosion[*12*], namely,

$$I_e = S_e \times R_{max}$$

where

$I_e$ = erosion intensity,
$R_{max}$ = maximum erosion rate, and
$S_e$ = erosion strength.

Since the erosion intensity does not change in seawater from distilled water under fixed conditions[*12*], the fact that $R_{max}$ increases in seawater indicates that the erosion strength must decrease in seawater; see Fig. 13. This decrease is independent of $I_e$ and is true for corrosion-sensitive materials only. Previous to this study, many researchers[*32*] thought the influence of corrosion on erosion was to reduce the material strength of a substance in one of several postulated ways. Now it is shown that corrosion does decrease the erosion strength, and only affects materials that are prone to corrode.

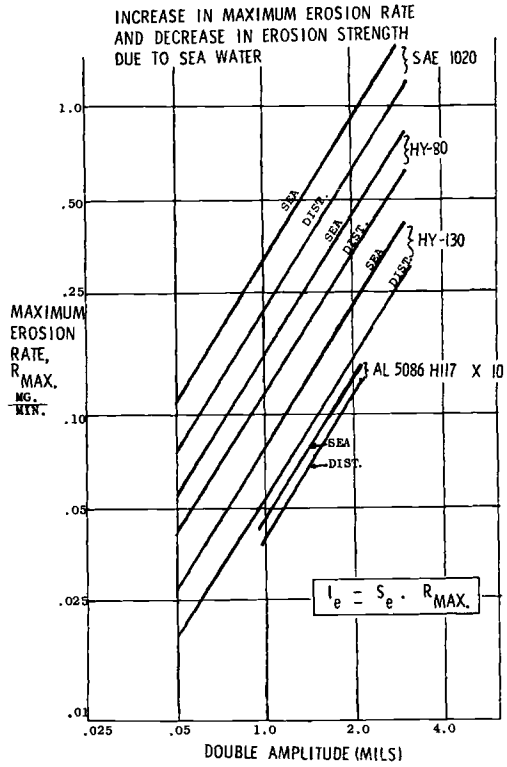


FIG. 13—*Maximum erosion rate versus amplitude.*

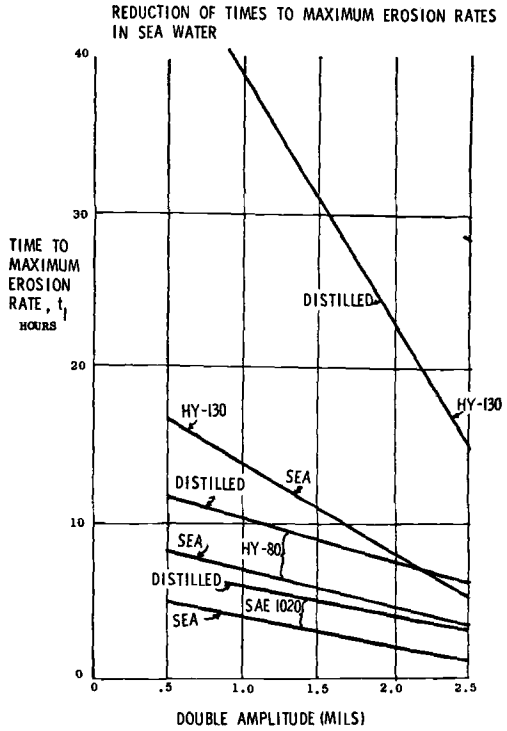


FIG. 14—*Characteristic time versus amplitude.*

This is a logical conclusion if one realizes that corrosion, by an electrochemical mechanism, will attack a susceptible material independently of the amount of cavitation erosion intensity at the material surface. A material either will be susceptible to corrosion or will not be susceptible, regardless of the fluid dynamic conditions (cavitation) present.

Using the foregoing conclusion, a new direct method of finding a material's erosion strength can be made with the use of a simple cavitation erosion apparatus. The direct method could eliminate the previous limitations for erosion strength calculations as outlined in Ref *33*.

Based on the results of Figs. 10, 11, 13, and 14, a method of predicting prototype performance (generating a material's erosion curve at any set of hydrodynamic conditions and environmental influences) can be proposed. As outlined in Fig. 15, the erosion history curve is defined fully knowing three items: the maximum erosion rate, $R_{max}$; the characteristic time, $t_1$; and the attenuation slope, $\alpha$. All of these variables are found from model testing as explained previously, and the values can be extrapolated over a wide range of erosion intensities, which is the governing hydrodynamic condition of the prototype.

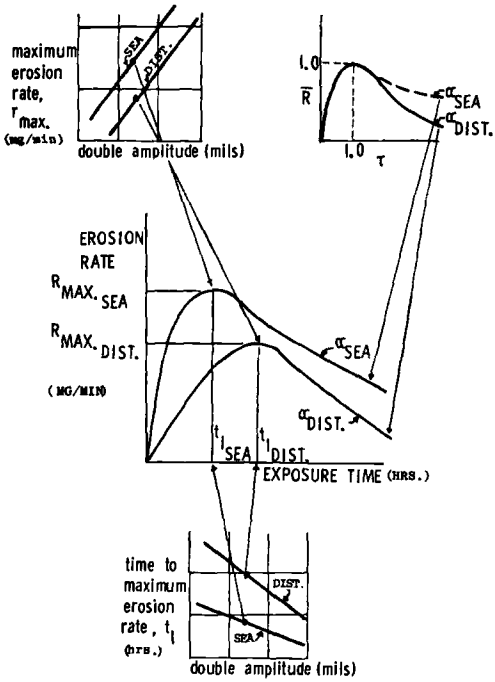


FIG. 15—*Prototype prediction from modeling scheme.*

In summary, it may be stated that the previous findings of Thiruvengadam[7] for noncorrosive environments are again confirmed by our present investigations. The value of the shape parameter for noncorrosive environments remained the same for the materials tested under this program both in synthetic seawater and in distilled water. However, the value decreased in a corrosive environment as the erosion intensity increased.

## A Mechanism Which Explains a Few Observations Peculiar to Corrosive Environments

The generally observed erosion pattern changes from distilled water to seawater for corrosion-prone materials are seen in Fig. 16. The erosion pattern in distilled water appeared shallower in the middle portion than on the outside deeper trough of the specimen. Seawater specimens, on the other hand, were generally eroded flat beginning inside the outer uneroded rim across to the specimen's center. Also, seawater specimens generally formed more pits shallower in depth than the distilled water specimens that initially only had deep pits in the middle "rise" area. The cross section of the seawater pattern in the deceleration zone, see Fig. 2, was always

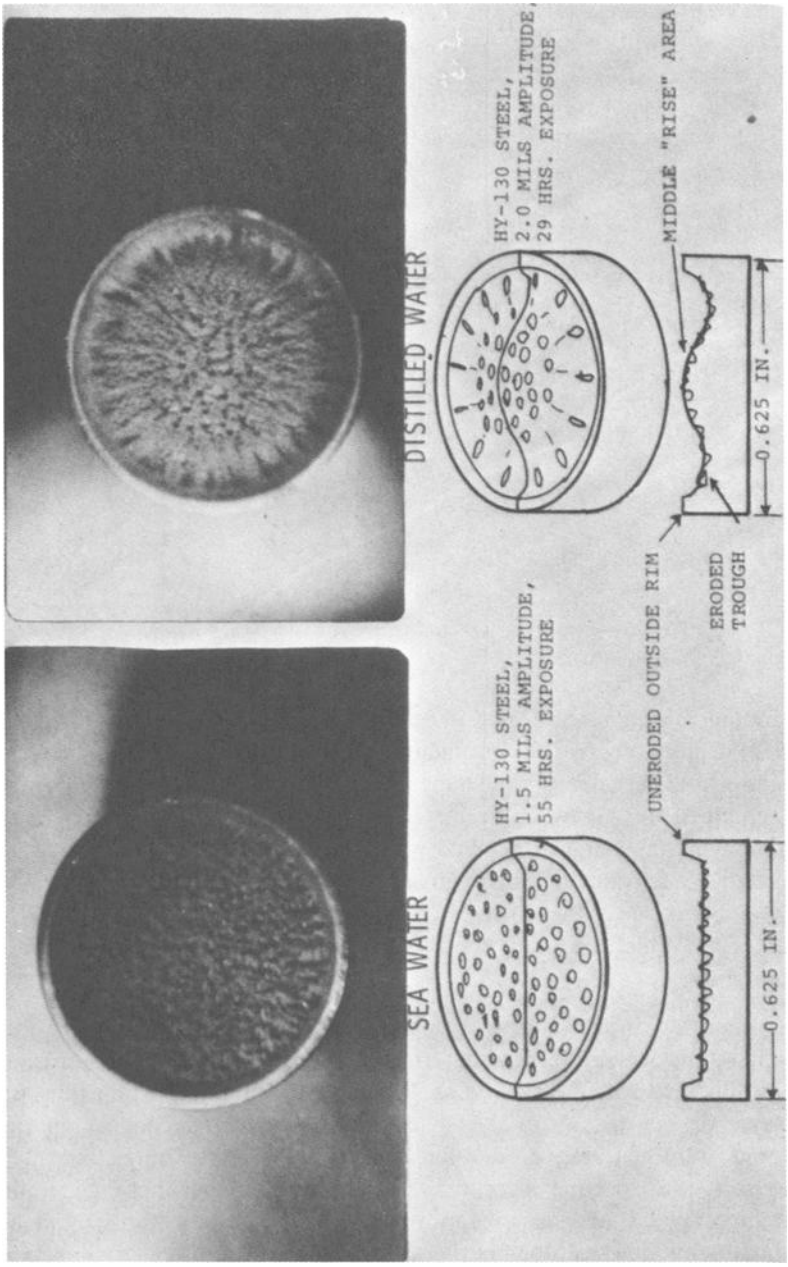


FIG. 16—*Erosion patterns of specimens.*

flatter, not as deeply pitted, and smoother in general appearance than the deeply pitted distilled water specimens.

The foregoing changes in the seawater pattern seemed to indicate a basic mechanism for the deceleration period of the erosion history curves. Figures 17 and 18 outline the mechanism which starts with Peterson's galvanic cell theory[*34*] at an initial erosion pit. Going one step further,

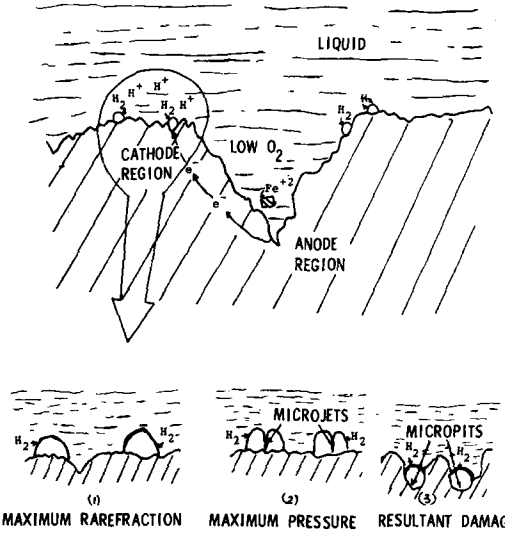


FIG. 17—*Mechanism of corrosion-accelerated cavitation damage.*

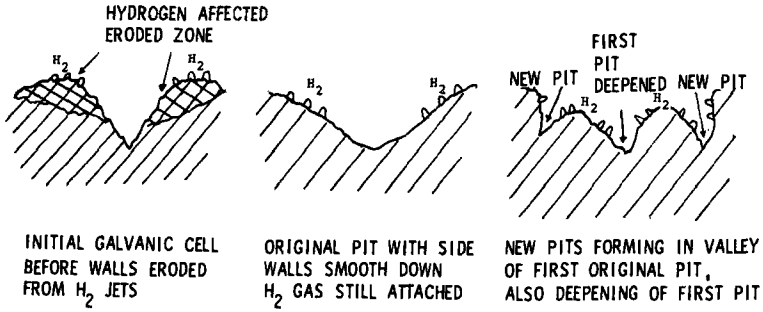


FIG. 18—*Scouring-down process of erosion pits by hydrogen gas.*

it is assumed that the hydrogen gas generated at the cathode acts as a stationary cavity when attached to the surface. With the aid of weak shocks from symmetrical bubble collapses, the hydrogen cavity produces

a microjet. This mechanism incorporates the recent theory of Tulin[*35*] of such a microjet or ultrajet possibility in asymmetrical bubble collapse. The ultrajets then cause severe local damage producing numerous micropits. Eventually, the original pit walls would be "smoothed down" by the micropit damage, allowing more damage to occur. The reason is because the efficiency of damage, based on the theory of erosion[*12*], depends, in part, on the bubble collapse distance from a material surface. The "smoothing down" process would decrease the average distance between surface and bubble collapse. Thus, the damage rate of "smooth" specimens would be greater than that for deeply pitted materials where the energies of collapsing bubbles is quickly attenuated by the relatively large distance to the pit bottoms. The erosion rate for seawater "smooth" specimens would continue at a high level due to corrosion-generated damage. The deceleration zone of the erosion history curve would reflect this higher erosion rate level by a lower shape parameter value as in Figs. 10 and 11. Referring to Fig. 9, it is recalled that the shape parameter value decreases for greater relative intensity and consequently for higher erosion rates.

## Conclusions

The interacting role of corrosion on erosion of materials was studied in a quantitative manner. At the intensities of erosion considered in this study, the erosion-corrosion rates increased with exposure period, reached a maximum and then decreased to a nearly steady value. This confirmed previous findings by many investigators primarily for noncorrosive environments. The relative erosion rates (the ratio between the maximum rate of erosion and the rate of erosion at any exposure period) depend only on the relative exposure periods (the ratio between the exposure period and the characteristic time) in noncorrosive systems. However, the shape parameter decreased as the erosion intensity increased in a corrosive environment. There seems to be a qualitative trend of dependency between the increase in galvanic potential and the decrease in the value of the shape parameter, noting the Al 5086 H117 exception explained previously. Furthermore, the corrosive influence decreased the characteristic time and increased the maximum erosion rate. These values have been quantitatively evaluated at various amplitudes of vibration both in synthetic seawater and in distilled water. A scheme for predicting prototype performance from model results was presented. The erosion pattern in distilled water generally appeared shallower in the middle of the test surface than on the outside deeper trough of the specimen with several deep pits present through the cross section. On the other hand, the pattern of erosion in seawater was

generally flatter and smoother from the outside noneroded rim to the middle of the test surface. Finally, a possible mechanism was presented to explain this observation that in corrosion-prone materials, increased damage was ascribed to hydrogen-generated micropits that attacked initial erosion pit walls, allowing further accelerated erosion damage.

*Acknowledgments*

This research was supported by the U. S. Office of Naval Research, Contract No. N00014-67-A-0377-0008 NR 062-436 and was carried out by Dr. T. McGuinness toward his Ph.D. thesis under the direction of Dr. A. Thiruvengadam at the Institute of Ocean Science and Engineering of The Catholic University of America.

## References

[1] Ramsay, W., *Engineering*, Vol. 93, 1912, pp. 687–690.
[2] Morgan, W. B. and Lichtman, J. Z., *Symposium on Cavitation State of Knowledge*, American Society of Mechanical Engineers, 1969, pp. 195–241.
[3] Speller, F. N. and LaQue, F. L., *Corrosion*, Vol. 6, No. 7, 1950, pp. 209–215.
[4] Uhlig, H., Ed., *Corrosion Handbook*, Wiley, New York, 1948.
[5] Thiruvengadam, A., "Scaling Laws for Cavitation Erosion," presented at the *Symposium on Flow of Water at High Speeds*, organized by The International Union of Theoretical and Applied Mechanics, Leningrad, USSR, 1971.
[6] American Society for Testing and Materials, G-2 Committee on Erosion and Wear, Erosion Testing Standard, March 1972.
[7] Thiruvengadam, A., "On the Selection of Modeling Materials to Scale Long Term Erosion Behavior of Prototype Systems," *Proceedings*, 3rd International Conference on Rain Erosion and Allied Phenomena, Royal Aircraft Establishment, Farnborough, England, 1970.
[8] Hobbs, J. M., in *Erosion by Cavitation or Impingement, ASTM STP 408*, American Society for Testing and Materials, 1967, pp. 159–179.
[9] Plesset, M. S. and Devine, R. E., *Journal of Basic Engineering, Transactions*, American Society of Mechanical Engineers, Dec. 1966.
[10] Thiruvengadam, A., "A Comparative Evaluation of Cavitation Damage Test Devices," *Proceedings*, Symposium on Cavitation Research Facilities and Techniques, American Society of Mechanical Engineers, New York, May 1964.
[11] Heymann, F. J., in *Erosion by Cavitation or Impingement, ASTM STP 408*, American Society for Testing and Materials, 1967, p. 70.
[12] Thiruvengadam, A., in *Proceedings*, 2nd Meersburg Conference on Rain Erosion and Allied Phenomena, Vol. II, A. A Fyall, Ed., Royal Aircraft Establishment, Farnborough, England, 1967, pp. 605–651.
[13] Thiruvengadam, A. and Preiser, H. S., *Journal of Ship Research*, Vol. 8, No. 3, Dec. 1964.
[14] Thiruvengadam, A. and Waring, S., *Journal of Ship Research*, Vol. 10, No. 1, March 1966.
[15] Tuthill, A. H. and Schillmoller, C. M., "Guidelines for Selection of Marine Materials," 2nd edition, International Nickel Co., New York, 1971.
[16] Catalog of Specimens, Kure Beach-Harbor Island Museum, International Nickel Co., New York.

[17] Smith, C. A., "Velocity Effects on the Corrosion Rates of Metals in Natural Sea Water," *Society of Naval Architects and Marine Engineers*, Southeast Section, 10 May 1968.
[18] Beeching, R., *Transactions*, Institution of Engineers and Shipbuilders in Scotland, Vol. 85, 1942, pp. 210–238.
[19] Evans, U. R., *Engineering*, Vol. 155, 1943, p. 454.
[20] Foltyn, V., *Strojirenstvi*, Czechoslovakia, Vol. 2, No. 9, Sept. 1952, pp. 402–408.
[21] Krenn, H., *Maschinenbau und Warmewirtschaft*, 1948, pp. 81–87.
[22] Lichtman, J. Z., Kallas, D. H., Chatten, C. K., and Cochran, E. P., Jr., *Transactions*, American Society of Mechanical Engineers, Vol. 80, 1958, pp. 1325–41.
[23] Lichtman, J. Z. and Weingram, E. R., in *Proceedings*, Symposium on Cavitation Research Facilities and Techniques, American Society of Mechanical Engineers, May 1964, pp. 185–196.
[24] Nechleba, Miroslav, *Maschinenbautechnik*, Vol. 2, Feb. 1955, pp. 81–88.
[25] Petracchi, G., *La Metallurgia Italiana*, Vol. 41, No. 1, Jan.-Feb. 1949, pp. 1–6.
[26] Preiser, H. S. and Tytell, B. H., *Corrosion*, Vol. 17, 1961, pp. 535t–549t.
[27] Shal'nev, K. K., *Doklady Akademii Nauk*, USSR, Vol. 95, No. 2, 1954, pp. 229–232.
[28] Waring, S., Preiser, H. S., and Thiruvengadam, A., *Journal of Ship Research*, Dec. 1965.
[29] Wheeler, W. H., "Indentation of Metals by Cavitation," *Journal of Basic Engineering*, Paper No. 59-Hyd-15, American Society of Mechanical Engineers, Hydraulic Conference, 13-15 April 1959.
[30] LaQue, F. L., "Effects of Specimen Size on Results of Corrosion Tests," International Conference on Corrosion, Tokyo, Japan, 1972.
[31] McGuinness, T., "Cavitation Erosion-Corrosion Modeling in an Ocean Environment," Ph.D. thesis, Department of Civil and Mechanical Engineering, The Catholic University of America, Washington, D. C., 1973.
[32] Eisenberg, P. E., Preiser, H. S., and Thiruvengadam, A., *Transactions*, Society of Naval Architects and Marine Engineers, Vol. 73, 1965, pp. 241–286.
[33] Thiruvengadam, A., in *Erosion by Cavitation or Impingement, ASTM STP 408*, American Society for Testing and Materials, 1967, p. 22.
[34] Peterson, F. B., "Relationship Between Corrosion and Cavitation Phenomena," MFPG Technical Report No. 8, April 1971.
[35] Tulin, M. P., "On the Creation of Ultra-jets," L. I. Sedov, 60th Anniversary Volume, *Problems of Hydrodynamics and Continuum Mechanics*, Moscow, 1969.

# DISCUSSION

*A. F. Conn*[1]—This question is actually to allow the authors to emphasize the differences one might expect between their corrosive magnetostrictive erosion tests and the effects which one might observe during cavitation erosion caused by flow of a corrosive fluid past a surface. This point was not brought out during the oral presentation of the paper. Since much of the discussion which occurred after the talk was related to concern about the proposed micromechanism of hydrogen stimulation of the generation of pits and how this model seems to differ from certain observations of field difficulties which involve flow-generated cavitation erosion, the differences for vibratory tests in the laboratory should be discussed.

*C. M. Preece*[2]—Although unstressed aluminum alloys may be passivated in distilled water, when they are subjected to a tensile stress, they are found to be susceptible to stress corrosion cracking even in moist air. You should, therefore, consider both salt water and distilled water as active, rather than inactive, environments for aluminum alloys.

You postulate that atomic hydrogen is produced during cavitation, yet you do not consider the role of hydrogen embrittlement in erosion. Should you not take this into account in view of the fact that all the alloys you studied are known to be susceptible to hydrogen embrittlement?

*J. W. Tichler*[3]—The results of this interesting study are interpreted exclusively in terms of Thiruvengadam's "Theory of Erosion."[4]

In this theory, Dr. Thiruvengadam attaches special importance to the peak rate of volume loss. The time at which this peak rate occurs ($t_1$) appears as a characteristic time in a distribution, associated with the

[1] Principal research scientist and head, Materials Sciences Division, HYDRONAUTICS, Incorporated, Laurel, Md. 20810.

[2] Associate professor, Materials Science Department, State University of New York at Stony Brook, Stony Brook, N. Y. 11790.

[3] Metal Research Institute TNO, Apeldoorn, The Netherlands.

[4] Thiruvengadam, A., in *Proceedings*, 2nd Meersburg Conference on Rain Erosion and Allied Phenomena, Vol. II, A. A. Fyall, Ed., Royal Aircraft Establishment, Farnborough, England, 1967, pp. 605–651.

break out of wear particles. However, as has been stated previously,[5] it is not readily understandable why this characteristic time, which should anyhow be related to material properties, must be equal to the time at which the rate volume loss goes through a maximum. In other words, $t_1$ appears in two formulas, namely, in the $r$ of Formulas 7 and 9 of the theory,[4] and it is not made clear, why $t_1$ stands for the same property in both these formulas.

Another problem is that the cause of the decrease in erosion intensity is not clearly described. It is suggested that the decrease of the erosion intensity should be due to an increase of distance between the eroding surface and the collapsing cavities. However, it is much more probable that the decrease in erosion intensity at increasing mean depth of erosion is related to the surface condition of the eroding material. Eisenberg et al[6] did already observe that the peak of the rate-time curve coincides with the appearance of the first deep craters in the eroding surface. They did not, however, attribute the effect to gas bubbles which can be trapped in the craters, as was shown by Tichler et al.[7] More objections against the theory have been formulated by Hammitt.[8]

From the foregoing it follows that the physical meaning of the constants introduced in Thiruvengadam's theory (namely, the characteristic time $t_1$, the "shape parameter" $\alpha$ and the "attenuation exponent" $n$) is not clear. Thus, expressing the effect of seawater (compared with distilled water) on these parameters is not very useful to deepen the insight.

In my opinion it is more useful to analyze the mean depth of erosion versus time curve (as strongly encouraged by the new ASTM standard, mentioned by the authors), rather than the rate-time curves, and to investigate the effect of corrosion on the phenomena of uniform material removal and pit formation.[5]

From the authors' observations, it turns out that the resistance against uniform material removal is lower in seawater than in distilled water. This effect is more pronounced for the HY 130 and SAE 1020 steels than

[5] Tichler, J. W. and De Gee, A. W. J., in *Proceedings*, 3rd International Conference on Rain Erosion and Associated Phenomena, Vol. II, A. A. Fyall, Ed., Royal Aircraft Establishment, Farnborough, England, 1970, pp. 847–879.

[6] Eisenberg, P. E., Preiser, H. S., and Thiruvengadam, A., *Transactions*, Society of Naval Architects and Marine Engineers, Vol. 73, 1965, pp. 241–286.

[7] Tichler, J. W., Van den Elsen, J. B., and De Gee, A. W. J., *Journal of Lubrication Technology, Transactions*, American Society of Mechanical Engineers, Series F, Vol. 92, 1970, pp. 220–227.

[8] Hammitt, F. G., discussion on "Theory of Erosion" by A. Thiruvengadam, *Proceedings*, 2nd Meersburg Conference on Rain Erosion and Allied Phenomena, Vol. II, A. A. Fyall, Ed., Royal Aircraft Establishment, Farnborough, England, 1967, pp. 650–651.

for the HY 80 steel, which might be attributed to the 1 to 2 percent of chromium content in the HY 80 steel. For Al 5086 H117 the effect is less pronounced than for the steels. If the effect cannot be explained by simple addition of the erosion and corrosion effects, there are two possible explanations: either the corrosion is highly accelerated by chemical activation of the surface due to the impingements, or the erosion is accelerated due to decrease of the erosion resistance of the surface material by corrosive (that is, chemical) effects. I have the impression that the latter explanation is the correct one.

Further, the authors observed that in seawater the craters are shallower than in distilled water. This observation, in combination with the observation that the decrease of erosion rate is less pronounced in seawater than in distilled water, substantiates the hypothesis that the decrease in erosion rate is due to bubbles trapped in the craters. Obviously, gas bubbles will be trapped in deep craters more easily than in shallow craters.

*Terence McGuinness and A. Thiruvengadam (authors' closure)*—The authors greatly appreciate the constructive comments and questions in the discussions. The problems highlighted could be the basis for further meaningful research.

In referring to the different conditions created by various tests, Dr. Conn has raised an interesting and often discussed question. The basis of the vibratory device was to serve as a screening test for material properties, and, as such, the necessity of simulating the flow field was not that critical. As discussed in Refs *5* and *31* of the paper, if various hydrodynamic parameters are controlled and dynamic similitude attained, the flow field is essentially modeled.

There are currently several laboratories performing parallel experiments on both continuous-flow, venturi-type devices and vibratory tests. A more definitive answer to Dr. Conn's question should be forthcoming. However, it is felt that the mechanism of hydrogen stimulation of micropits is independent of the type of fluid flow involved in generating cavitation. Hydrogen remains on the surface of hydrophobic (water hating) and corrosion-prone alloys (Ref *31* of the paper). Hydrophobic materials are those materials that have low wetting abilities and thus have a tendency to form gas cavities with an adjacent liquid in cracks and crevices (Ref *31* of the paper). Also, hydrogen, acting as a stationary cavity, would follow the course of a pit into a material surface. Tulin's theory (Ref *35* of the paper) did not specify how the cavitation bubbles were generated. The important parameters were the present of a stationary cavity and the shock wave of a nearby imploding bubble or jet.

The proposed mechanism of micropit formation at the cathode region

by hydrogen stimulation, nevertheless, does not exclude other additional causes of accelerated cavitation erosion. Such damage by hydrogen can be caused by electrochemical action at anode areas deep within erosion pits.

Hydrogen embrittlement could possibly be another cause of accelerated erosion damage. There are results indicating that many alloys are susceptible to embrittlement. Thus, such a phenomenon could be examined further in relation to erosion, as Dr. Preece indicated.

The implication of hydrogen embrittlement is not in contrast to the authors' mechanism of pit formation. Both mechanisms lead to local weakening of the material surface, the initiation of pits or cracks within the material and the focusing of energies in small volumes of material. Only the origins of the two mechanisms differ. Thus, for corrosion-prone materials, electrochemical action could initiate hydrogen formation. Even without a corrosive environment, hydrogen embrittlement could be acting at the surface, locally weakening the material's erosion strength. However, at the high strain rates of cavitation, it is very likely that hydrogen is not forced into the surface but rather remains as a gas bubble affixed to the surface ready to act as an ultrajet (Ref *31* of the paper).

Dr. Tichler's question of the physical meaning of the various constraints in the "Theory of Erosion" has been raised for several years. Actually both Tichler's research and others have demonstrated exactly the characteristics of the theory in question. The difference lies only in the intensity of erosion found in the test apparatus. Dr. Tichler's research, for the most part, has been concerned with intensities near the threshold of erosion. The resulting data often were much more erratic than results from higher intensity tests. One simple reason is related to the fatigue failure mechanism of material loss. Since fatigue failure and erosion are assumed to be statistical in nature, it is quite possible that for numerous test intervals in a threshold intensity test, a material might not exhibit substantial weight losses. The resulting curve of weight loss or mean depth of erosion versus time would be very erratic. It is suggested that Dr. Tichler conduct further tests in the range of the ASTM standard (Ref *6* of the paper) one watt per meter squared intensity to confirm these statements.

Even though the hydrogen stimulation mechanism is electrochemical in nature, the proposed erosion is assumed to be purely mechanical. This, of course, does not preclude changes in surface conditions, but the conditions only prepare the material surface for accelerated damage by reducing the erosion strength.

The resistance against uniform material removal, as mentioned by Dr. Tichler, was observed to be lower in seawater than in distilled water. But the cause of shallower craters was explained in Fig. 17. More

erosion occurred on the walls of the initial pit than in the bottom of the pit. The total amount of material removal is greater when the walls are damaged more quickly than the pit bottom due to the smaller distance between the mean eroded surface and the origin of erosion intensity. The formation of gas bubbles trapped in deep craters is not necessarily the reason for the erosion rate decrease. Even without the entrapped bubbles, a deep cratered material would have its mean surface of erosion at a much further distance away from the collapsing bubbles than the material just mentioned.

*J. W. Tichler,*[1] *A. W. J. de Gee,*[1] *and H. C. van Elst* [1]

# Applied Cavitation Erosion Testing

**REFERENCE:** Tichler, J. W., de Gee, A. W. J., and van Elst, H. C., "Applied Cavitation Erosion Testing," *Erosion, Wear, and Interfaces with Corrosion, ASTM STP 567*, American Society for Testing and Materials, 1974, pp. 56–76.

**ABSTRACT:** When a material has to be applied on locations where cavitation is expected, the resistance against uniform material removal from the surface ($R_e$) and the resistance against pit formation ($r_p$) are of paramount importance.

Experiments with steels and copper-nickel alloys showed that for these materials $R_e$ is proportional to the true ultimate tensile strength ($\sigma_B^*$) to the 2.3rd power. The tests with the steels were performed under different pressures and at different temperatures. It was found that variations in pressure and temperature did not affect the value of the power exponent. It was further shown that deformation can have a considerable and essentially unpredictable influence on the erosion resistance of materials with a relatively complicated structure. In particular grain boundary precipitation is important in this respect.

Experiments with nitriding steel, carburizing steel, maraging steel, and two cobalt alloys in different conditions of application showed that $r_p$ is determined primarily by the structure of the materials. In this case the product of $R_e$ and $r_p$ (that is, the time to pitting $t_p$) was found to be particularly useful for screening purposes. In the mechanism of pit formation, surface fatigue as well as corrosion can play important roles.

**KEY WORDS:** erosion, cavitation, erosion resistance, pit formation, strength, spalling fatigue, corrosion, metals, magnetostrictive oscillator, evaluation, tests

The cavitation behavior of materials is generally described in terms of the mean depth of erosion rate[*1*].[2] Hirotsu[*2*] draws some attention to

[1] Project leader, head of the Tribology Department and head of the Physical Department, respectively, Metal Research Institute TNO, Apeldoorn, The Netherlands.

[2] The italic numbers in brackets refer to the list of references appended to this paper.

the phenomenon of crater formation in relation to the rate of erosion. So does Gould[3], without using the terms "crater formation" and "pit formation," but describing the phenomenon in terms of surface topography. Thiruvengadam et al[4,5], in describing the erosion rate time curve, introduced an "attenuation exponent," but did not explicitly relate the attenuation of the erosion rate to the phenomenon of crater formation. This has been done, for example, by Plesset and Devine[6] and Tichler et al[7].

The latter authors distinguished between a resistance against uniform material removal ($R_e$) and a resistance against pit formation ($r_p$). They found a good correlation between $R_e$ and the true ultimate tensile strength ($\sigma_B^*$). For steels with $\sigma_B^*$ values in the range from 570 to 1260 MN/m$^2$, they found an empirical relation between $R_e$ *and* $\sigma_B^*$ of the form

$$R_e = (R_e)_o + b\sigma_B^* \tag{1}$$

Actually, the correlation proved very good, with a correlation coefficient of 0.995. However, the curve of Eq 1 was found to intersect the $\sigma_B^*$-axis at $\sigma_B^* = 400$ MN/m$^2$. Thus it had to be concluded that Eq 1 obviously did not apply for materials with a $\sigma_B^*$-value appreciably lower than 570 MN/m$^2$, the lower limit of the measuring range, applied at that time. In the present research program it was tried to find a functional relation, valid for a wider range of $\sigma_B^*$-values. To that purpose, cavitation erosion experiments were performed with a series of copper-nickel alloys with $\sigma_B^*$-values ranging from about 300 to about 500 MN/m$^2$. In addition, experiments were performed with six steels, tested previously[7], under different conditions of pressure and temperature.

Next, experiments were performed with pure nickel, a martensitic and a ferritic steel, cold worked to different degrees of deformation. In general, deformation does not influence the true ultimate tensile strength ($\sigma_B^*$) of metals[8]. There was, however, some evidence that forging to high degrees of deformation can influence $R_e$[9].

Finally, the present paper describes the results of experiments with steels and cobalt alloys of the Stellite type, performed in order to demonstrate that pit formation is indeed a discrete phenomenon occurring at a well-defined depth of uniform erosion. Actually, it is shown that for practical applications as in controlling valves, fuel atomizers, etc., it is not sufficient to characterize the resistance against erosion in terms of a resistance against uniform material removal alone.

## Resistance Against Uniform Material Removal

### *Experimental*

The cavitation erosion tests were performed with a 20-kHz magnetostrictive oscillator adapted for the performance of tests at 0.7, 1.0, and 1.5 bar pressure. A detailed description of the experimental procedure can be found in Ref 7. The experiments were performed in water, at temperatures of 22 and 35°C (72 and 95°F). In each test run the weight loss of the specimens was determined after preset values of time. Thus values for the mean depth of erosion ($r$) could be obtained as a function of time. The resistance against uniform material removal ($R_e$) was defined as the reciprocal slope of the mean depth of erosion ($r$) versus time ($t$) curve during the first steady-state period, that is, after termination of the acceleration period and before deceleration due to crater formation. In order to obtain a homogeneous attack of the specimen surfaces, rimmed specimens were used, as proposed by Hirotsu and Abe[*10*]. If flat specimens are used the center part of the specimen frequently is already in the stage of crater formation when at the edge of the specimen the acceleration period has not yet terminated. Consequently a steady-state period is not observed and a proper measurement of the erosion resistance as just defined is not possible.

For the materials tested in this part of the program the true ultimate tensile strength ($\sigma_B^*$) was determined by means of static tension tests. For the copper-nickel alloys (see the following) the true maximum strength ($\sigma_m^*$) under conditions of dynamic compression was determined as well, namely, by means of split Hopkinson pressure bar experiments. In these tests the rate of deformation $\delta$ was equal to $2 \times 10^4$ $s^{-1}$. The results of these tests were interpreted as described by Van Elst[*11*]. The precise definitions of $\sigma_B^*$ and $\sigma_m^*$ follow from Fig. 1.

### *Materials*

The present test series was performed with six different steels, six copper-nickel alloys, and pure nickel. Table 1 gives the chemical compositions, the structural conditions, and the Vickers hardness numbers of the steels.

The copper-nickel alloys were chill cast with nickel percentages ranging from 10 to 60 percent. The chemical composition of these alloys is given in Table 2. Silicon was added for deoxidation purposes. The castings were homogenized during 2 h. Column 6 of Table 2 gives the homogenizing temperatures. After rolling (15 percent reduction in diameter), the ingots

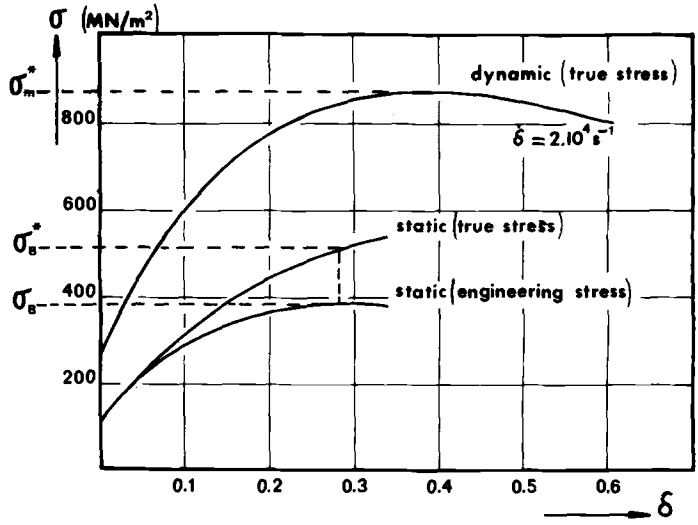


FIG. 1—*Example of stress-strain curves (copper-nickel Alloy 6): δ is defined as logarithmic degree of deformation in tension tests, δ = log (l/l₀); in compression tests, δ = −log (l/l₀), with l₀ and l being the length of the specimen, respectively prior to and during testing.*

TABLE 1—*Chemical compositions, structural conditions, and hardness numbers of the steels.*

| Steels No. | Chemical Compositions, weight % | | | | | | Structural Conditions[a] | $HV_{10}$ |
|---|---|---|---|---|---|---|---|---|
| | C | Cr | Ni | Cu | Mo | Cb | | |
| 1 | 0.1 | 13 | ... | ... | ... | ... | F | 187 |
| 2 | 0.1 | 13 | ... | ... | ... | ... | TM | 184 |
| 3 | 0.15 | 13 | ... | ... | 0.2 | ... | TM(+F) | 240 |
| 4 | 0.2 | 13 | ... | ... | ... | ... | TM | 224 |
| 5 | 0.2 | 25 | 4 | ... | ... | ... | A+F | 254 |
| 6 | <0.05 | 17 | 4 | 4 | ... | 0.2 | PH | 470 |

[a] F = ferrite.
TM = tempered martensite.
TM(+F) = tempered martensite (+ ferrite).
A+F = austenite + ferrite.
PH = precipitation hardened.

were recrystallized during 10 min. The resulting Vickers hardness numbers are given in Column 7 of Table 2.

The pure nickel was taken from a commercially obtained hot-rolled bar. The material was annealed during 30 min at 950°C (1742°F). After annealing, the Rockwell B hardness number was 27 (and the Vickers hardness number was 74 for a load of 30 kgf).

*Results*

Table 3 shows the results of $\sigma_B^*$ (static) and $R_e$ determinations for Steels 1 through 6, obtained under different conditions of pressure and temperature, and the results obtained with pure nickel at $P = 1.0$ bar and $T = 22°C$ (72°F).

TABLE 2—*Chemical compositions (analyzed after casting), homogenizing temperatures, and Vickers hardness numbers of the copper-nickel alloys.*

| Alloy No. | Chemical Composition, weight % | | | Atomic % | Temperature, | |
|---|---|---|---|---|---|---|
| | Cu | Ni | Si | Ni[a] | °C | $HV_{50}$ |
| 1 | 92.0 | 7.0 | <0.005 | 8.1 | 1060(1940°F) | 57 |
| 2 | 76.8 | 22.9 | <0.005 | 24.5 | 1090(1994°F) | 78 |
| 3 | 67.4 | 31.4 | <0.005 | 33.4 | 1110(2030°F) | 88 |
| 4 | 59.2 | 40.5 | 0.09 | 42.5 | 1140(2084°F) | 80 |
| 5 | 47.9 | 51.8 | 0.005 | 53.9 | 1180(2156°F) | 86 |
| 6 | 39.4 | 60.1 | 0.08 | 62.3 | 1220(2228°F) | 89 |

[a] Calculated on the basis Cu + Ni = 100 atomic %.

TABLE 3—*Results of strength and erosion tests of pure nickel and of steels under different conditions.*

| Materials | $\sigma_B^*$ (Static) MN/m² | $R_e$, s/μm | | | |
|---|---|---|---|---|---|
| | | $P = 0.7$ bar $T = 35°C$(95°F) | 1.0 bar 22°C(72°F) | 1.0 bar 35°C(95°F) | 1.5 bar 35°C(95°F) |
| Pure nickel | 530 | ... | 630 | ... | ... |
| Steel 1 | 570 | 6 920 | 683 | 329 | 228 |
| Steel 2 | 671 | 10 700 | 975 | 554 | 312 |
| Steel 3 | 778 | 19 500 | 1 500 | 767 | 440 |
| Steel 4 | 784 | ... | 1 640 | 865 | ... |
| Steel 5 | 915 | 32 100 | 2 130 | 1 130 | 805 |
| Steel 6 | 1 490 | 70 100 | 5 400 | 2 840 | 2 010 |

The results of $\sigma_B^*$ (static) and $R_e$ determinations with the copper-nickel alloys are shown in Table 4. The last column of Table 4 contains the results of $\sigma_m^*$ (dynamic) determinations.

Table 5, finally, contains the results of the erosion tests performed with the cold-worked materials (pure nickel, Steel 1 and Steel 4). The degrees of deformation are expressed as logarithmic values: $\delta = -\log (1/1_0)$. They correspond with, respectively, 0, 25, 45, and 60 percent reduction in length of the compressed specimens.

## Discussion

In Fig. 2 the $R_e$ data for Steels 1 through 6 and nickel, tested at 1.0 bar and 22°C (72°F) (Column 4 of Table 3), and the $R_e$ data for the copper-nickel alloys tested under the same experimental conditions (Table 4), are plotted as a function of $\sigma_B^*$. It can be seen that the best curve through the measuring points gradually slopes down to zero at decreasing values of $\sigma_B^*$.

TABLE 4—*Results of strength and erosion tests of copper-nickel alloys; P = 1.0 bar; T = 22°C(72°F).*

| Cu-Ni Alloy No. | $\sigma_B^*$ (Static) MN/m² | $R_e$, s/μm | $\sigma_m^*$ (Dynamic), MN/m² |
|---|---|---|---|
| 1 | 303 | 144 | 520 |
| 2 | 386 | 270 | 630 |
| 3 | 396 | 296 | 700 |
| 4 | 476 | 423 | 810 |
| 5 | 494 | 489 | 860 |
| 6 | 515 | 540 | 880 |

TABLE 5—*Resistance against uniform material removal* ($R_e$) *of materials in different degrees of deformation* ($\delta$).

| | $R_e$, s/μm | | |
|---|---|---|---|
| $\delta$ | Pure Nickel | Steel No. 1 | Steel No. 4 |
| 0 | 630 | 683 | 1640 |
| 0.3 | 591 | 507 | 1770 |
| 0.6 | 603 | 390 | 728 |
| 0.9 | 626 | 328 | 548 |

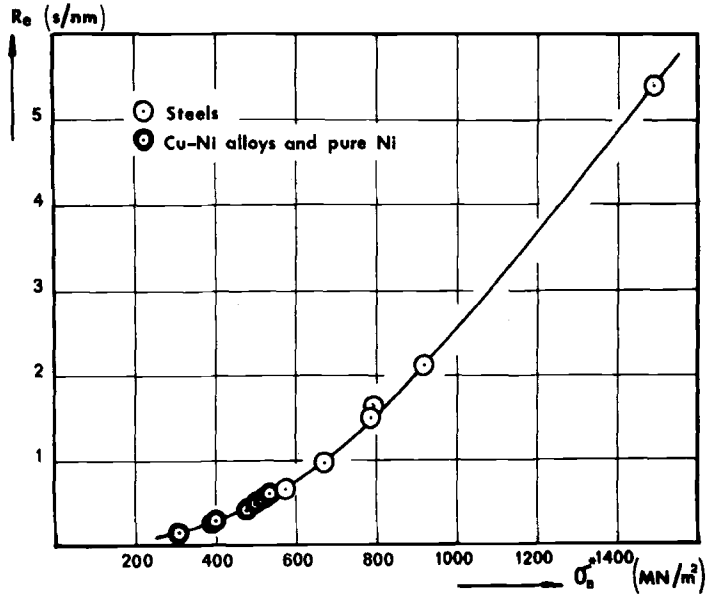


FIG. 2—*Erosion resistance under conditions of uniform material removal* ($R_e$) *versus static true ultimate tensile strength* ($\sigma_B^*$) *of copper-nickel alloys, pure nickel and steels, at* P = *1.0 bar and* T = *22°C (72°F).*

In Fig. 3 the same data and also the data obtained at other values of $P$ and $T$ (Columns 3, 5, and 6 of Table 3) are plotted on logarithmic scales. It can be seen that the measuring points in this diagram lie on straight lines, corresponding to the equation

$$R_e = A\sigma_B^{*n} \tag{2}$$

In this equation the exponent $n$ is approximately equal to 2.3, independent of the temperature and the pressure of the test liquid. In the Appendix, considerations are given which substantiate Eq 2.

The fact that the data obtained with the copper-nickel alloys obviously belong to the same "family" as the data obtained with steel implies that the true ultimate tensile strength criterion applies for at least these two groups of materials. So far, reported attempts to find a simple criterion for a large group of materials with widely different mechanical properties did not prove successful; for example, Ref *12*. A possible reason for this

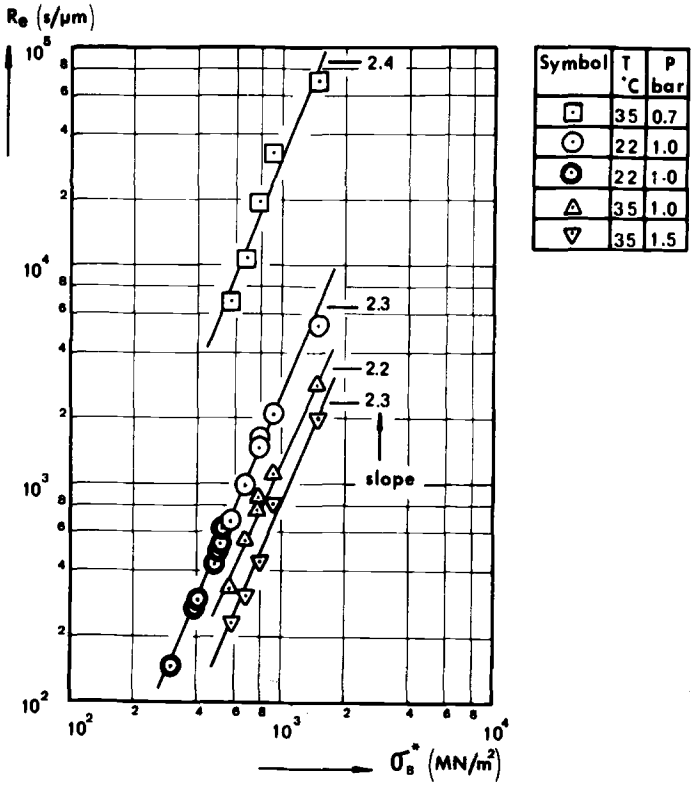


FIG. 3—*Erosion resistance under conditions of uniform material removal* ($R_e$) *versus true ultimate tensile strength* ($\sigma_B^*$) *of copper-nickel alloys and steels. For the meaning of the symbols, see also Fig. 2.*

might be that the rate of erosion may well depend on the material properties under dynamic deformation conditions rather than on those under static deformation conditions. In the present case this could not be verified because, for the only group of materials for which the strength ($\sigma_m^*$) was determined under dynamic conditions (that is, the copper-nickel alloys), the dynamic strength was found to be proportional to the static strength (see Table 4 and Fig. 4).

Table 5 shows that gross deformation of pure nickel does not affect its erosion resistance. However, with Steels 1 and 4, which contain carbide precipitates along the grain boundaries, deformation has a very unfavorable influence. Figures 5 and 6 show photomicrographs of the cross sections of the eroded surfaces of these two steels in the various degrees of deformation. It can be seen that—upon deformation in a direction perpendicular

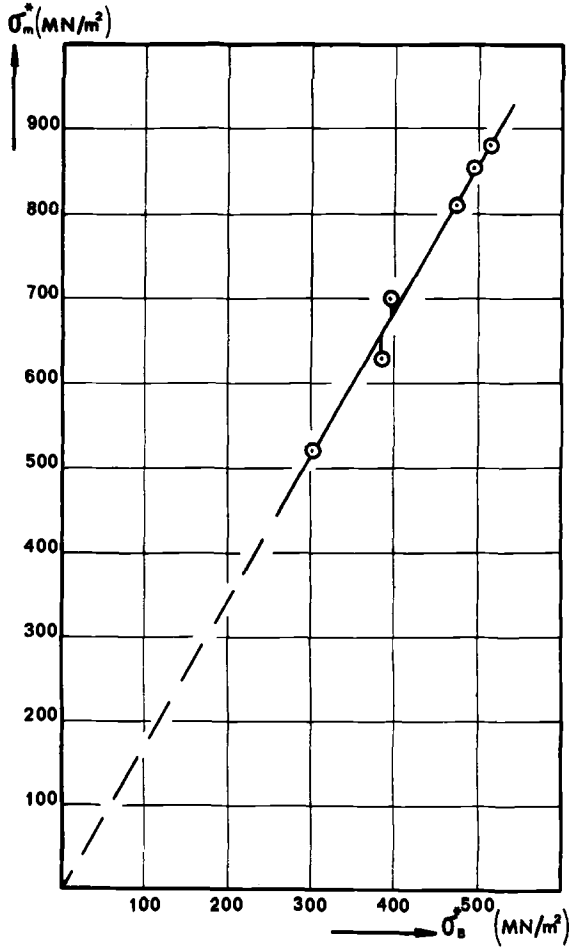


FIG. 4—$\sigma_m^*$ *(dynamic) versus* $\sigma_B^*$ *(static) for copper-nickel alloys.*

to the test surface—the individual grains became elongated in a direction parallel to the test surface. This resulted in the fact that with undeformed steels small and regularly shaped wear debris formed, whereas in the case of the highly deformed steels large chips flaked off from the eroding surfaces. This unfavorable effect of cold working in a direction perpendicular to the test surfaces is contradictory to the beneficial effect of forging in the same direction, observed by Hoff et al[9] working with Stellites. Whether the influence of deformation will be favorable, unfavorable, or not noticeable probably depends on the precise nature of the deformations that occur as well as on the structure of the material at hand. This finding

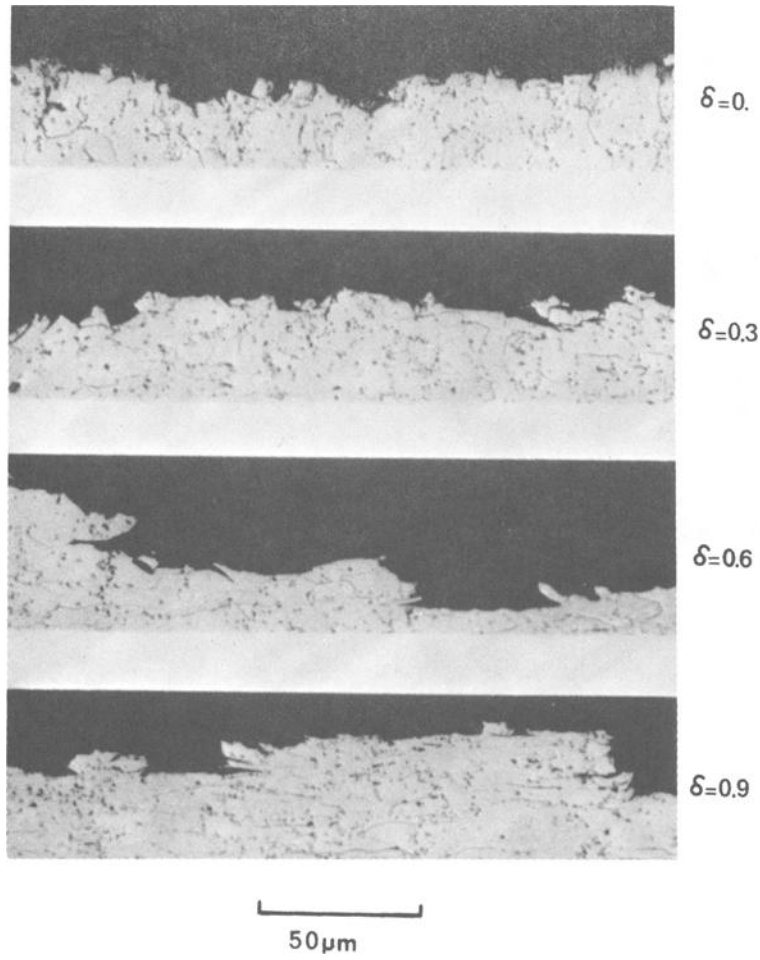


FIG. 5—*Cross sections of eroded surfaces of Steel No. 1 (ferritic) in different degrees of deformation.*

substantiates the view that for such complicated materials as are usually applied in practice the mechanical properties ($\sigma_B^*$-values) do not quite determine the behavior under conditions of cavitation erosion. Instead, erosion tests will always be necessary if one considers the use of new materials.

There are two more reasons for promoting the performance of erosion tests for screening materials for a practical application. The first reason

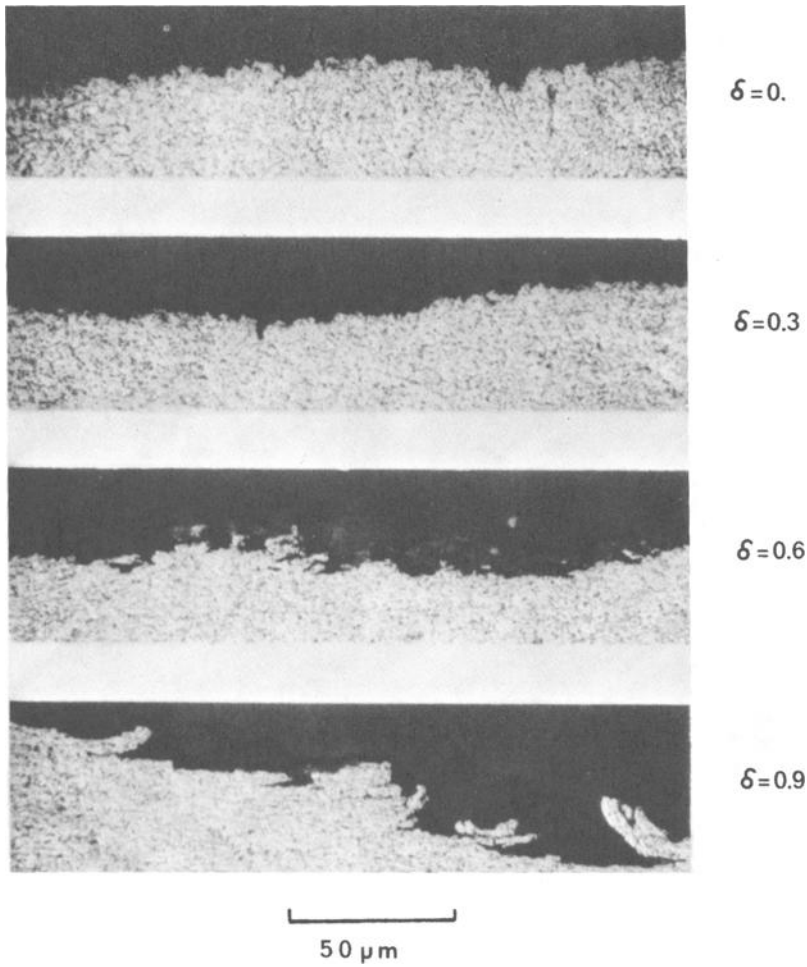


FIG. 6—*Cross sections of eroded surfaces of Steel No. 4 (tempered martensite) in different degrees of deformation.*

is that determination of the appropriate mechanical properties, whether static or dynamic, is difficult—if possible at all—for many of the erosion-resistant materials applied in practice. The second and most stringent reason is that the foregoing considerations concerning the resistance against uniform material removal ignore the effect of crater formation. The magnitude of this effect can differ considerably from one material to the other, as is shown in the following section.

## Pit Formation

### *Experimental*

Tichler et al[7] attributed the deceleration in the rate of erosion observed after the steady-state period to the presence of gas bubbles trapped in craters. This idea was worked out mathematically[*13*], resulting in a method whereby the mean depth of erosion at which the first bubbles became trapped ($r_b$) could be found by graphic analysis of the shape of the mean depth of erosion ($r$) versus time ($t$) curve. This graphic method is rather complicated and, also, the experiments have to be continued until a considerable depth of erosion has occurred. This is a time-consuming procedure in the case of materials for practical erosion protection, as such materials obviously possess a high resistance against erosion. Fortunately, a readily applicable criterion for the resistance against pit formation can be found in the mean depth of erosion at which the first tiny pits can be observed ($r_p$). Such pits grow to larger craters upon continuing the erosion test. For two cobalt alloys and three steels (given later) $r_p$ was determined as follows. After each individual erosion period the test specimen was not only weighed, but its surface was photographed with a 5-fold magnification. When after continued testing well-developed craters had formed, the photograph was selected at which the first tiny pits, in location corresponding to the aforementioned craters, were visible. This procedure eliminated the possibility that stationary pits in the surface, which did not grow to larger craters, were erroneously attributed to the erosion process. After selection of the "critical photograph," $r_p$ could be calculated readily from the weight loss of the specimen at the time the critical photograph was taken.

The present tests were performed in water with bichromate corrosion inhibitor. The pressure and temperature of the water were 1.0 bar and 35°C (95°F), respectively.

### *Materials*

The materials tested in this series were two cobalt alloys of the Stellite type, a nitriding steel, a carburizing steel, and a maraging steel. The cobalt alloys were applied by several different processes, as shown in Table 6. This table also gives the chemical compositions of the materials, in the case of the cobalt alloys, determined before application.

### *Results*

The $R_e$ and $r_p$ values found with the materials just given are listed in Table 7. The product of $R_e$ and $r_p$ is a measure for the time to formation

TABLE 6—*Chemical compositions and application processes of materials for pracitcal applications.*

| Materials | Chemical Compositions, weight % | | | | | | | Processes[a] |
|---|---|---|---|---|---|---|---|---|
| | C | Cr | Ni | Co | Mo | W | Others | |
| Co-alloy 1 | 1 | 28 | ... | 67 | ... | 4 | ... | ESR, TIG, EBM, MA, OA |
| Co-alloy 2 | 1 | 19 | 13 | 55 | ... | 8 | 4B+Si | FS |
| Nitriding steel | 0.45 | 1.5 | ... | ... | 0.2 | ... | 1 Al | nitriding |
| Carburizing steel | 0.08 | 4 | ... | ... | 0.05 | ... | ... | carburizing |
| Maraging steel | 0.02 | ... | 18 | 8 | 5 | ... | O.4Ti;0.1Al | maraging |

[a] ESR = electro-slag remelting.
TIG = tungsten inert gas process.
EBM = electron beam melting.
MA = manual arc process.
OA = oxyacetylene process.
FS = flame spray—fuse process.

TABLE 7—*Results of cavitation erosion experiments with materials for practical applications.*

| Materials | Processes[a] | $R_e$, s/nm | $r_p$, μm | $R_e r_p = t_p$, ks |
|---|---|---|---|---|
| Co-alloy 1 | ESR | 38 | 24 | 900 |
| Co-alloy 2 | TIG | 17 | 50 | 800 |
| Nitriding steel | nitriding | 45 | 12 | 500 |
| Co-alloy 1 | EBM | 14 | 20 | 300 |
| Carburizing steel | carburizing | 8.8 | 27 | 200 |
| Co-alloy 2 | FS | 16 | 13 | 200 |
| Co-alloy 1 | MA | 5.7 | 20 | 100 |
| Maraging steel | maraging | 5.8 | 17 | 100 |
| Co-alloy 1 | OA | 10 | 1 | 10 |

[a] See footnote to Table 6.

of the first pit(s), ($t_p$). The values of $t_p$ are given in the last column of Table 7. The order of sequence of the materials in Table 7 is that of decreasing values of $t_p$.

*Discussion*

Failure of erosion-resistant materials applied in practice is frequently due to pit formation rather than to uniform removal of material from the surface. Thus, the $t_p$ data given in the last column of Table 7 are a good measure for the quality of such materials. Obviously, on the basis of the $R_e$ values alone, the materials would have been classified in a completely different (and wrong!) order of quality. It can be observed that the $r_p$ values vary considerably from one test surface to the other. This is further illustrated by Fig. 7, which shows photographs of the surfaces of the specimens of the first two materials of Table 6 in different stages of erosion. It can be seen that the electro-slag remelted (ESR) cobalt alloy was already in a stage of considerable pit formation when the surface of the tungsten inert gas (TIG) surfaced cobalt alloy was still entirely free of pits.

Because of the observation that considerable differences can exist in the stage of pit formation at equal stages of uniform material removal, it is concluded that the two different erosion processes, described in this paper, must indeed be properly distinguished from each other. To that purpose it is absolutely necessary to ensure homogeneous attack of the surfaces.

It has been shown previously[7] that the structure of materials considerably affects their resistance against crater formation. The mechanism of pit formation, however, is not yet known precisely. Probably the mecha-

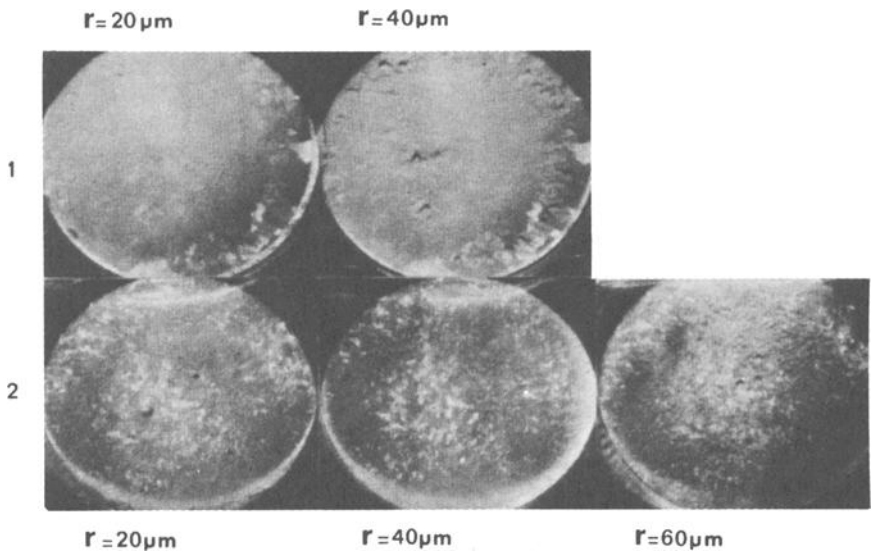


FIG. 7—*Specimen surfaces of electro-slag remelted* (1) *and tungsten inert gas surfaced* (2) *Co-alloys after different mean depths of erosion* (r).

nism resembles that of spalling fatigue, as is observed in rolling element bearings[*14*]. It has also been shown that atmospheric corrosion can play an important role[*15*]. With cobalt-bonded tungsten carbide cermets, pit formation is accelerated by a process of atmospheric corrosion along the grain boundaries. Obviously, similar effects can also play an important role in the erosion mechanism of other materials. Thus, in screening materials with respect to time to pitting, care should be taken to simulate as much as possible the environmental conditions that apply in practice.

## Conclusions

1. For six copper-nickel alloys with nickel percentages ranging from 10 to 60 percent and six steels of different chemical composition and structure, the following exponential relation between the resistance against uniform material removal ($R_e$) and the true ultimate tensile strength ($\sigma_B^*$) applies:

$$R_e = A\sigma_B^{*2.3}$$

2. Pressure and temperature of the test liquid do not affect the power exponent in the foregoing relation. Thus pressure and temperature of the test liquid do not influence the results of screening tests, which aim at

classifying materials with respect to their $R_e$ values, within the experimental limits of these tests.

3. Deformation does not affect the $R_e$ value of pure nickel. However, there can be a pronounced and essentially unpredictable effect of deformation upon the $R_e$ value of materials with a more complicated structure. Grain boundary precipitation is particularly important in this respect.

4. Next to the resistance against uniform material removal, the resistance against pit formation is of considerable importance. Materials with a high $R_e$ value may have a low $r_p$ value, and vice versa. The processes of uniform material removal and pit formation must be properly distinguished from each other in testing and describing the cavitation erosion behavior of materials.

*Acknowledgments*

The authors are indebted to F. W. Twilt and to C. Koning and W. van Zwieten, who skillfully performed the cavitation erosion experiments and the dynamic compression experiments.

# APPENDIX

## Nomenclature for Appendix

$A$ Amplitude of relevant stress wave
$a_S$ Average volume of removed solid particles
$E$ Young's modulus
$F$ Area of eroded surface
$G_S$ Fracture toughness = effective surface energy for solid
$h$ Energy content of relevant stress wave
$K_L$ Modulus of liquid
$N_L$ Number of impinging liquid jets
$N_S$ Number of solid particles removed from surface
$r$ Mean depth of erosion
$R_e$ $1/\dot{r}$ = resistance against uniform material removal
$Z$ Characteristic acoustic impedance
$\alpha$ Constant depending on average geometry of solid particles
$\beta$ Constant $= \frac{\alpha}{4a_S^{1/3}h_L Z_L} \times \frac{F}{N_L}$
$\gamma$ Constant $= \sqrt{\rho_L K_L/\rho_S}$
$\delta$ Deformation, logarithmic value (see also caption to Fig. 1 of paper)
$\lambda$ Average effective defect size in solid
$\phi$ Possible relevant geometrical factor for fracture toughness in solid surface crack configuration
$\rho$ Density

$\sigma$ Engineering stress
$\sigma_B^*$ True ultimate tensile strength
$\tau$ Stress wave duration at impact = impact time

*Indices*

$L$ Liquid
$S$ Solid

## Dependence of $R_e$ on Material Properties

A tentative schematic description is suggested which accounts for the observed dependence of $R_e$ on $\sigma_B^*$ in an orientating way. This is based on mass balance and energy balance. Mass balance

$$rF = N_S a_S \tag{3}$$

or

$$R_e = 1/\dot{r} = F/\dot{N}_S a_s \tag{4}$$

Energy balance: It is assumed that the energy for removal of solid particles is procured by partial absorption of the kinetic energy of impinging liquid jets. One removed solid particle requires an energy $\alpha a_S^{2/3} G_S$. For the energy contents of the stress waves generated in the solid, one has

$$h_S \approx \frac{2\pi^2 Z_S A_S^2}{\tau} \tag{5}$$

According to Kolsky[*16*]

$$A_S = A_L \frac{2Z_L}{Z_S + Z_L} \tag{6}$$

Substituting Eq 6 in Eq 5, one finds

$$h_S \approx \frac{2\pi^2 Z_S}{\tau} A_L^2 \frac{4Z_L^2}{(Z_S + Z_L)^2} = h_L \frac{2Z_S Z_L}{(Z_S + Z_L)^2} \tag{7}$$

(See also, for example, Ref *17*.)

Thus, the energy balance is expressed as

$$N_S \alpha a_S^{2/3} G_S = N_L h_L \frac{4Z_S Z_L}{(Z_S + Z_L)^2} \tag{8}$$

Combining the mass balance (Eq 4) and the energy balance (Eq 8), the following expression for $R_e$ can be found

$$R_e = \beta G_S Z_S (1 + Z_L/Z_S)^2 \tag{9}$$

Assume[*18*]

$$G_s' = \frac{\sigma_B^{*2} \lambda \phi}{E} \tag{10}$$

and

$$Z_s = \sqrt{\rho_s \left( \frac{d\sigma^*}{d\delta} \right)_{\sigma = \max}} = \sqrt{\rho_s \sigma_B^*} \tag{11}$$

which appears justified after sufficient hardening. Substituting Eq 10 and Eq 11 in Eq 9, one finds

$$R_e = \frac{\beta \lambda \phi \rho_s^{0.5}}{E} \left( \sigma_B^{*2.5} + 2\gamma \sigma_B^{*2} + \gamma^2 \sigma_B^{*1.5} \right) \tag{12}$$

which will be nearly represented by the empirically found relation.

## References


[*1*] *Characterization and Determination of Erosion Resistance, ASTM STP 474,* American Society for Testing and Materials, 1970.

[*2*] Hirotsu, M., in *Characterization and Determination of Erosion Resistance, ASTM STP 474,* American Society for Testing and Materials, 1970, pp. 48–66.

[*3*] Gould, G. C., in *Characterization and Determination of Erosion Resistance, ASTM STP 474,* American Society for Testing and Materials, 1970, pp. 182–211.

[*4*] Thiruvengadam, A., Rudy, S. L., and Gunasekaran, M., in *Characterization and Determination of Erosion Resistance, ASTM STP 474,* American Society for Testing and Materials, 1970, pp. 249–287.

[*5*] Thiruvengadam, A., "Theory of Erosion," *Proceedings,* Second Meersburg Conference on Rain Erosion and Associated Phenomena, Vol. II, A. A. Fyall, Ed., Royal Aircraft Establishment, Farnborough, England, 1967, pp. 605–651.

[*6*] Plesset, M. S. and Devine, R. E., "Effect of Exposure Time on Cavitation Damage," *Journal of Basic Engineering, Transactions,* American Society of Mechanical Engineers, Series D, Vol. 88, 1966, pp. 691–705.

[*7*] Tichler, J. W., van den Elsen, J. B., and de Gee, A. W. J., *Journal of Lubrication Technology, Transactions,* American Society of Mechanical Engineers, Series F, Vol. 92, 1970, pp. 220–227.

[*8*] Tabor, D., *The Hardness of Metals,* Clarendon Press, Oxford, England, 1951, Chapter 3.

[*9*] Hoff, G., Herbert, W., and Rieger, H., in *Characterization and Determination of Erosion Resistance, ASTM STP 474,* American Society for Testing and Materials, 1970, p. 371.

[*10*] Hirotsu, M. and Abe, Y., *Bulletin of the Japan Society of Mechanical Engineers,* Vol. 10, No. 41, 1967, pp. 786–793.

[*11*] Van Elst, H. C., *Proceedings,* Second Conference on Dimensioning and Strength Calculations, L. Kisbocskóy, Ed., Hungarian Academy of Sciences, Budapest, 1965, pp. 484–507; see especially pp. 488–493.

[*12*] Hammitt, F. G., discussion on Ref *15, Lubrication Engineering, Journal of the American Society of Lubrication Engineers,* Vol. 28, No. 1, Jan. 1972, p. 26.

[*13*] Tichler, J. W. and de Gee, A. W. J., "Time Dependence of Cavitation Erosion and the Effect of Some Material Properties," *Proceedings,* Third International Conference on Rain Erosion and Associated Phenomena, Vol. 2, A. A. Fyall, Ed., Royal Aircraft Establishment, Farnborough, England, 1970, pp. 847–879.

[*14*] Tichler, J. W. and Scott, D., *Wear,* Vol. 16, 1970, pp. 229–233.

[*15*] Tichler, J. W. and de Gee, A. W. J., *Lubrication Engineering, Journal of the American Society of Lubrication Engineers,* Vol. 27, No. 12, Dec. 1971, pp. 428–432.

[*16*] Kolsky, H., *Stress Waves in Solids,* Clarendon Press, Oxford, England, 1953, p. 34.

[*17*] Hammitt, F. G., Huang, Y. C., Kling, C. L., Mitchell, T. M., Jr., and Solomon, P., in *Characterization and Determination of Erosion Resistance, ASTM STP 474,* American Society for Testing and Materials, 1970, p. 306.

[*18*] Paris, P. C. and Sih, G. C., in *Fracture Toughness Testing and Its Applications, ASTM STP 381,* American Society for Testing and Materials, 1964, pp. 60–83.

# DISCUSSION

*A. F. Conn*[1]—This question actually pertains to discussions which we have had with the authors, and only indirectly to the ideas contained in the paper. Specifically, the authors have advised us that the shape of the rate of erosion versus time curves which they obtained in their magnetostrictive erosion tests differs from those curves obtained in such tests at HYDRONAUTICS, Incorporated. In particular the TNO rate versus time curves show a long, flat region at the maximum rate as opposed to the rather peaked curves at the maximum erosion rate which are obtained in results reported from tests in the discusser's laboratory. I wonder if perhaps these differences are actually related to the very large differences in maximum mean depths which are obtained at TNO versus those at HYDRONAUTICS and in other standard erosion tests because of the relatively small intensities of cavitation used by TNO. The TNO tests have peak depths which are on the order of 60 to 200 $\mu$m, whereas many of the tests at HYDRONAUTICS and elsewhere have peak depths on the order of 1/8 in. (3200 $\mu$m) or more. Perhaps basically different mechanisms are operating at these two extremal values of cavitation intensity, and hence the differences in the rate curves are not due to testing procedures or material variables?

*J. W. Tichler (authors' closure)*—The authors appreciate Dr. Conn's critical remark on their work in general. Before giving my opinion upon this point, it seems to me that it is good to erase some possible misunderstanding upon the meaning of "peak depth" in Dr. Conn's discussion. Obviously, the meaning of "peak depth" is not the mean depth of erosion at the point where the erosion rate reaches its maximum, because this maximum in general occurs at mean depths of erosion on the order of 10 to 100 $\mu$m. Thus, with peak depth the maximum mean depth of erosion (that is, at the end of the erosion test) is meant. This maximum mean depth of erosion obviously depends on erosion intensity *and* test duration.

In my opinion, the sloping down of the erosion rate (that is, the existence

[1] Principal research scientist and head, Materials Sciences Division, HYDRONAUTICS, Incorporated, Laurel, Md. 20810.

of a maximum or peak rate) is connected with changes in the surface condition of the eroding material. This has also been concluded from work in the discusser's laboratory. In Ref 7 of the paper, the deceleration of the erosion process is attributed to the appearance of craters in the eroding surface, and the hypothesis is put forward that the deceleration is due to the protective action of gas bubbles, trapped in craters with appropriate size and shape. This idea has been worked out quantitatively in Ref *13* of the paper. From these considerations, it follows that the authors do *not* have the opinion that for each material a flat peak should be found, which is illustrated by Fig. 5 of Ref 7. A sharp peak will be found for materials with a high tendency toward crater formation, in which craters are formed in an early stage of the erosive process. Conversely, a flat peak will be found for materials with a high resistance against pit formation ($r_p$), in which the larger, bubble-trapping craters are formed only after longer times of exposure to the erosion process, especially when the materials have also a larger resistance against uniform material removal ($R_e$). Some such materials have been presented in Table 7 of the paper. It is obvious that one tends to find flat peaks when developing materials for practical applications in which these properties are especially favorable.

It is the authors' opinion that sharp peaks can also be found, if no measures are taken such as to obtain a homogeneous attack of the eroding specimen surfaces. If the attack is inhomogeneously divided along the surface of the specimen, craters appear already in the heaviest attacked parts of the specimen surface when other parts of the attacked surface are still in the incubation period, as was illustrated in Fig. 1 of Ref 7 of the paper.

When performing tests for extremely prolonged test times, one should well keep in mind the trivial effect that the peak *seems* to be sharper due to the necessary compression of the time scale in the erosion rate versus time diagram. Another effect is that, when measuring at higher erosion intensities, one tends to perform the erosion tests with larger steps, which introduces larger inaccuracies in deriving the erosion rate versus time curve from the mean depth of erosion versus time curve. This can result also in the observation of a sharper peak. However, all these differences are gradual, not essential. The authors did not find any essential difference in erosion mechanisms when operating at varying intensities of erosion.

*B. Vyas* [1] *and C. M. Preece* [1]

# Cavitation-Induced Deformation of Aluminum

**REFERENCE:** Vyas, B. and Preece, C. M., "**Cavitation-Induced Deformation of Almuinum,**" *Erosion, Wear, and Interfaces with Corrosion, ASTM STP 567,* American Society for Testing and Materials, 1974, pp. 77–105.

**ABSTRACT:** A metallographic study has been made of the damage produced in pure aluminum by cavitation at ultrasonic frequencies. Scanning electron microscopy and transmission electron microscopy of eroded specimens indicate that the extensive slip steps and massive undulations produced on the surface result from shock deformation. It is proposed that shock loading is caused by the pressure pulse of a cloud of cavities collapsing in concert. It is apparent that fatigue (in the conventional metallurgical sense), corrosion, or localized melting cannot be considered responsible for the observed cavitation damage.

**KEY WORDS:** cavitation erosion, aluminum, surface deformation, slip lines, dislocation structure, mechanical stressing, erosion

Considerable effort has been expended in recent years in understanding the mechanism of erosion of solids by cavitation. However, much of this effort has been concentrated on the fundamentals and statistical characteristics of the cavitation phenomenon[*1–8*][2] rather than on studies of the eroded materials themselves. Moreover, studies of the latter type have largely been limited to weight loss measurements, and the actual mechanism by which material is lost from the surface has received little attention.

Many attempts have been made to correlate the results of weight loss studies with various mechanical properties of the solid such as strain energy, hardness, yield strength, or fatigue life[*9–14*]. On the basis of these studies, erosion has been attributed by many investigators simply

[1] Graduate research assistant and associate professor, respectively, Materials Science Department, University of New York at Stony Brook, Stony Brook, N. Y. 11790.

[2] The italic numbers in brackets refer to the list of references appended to this paper.

to fatigue failure[*5,10,15,16*]. Alternative theories have proposed accelerated corrosion[*17,18*] work hardening leading to brittle failure[*19*], shock deformation[*20,21*], or localized melting[*22*] as the mechanism controlling the phenomenon. Yet, except for a few isolated investigations[*21,23–25*], little attempt has been made to examine the eroded material in detail to determine the validity of these theories.

The aim of the present work was, therefore, to make an extensive metallographic study of the damage produced in a metal by ultrasonically induced cavitation and to compare the structure of the eroded metal with those produced by more conventional stress modes. Emphasis has been placed on the damage produced prior to any actual material loss, that is within the incubation period, because (1) this is the area in which structural designers obviously have the greatest interest, (2) it has received little attention to date, and (3) it is felt that the mode of damage produced in this region controls the rate of material loss at subsequent stages.

Pure aluminum was chosen as the initial candidate material on the basis of (1) its simple crystal structure and well-characterized slip mechanisms, (2) the availability of extensive data on its fatigue properties and corrosion characteristics, and (3) its poor erosion resistance. It was felt that an understanding of the basic erosion mechanism of pure aluminum could later be extended to the commercial aluminum alloys and allow their composition and thermomechanical treatment to be chosen to optimize resistance to cavitation.

## Experimental Procedure

The aluminum used in this investigation was obtained from the following sources: Al-99.999 polycrystalline sheet, 0.5 mm thick, from A. D. MacKay, New York; Al-99.999 single crystals, 12.5 mm diameter, from M. R. C., New York; and Al-99.997 bicrystal sheet, 2.0 mm thick, from Windsor Metalcrystals, Windsor, Md. Samples were cut from the starting material by spark erosion and were electropolished in a 2:1 solution of methanol and nitric acid to obtain flat, deformation-free surfaces.

Cavitation was produced by an "Ultralab" vibratory unit at a frequency of 20 kHz and variable amplitude. The specimen was not attached directly to the unit since it has been shown that the ultrasonic vibrations can themselves produce fatigue failure in the specimen even in the absence of any cavitation[*24*,26]. Instead, the specimen was held stationary, 115 $\mu$m below the surface of the horn in distilled water maintained at 25°C (77°F).

The damaged surfaces of the specimens were examined by scanning electron microscopy (SEM) after 2 s exposure to cavitation and at subsequent intervals of 5 s until a loss in weight was detected.

The dislocation substructure of the eroded polycrystalline material was examined by transmission electron microscopy (TEM). For these studies, specimens were electrolytically thinned, in a 4:1 solution of methanol and perchloric acid, from the back (uneroded) surface to retain a thin foil of the surface exposed to cavitation. Specimens were examined after 5 s exposure at vibrational amplitudes varying from 43 to 128 $\mu$m, and after 30 s exposure at an amplitude of 88 $\mu$m. Observations were made within 24 h of the erosion and, in addition, after 4 days and 2 weeks at room temperature following erosion.

## Results

### *Scanning Electron Microscopy*

Examination of the eroded surface of polycrystalline specimens revealed that, within the first 5 s, the grain boundaries were delineated and, in some areas, the deformation was such that individual grains appeared to be depressed below the general level of the surface. Further exposure to cavitation resulted in the edges of the adjacent grains flowing over the depressed area, Fig. 1. Such behavior is not generally observed in deformed metals and may be unique to this mode of deformation. Also at very early stages of erosion, coarse slip bands became visible in some

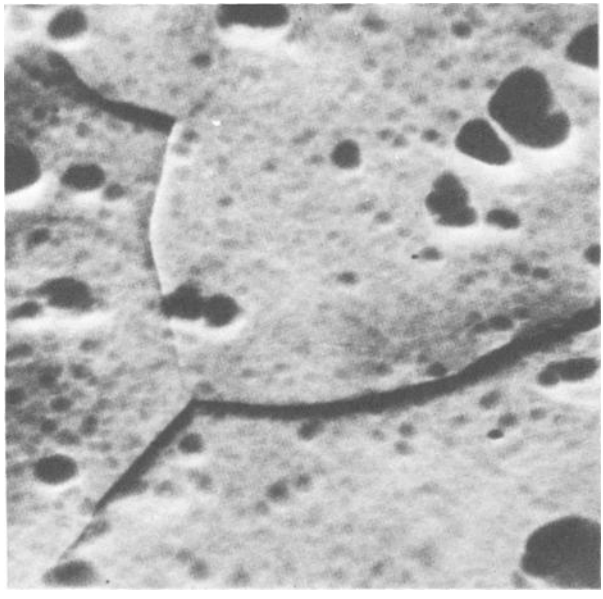

FIG. 1—*Grain boundary delineation in polycrystalline aluminum eroded for 15 s.*

grains, but were not a general characteristic of early deformation as was the grain boundary delineation. In some areas the slip bands were evenly spaced and similar in appearance to those produced by fatigue. The significant degree of plastic flow occurring within a few seconds of exposure to cavitation was further evidenced by a general, and fairly uniform, undulation of the surface and the formation of small smooth-edged pits ~1–10 $\mu$m diameter.

These observations suggested that erosion rates may be different for crystals of different orientation, and that more extensive deformation may occur at the grain boundaries than in the grain centers. Accordingly, single crystals with surfaces parallel to the {100}, {110}, or {111} crystal planes and bicrystals of the orientations given in Fig. 2 were examined for further evidence of these features.

Figures 3*a–e* show the development of deformation on the {110} surface of a single crystal. The surface features observed in polycrystals, namely, slip bands extending throughout the sample, small pits, and a general undulation of the surface, are all visible in this crystal after 2 s of erosion. Slip bands on four different slip systems are apparent in crystals of this orientation. Moreover, they persist throughout the time sequence studied in spite of the massive surface rumpling, and can be readily observed at all stages of deformation as illustrated in Figs. 4*a–c*.

Slip bands were less extensive in crystals of {100} orientation than in

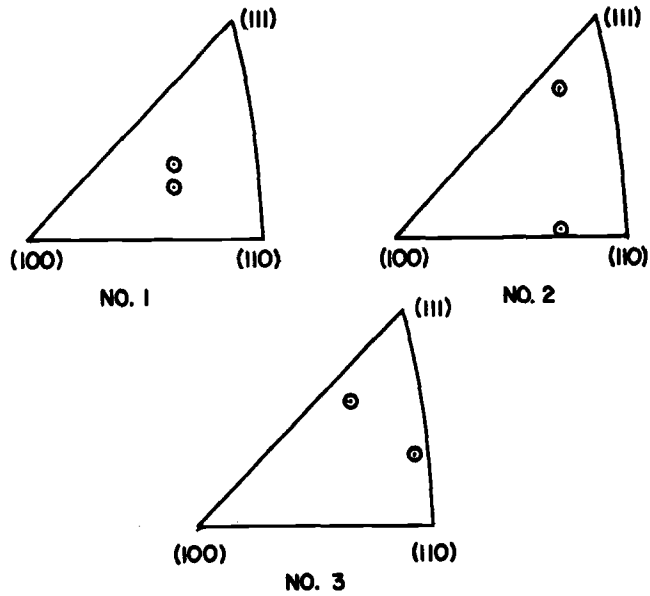


FIG. 2—*Orientation of bicrystals.*

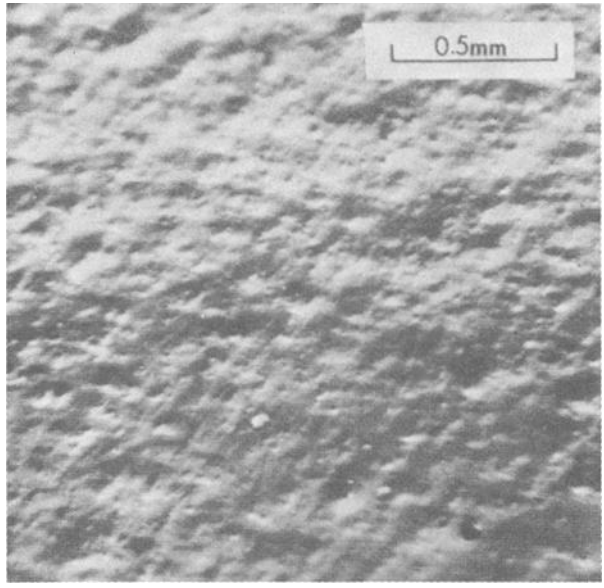


FIG. 3a—*Surface features of {110} surface of aluminum single crystal after 2 s of cavitation.*

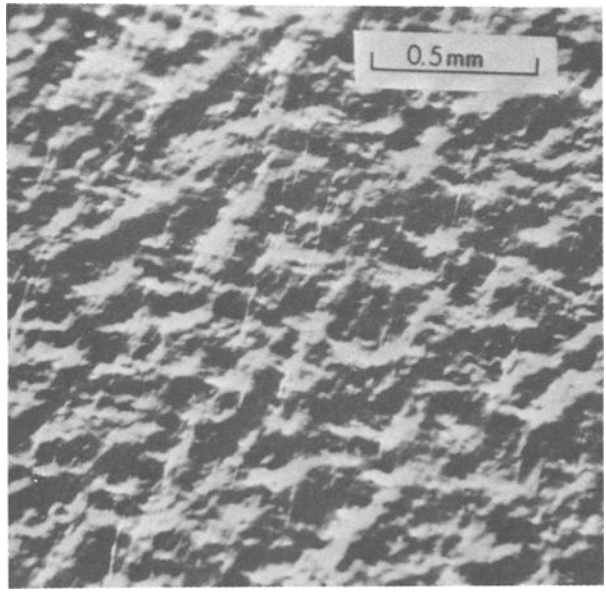


FIG. 3b—*Surface features of {110} surface of aluminum single crystal after 20 s of cavitation.*

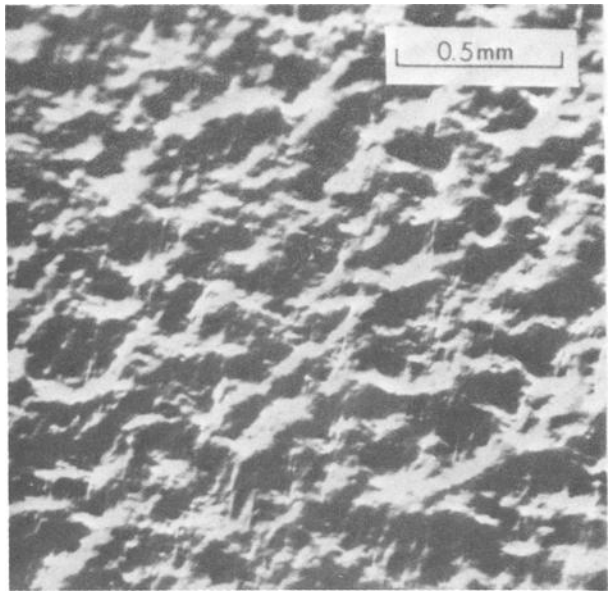


FIG. 3c—*Surface features of {110} surface of aluminum single crystal after 35 s of cavitation.*

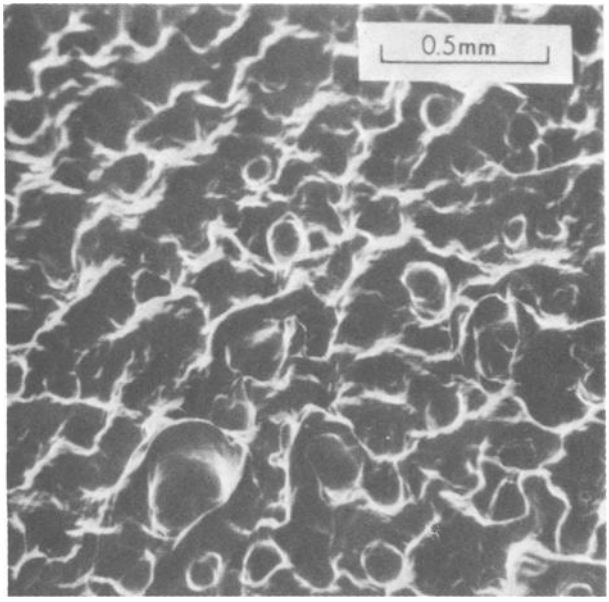


FIG. 3d—*Surface features of {110} surface of aluminum single crystal after 62 s of cavitation.*

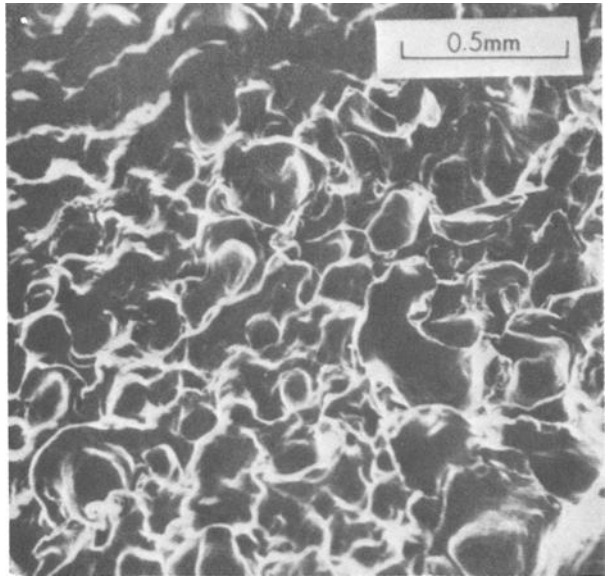


FIG. 3e—*Surface features of {110} surface of aluminum single crystal after 82 s of cavitation.*

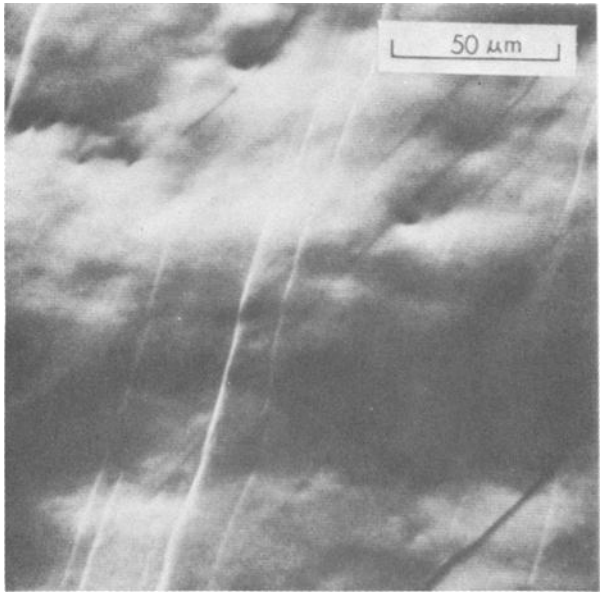


FIG. 4a—*Multiple slip on the {110} single-crystal surface after 5 s of erosion.*

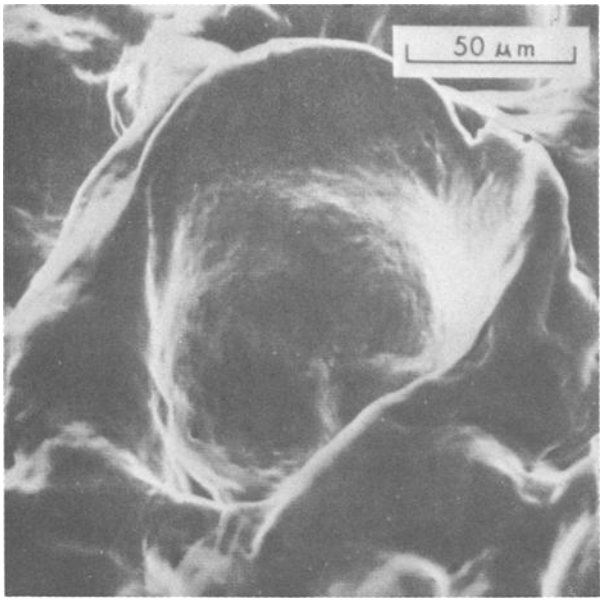


FIG. 4*b*—*Crater formation on {110} surface of aluminum single crystal after 62 s of erosion. Slip bands still persist on the surface.*

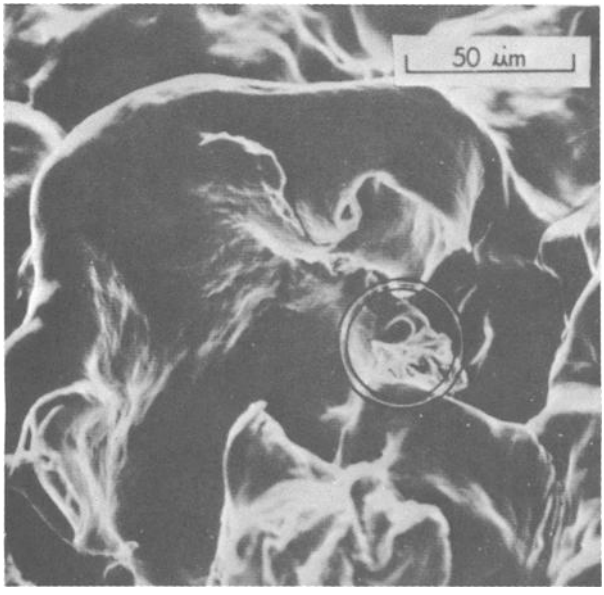


FIG. 4*c*—*Development of crater after 82 s of erosion on the {110} surface of aluminum single crystal. Material loss has occurred from the circled area.*

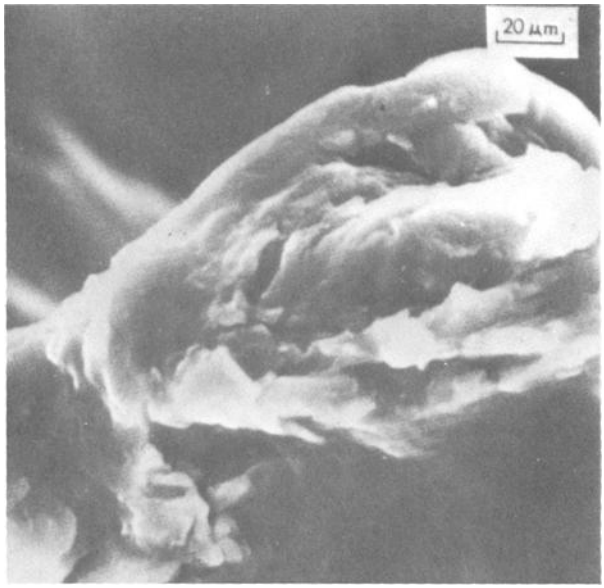


FIG. 4*d*—*Magnification of circled area in Fig. 4c.*

the {110} sample shown in Figs. 3 and 4, and were not visible at all in crystals of {111} orientation. This is simply a geometric property of the crystals; however, the Burgers vector of the slip dislocations has a larger component normal to the {110} than the {100} or {111} crystal planes. The difference in visible slip cannot, therefore, be attributed to a greater degree of deformation in the {110} specimen. The variation in type and degree of deformation with orientation is, in fact, negligible as indicated by the structures in Fig. 5, taken after 50 s of erosion.

At the end of the incubation period, the general undulations develop into crater-like depressions with large smooth lips. Material loss occurs from the lips of the craters. It is obvious from the plasticity of aluminum, even at this stage of deformation, that particles are removed by ductile rupture rather than by brittle fracture. Details of a typical fracture area, circled in Fig. 4*c*, are shown in Fig. 4*d*.

The SEMs of bicrystal No. 1, Figs. 6*a*, *b*, illustrate the general influence of crystal orientation on the erosion damage. The grain boundary is discernable at high erosion times only because of the orientation of the slip lines and of the over-all wavy nature of the cavitation-induced craters. These micrographs and those of bicrystal No. 2 in Figs. 7*a*, *b* show that, apart from the delineation due to the different slip systems operating in

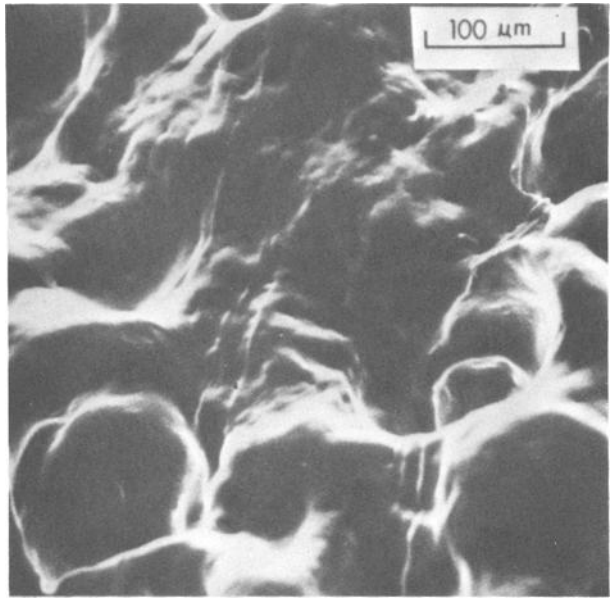


FIG. 5a—*Surface of aluminum single crystal of {110} orientation after 50 s of erosion.*

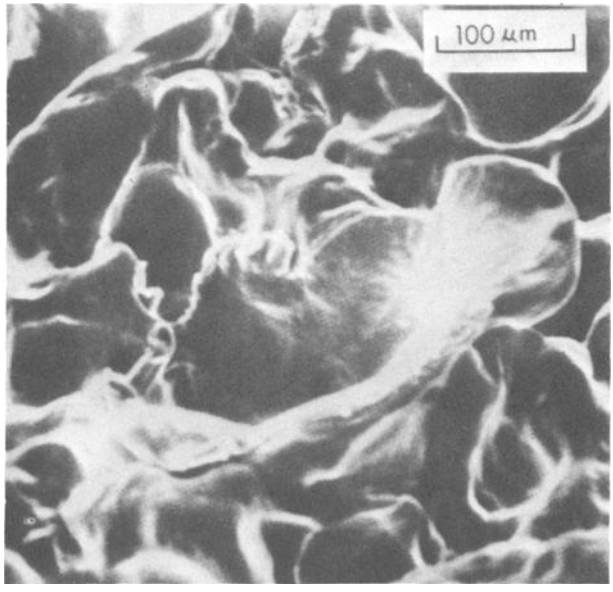


FIG. 5b—*Surface of aluminum single crystal of {100} orientation after 50 s of erosion.*

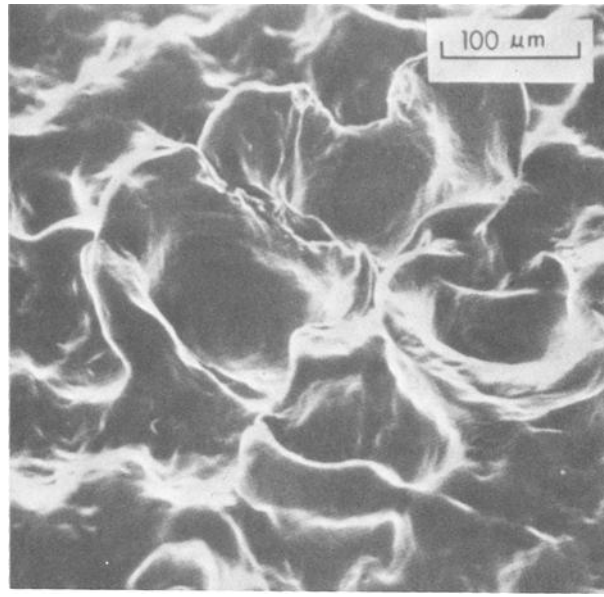


FIG. 5c—*Surface of aluminum single crystal of {111} orientation after 50 s of erosion.*

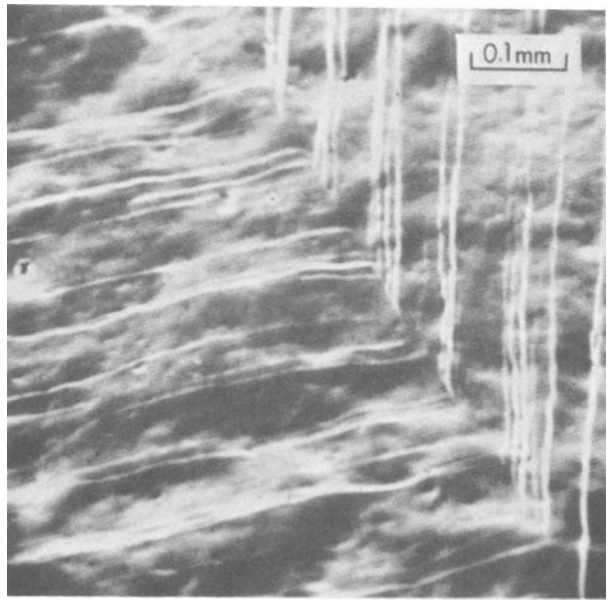


FIG. 6a—*Formation of slip bands in both grains of bicrystal No. 1 after 10 s of erosion.*

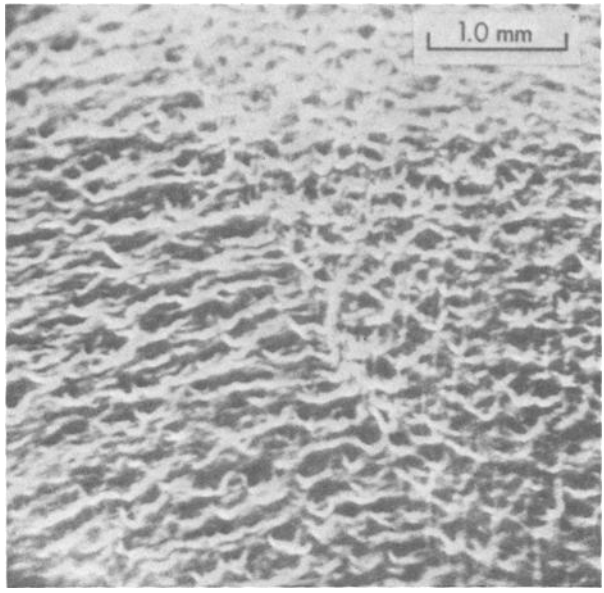


FIG. 6b—*Surface feature of bicrystal No. 1 after 50 s of erosion.*

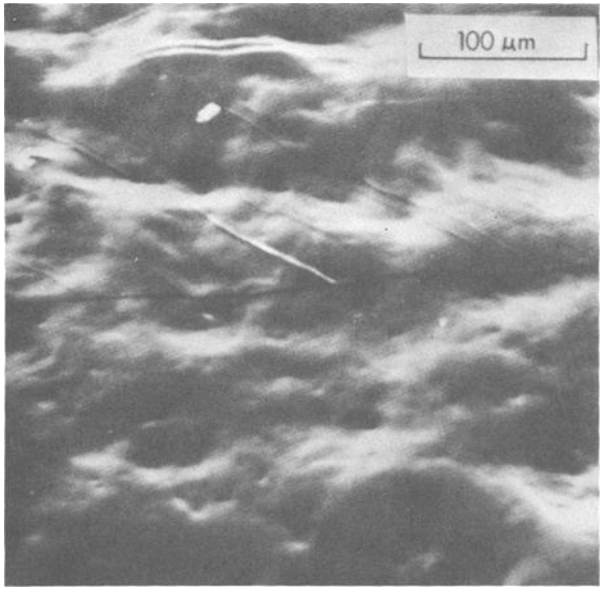


FIG. 7a—*Slip band formation on the surface of one grain in bicrystal No. 2 after 10 s of erosion.*

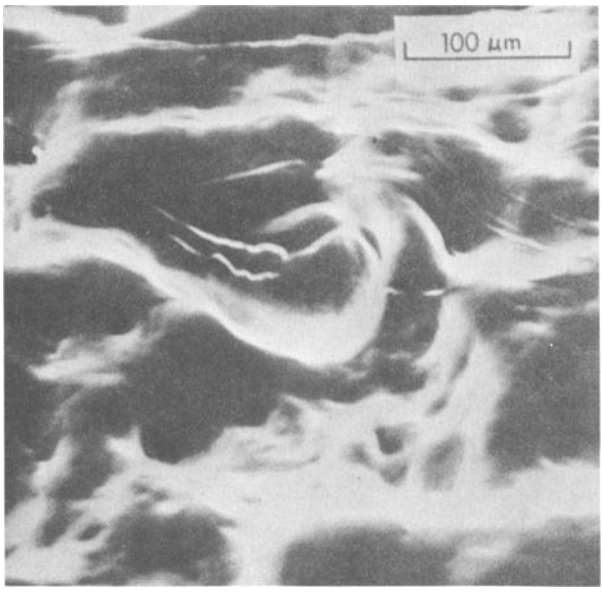


FIG. *7b—Surface feature of bicrystal No. 2 after 40 s of erosion.*

each grain, the grain boundaries have little effect on erosion. However, in addition to the high degree of plasticity at the grain boundaries shown in Fig. 1, other unusual effects have been observed. For example, in Fig. 8 the grain boundary appears to be pulled apart to form a groove. It was anticipated that the groove would act as a crack nucleus and grow deeper with subsequent exposure to cavitation. Figures 8*b*, *c*, taken after a further 50 s of erosion, show that this did not occur and that plastic deformation continued at the grain boundary, effectively closing up the groove.

*Transmission Electron Microscopy*

Electron micrographs of samples eroded for 5 s at different amplitudes of vibration are shown in Figs. 9*a–e*. All specimens contain a high concentration of point defect clusters and heavily jogged dislocations, and there is no indication of the cell structure usually observed in deformed aluminum. There appears to be little change in the density of these defects with amplitude, though it is well known that increasing the amplitude produces an increase in erosion rate and shortens the incubation period.

The SEM studies would suggest that lengthening the time of exposure

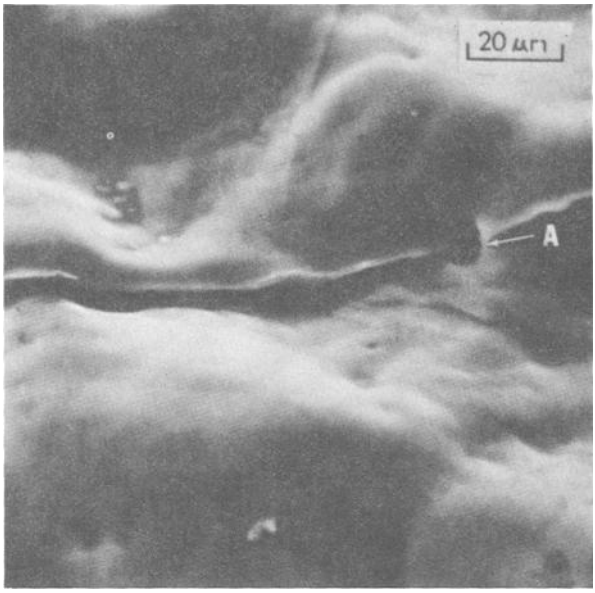


FIG. 8*a*—*Grain boundary pulled apart after 15 s of erosion in bicrystal No. 3. The pit labelled* A *is typical of those considered to be caused by the collapse of a single bubble.*

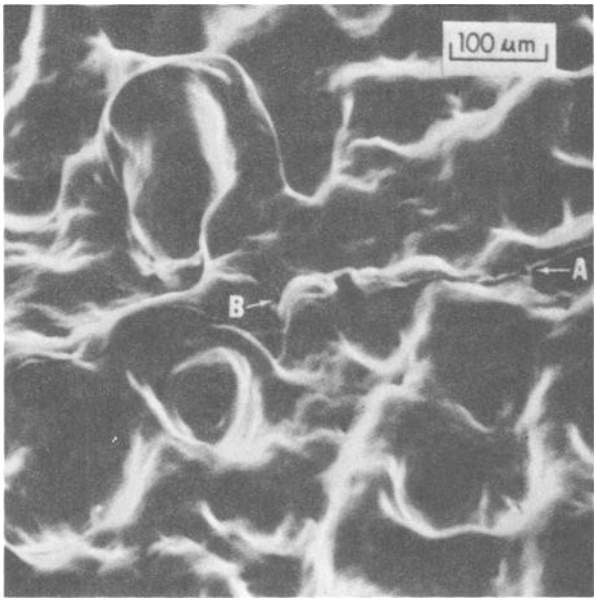


FIG. 8*b*—*Grain boundary of bicrystal No. 3 after 65 s of erosion. Note that the pit labelled* A *has not grown is size with the increased erosion time.*

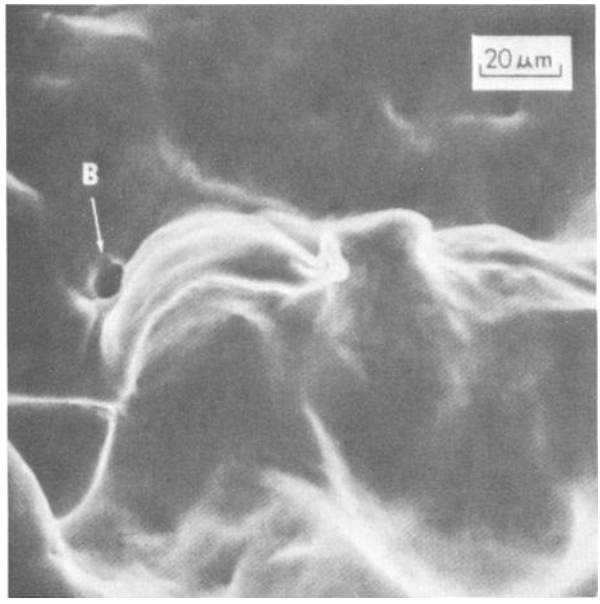


FIG. 8c—*Magnification of region around the pit labelled* B *in Fig. 8b. No grain boundary grooving is visible at this stage of erosion.*

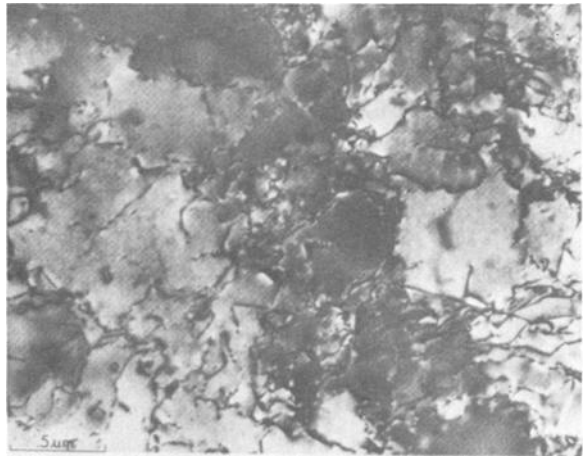

FIG. 9a—*TEM of polycrystalline aluminum after 5 s of erosion at an amplitude of 43 μm.*

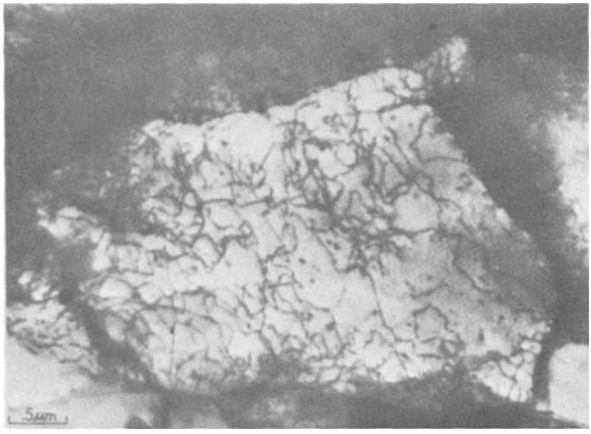

FIG. 9*b*—*TEM of polycrystalline aluminum after 5 s of erosion at an amplitude of 66 μm.*

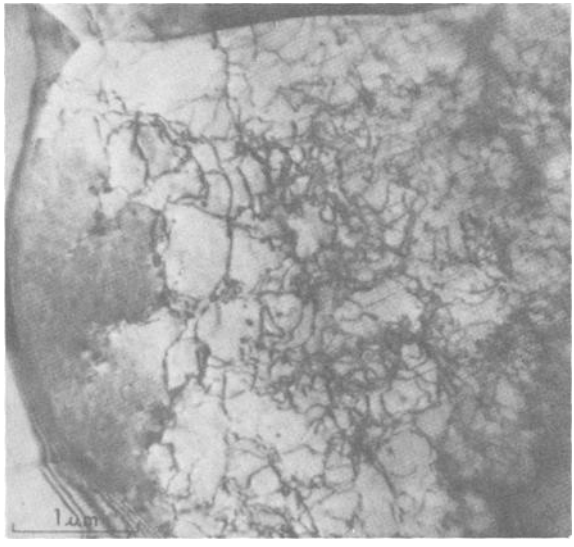

FIG. 9*c*—*TEM of polycrystalline aluminum after 5 s of erosion at an amplitude of 88 μm.*

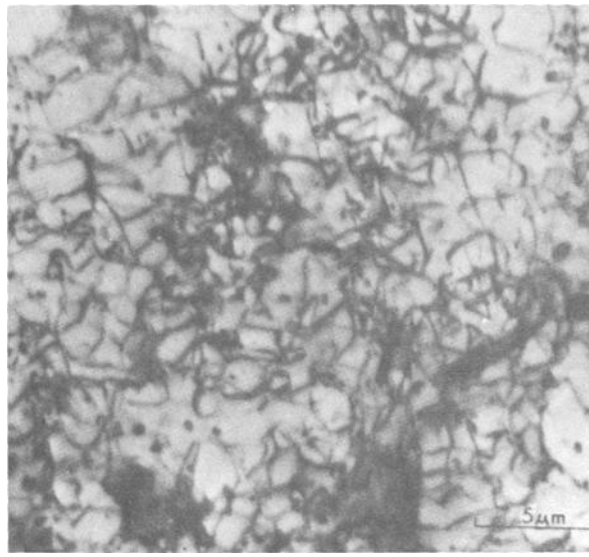


FIG. 9*d*—*TEM of polycrystalline aluminum after 5 s of erosion at an amplitude of 109 μm.*

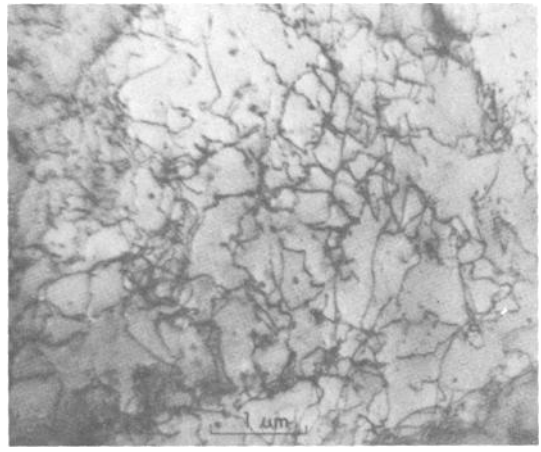


FIG. 9*e*—*TEM of polycrystalline aluminum after 5 s of erosion at an amplitude of 128 μm.*

to cavitation should result in a considerably higher density of dislocations since the macroscopic deformation increases severely. A TEM of a specimen exposed for 30 s at an amplitude of 88 $\mu$m, Fig. 10, does show a

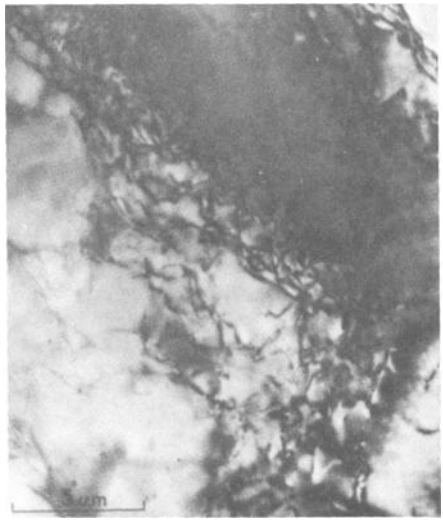

FIG. 10—*TEM of polycrystalline aluminum after 30 s of erosion at an amplitude of 88 $\mu$m.*

slightly higher dislocation density than those exposed for only 5 s. but the increase is not as large as expected. It is probable that the insignificant variation in defect density with amplitude of vibration or time of exposure to cavitation may be attributed to dynamic recovery of the specimens.

## Discussion

The various theories proposed to explain the mechanism of cavitation erosion may be classified into three areas—accelerated corrosion, localized melting, and mechanical stressing—the latter being subdivided according to the proposed mode of stress. It is appropriate to consider the results of the present study in terms of these three classes of theories.

### *Accelerated Corrosion*

Oxidation and the formation of hydroxides undoubtedly occur during cavitation erosion of aluminum and, when allowed to grow to scale thickness, are found to contribute significantly to the erosion process. In the experiments described here, however, conditions for oxide growth were kept to a minimum and corrosion is not considered of consequence since

it is apparent from the micrographs that mechanical deformation plays the major role. It may be argued that the interaction of environment and mechanical stressing could result in stress corrosion cracking, but pure aluminum has never been found to be susceptible to that phenomenon[*27*] and, furthermore, the highly ductile fracture mode produced by cavitation, Fig. 4*d*, is unlike those observed in stress-corroded metals, especially the aluminum alloys. Corrosion fatigue may be proposed as an alternative mode of failure, but again this appears unlikely since metals are not generally susceptible to corrosion fatigue at ultrasonic frequencies[*28*]. This is thought to be because of insufficient time available in each cycle for the corrosion reaction to occur.

*Localized Melting and Thermal Effects*

The highly ductile craters shown in Figs. 3–8 could be attributed to very high stresses or to an increase in the temperature of the metal surface. Actual melting of the surface layers would remove all traces of slip lines and of the dislocations observed by TEM and must, therefore, be disregarded. Attempts were made to measure any temperature increase using a thin-film thermocouple plated beneath a foil sample. The results indicated an increase of only ~ 30°C (86°F) but were not considered reliable because the mechanical stressing of the composite specimen was sufficient to separate the layers.

Aluminum recovers and recrystallizes very rapidly at temperatures greater than ~ 100°C (212°F)[*29*] and any significant rise in temperature during stressing would result in simultaneous recovery and a subgrain structure. The dislocation arrays observed in specimens within 24 h of erosion showed little sign of recovery, but after four days at room temperature the dislocations were observed to be forming into subgrain walls, Fig. 11, and, after two weeks, recovery was complete, as indicated by the well-defined subgrain structure in Fig. 12.

It is apparent, therefore, that the structures in Figs. 9 and 10 may already have recovered to some extent, which would account for the little variation in defect density, but obviously no significant degree of recovery could have occurred during actual exposure to cavitation. This indicates either that any thermal effects are small, as suggested by the temperature measurements, or that their duration is too short to contribute effectively to thermally activated processes in the metal.

*Mechanical Stressing*

It is evident from many studies that mechanical deformation plays a major role in erosion by cavitation and this is readily discernable in a ductile metal such as aluminum. Pure aluminum has a high stacking fault

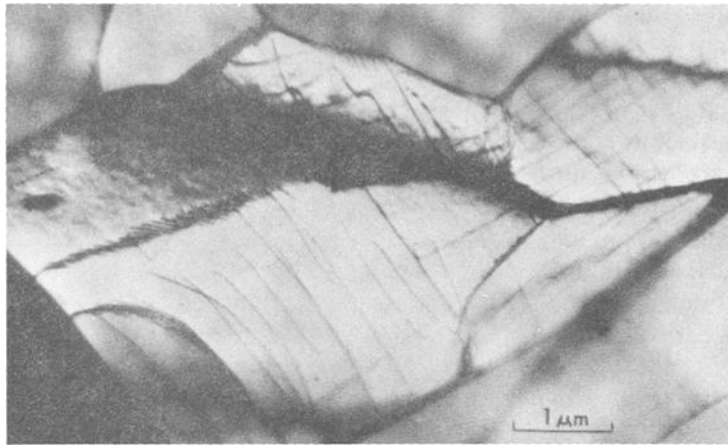


FIG. 11—*TEM of polycrystalline aluminum observed four days after erosion for 5 s.*

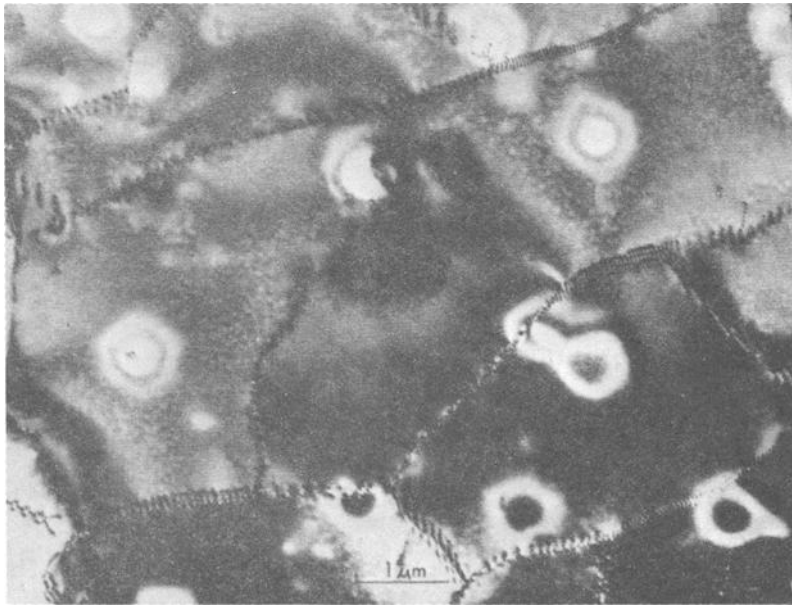


FIG. 12—*TEM of polycrystalline aluminum observed two weeks after erosion for 5 s.*

energy[*30*] and, hence, dislocations can cross slip easily, resulting in a low work-hardening rate and a low recovery temperature, as discussed in the foregoing. However, under more common deformation modes, such as tension, bending, or rolling, dislocation cell structures such as that shown in Fig. 13 are invariably formed[*29*]. Under cyclic stressing at all (including ultrasonic) frequencies, multiple slip is not generally observed

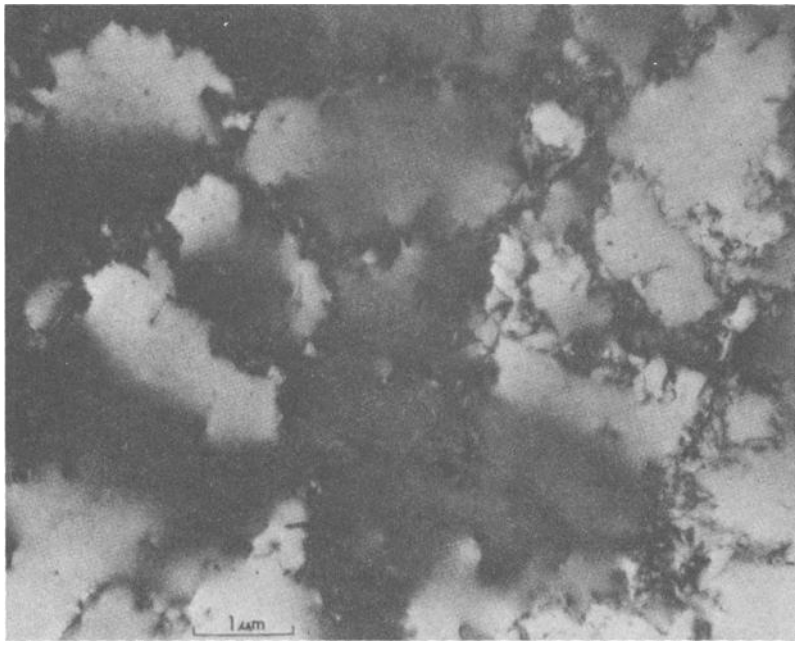


FIG. 13—*Cell structure in polycrystalline aluminum rolled 5 per cent at room temperature.*

and deformation is confined to relatively few slip bands which grow in intensity with increasing number of cycles[*26,31,32*]. Dislocation cell structures are again formed, their size and intensity depending on the frequency and stress level[*31–33*]. Failure by fatigue, however, occurs only under conditions where there is a tensile component of the stress, and results from void growth and coalescence along the slip bands. In cavitation, the only possibility of a tensile stress appears to be in the lips of the craters where the material is forced upwards between the adjacent depressions. It is interesting to note that this is the area from which material does, in fact, fail.

The only stress mode which has been shown to give a dislocation structure similar to those observed in this investigation is shock loading. Figure 14 shows the structure of aluminum shock loaded at 65 kilobar pressure at room temperature[*34*]. The random jogged dislocations and high density of point defect clusters are remarkably similar to those in Fig. 9.

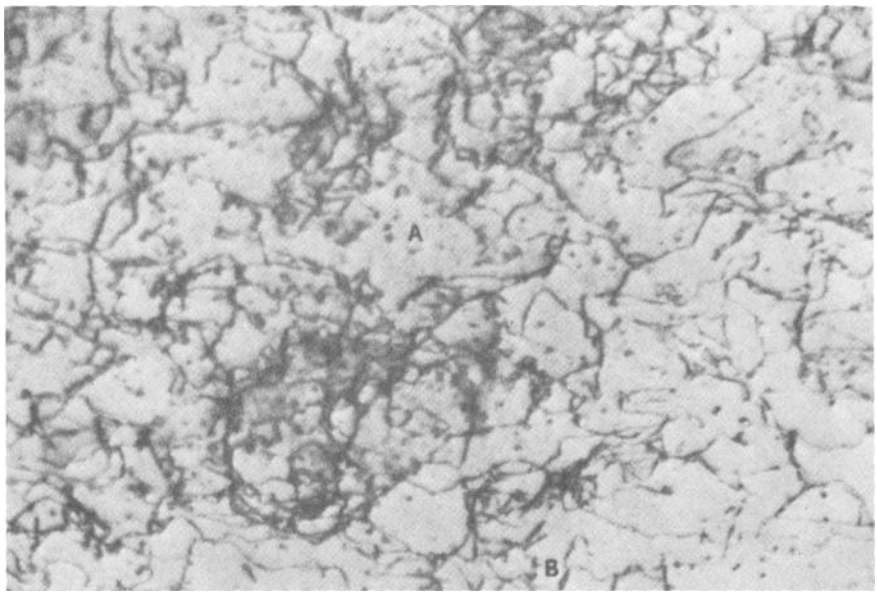


FIG. 14—*TEM of polycrystalline aluminum shock-loaded at 65-kbar pressure at room temperature. (Ref* 34, *by permission of Pergamon Press.)*

It has been shown that the collapse of a cavity is capable of producing a shock pulse of ~ 1 kilobar[*5,15,35,36*]—easily sufficient to severely damage a metal. However, on the basis of calculations of the attenuation of the pulse from a single collapsing cavity, it has been suggested by many investigators that the damage produced in a solid is due only to the collapse of those individual bubbles which are in the close vicinity of the solid surface. Those cavities at distances from the solid greater than their radius are considered to have an insignificant effect on its erosion[*3,15,37*]. Nevertheless, while it is conceivable that the collapse of an individual bubble could produce a pit of the same order of magnitude as itself, such as those labeled *A and B* in Fig. 8, it is difficult to understand how slip lines extending throughout a crystal of 12.5 mm diameter and general undulations of the surface (> 150 $\mu$m diameter) could be produced unless it is by the impact pressure of many thousands of collapsing bubbles acting

in concert. The pressure exerted by such a cloud of bubbles has been determined empirically to be ~ 30 kilobar[*1*].

It has been argued that, in spite of the magnitude of the pressure shocks emitted by a collapsing cavity, they appear unlikely to produce the observed damage because of their short duration[*38*]. However, shock pulses of the order of microseconds are commonly found to produce severe damage to solids[*39*], and the minimum estimate of the duration of those produced by cavitation at kHz frequencies is ~ 1 $\mu$s[*5*].

If the general undulations of the surface are considered to result from the combined pressure pulse of a large number of bubbles, then those pulses must also be held responsible for the macroscopic deformation and ultimate removal of material, because it is obvious from the sequence of micrographs in Fig. 3 that the undulations develop into the large craters, after which particles are removed from their edges by ductile rupture. Thus the shock- or jet-action of individual bubbles cannot be considered the only major source of mechanical stressing.

The grain boundaries play only a minor role in erosion and do not act as sites for preferential attack. They do provide barrier to initial bulk plastic flow, but appear to have little influence in preventing crater formation or removal of material. It is expected, however, that in an alloy system in which solute segregation or precipitation occurs, the grain boundaries may be more effective in inhibiting the initial deformation that leads to crater formation.

## Conclusions

The crystallographic orientation of a specimen does not appear to influence its rate of erosion. Although the formation of coarse slip steps on the surface is a function of orientation, the steps do not play a role in subsequent deformation and do not act as site for particle removal.

Grain boundaries provide a barrier to slip in the initial stages of deformation and a considerable degree of plastic flow occurs in the grain boundary regions, particularly in the vicinity of triple points. However, at later stages of deformation, the grain boundaries have little influence; they do not inhibit crater formation or material loss nor do they provide a preferential site for erosion.

The small pits on the surface are attributed to the collapse of individual bubbles in the immediate vicinity of the surface. On the other hand, the extensive slip lines and large craters, from the edges of which material loss occurs, are considered to be produced by the pressure pulse of a large number of bubbles collapsing in concert.

The dislocation substructures produced by cavitation show no sign of

the cell formation which is readily apparent in aluminum after it has been subjected to fatigue stressing or other modes of deformation such as rolling. The structures observed, which consist of a high density of random, heavily jogged dislocations and numerous point defect clusters, are remarkably similar to those formed in aluminum by shock pressures produced by explosive loading. It must be concluded, therefore, that the pressure wave produced by the cloud of collapsing bubbles has the characteristics of a shock pulse.

*Acknowledgments*

The authors would like to acknowledge the support of the National Science Foundation under grant number HO35940.

## References

[1] Eisenberg, P., *Transactions*, Society of Naval Architects and Marine Engineers, Vol. 73, 1965, p. 241.

[2] Eisenberg, P., in *Characterization and Determination of Erosion Resistance, ASTM STP 474*, American Society for Testing and Materials, 1969, p. 1.

[3] Knapp, R. T., *Transactions*, American Society of Mechanical Engineers, Vol. 77, 1955, p. 1045.

[4] Naude, C. F. and Ellis, A. T., *Transactions*, American Society of Mechanical Engineers, Vol. 83D, 1961, p. 648.

[5] Benjamin, T. B. and Ellis, A. T., *Philosophical Transactions of the Royal Society*, Vol. 206A, 1966, p. 221.

[6] Knapp, R. T., Daily, J. W., and Flammitt, F. G., *Cavitation*, McGraw-Hill, New York, 1970.

[7] Neppiras, E. A. and Fill, A. A., *Journal of the Acoustical Society of America*, Vol. 46, No. 5, 1969, p. 1264.

[8] Plesset, M. S. and Chapman, R. B., *Journal of Fluid Mechanics*, Vol. 47, Part 2, 1971, p. 283.

[9] Garcia, R., Hammitt, F. G., and Nystrom, E.R., in *Erosion by Cavitation or Impingement, STP 408*, American Society for Testing and Materials, 1967, p. 239.

[10] Thiruvengadam, A., *Transactions*, American Society of Mechanical Engineers, Vol. 85D, 1963, p. 365.

[11] Tichler, J. W., Van der Elsen, J. B., and de Gee, A. W. T., *Transactions*, American Society of Mechanical Engineers, Vol. 92F, 1970, p. 220.

[12] Bush, H., Hoff, G., and Langbien, G., *Philosophical Transactions of the Royal Society*, Vol. 260A, 1966, p. 168.

[13] Beckwith, D. J. and Marriott, J. B., *Proceedings*, Second Meersburg Conference on Rain Erosion and Allied Phenomena, 1967, p. 761.

[14] Hammitt, F. G., Huang, Y. C., Kling, C. L., Mitchell, T. M., and Soloman, L. P., in *Characterization and Determination of Erosion Resistance, ASTM STP 474*, American Society for Testing and Materials, 1969, p. 288.

[15] Brunton, J. H., *Proceedings*, Third International Conference on Rain Erosion and Allied Phenomena, 1970, p. 821.

[16] Eisenberg, P., in *Characterization and Determination of Erosion Resistance, ASTM STP 474*, American Society for Testing and Materials, 1969, p. 15.

[17] Callis, G. T., *Cavitation in Hydrodynamics*, Her Majesty's Stationary Office, London, 1956.
[18] Erdmann-Jasnitzer, F. and Borbe, P. C., *Archiv für das Eisenhüttenwesen*, Vol. 38, 1967, p. 63.
[19] Engel, O., *Proceedings*, Third International Conference on Rain Erosion and Allied Phenomena, 1970, p. 449.
[20] Hornbogen, E., *Proceedings*, Meersburg Rain Erosion Conference, 1965, p. 190.
[21] Reiger, H., *Proceedings*, Second Meersburg Conference on Rain Erosion and Allied Phenomena, 1967, p. 793.
[22] Vasvari, F., *Acta Technica Academicae Scientiarum Hungaricae*, Vol. 39, 1962, p. 101.
[23] Gould, G. C., in *Characterization and Determination of Corrosion Resistance, ASTM STP 474*, American Society for Testing and Materials, 1969, p. 181.
[24] Gould, G. C., *Proceedings*, Third International Conference on Rain Erosion and Allied Phenomena, 1970, p. 881.
[25] Woodford, D. A., *Metallurgical Transactions*, Vol. 3, 1972, p. 1137.
[26] Mason, W. and Wood, W. A., *Journal of Applied Physics*, Vol. 39, No. 12, 1968, p. 558.
[27] Uhlig, H. H., *Fracture*, H. Liebowitz, Ed., Academic Press, New York, 1971.
[28] Duquette, D. J., *Corrosion Fatigue*, A. S. McEvily and R. W. Stachle, Eds., National Association of Corrosion Engineers, Houston, 1972, p. 12.
[29] Reed, R. P., *Cryogenics*, Vol. 12, No. 4, 1972, p. 259.
[30] Barrett, C. S. and Massalski, T. B., *Structure of Metals*, McGraw-Hill, New York, 1966, p. 392.
[31] Grosskreutz, J. C. and Waldow, P., *Acta Metallurgica*, Vol. 11, 1963, p. 717.
[32] Feltner, C. E., *Acta Metallurgica*, Vol. 11, 1963, p. 817.
[33] Maurer, K. L., *Proceedings*, First International Symposium on High Power Ultrasonics, 1970, p. 53.
[34] Rose, M. F. and Berger, T. L., *Philosophical Magazine*, Vol. 17, No. 150, 1968, p. 1121.
[35] Hickling, R. and Plesset, M. S., *Physics of Fluids*, Vol. 7, 1964, p. 7.
[36] Schulmeister, R., *Proceedings*, Meersburg Rain Erosion Conference, 1965, p. 95.
[37] Knapp, R. T., *Transactions*, American Society of Mechanical Engineers, Vol. 80, 1958, p. 91.
[38] Plesset, M. S., *Philosophical Transactions of the Royal Society*, Vol. 260A, 1966, p. 241.
[39] Duvall, G. E., *Response of Metals to High Velocity Deformation*, Wiley (Interscience), New York, 1961, p. 165.

# DISCUSSION

*A. F. Conn*[1]—The authors are to be congratulated for a most thorough study of the micromechanisms responsible for cavitation erosion of soft aluminum. Although describing the loss of small pieces of material near the edge of pits, they did not say just how these pieces were caused to break off. I wonder if the authors would care to conjecture on how these pieces are removed?

*B. Vyas (authors' closure)*—Observation of the eroded surface of aluminum by SEM indicates that material is removed by ductile rupture at the edges of the deformation craters. This view is endorsed by optical metallography of cross sections of the sample, which shows internal void formation and necking of the edges of the craters; see Fig. 15.

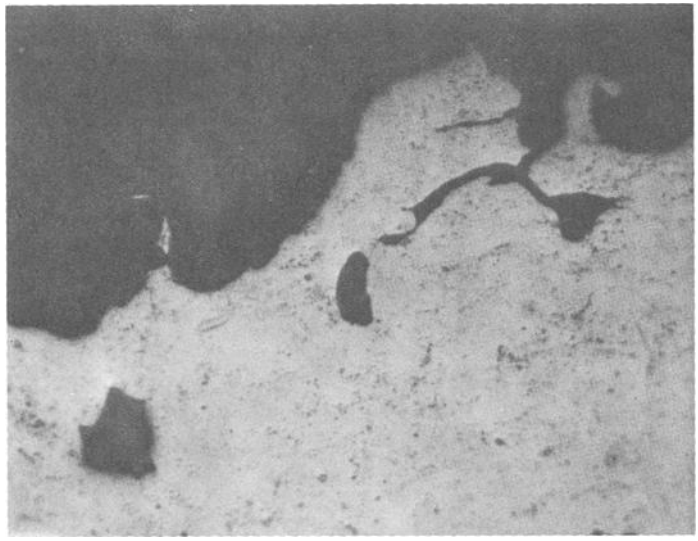

FIG. 15—*Cross section of eroded sample of aluminum showing necking at edges of the deformation craters after 120 s exposure to cavitation. Optical micrograph,* ×*260.*

[1] Principal research scientist and head, Material Sciences Division, HYDRONAUTICS, Incorporated, Laurel, Md. 20810.

*W. T. Ebihara*[2]—The SEMs showing the apparent dislodgment of the aluminum grains are quite interesting. Would you please comment as to how this phenomenon could take place? Would the cavitation loading be of such magnitude to cause such displacement of grains or could this be caused by removal of the grain boundary atoms?

*B. Vyas (authors' closure)*—Removal of grain boundary atoms would be expected to produce a groove along the boundary, rather than the depression of whole grains as the micrographs suggest. Our calculations indicate that, for the latter to result from material removal over the whole surface of the grain, some weight loss should be detectable. Since we are not able to detect any loss in weight at this stage of the erosion process, we can only assume that the depression is a result of mechanical deformation. This is not unlikely if erosion is caused by a shock pulse as we propose. The magnitude of such a pulse would be easily sufficient to produce the observed effect.

*J. W. Tichler*[3]—By means of the SEM, the authors studied aluminum surfaces in the incubation stage and in the very beginning of what we call the stage of uniform material removal.[4] One of the significant observations is that the break-off of wear debris is ductile in nature, at least for aluminum. The material removal is apparently *not* due to a fatigue mechanism for this material.

Several authors proposed a statistical model for the breakout of wear particles from the eroding surface, based on the assumption that this breakout is due to a fatigue mechanism. This assumption is not necessary. The break-off of particles is a stochastic process, whether it is due to fatigue or not.

On the other hand, fatigue probably plays an important role in the mechanism of pit formation, as has been shown by Tichler and Scott.[5]

*B. Vyas (authors' closure)*—We thank Dr. Tichler for his comments. However, it cannot be concluded that pit formation due to cavitation is a fatigue process, simply because a certain group of steels is rated in the same order of performance for resistance to rolling contact fatigue and to cavitation erosion. As Dr. Tichler himself suggests,[5] an equally likely explanation is that cavitation occurs in the lubricant during rolling contact fatigue.

[2] Research metallurgist, Rodman Laboratory, Rock Island Arsenal, Rock Island, Ill. 61201.

[3] Metal Research Institute TNO, Apeldoorn, The Netherlands.

[4] See page 56 of this volume (Tichler et al, "Applied Cavitation Erosion Testing").

[5] Tichler, J. W. and Scott, D., *Wear*, Vol. 16, 1970, pp. 229–233.

*W. F. Adler*[6]—I would like to congratulate Vyas and Preece for an excellent presentation of this most interesting and significant research. Since this research parallels a portion of the program in particulate and cavitation erosion at Bell Aerospace, I would like to take this opportunity to provide some perspective on the importance of studying erosion mechanisms during the very early stages of the erosion process.

First, one has to decide whether the application for the experimentally evaluated erosion behavior is the development of more erosion-resistant materials of the same general character as some reference material or the estimation of the lifetime of a given material exposed to a specified erosive environment. Professor Thiruvengadam's models,[7] for example, are directed toward this latter objective. He is attempting to obtain a universal curve which describes the steady-state erosion rates for a variety of materials in terms of a limited number of engineering parameters. On the other hand, microscopic examination of the very early stages of the erosion process affords one the opportunity to discover what microstructural features of a given material contribute to its erosion behavior. The localized features of the material on a scale which interacts with the erosive medium control its erosive response. By understanding the material characteristics on a microscopic level which govern the erosion behavior, it may be possible to modify the microstructural characteristics to greatly improve a material's erosion resistance without changing its overall strength levels. This means that the incubation period can be extended as indicated in Fig. 16. It is conjectured that the same material properties which influence the onset of erosion damage will also have some influence on the erosion behavior during the steady-state erosion range in the manner suggested in Fig. 16. The long-term weight loss can be changed significantly by a possibly simple microstructural modification or by the selection of a metallic alloy from a homologous series once the controlling microscopic erosion mechanisms are understood.

Detailed microscopic investigations and metallographic analyses as represented in the work of Vyas and Preece provide the basis for isolating the material characteristics which most significantly affect the erosion behavior of that material. These characteristics can be quite distinct from the usual engineering properties: yield strength, ultimate strength, hardness, and so on. It is fairly well established that the initial erosive response of a metallic specimen is not governed by its mechanical characteristics

[6] Principal scientist, Advanced Materials Research Department, Bell Aerospace Company, Buffalo, N. Y. 14240.

[7] Thiruvengadam, A., *Proceedings*, Third International Conference on Rain Erosion and Associated Phenomena, 1970, p. 565.

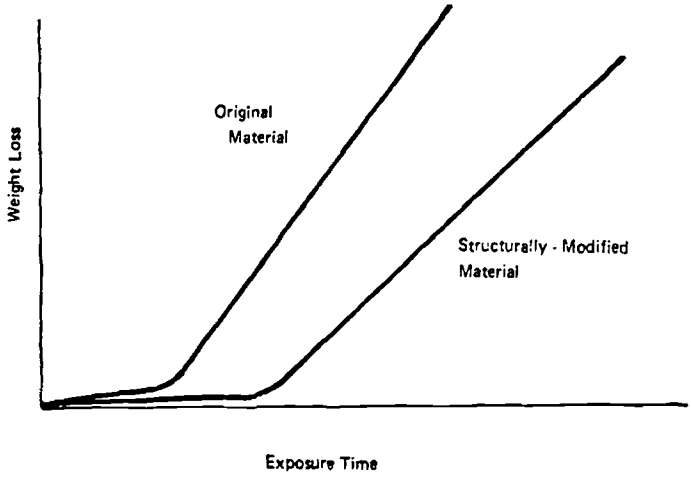


FIG. 16—*Modification in weight-loss data due to extended incubation period.*

evaluated on a gross scale[8,9] but by the microstructural features which interact with the erosive environment.[10,11] This observation can be further supported by the fact that erosion damage due to liquid droplet impacts occurs at impact pressures well below the ultimate and often even the yield strength of the specimen. Our microscopic investigations of rain erosion damage in annealed Ti-6Al-4V specimens reveal that damage occurs on a microscopic scale during the first few droplet impacts on the same area even when the magnitude of the maximum applied pressure pulse (computed according to the water hammer equation) is approximately one half the gross yield strength for this material.[11] On the basis of these microscopic investigations more representative analyses can be made of a material's response to an erosive environment. It is in this context that research along the lines presented by Vyas and Preece will greatly advance fundamental understanding of how to select and develop more erosion-resistant materials.

[8] Garcia, R., Hammitt, F. G., and Nystrom, R. E., in *Erosion by Cavitation or Impingement, ASTM STP 408,* American Society for Testing and Materials, 1967, p. 239.

[9] Morris, J. W. and Bates, C. H., *Proceedings,* Third International Conference on Rain Erosion and Associated Phenomena, 1970, p. 261.

[10] Hackworth, J. V. and Adler, W. F., "Microscopic Investigation of Cavitation Erosion Damage in Metals," presented at the Conference on the Role of Cavitation in Mechanical Failures, Boulder, Colo., Oct. 1973.

[11] Adler, W. F. and Vyhnal, R. F., "Rain Erosion of Ti-6Al-4V," presented at the Fourth International Conference on Rain Erosion and Related Phenomena, Meersburg, Germany, May 1974.

*G. S. Springer* [1] *and C. B. Baxi* [1]

# A Model for Rain Erosion of Homogeneous Materials

**REFERENCE:** Springer, G. S. and Baxi, C. B., "A Model for Rain Erosion of Homogeneous Materials," *Erosion, Wear, and Interfaces with Corrosion, ASTM STP 567*, American Society for Testing and Materials, 1974, pp. 106–127.

**ABSTRACT:** In this report the behavior of homogeneous materials subjected to repeated impingements of liquid droplets was investigated. Based on fatigue theorems, a model was presented for describing both the incubation period $n_i$ (that is, the time elapsed before the mass loss of the material becomes appreciable), and the mass loss past the incubation period $m$. The parameters were established which govern the length of the incubation period and the subsequent mass loss rate, and simple algebraic expressions were developed relating $n_i$ and $m$ to the properties of the impinging droplets and the material. The limits of applicability of the model was also established.

The results obtained were compared to available experimental data. Reasonable agreement was found between the present results and the data, indicating that the model developed can be used to estimate the incubation period and the mass loss of the material.

**KEY WORDS:** rain erosion, liquid impingement, erosion mechanism, fatigue model, incubation period, erosion

Aircraft components such as radomes, leading-edge surfaces, helicopter blades, and various structural members may experience heavy damage when subjected to repeated impingements of rain droplets. Liquid droplets may also cause significant damage to steam turbine blades. Owing to the severity of the problem, numerous investigations have been concerned with the effects of liquid impingement on surfaces. Excellent reviews summarizing previous experimental and analytical work have been given by,

[1] Professor and research associate, respectively, Department of Mechanical Engineering, University of Michigan, Ann Arbor, Mich. 48104.

among others, Eisenberg[*1*],[2] Engel[*2*], Heymann[*3,4*], Heymann and Arcella[*5*] and Wahl[*6*]. Many of the recent studies dealing with the problem are also described in Refs *7–9*.

The majority of previous studies on the subject of rain erosion have been experimental in nature, with the bulk of prior research concentrating on the measurement of an erosion parameter (for example, total weight loss) of a specimen subjected to specific conditions. Such empirical studies provide information on the behavior of a given material under a given condition, but fail to describe material behavior beyond the range of the experiments in which they were obtained. Recently, attempts have been made to derive analytical or semi-empirical formulas which describe the dependence of material damage on selected operating variables, such as impact velocity and droplet size[*3–5,10–12*]. Although these studies shed light on some of the mechanisms which contribute to material damage, a satisfactory method has not yet been devised which is capable of correlating the existing data and generalizing the results obtained from a few experiments. The objective of this investigation is to develop a model which is consistent with experimental observations and which predicts quantitatively "erosion" of materials under previously untested conditions. It is evident that such a model is needed for the selection of the proper materials and for the design of appropriate structures and components subject to severe liquid impingement.

The model proposed here is aimed at describing (*a*) the "incubation period," that is, the time elapsed before the mass loss of the material becomes appreciable, and (*b*) the degradation of the material past the incubation period as manifested by its mass loss. The existence of an incubation period suggests that the damage produced in the material is the consequence of cumulative fatigue damage produced by the repeated impacts of the droplets. Therefore, the present model is based on fatigue concepts. The role of fatigue in rain erosion has been recognized in the past[*13–17*] and attempts have been made to describe the material damage in terms of fatigue parameters[*3,4,18*]. However, expressions for the incubation period and for the subsequent material loss have not yet been derived.

## The Problem

The problem investigated is the following. Spherical liquid droplets of constant diameter $d$ impinge repeatedly upon a semi-infinite, homogeneous

[2] The italic numbers in brackets refer to the list of references appended to this paper.

material (Fig. 1). The angle of incidence of the droplets $\theta$ and the velocity of impact $V$ are taken to be constant. The spatial distribution of the droplets is considered to be uniform. Thus, the number of droplets impinging on unit area in time $t$ is

$$n = (V \cos\theta) q\, t \tag{1}$$

where $q$ is the number of droplets per unit volume. Rain, falling with constant terminal velocity $V_t$ is usually characterized by a parameter $I$, called "intensity," which is related to $q$ by the expression

$$q = \frac{6}{\pi} \frac{I}{V_t d^3} \tag{2}$$[3]

In Eq 2 $I$ has the units of length/time. Values for $V_t$ may be obtained from charts[*19*] or may be calculated from the empirical relationship[*20*]

$$V_t = 965 - 1030\, e^{-6d} \text{ (cm/s)} \tag{3}$$

where $d$ is in centimeters. Equations 1 and 2 may be combined to yield

$$n = \frac{6}{\pi} \frac{(V \cos\theta) I}{V_t d^3} t \tag{4}$$

The impingement rate is assumed to be sufficiently low so that all the effects produced by the impact of one droplet diminish before the impact

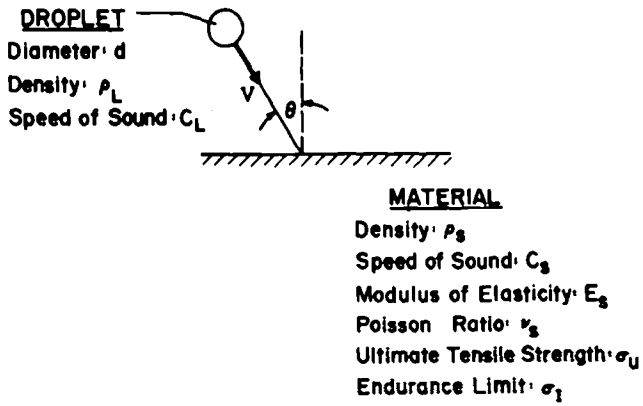


FIG. 1—*Droplet impingement on a homogeneous material. Description of the problem.*

[3] Any consistent set of units may be used in Eq 2. Customarily $I$ is expressed in in./h, $V_t$ in ft/s and $d$ in mm. For these units

$$q \cong 1250 \frac{I}{V_t d^3} \text{ (number/ft}^3\text{)}$$

of the next droplet. This assumption is justified since, in practice, the time between subsequent impingements at a point is of the order of $10^{-2}$ s, while the stresses produced in the material become negligible in about $10^{-6}$ s.

The pressure within the droplet varies both with position and with time. For simplicity, the pressure will be taken to be constant, its value being given by the water hammer pressure[21]

$$P = \frac{\rho_L C_L V \cos\theta}{1 + \frac{\rho_L C_L}{\rho_s C_s}} \tag{5}$$

where $\rho$ is the density and $C$ the speed of sound. The subscripts $L$ and $s$ refer to the liquid and the solid, respectively. In terms of the modulus of elasticity $E_s$

$$C_s = \sqrt{E_s/\rho_s} \tag{6}$$

Although more accurate representation of the pressure is possible[21], the accuracies afforded by the use of Eq 5 will suffice in the present analysis. Thus, the force imparted to the surface by each droplet is

$$F = P \frac{\pi d^2}{4} \tag{7}$$

The forces created by the repeated droplet impacts damage the material as manifested by the formation of pits and cracks on the surface, and by weight loss of the material. Experimental evidence indicates that under a wide range of conditions the weight loss $W$ varies with time $t$, as shown schematically in Fig. 2*a*. For some period of time, referred to as the incubation period, the weight loss is insignificant. Between the end of the incubation period $t_i$ and a time denoted by $t_f$ the weight loss varies nearly linearly with time. After $t_f$ the relationship between $W$ and $t$ becomes more complex. Here, we will be concerned only with the behavior of the material up to time $t_f$.

It is advantageous to replace the total weight loss of the specimen by the mass loss per unit area $m$, and the time by the number of droplets impinging upon unit area $n$. In terms of the parameters $m$ and $n$, schematic representation of the data is given in Fig. 2*b*. It is now assumed that the data can be approximated by two straight lines as shown in Fig. 2*b*, that is

$$m = 0, \qquad 0 < n < n_i \tag{8a}$$

$$m = \alpha(n - n_i), \qquad n_i < n < n_f \tag{8b}$$

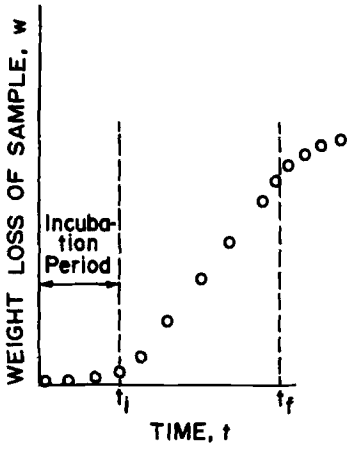


FIG. 2*a*—*Schematic of the experimental results.*

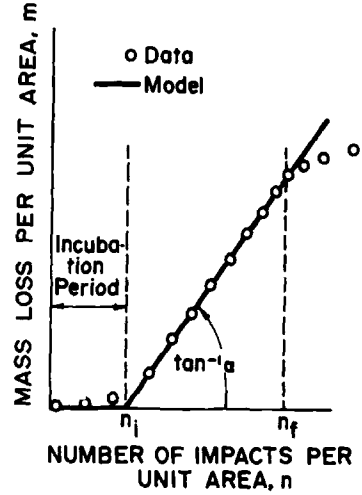


FIG. 2*b*—*The solution model.*

Thus, the material loss $m$ produced by a certain number of impacts $n$ can be calculated once the incubation period $n_i$, and the rate of subsequent mass loss (as characterized by the slope $\alpha$ are known. Therefore, the problem at hand is to determine the parameters $n_i$, $\alpha$, and $n_f$, the latter being the upper limit of validity of Eq 8*b*.

It is noted here that the foregoing model is valid only if there is an incubation period. It has been observed experimentally that under some conditions even one impact will result in appreciable damage, a situation in which $t_i = 0$.

### Incubation Period, $n_i$

It has been recognized that fatigue plays an important role in the erosion process [*3,4,13–18*], particularly in the "early" stages of the process, corresponding to the incubation period. Therefore, it is expected that fatigue theorems established for the torsion and bending of bars might be applied, at least qualitatively, to materials subjected to repeated liquid impingement. The failures of bars undergoing repeated torsion or bending have been found to follow Miner's rule[*22*], which is expressed by

$$\frac{f_1}{N_1} + \frac{f_2}{N_2} + \ldots \frac{f_k}{N_k} = a_1 \tag{9}$$

where $f_1, f_2 \ldots f_k$ represent the number of cycles the specimen is subjected to specified overstress levels, $\sigma_1, \sigma_2 \ldots \sigma_k$, and $N_1, N_2 \ldots N_k$

represent the life (in cycles) at these overstress levels, as given by the fatigue ($\sigma$ versus $N$) curve; $a_1$ is a constant which in torsion and bending tests generally varies between 0.6 and 2.2.

Let us now consider one element at point $B$ on the surface of the material as shown in Fig. 3. Each droplet impinging on the surface will

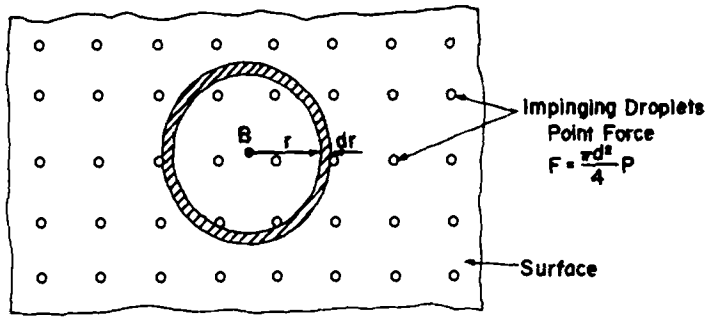


FIG. 3—*Force distribution on the surface.*

create a stress at point $B$. Assuming that the force created by the droplet at its point of impact is a "point force," the stress at point $B$ due to any one droplet is[*23*]

$$\sigma(r) = \frac{F(1 - 2\nu_s)}{2\pi r^2} \tag{10}$$

where $\nu_s$ is the Poisson ratio. Every droplet which falls at a radius $r$ produces the same stress at point $B$. Therefore, the number of cycles for which the material at point $B$ is subjected to a given stress between $\sigma$ and $\sigma + d\sigma$ is equal to the number of impacts on a $dr$ wide annulus located at $r$ (Fig. 3). During the incubation period the total number of impacts on the annulus is

$$f(r) = n_i 2\pi r dr \tag{11}$$

Therefore, $f_1, f_2 \ldots f_k$ in Eq 9 are replaced by $f(r_1), f(r_2) \ldots f(r_k)$, that is,

$$\frac{f(r_1)}{N_1} + \frac{f(r_2)}{N_2} + \ldots \frac{f(r_k)}{N_k} = a_1 \tag{12}$$

Since $r$ varies continuously from zero to infinity, Eqs 11 and 12 may be written as

$$\int_0^\infty \frac{n_i 2\pi r dr}{N} = a_1 \tag{13}$$

Using Eq 10, $rdr$ can be expressed in terms of $\sigma$

$$rdr = -\frac{1}{2\pi}\frac{F(1-2\nu_s)}{2\sigma^2}\,d\sigma \tag{14}$$

Equations 13 and 14 together with Eq 7 yield

$$-\int_{\sigma_u}^{\sigma_l}\frac{n_i[P\frac{\pi d^2}{4}\ (1-2\nu_s)/2\sigma^2]}{N}\,d\sigma = a_1 \tag{15}$$

The lower and upper limits of the integrals have been changed to the ultimate tensile strength $\sigma_u$ and the endurance limit $\sigma_l$, respectively. In order to perform the integration, the fatigue life $N$ must be known as a function of $\sigma$. For most materials the fatigue curve between $\sigma_u$ and $\sigma_l$ may be approximated by (Fig. 4)

$$N = b_1\sigma^{-b} \tag{16}$$

where $b$ and $b_1$ are constants. Equation 16 must satisfy the conditions

$$N = 1 \quad \text{for} \quad \sigma = \sigma_u \tag{17a}$$
$$N = 10 \quad \text{for} \quad \sigma = \sigma_l \tag{17b}$$

In Eq 17$b$, $10^{b_2}$ corresponds to the "knee" in the fatigue curve (Fig. 4). Equations 16 and 17 yield

$$N = \left(\frac{\sigma_u}{\sigma}\right)^b \tag{18}$$

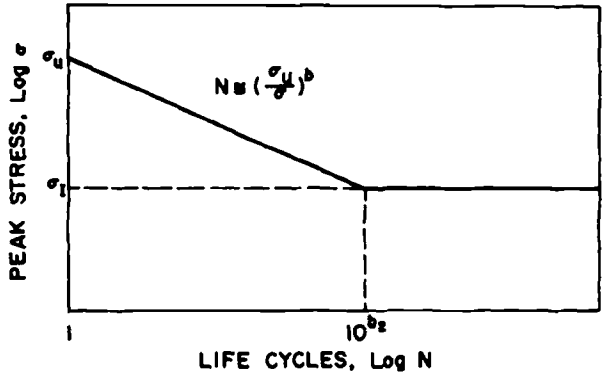


FIG. 4—*Idealized σ-N curve.*

$$b \equiv \frac{b_2}{\log_{10}\left(\frac{\sigma_u}{\sigma_l}\right)} \tag{19}$$

Substituting Eq 18 into Eq 15 and integrating, we obtain

$$\frac{\pi d^2}{4} n_i P(1 - 2\nu_s) \frac{\sigma_u^{b-1} - \sigma_l^{b-1}}{2(b-1)\sigma_u^{b}} = a_1 \tag{20}$$

Introducing the definitions

$$S \equiv \frac{2\sigma_u(b-1)}{(1-2\nu_s)\left[1 - \left(\frac{\sigma_l}{\sigma_u}\right)^{b-1}\right]} \cong \frac{2\sigma_u(b-1)}{1-2\nu_s} \tag{21}$$

$$n_i^* \equiv n_i \frac{\pi d^2}{4} \tag{22}$$

Eq 20 becomes

$$n_i^* = a_1 \frac{S}{P} \tag{23}$$

Defining by "site" the surface area equal to the cross-sectional area of one droplet, the number of sites per area $A$ is $A/(\pi d^2/4)$. Since $n_i$ is the number of impacts per unit area, $n_i^*$ is the total number of impacts per site. The minimum value of $n_i^*$ is unity.

The parameter $S$ characterizes the "strength" of the material. Thus, the number of impacts per site needed to initiate damage is proportional to the ratio of the strength of the material $S$ to the stress $P$ produced by the impinging droplets. Such a dependence of $n_i^*$ on $S$ and $P$ is reasonable, since the length of the incubation period is expected to increase with increasing $S$ and with decreasing $P$. However, in view of the fact that Eq 23 is based on the fatigue properties of materials in pure torsion and bending, one cannot expect a linear relationship to hold between $n_i^*$ and $S/P$. In order to extend the range of applicability of Eq 23 while retaining its major feature (namely, the functional dependence of $n_i^*$ on $S/P$), we write

$$n_i^* = a_1 \left(\frac{S}{P}\right)^{a_2} \tag{24}$$

where both $a_1$ and $a_2$ are as yet underdetermined constants. Since the form of the foregoing functional relationship between $n_i^*$ and $S/P$ is arbitrary, its validity must be evaluated by plotting experimentally observed

values of $n_i^*$ versus $S/P$. The relationship will prove to be correct if on a log-log scale such a plot results in a straight line. The equation of this line would provide the constants $a_1$ and $a_2$.

The $n_i^*$ and $S/P$ values deduced from all the available experimental data are shown in Fig. 5. The symbols used in this figure and the corresponding experimental conditions are identified in Table 1. It must be pointed out that only those data could be included in Fig. 5 for which not only $n_i$ but

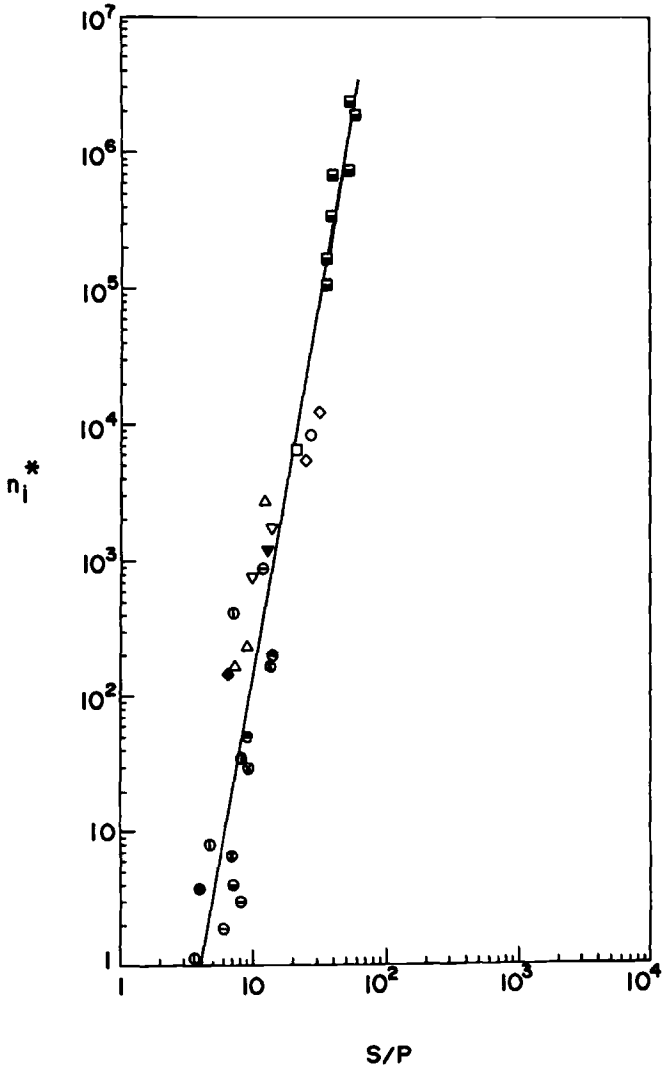


FIG. 5—*Incubation period versus* S/P. *Symbols for data defined in Table 1. Solid line: best fit to data.*

also the material properties ($\sigma_u$, $\sigma_1$, $b_2$, $\nu_s$, $E_s$, $\rho_s$) were available. It is seen from Fig. 5 that all the data can be correlated by a straight line. The equation of this line, obtained by a least-square fit of the data, is

$$n_i^* = 3.7 \times 10^{-4}(S/P)^{5.7} \tag{25}$$

The excellent correlation in Fig. 5 lends support to the validity of the model.

As was discussed in the previous section, the present model is valid only when the incubation time is greater than zero. This condition is met when $n_i^* > 1$ or, according to Eq 25, when $S/P > 4.0$. Thus, an incubation period exists if

$$\begin{matrix} n_i^* > 1 \\ S/P > 4.0 \end{matrix} \tag{26}$$

The foregoing analysis (Eq 25) can be applied only when the foregoing conditions are satisfied. When $S/P$ is equal to or less than 4.0, damage will occur even upon one impact per site.

### Rate of Mass Removal, $\alpha$

Beyond the incubation period, erosion of the surface of the material (as expressed in terms of mass loss) proceeds at a nearly constant rate as shown in Fig. 2*b*. In order to calculate this erosion rate, an analogy is drawn again between the behavior of the material upon which liquid droplets impinge and the behavior of specimens subjected to torsion or bending fatigue tests. Experimental observations show that in the latter case the specimens do not all fail at once at some "minimum life," but that their failure is scattered around a "characteristic life." For specimens in torsion and bending tests the probability that failure will occur between minimum life $n_i$ and any arbitrary longer life $n$ may be estimated from the Wiebull distribution[*24*]

$$p = 1 - \exp\left[-\left(\frac{n - n_i}{n_a}\right)^{\beta}\right] \tag{27}$$

where $n_a$ is the characteristic life corresponding to the 63.2 percent failure point and $\beta$ is a constant (Weibull slope). For $(n - n_i)/n_a << 1$, Eq 27 may be approximated by

$$p \cong \left(\frac{n - n_i}{n_a}\right)^{\beta} \tag{28}$$

The probability $p$ can also be taken as the number of specimens that fail between $n_i$ and $n$. If the material undergoing erosion due to liquid impinge-

ments is considered to be made up of many small "parts," then the amount of material eroded (mass loss) is proportional to $p$, that is

$$\frac{m}{\rho_s d} = a_3 \left(\frac{n - n_i}{n_a}\right)^{\beta} = a_3 \left(\frac{n^* - n_i^*}{n_a^*}\right)^{\beta} \tag{29}$$

In Eq 29, $m$ was nondimensionalized with respect to $\rho_s d$ in order to render the proportionality constant $a_3$ dimensionless. Equation 8*b* is now rewritten in dimensionless form

$$\frac{m}{\rho_s d} = \frac{a}{\pi \rho_s d^3/4} (n^* - n_i^*) \tag{30}$$

Equating Eqs 29 and 30, we obtain

$$\frac{a}{\pi \rho_s d^3/4} = a_3 \frac{(n^* - n_i^*)^{\beta - 1}}{(n_a^*)^{\beta}} \tag{31}$$

According to Eq 31 the mass loss rate $a$ depends on the total number of impacts $n$. However, our model postulates a constant mass loss rate (that is, $a$ is independent of $n$; see Fig. 2*b*), at least when $n_i < n < n_f$. This requirement can be met by setting $\beta = 1$. Such a value for $\beta$ is not unreasonable under high-frequency loading[*17*]. The characteristic life $n_a$ is related to the minimum life $n_i$. This relationship may be expressed suitably as

$$n_a^* = a_4 n_i^{*a_5} \tag{32}$$

where $a_4$ and $a_5$ are constants. Introducing the dimensionless mass loss rate

$$a^* \equiv \frac{a}{\pi \rho_s d^3/4} \tag{33}$$

Eqs 31 to 33, together with the assumption $\beta = 1$, yield

$$a^* = a_6 \frac{1}{(n_i^*)^{a_5}} \tag{34}$$

The new constant $a_6$ was introduced in place of $a_3/a_4$.

The validity of Eq 34 can be assessed (and the constants $a_3$ and $a_6$ can be determined) by plotting experimentally obtained values of $a^*$ versus $(1/n_i^*)$. According to Eq 34, on a log-log scale such a plot should result in a straight line. All the available experimental data are presented in

such a manner in Fig. 6. As can be seen, the data follow reasonably closely a straight line of the equation

$$\alpha^* = 0.023 \left(\frac{1}{n_i^*}\right)^{0.7} \tag{35}$$

indicating that the arguments leading to Eq 35 were reasonable. The somewhat larger scatter of these data as compared with the data on the $n_i^*$ versus $S/P$ curve is due to the fact that, first, $n_i$ can be estimated more accurately from the available data than the slope of $\alpha$, and second, all available data have a rather wide margin of error, but the value of $n_i$ is less sensitive to these errors than the value of $\alpha$.

Instead of plotting $\alpha^*$ versus $1/n_i^*$ as was done in Fig. 6, $\alpha^*$ could have been correlated directly with the parameter $S/P$ by using the relationship between $n_i^*$ and $S/P$ given in Eq 25. However, if $\alpha^*$ were plotted

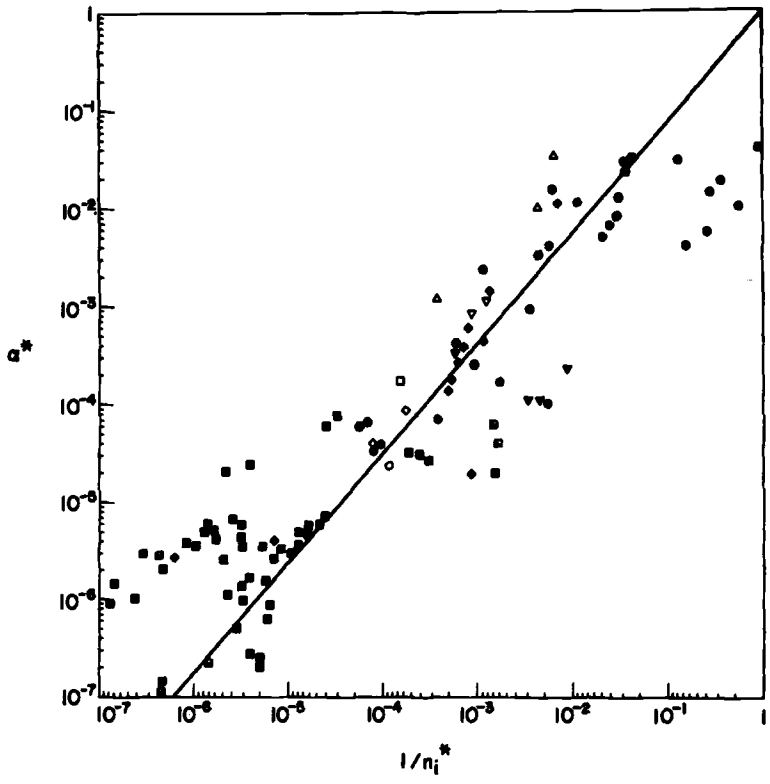


FIG. 6—*Rate of erosion versus the inverse of the incubation period. Symbols for data defined in Table 1. Solid line: best fit to data.*

versus $S/P$, then in this figure only those data could be included for which the material properties needed for calculating $S$ were known. By plotting $a^*$ against $1/n_i^*$, the use of these properties could be avoided—an advantage because for many of the data only $n_i^*$ were known but not the material properties.

The relationship between the time rate of mass loss ($\partial m/\partial t$) and the impact velocity $V$ can now be established. For a rain of constant diameter and intensity impinging upon a given material, $a$ may be expressed as

$$a = \frac{\pi \rho_s d^3}{4} a^* = \frac{\pi \rho_s d^3}{4} \left[ 0.023 \left( \frac{1}{n_i^*} \right)^{0.7} \right] \sim P^4 \sim V^4 \quad (36)$$

Noting that $\partial n/\partial t = Vq \cos\theta$ (see Eq 1), we may write

$$\frac{\partial m}{\partial t} = \frac{\partial m}{\partial n} \frac{\partial n}{\partial t} = aVq \cos\theta \sim aV \sim V^5 \quad (37)$$

This result is consistent with the experimental observation that the time rate of mass loss varies approximately with the 5th power of the impact velocity.

## Total Mass Loss

In Fig. 5 and 6 only those data could be included for which the variation of the mass (or weight loss) with time was known. There are numerous data available where such complete information is unavailable, but where the mass loss is given at one instant of time. A comparison of the present model with the latter "single-point" results would be desirable, since agreement with such "single" data points would lend confidence to the validity of the model. To facilitate such a comparison Eq 8*b* is rewritten in dimensionless form

$$m^* = a^* (n^* - n_i^*) \quad (38)$$

or

$$\frac{m^*}{a^*} = n^* - n_i^* \quad (39)$$

where the dimensionless mass loss is defined as

$$m^* \equiv \frac{m}{\rho_s d} \quad (40)$$

According to our model, expressed by Eq 39, all data should be correlated on an $m^*/a^*$ versus $(n^* - n_i^*)$ plot. Such a correlation is presented in

Fig. 7. This figure includes all existing data known to us in which droplets impinge continuously on a homogeneous material (see Table 1). The results of experiments in which a jet impinges upon the surface[25–28] were not included in this figure. As can be seen, the agreement between data and the theoretical line given by Eq 39 is quite reasonable, particularly in view of the large errors inherent in most of the experimental data.

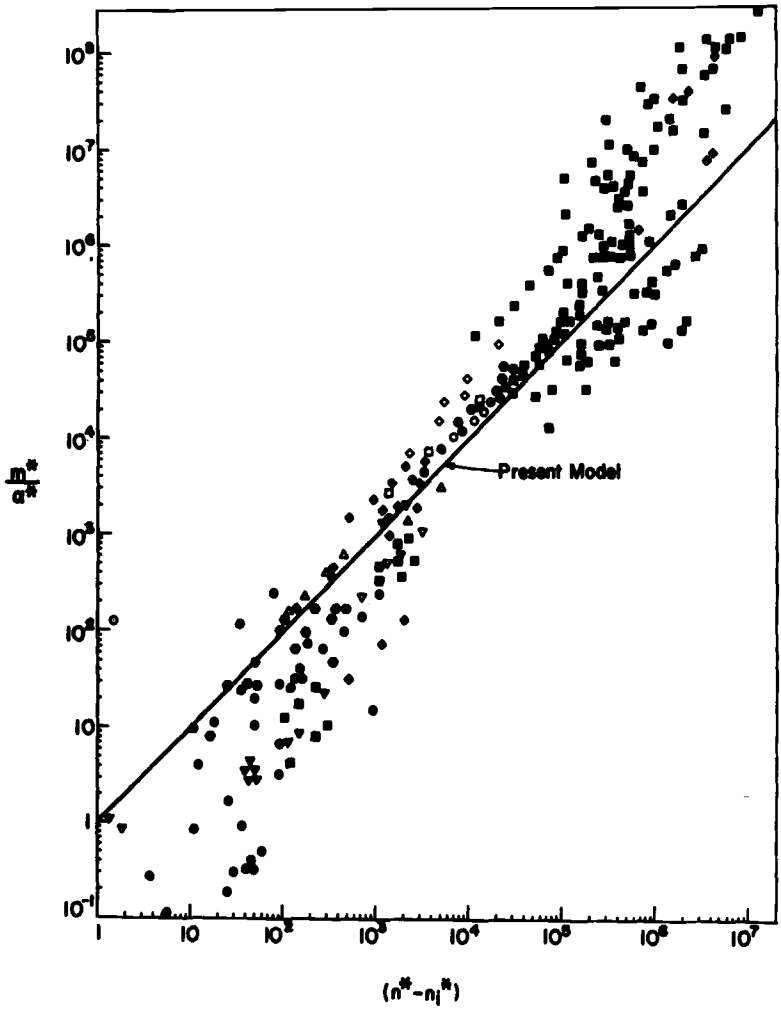


FIG. 7—*Comparison of present model (solid line, Eq 38) with experimental results. Symbols for data defined in Table 1.*

*Acknowledgments*

This work was supported by Air Force Contract F33615-71-C-1572, and administered by the Air Force Materials Laboratory, Wright-Patterson Air Force Base.

The authors wish to thank P. S. Larsen for his many helpful suggestions. They are also grateful to G. F. Schmitt, Jr., for his valuable comments and for providing many of the references and data used in this investigation.

TABLE 1—*Description of data and symbols used in Figs. 5, 6, and 7.*

| Symbol | Material | Velocity (ft/sec) | Diameter of Drop (mm) | Author |
|---|---|---|---|---|
| △ | Perspex | 730 | 1.9 | Fyall et al Ref. [29] |
| ◭ | | 1180 | 1.9 | Schmitt et al Ref. [30] |
| ◭ | | 1395 | 2.0 | King Ref. [31] |
| ▽ | Alkathane 2 | 585–730 | 1.9 | Fyall et al Ref. [29] |
| ▼ | Q.S. -4 Polyethylene | 730 | 1.9 | Fyall et al Ref. [29] |
| ▼ | Polyphenylene Oxide | 535–3720 | 1.9 | Schmitt et al Ref. [30] |
| ▽ | Cast Urethane | 730 | 1.8 | Morris & Wahl Ref. [32] |
| ▼ | Polypropylene | 980–1470 | 1.2 | King Ref. [33] |
| ▶ | Teflon | 1180 | 1.9 | Schmitt et al Ref. [30] |
| ○ | Aluminum Alloy, D.T.D. 423B | 730 | 1.9 | Fyall et al Ref. [29] |
| ● | 1100-0 Aluminum | 1120 | 1.8 | Morris & Wahl Ref. [11] |
| ◓ | 2024-T6 Aluminum | 1120–2240 | 1.8 | Morris & Wahl Ref. [11] |
| ◑ | 1145-H19 Aluminum | 1120–2240 | 1.8 | Morris & Wahl Ref. [11] |
| ◐ | 5052-0 Aluminum | 1120 | 1.8 | Morris & Wahl Ref. [11] |
| ⊖ | 6061-T6 Aluminum | 1120–2240 | 1.8 | Morris & Wahl Ref. [11] |

TABLE 1—*(Continued.)*

| Symbol | Material | Velocity (ft/sec) | Diameter of Drop (mm) | Author |
|---|---|---|---|---|
| ⊗ | 7075-T6 Aluminum | 1120-2240 | 1.8 | Morris & Wahl Ref. [11] |
| | | 1120 | | Morris & Wahl Ref. [32] |
| ⊗ | Aluminum (Pure) | 820-980 | 1.2 | King Ref. [33] |
| ⊗ | Aluminum | 1650-1420 | 1.2 | Rieger Ref. [34] |
| ⊗ | Aluminum Alloys | 1340 | 1.2 | Hoff et al Ref. [35] |
| □ | Magnesium Alloy D.T.D. 259 | 730 | 1.9 | Fyall et al Ref. [29] |
| ◇ | Copper Alloy B.S. 1433 | 585-730 | 1.9 | Fyall et al Ref. [29] |
| ◆ | Copper (Electrolytic) | 1120 | 1.8 | Morris & Wahl Ref. [11] |
| ◧ | Nickel | 1000 | 0.866 | Engel et al Ref. [36] |
| ◪ | | 1120 | 1.8 | Morris & Wahl Ref. [32] |
| ⬓ | Cobalt-Chromium Alloys | 1020 | 0.66 | Baker et al Ref. [37] |
| ⊟ | Iron | 1000 | 0.866 | Engel et al Ref. [36] |
| ⊠ | Steels | 1020 | 0.66 | Baker et al Ref. [38] |
| ⊠ | | 1455 | 0.64 | Herbert Ref. [39] |
| ⊠ | | 1120 | 1.8 | Morris & Wahl Ref. [32] |

TABLE 1—*(Continued.)*

| Symbol | Material | Velocity (ft/sec) | Diameter of Drop (mm) | Author |
|---|---|---|---|---|
| ◆ | Titanium Alloys | 1020 | 0.66 | Baker et al Ref. [38] |
| ◆ | | 1120 | 1.8 | Morris & Wahl Ref. [32] |
| ◆ | | 1340 | 1.2 | Hoff et al Ref. [40] |
| ◆ | Tantalum | 1000 | 0.866 | Engel et al Ref. [36] |
| ◆ | Udimet 700 | 1000 | 0.866 | Engel et al Ref. [36] |
| ◆ | Magnesia Ceramic | 1340 | 1.2 | Hoff Ref. [40] |
| ◆ | Zirconia | 1340 | 1.2 | Hoff Ref. [40] |
| ◆ | Alumina Ceramic | 1340 | 1.2 | Hoff Ref. [40] |
| ◆ | Spinell | 1340 | 1.2 | Hoff Ref. [40] |
| ◆ | Glass | 1340 | 1.2 | Hoff Ref. [40] |

## References


[1] Eisenberg, P., in *Characterization and Determination of Erosion Resistance. ASTM STP 474*, American Society for Testing and Materials, 1970, pp. 3–28.

[2] Engel, O., "Mechanism of Rain Erosion—A Critical Review of Erosion by Water Drop Impact," WADC Technical Report 53-192, Part 2, Wright-Patterson Air Force Base, Dayton, Ohio, Aug. 1953.

[3] Heymann, F. J., *Proceedings*, Second Meersburg Conference on Rain Erosion and Allied Phenomena, A. A. Fyall and R. B. King, Eds., Royal Aircraft Establishment, Farnborough, England, Aug. 1967, pp. 683–760.

[4] Heymann, F., "Erosion by Cavitation, Liquid Impingement and Solid Impingement: A Review," Engineering Report E-1460, Westinghouse Electric Corp., Lester, Pa., March 1968.

[5] Heymann, F. and Arcella, F., "Analytical Investigation of Turbine Erosion Phenomena," WANL-PR-(DD)-014, Westinghouse Astronuclear Laboratory, Westinghouse Electric Corp., Lester, Pa., Nov. 1966.

[6] Wahl, N. E., "Investigation of the Phenomena of Rain Erosion at Subsonic and Supersonic Speeds," AFML-TR-65-330, Air Force Materials Laboratory, Wright-Patterson Air Force Base, Dayton, Ohio, Oct. 1965.

[7] *Proceedings*, Rain Erosion Conference, A. A. Fyall and R. B. King, Eds., Meersburg, West Germany, May 1965; translation obtainable from the Royal Aircraft Establishment, Farnborough, England.

[8] *Proceedings*, Second Meersburg Conference on Rain Erosion and Allied Phenomena, A. A. Fyall and R. B. King, Eds., Aug. 1967; translation available from the Royal Aircraft Establishment, Farnborough, England.

[9] *Proceedings*, Third Conference on Rain Erosion and Allied Phenomena, A. A. Fyall, Ed., Royal Aircraft Establishment, Farnborough, England, Aug. 1970.

[10] Hammitt, F. G., Huang, Y. C., Kling, C. L., Mitchell, T. M., Jr., and Solomon, L. P., in *Characterization and Determination of Erosion Resistance, ASTM STP 474*, American Society for Testing and Materials, 1970, pp. 288–322.

[11] Morris, J. W., Jr. and Wahl, N. E., "Supersonic Rain and Sand Erosion Research: Erosion Characteristics of Aerospace Materials," AFML-TR-7-0265, Air Force Materials Laboratory, Wright-Patterson Air Force Base, Dayton, Ohio, Nov. 1970.

[12] Schmitt, G. F., Jr., Tatnall, G. J., and Foulke, K. W., "Joint Air Force-Navy Supersonic Rain Erosion Evaluations of Materials," AFML-TR-67-164, Air Force Materials Laboratory, Wright-Patterson Air Force Base, Dayton, Ohio, Dec. 1967.

[13] Brunton, J. H., "Liquid Impact and Material Removal Phenomena," Technical Memorandum No. 33-354, Jet Propulsion Laboratory, California Institute of Technology, Pasadena, Calif., June 1967.

[14] Leith, W. C. and Thompson, A. L., *Transactions*, American Society of Mechanical Engineers, *Journal of Basic Engineering*, Vol. 82D, 1960, pp. 795–807.

[15] Mathieson, R. and Hobbs, J. M., *Engineering*, Vol. 189, 1960, pp. 136–137.

[16] Ripken, J. F., in *Erosion by Cavitation or Impingement, ASTM STP 408*, American Society for Testing and Materials, 1967, pp. 3–11.

[17] Thiruvengadam, A., Rudy, S. L., and Gunasekaran, M., in *Characterization and Determination of Erosion Resistance, ASTM STP 474*, American Society for Testing and Materials, 1970, pp. 249–287.

[18] Mok, C. H., *Journal*, American Institute of Aeronautics and Astronautics, Vol. 7, 1969, pp. 751–753.

[19] Fyall, A. A., *Proceedings*, Meersburg Conference on Rain Erosion and Allied Phenomena, A. A. Fyall and R. B. King, Eds., Royal Aircraft Establishment, Farnborough, England, May 1965, pp. 30–42.

[20] Atlas, D., Srivastava, R. C., and Sekhon, R. S., "Doppler Radar Characteristics of Precipitation at Vertical Incidence," Technical Report No. 22, Laboratory for Atmospheric Probing, Department of Geophysical Sciences, University of Chicago, and Electrical Engineering Department, Illinois Institute of Technology, Chicago, Ill., May 1971.

[21] Heymann, F., *Transactions*, American Society of Mechanical Engineers, *Journal of Basic Engineering*, Vol. 90, 1968, pp. 400–405.

[22] Miner, M. A., *Journal of Applied Mechanics*, Vol. 12, 1945, pp. A159–A164.

[23] Timoshenko, S., *Theory of Elasticity*, McGraw-Hill, New York, 1934.

[24] Weibull, W., *Fatigue Testing and Analysis of Results*, Pergamon Press, New York, 1961.

[25] Beckwith, D. J. and Marriott, J. B., "Erosion Damage in a Cobalt-Chromium-Tungsten Alloy," Paper No. 126, Central Metallurgical Laboratories, English Electric, Whetstone, Leicester, England, June 1966.

[26] Beckwith, D. J. and Marriott, J. B., *Proceedings*, Second Meersburg Conference on Rain Erosion and Allied Phenomena, A. A. Fyall and R. B. King, Eds., Royal Aircraft Establishment, Farnborough, England, Aug. 1967, pp. 761–784.

[27] Hobbs, J. M., "Factors Affecting Damage Caused by Liquid Impact," NEL Report No. 262, National Engineering Laboratory, East Kilbridge, Glasgow, Scotland, Dec. 1966.

[28] Hobbs, J. M. and Brunton, W. C., "Comparative Erosion Tests on Ferrous Materials, Part I: Drop Impact Tests," NEL Report No. 205, National Engineering Laboratory, East Kilbridge, Glasgow, Scotland, Nov. 1965.

[29] Fyall, A. A., King, R. B., and Strain, R. N. C., "A Gravimetric Assessment of the Erosion Resistance of Various Materials," Report No. Chem. 513, Royal Aircraft Establishment, Farnborough, England, 1957.

[30] Schmitt, G. F., Jr. and Krabill, A. H., "Velocity-Erosion Rate Relationships of Materials in Rain at Supersonic Speeds," AFML-TR-70-44, Air Force Materials Laboratory, Wright-Patterson Air Force Base, Dayton, Ohio, Oct. 1970.

[31] King, R. B., *Proceedings*, Rain Erosion Conference, Meersburg, West Germany, A. A. Fyall and R. B. King, Eds., Royal Aircraft Establishment, Farnborough, England, May 1965, pp. 49–57.

[32] Morris, J. W., Jr., Adler, W. F., and Wahl, N. E., "Supersonic Rain and Sand Erosion Research: Characterization and Development of Erosion Resistant Materials," AFML-TR-72-85, Air Force Materials Laboratory, Wright-Patterson Air Force Base, Dayton, Ohio, May 1972.

[33] King, R. B., *Proceedings*, Second Meersburg Conference on Rain Erosion and Allied Phenomena, A. A. Fyall and R. B. King, Eds., Royal Aircraft Establishment, Farnborough, England, Aug. 1967, pp. 201–213.

[34] Rieger, H., *Proceedings*, Rain Erosion Conference, Meersburg, West Germany, A. A. Fyall and R. B. King, Eds., Royal Aircraft Establishment, Farnborough, England, May 1965, pp. 107–113.

[35] Hoff, G., Herbert, W., and Rieger, H., in *Characterization and Determination of Erosion Resistance, ASTM STP 474*, American Society for Testing and Materials, 1970, pp. 353–382.

[36] Engel, O. and Almo, J. A., "A Model for Multiple-Drop-Impact Erosion of Brittle Solids," Contract NASW-1481, Nuclear Systems Program Space Division, General Electric Company, Cincinnati, Ohio, May 1971.

[37] Baker, D. W. C., Jolliffe, K. M., and Pearson, D., *Philosophical Transactions of the Royal Society*, Vol. A260, 1966, pp. 193–203.

[38] Baker, D. W. C., Elliott, D. E., Jones, D. C., and Pearson, D., *Proceedings*, Second Meersburg Conference on Rain Erosion and Allied Phenomena, A. A. Fyall and R. B. King, Eds., Royal Aircraft Establishment, Farnborough, England, Aug. 1967, pp. 449–515.

[39] Herbert, W., *Proceedings*, Rain Erosion Conference, Meersburg, West Germany, A. A. Fyall and R. B. King, Eds., Royal Aircraft Establishment, Farnborough, England, May 1965, pp. 114–119.

[40] Hoff, G., *Proceedings*, Rain Erosion Conference, Meersburg, West Germany, A. A. Fyall and R. B. King, Eds., Royal Aircraft Establishment, Farnborough, England, May 1965, pp. 90–94.

# DISCUSSION

*A. F. Conn*[1]—In the oral presentation of this paper, the method was not described whereby, given a certain density of rainfall, the number of impacts per unit area can be calculated. As we have also made such calculations,[2,3] I think a brief description of the authors' method for estimating numbers of impacts would be useful for the record, if this procedure is not already in the written version of the paper.

*G. S. Springer and C. B. Baxi (authors' closure)*—The authors wish to thank Dr. Conn for suggesting that the method of estimating the numbers of impacts be included in the paper. The method is now shown in Eqs 1 to 4.

*F. G. Hammitt*[4]—The only way we can judge a new correlation is by its success in correlating the existing data. On this basis at any rate, the presently proposed correlation seems to represent a large backward step when compared with other published correlations over the past years, for example, at the last ASTM Symposium on this very subject.

Figure 7 of the present paper is a log-log plot of the final results. I note that for any value of the abscissa, the data spread is by a factor between $10^2$ and $10^3$, so that the standard deviation must be by $\times$ 10 or more. I would like to ask the authors what is the calculated standard deviation for this data fit?

Numerous correlations between mechanical properties and erosion resistance for similarly comprehensive data sets have been published by Hammitt et al[*10*], Heymann (discussion of Ref *10*), Rao et al,[5] and others. The

[1] Principal research scientist and head, Materials Sciences Division, HYDRONAUTICS, Incorporated, Laurel, Md. 20810.

[2] Conn, A. F., "Relating Dynamic Properties of Materials and Resistance to Damage by Rain Impact," Technical Report 905-1, HYDRONAUTICS, Incorporated, Laurel, Md., Jan. 1970.

[3] Conn, A. F. and Thiruvengadam, A., *Journal of Materials*, Vol. 5, No. 3, Sept. 1970, pp. 698–718.

[4] Professor, Department of Mechanical Engineering, Cavitation and Multiphase Flow Laboratory, University of Michigan, Ann Arbor, Mich. 48104.

[5] Rao, B. C. S., Rao, N. S. L., and Seetharamiah, K., *Transactions*, American Society of Mechanical Engineers, *Journal of Basic Engineering*, Sept. 1970, pp. 573–576.

TABLE 2—*Results for MDPR from Ref.* 10.

| Correlating Relation | $n$ (where applicable) | Sample Correlation Coefficient | 95% Confidence Limits for Population Correlation Coefficients | Factorial Standard Error of Estimate |
|---|---|---|---|---|
| $\frac{1}{MDPR} = C(UR)^n$ | 0.998 | 0.811 | 0.64 to 0.91 | 2.52 |
| $\frac{1}{MDPR} = C(UR)$ | ... | 0.811 | 0.64 to 0.91 | 2.52 |
| $\frac{1}{MDPR} = C(UR \times BHN)^n$ | 0.720 | 0.798 | 0.62 to 0.89 | 2.25 |
| $\frac{1}{MDPR} = C(UR \times E^2)^n$ | 0.659 | 0.744 | 0.52 to 0.86 | 2.35 |
| $\frac{1}{MDPR} = C(BHN)$ | ... | 0.742 | 0.52 to 0.86 | 2.75 |
| $\frac{1}{MDPR} = C(BHN)^n$ | 1.788 | 0.734 | 0.52 to 0.85 | 2.38 |
| $\frac{1}{MDPR} = C(UR \times BHN)$ | ... | 0.716 | 0.49 to 0.84 | 2.57 |
| $\frac{1}{MDPR} = C(UR \times E^2)$ | ... | 0.684 | 0.44 to 0.82 | 2.86 |
| $\frac{1}{MDPR} = C(SE)^n$ | 0.738 | 0.517 | 0.21 to 0.73 | 3.24 |
| $\frac{1}{MDPR} = C(SE)$ | ... | 0.498 | 0.17 to 0.72 | 3.30 |

standard deviation for most of these is ~2-3, rather than ~10, as apparently is true in the present case. Much (though not all) of the material to which I refer comes from *Characterization and Determination of Erosion Resistance, ASTM STP 474,* 1970. Table 2 summarizes our previously published numerical work in this regard. Typical of these data fits is Fig. 3 of Ref *10*; also, see Fig. 4 of Heymann's discussion of the same reference.

In conclusion, why do the authors feel that their correlation is preferable even though it apparently produces much poorer results than the various correlations previously published?

*G. S. Springer and C. B. Baxi (authors' closure)*—We can discern no technical basis for the objections expressed by Dr. Hammitt. The correlation proposed by Hammitt et al applies only to the mean depth of penetration (MDPR). Unlike our model, it does not provide such very important and practical parameters as the incubation period ($n_i$), rate of mass removal after the incubation period ($a$), and the total mass loss ($m$).

Our model not only provides considerably more information than Hammitt's correlation but, apparently, it also gives more accurate results. The average standard deviations for our model are 1.2 for $n_i$, 1.7 for $a$, 2.0 for $m$. In comparison, Hammitt's correlation yields standard deviations in the range of 2 to 3, in spite of the fact that it is entirely empirical; is based on fewer data; covers a much narrower range of experimental conditions; and is restricted to MDPR, which is easier to determine from the experiments.

It is also worth noting that the available experimental data (with which our model is compared) are very widely scattered. The standard deviations about the mean of the data themselves are generally of the order of 1 to 2.

*M. C. Rochester* [1] *and J. H. Brunton* [1]

# Influence of Physical Properties of the Liquid on the Erosion of Solids

REFERENCE: Rochester, M. C. and Brunton, J. H., "Influence of Physical Properties of the Liquid on the Erosion of Solids," *Erosion, Wear, and Interfaces with Corrosion, ASTM STP 567*, American Society for Testing and Materials, 1974, pp. 128–151.

ABSTRACT: Results are presented for the erosion of nickel in a series of experiments involving ten different liquids chosen so that the effects of density, acoustic impedance, and viscosity could be investigated separately. The shape of the erosion curve was not greatly affected by changes in the physical properties of the liquid. The level of damage in all stages of erosion was strongly dependent on acoustic impedence and viscosity; changes in density affected only the later stages of erosion. When carbon tetrachloride was used as the eroding fluid it was found that the damage during the second stage of erosion was proportional to the fifth power of the impact velocity, a result similar to that reported for water.

Measurements of the impact pressure distribution under the surface of a 5.0-mm-diameter water drop at velocities up to 140 m/s are presented. The distribution was found to be symmetrical about the center of impact with a central maximum of 0.7 $\rho_0 c_0 V$. The distribution along the central axis of the drop was also measured. No evidence of high pressures other than at the center of impact was found.

KEY WORDS: erosion, liquid properties, density, acoustic impedance, viscosity, impact pressure distribution

In studies of steam turbine blade erosion and rain erosion, various measures of damage have been proposed from time to time. Most of this work has shown that the damage, however measured, does not correlate precisely with any one strength property. Of the correlations which exist it would seem that hardness and strain energy to fracture[*1*,*2*][2] provide

[1] Doctoral candidate and lecturer, respectively, Engineering Department, Cambridge University, England. Mr. Rochester presently is lecturer in civil engineering, Plymouth Polytechnic, Plymouth, Devon, England.

[2] The italic numbers in brackets refer to the list of references appended to this paper.

the best indications of resistance to drop impact erosion. Theories of erosion which involve impact stress[3] or impact energy[4,5] yield expressions involving physical constants of the liquid such as density and sound speed. Only a few experiments seem to have been done on the effect of these properties on erosion damage[6]. Information on this subject would not only contribute to an understanding of basic erosion mechanisms but would also be of practical interest in connection with metal vapor power systems.

Other studies have been concerned with the mechanism of damage in a single impact[7,8]. These have shown that high initial pressures lasting for a small fraction of the total impact time are responsible for much of the damage. The same work has established the erosive effects of high-speed liquid flow across the surface from the center of impact. Some attempt has been made to measure the impact forces[7,9,10] but much controversy still surrounds the various measurements and estimates [7–14]. Very little is known about the pressure distribution across the impact surface and within the impinging drop.

It is clear from these remarks that more-detailed studies of the effect of liquid properties on erosion and measurements of both the peak impact pressure and the pressure distribution under a drop are required. In this paper experiments are described on the erosion of nickel using ten different liquids chosen so that the effects of density, acoustic impedance, and viscosity could be investigated separately, and measurements are presented of the distribution of peak impact pressure both under and within a water drop over a range of impact velocities.

## Experimental Techniques

### *Erosion Experiments*

In these experiments, nickel specimens were eroded by several liquids in a wheel and jet machine. The liquids used in the work are listed in Table 1 together with their relevant physical properties. They are classified in two groups. In the first group the densities and sound speeds vary but the viscosities have more or less the same low values. In the second group the densities and sound speeds are almost the same but the viscosities vary over a wide range.

The nickel specimens, 2 mm long, 6 mm wide and 3 mm deep, were machined from cold-rolled bar stock. They were annealed in a vacuum furnace at 900°C (1652°F) for one hour. The target surfaces were polished on a range of silicon carbide papers and a diamond-impregnated cloth to give a CLA surface roughness of the order of 1 $\mu$m. The mean hardness of the polished face was measured and from this figure the ap-

TABLE 1—*Physical properties of liquids used in erosion experiments.*[a]

| Liquid | Density, kg/m³ | Sound Speed, m/s | Acoustic Impedance, kg/m²-s | Viscosity, cP |
|---|---|---|---|---|
| Group 1[b] | | | | |
| Ethyl alcohol | $0.79 \times 10^3$ | 1162 | $0.92 \times 10^6$ | 1.20 |
| Paraffin | 0.80 | 1325 | 1.06 | 1.36 |
| Water | 1.00 | 1483 | 1.48 | 1.00 |
| Bromobenzene | 1.50 | 1074/50 | 1.61 | 1.49 |
| Carbon tetrachloride | 1.63 | 938 | 1.53 | 0.97 |
| Mercury | 13.5 | 1454 | 19.7 | 1.55 |
| Group 2[c] | | | | |
| Oil 1 | 0.825 | 1430 | 1.23 | 5.5±0.1 |
| Oil 2 | 0.870 | 1420 | 1.23 | 16.5±0.5 |
| Oil 3 | 0.870 | 1430 | 1.25 | 24 ±1 |
| Oil 4 | 0.870 | 1460 | 1.27 | 64 ±2 |

[a] All values measured at room temperature unless otherwise indicated.
[b] Kaye, G. W. C. and Laby, T. H., *Tables of Physical and Chemical Constants*, Longmans, 1966.
[c] Alexander Duckham Ltd.

TABLE 2—*Physical properties of nickel specimens used in erosion experiments.*

| Composition, % | Density,[a] kg/m³ | Sound Speed,[a] m/s | Acoustic Impedance, kg/m²-s | Hardness, kg/mm³ | Yield Stress, MN/m² (approximate) |
|---|---|---|---|---|---|
| 99.995 | $8.9 \times 10^3$ | 4974 | $44.3 \times 10^6$ | 66±4 | 220 |

[a] Kaye, G. W. C. and Laby, T. H., *Tables of Physical and Chemical Constants*, Longmans, 1966.

proximate yield stress of the material was calculated. These values, and other relevant physical properties of nickel, are collected together in Table 2.

The wheel and jet machine was a modified version of an earlier design[2]. Two specimens were bolted opposite one another to the rim of a duralumin disk which was rotated at high speed by an electric motor. The disk was enclosed in a heavy steel tank. Once every revolution the target faces of the specimens cut across a steady jet of liquid issued

from a nozzle screwed into the side of the tank. The nozzle was cast in araldite inside a brass shield which protected the jet from the air flow set up by the rotating disk. There was a very small clearance between the edge of the shield and the side of the specimens. It was found that the jet shape was deformed if this gap was too large and that this has a significant effect on the erosion of the material. The impact frequency was measured with a phototransistor system and a digital counter. The frequency could be varied between 80 and 600 Hz and the impact velocity between 50 and 280 m/s.

The liquid was pumped through the system. The temperature was measured with a thermocouple placed in the line upstream from the nozzle. Good temperature control was important when using the oils because their viscosities changed rapidly with temperature. For this purpose the oil reservoir in the circuit was water-cooled. Throughout the experiments the temperature was 20 ± 1°C (68°F).

The jet velocity was maintained at a speed sufficient to ensure that the jet axis was parallel to the axis of rotation and that it reformed between impacts. This was checked with a stroboscope.

When mercury was used as the eroding fluid the pump and reservoir were replaced by a steel tube from which the mercury was forced by a stream of compressed air. The disk which carried the specimens and all other components within the tank was made of steel.

During an experiment the erosion chamber was purged with nitrogen. This reduced any danger of explosions and carried toxic fumes out of the laboratory.

Experiments at an impact velocity of 100 m/s were carried out with all the liquids and for the range 100 to 210 m/s with carbon tetrachloride. Experimental details are given in Table 3. Two specimens were eroded in each experiment, during which mass loss measurements were made at regular intervals.

TABLE 3—*Erosion experiments.*

| Impact Velocity, m/s | Impact Frequency, Hz | Jet Diameter, mm | Specimen Width, mm |
|---|---|---|---|
| 100±2 | 166±4 | 1.5 | 3.0 |
| 140±2 | 232±4 | 1.5 | 3.0 |
| 180±4 | 188±4 | 1.5 | 3.0 |
| 210±4 | 217±4 | 1.5 | 3.0 |

*Impact Pressure Experiments*

The impact pressure distribution was measured by firing a thin, oblong-sectioned bullet, 20 mm long, 15 mm wide, and 1.5 mm deep, from a special gas gun at a stationary water drop held between two Perspex windows. For measurements of the pressure under the drop, a small piezoelectric ceramic (PZT 4), 0.5 mm long, 0.9 mm wide, and 0.8 mm deep, was mounted at the front surface of the bullet and the signal generated during the impact was fed to an oscilloscope through an arrangement of sliding contacts between the bullet and the inside surface of one of the windows. The principle of the method is shown in Fig. 1. The pressure

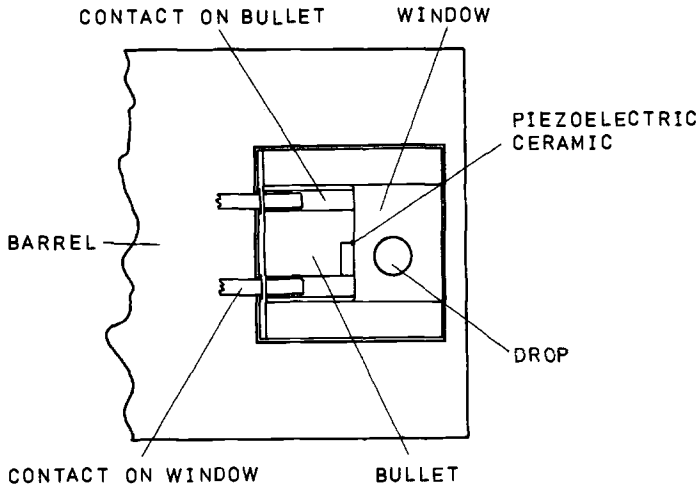


FIG. 1—*Principle of method used to measure the impact pressure distribution under a water drop.*

along the central axis of the drop was measured by a piezoelectric ceramic mounted in the middle of the inside face of an insulating block. The block replaced one of the windows.

The bullet velocity could be varied between 10 and 230 m/s. The velocity was measured by means of two photodiodes mounted 20 mm apart in the side of the barrel about 30 mm in front of the drop. The photodiodes operated a digital counter through a fast, high-grain amplifier.

The gages were calibrated using a swinging-pendulum technique similar to that used by Crook[*15*]. The gage was held tightly in a heavy clamp and a steel ball was placed in contact with the ceramic. Another steel

ball was swung against this arrangement from a known height and the output from the gage was displayed on an oscilloscope. Under these conditions it can be shown that

$$m[2g(h_1 + h_2)]^{1/2} = \frac{C}{kd} \frac{2V_{max}\tau}{3}$$

where $m$ is the mass of the ball, $h_1$ the height from which it falls, $h_2$ the height to which it rebounds, $g$ the acceleration due to gravity, $V_{max}$ the maximum output of the gage, $\tau$ the duration of the impact, $d$ the piezoelectric constant of the ceramic, $k$ the gage constant, and $C$ the combined capacitance of the ceramic, the pickup, the leads, and the oscilloscope input.

Mass $m$ and capacitance $C$ were measured and $h_2$, $V_{max}$, and $\tau$ noted for a range of $h_1$. The largest voltage observed was greater than any that appeared in the experiments. A graph of $m[2g(h_1 + h_2)]^{1/2}$ versus $V_{max}\tau$ was plotted and was found to be linear within 5 percent. The product of the piezoelectric constant and the gage constant was $260 \pm 12 \times 10^{-12}$ mV for both gages.

It can be shown that the pressure on the gage during an impact is

$$p = \frac{CV}{kdA}$$

where $V$ is the output of the gage and $A$ is the area of the ceramic. The area of each ceramic was calculated and substituted into this equation with the value of $C$ and $kd$ obtained in the foregoing to give

$$p = 2.1 \pm 0.1V \text{ MN/m}^2$$

for the bullet gage and

$$p = 8.0 \pm 0.4V \text{ MN/m}^2$$

for the sidewall gage.

The measurements of peak impact pressure along the contact surface were performed in the following manner. The gun was clamped on its side and a 5.0-mm-diameter water drop was inserted between the windows at some predetermined position against a graticule. A thin paper diaphragm was placed in a slit across the barrel in order to prevent the air blast disturbing the drop before the bullet arrived. High-speed photographs showed that pieces of the burst diaphragm did not reach the drop or interfere with the impact. The signal developed by the impact was monitored on the oscilloscope and the speed of the bullet on the counter.

Four firings were made at each position. The pulse heights were measured and the pressures calculated from the relation given in the foregoing. Measurements were made across the drop from −1.0 to 3.0 mm in 0.5-mm steps.

Using the sidewall gage, peak pressure measurements were made at 0.5-mm intervals along the central axis of the drop. Again, four separate measurements were made at each position.

Finally, the peak pressure at the center of impact was measured at 60, 80, 100, 120, and 140 m/s.

The pressures measured in these experiments were derived solely from forces on the face of the ceramic. This was established by applying a large force to the surface of the gage adjacent to the ceramic. The output was only a small fraction of that obtained when the ceramic was loaded directly.

## Results and Discussion

### *Erosion Experiments*

In earlier investigations it has been the custom to plot graphs of mass loss against time or against the number of impacts. Although this is convenient, it makes comparison with data obtained under different experimental conditions difficult. Therefore, for purposes of correlation with other studies of erosion, we follow Heymann[*3*,*16*] in using two parameters, the mean depth of erosion, $Y_e$, and the mean height of impingement, $H_i$. They are defined as follows:

$$Y_e = \frac{\text{volume of material removed}}{\text{projected area of impact}}$$

$$= \frac{\text{mass loss}}{\text{solid density} \times \text{jet diameter} \times \text{specimen width}}$$

$$H_i = \frac{\text{volume of liquid impinged}}{\text{projected area of impact}}$$

$$= \frac{\text{volume of cylinder cut by jet in single impact} \times \text{impact frequency} \times \text{time}}{\text{jet diameter} \times \text{specimen width}}$$

It will be noted that $Y_e$ is proportional to mass loss and $H_i$ to number of impacts.

### *Shape of Erosion Curve*

Graphs of $Y_e$ versus $H_i$ are shown in Fig. 2 for a selected number of liquids. With the exception of the result for mercury and those for carbon tetrachloride at the higher impact velocities (not shown), there are three

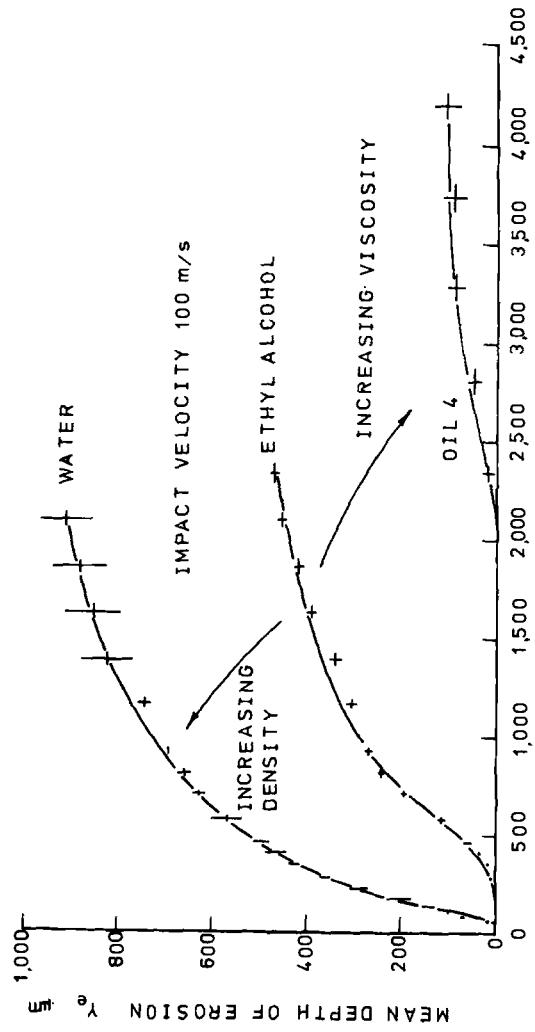


FIG. 2—*Mean depth of erosion, $Y_e$, versus mean height of impingement, $H_i$.*

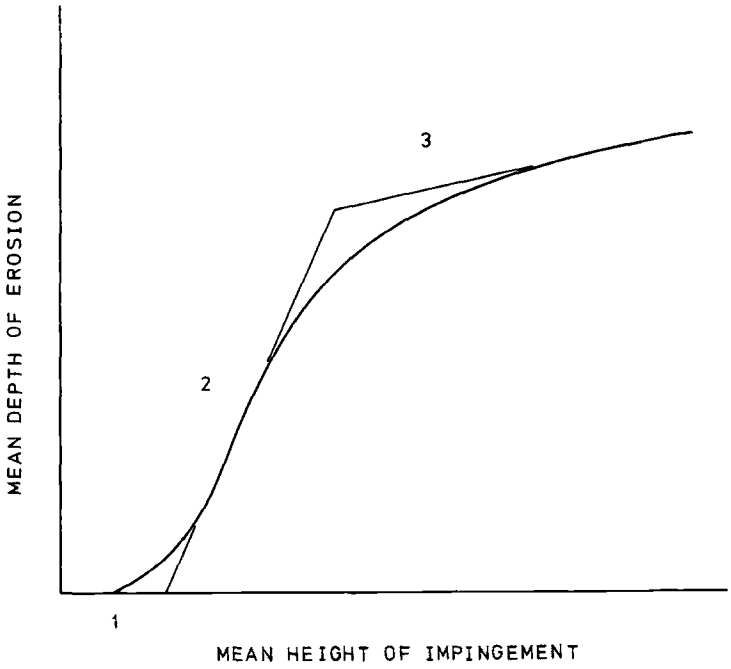


FIG. 3—*Stages in the erosion process.*

clearly defined stages. These are set out in Fig. 3. Stage 1 was not observed with carbon tetrachloride at 210 m/s and Stages 1 and 3 were not observed with mercury. As the density of the fluid increases, the difference in the slopes of the curve during Stages 2 and 3 tends to disappear. In general, the results show that the physical properties of the fluid influence the duration of Stages 1 and 2 and the magnitude and rate of change of the mean depth of erosion during Stages 2 and 3.

The appearance of the surface during erosion followed the pattern described in other investigations[*2*,*10*]. The main differences were for mercury and for carbon tetrachloride at 210 m/s, where deformation and mass loss occurred after only a few impacts. Readings were taken at the end of 2 s (about 300 impacts) for mercury and after 30 s (about 7500 impacts) for carbon tetrachloride; in both instances a significant mass loss had occurred.

### *Relation Between Liquid Properties and Erosion Damage*

In order to look for relations between liquid properties and erosion damage, suitable measures of damage must be chosen. Since the shapes of the erosion curves are similar and correspond to the curve in Fig. 3,

it was decided to use equivalent points on the curves as a basis for measurements of erosion damage. One such point corresponds to the end of Stage 1 and another to the end of Stage 2. Using these points, the following measures of erosion damage may be defined: (1) the mean height of impingement at the end of Stage 1, $H_1$; (2) the rate of change of the mean depth of erosion during Stage 2, $Y_2'$; and (3) the rate of change of the mean depth of erosion during Stage 3, $Y_3'$. These definitions are illustrated in Fig. 4.

The parameters (1) to (3) were measured for each liquid from the curves in Fig. 2 and from those for the other liquids. Graphs of each of these parameters were then plotted against density, acoustic impedance, and viscosity. These are shown in Fig. 5. The behavior of paraffin and oil No. 2 appeared anomalous and these results were not included when fitting curves to the points.

Density is related to the energy of the impinging fluid, and acoustic impedance to the magnitude of the impact pressure. Since $H_1$ is not correlated with density but strongly with acoustic impedance, and since both $Y_2'$ and $Y_3'$ are correlated with density *and* acoustic impedance, it may be concluded that the physical processes occurring during Stage 1 are

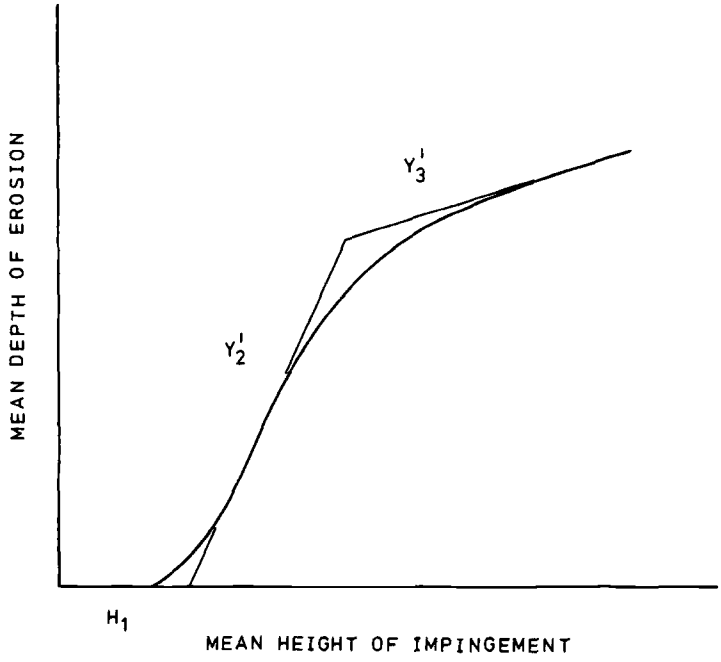


FIG. 4—*Measures of erosion damage.*

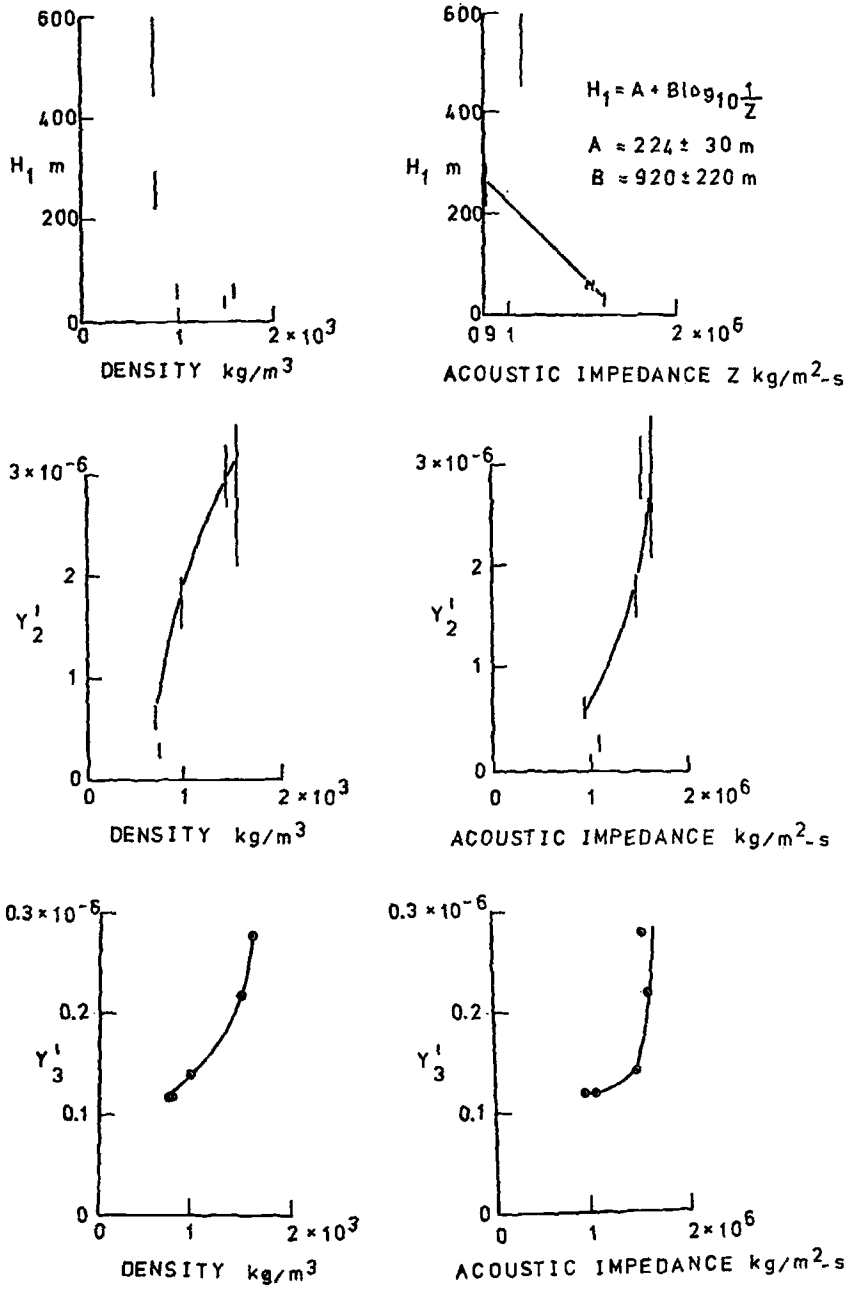


FIG. 5—*Damage parameters versus density, acoustic impedance, and viscosity.*

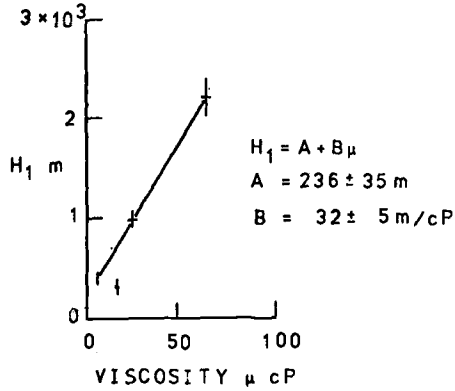


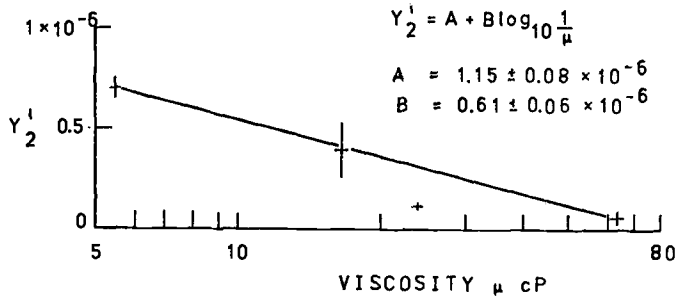


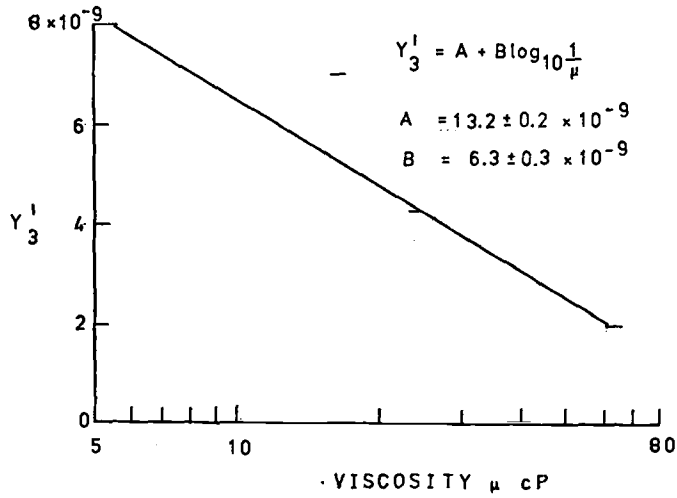


FIG. 5—(*Continued*).

governed by the impact pressure and that those occurring during Stages 2 and 3 are connected with both energy transfer from the impinging fluid and with the impact pressure. It can be seen that the viscosity of the liquid has a significant effect on each stage. It is likely that high-viscosity fluids adhere as a thin film to smooth surfaces and lie in the bottom of pits on heavily eroded surfaces. Consequently the surface would be cushioned against the impact forces.

From the correlations illustrated in Fig. 5 it may be concluded that a theory developed for predicting the erosion curve under different erosive conditions must include energy transfer, impact pressure, and viscosity terms. This is considerably more complex than anything that has been attempted so far.

### *Relation Between Damage Parameters and Impact Velocity*

It has now been well established that when water is used as the eroding fluid $Y_2'$ is related to the impact velocity by the equation

$$Y_2' = aV^n$$

where $a$ is a constant for a particular material and $n$ lies between 4 and 6[*3,16*].

A graph of $Y_2$ against $V$ for carbon tetrachloride is plotted on a logarithmic scale in Fig. 6. From the straight line obtained it can be seen that it has the same form as the foregoing and that $n = 4.8 \pm 0.2$. This is much the same as the result found for water despite the fact that water is about 50 percent less dense that carbon tetrachloride. It suggests that the physical properties of the liquid as they affect erosion are independent of flow velocity during impact.

## Impact Pressure Experiments

### *Pressure Distribution Under the Drop*

The interpretation of the erosion results presented in the foregoing would be facilitated by some knowledge of the impact forces generated by different liquids. With this object in mind, measurements are being made on the pressure distribution under an impacted drop. Some preliminary results for water are presented in this section.

The measurements with the bullet probe of the peak pressure versus position under the drop are plotted in Fig. 7. The curves for impact velocities of 100 and 140 m/s are similar and symmetrical about the center of impact. The maximum pressure during the impact occurs at the center and falls off steeply on either side. The peak pressure is about

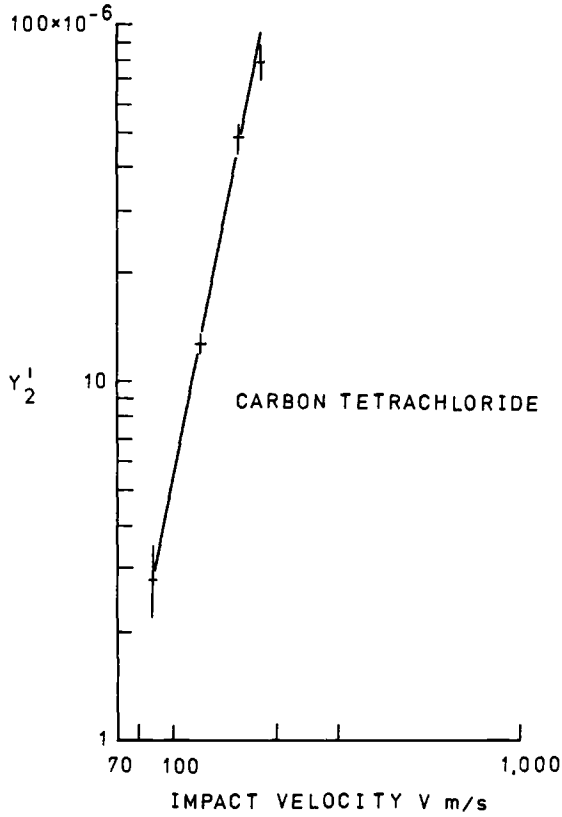


FIG. 6—*Erosion rate during Stage 2, $Y_2'$, versus impact velocity, V, for carbon tetrachloride.*

$0.7\rho_0 c_0 V'$ at both impact velocities. These values agree with those of Huang et al[*13,14*] obtained numerically using drops with slightly different shapes from those used here.

At standard conditions, $1\rho_0$ and $c_0$ are the density and sound speed respectively.

The measurements show no evidence for a region of high edge pressure even though the central region within 1.0 mm of the center was explored thoroughly. This result and those just presented differ from the predictions of Engel[*9*], who proposed that there is an annular region of high pressure about $0.5\rho_0 c_0 V$, and of Heymann[*12*], who estimated that there is a narrow edge zone where the pressures are as high as $3\rho_0 c_0 V$. If a narrow region of high pressure does exist, it must be beyond both the space and time resolution of the gage. Pressure changes over a zone narrower than the ceramic, less than say 0.1 mm, would not be completely

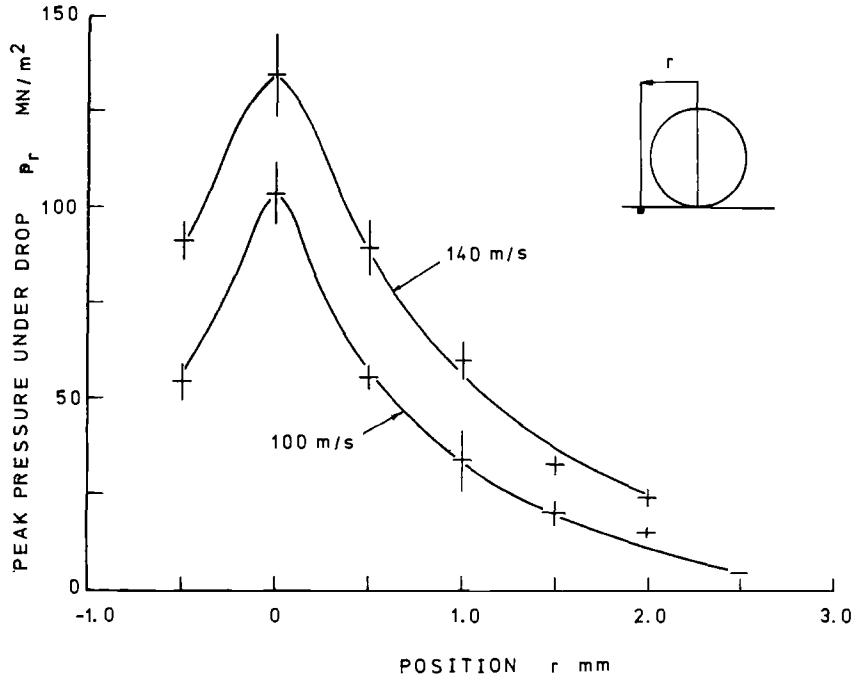


FIG. 7—*Peak impact pressure under a water drop,* $p_r$, *versus position,* r.

resolved, and it seems unlikely that the gage would respond to pressure changes which last shorter than the transit time of a stress wave through the ceramic (about 0.2 $\mu$s). The measurements which have been made do not preclude the possibility of high edge pressures in the later stages of impact. However, by this time all pressures will have fallen to levels much lower than the initial central pressure. Since the position of the liquids edge during the impact is not known with certainty, it has not been possible to confirm this point yet. Work is still in progress on measuring the pressure at several positions under the drop in relation to the instant of first contact.

### *Pressure Distribution Along Central Axis of the Drop*

The measurements with the sidewall gage of the peak pressure along the central axis of the drop are shown in Fig. 8. As might be expected, the maximum pressure occurs at the point of impact and decreases with distance along the axis. The curve is not hyperbolic, so that the wave proagated along this axis does not behave like a spherical wave which was generated at a single point. It is probable that its behavior is influenced

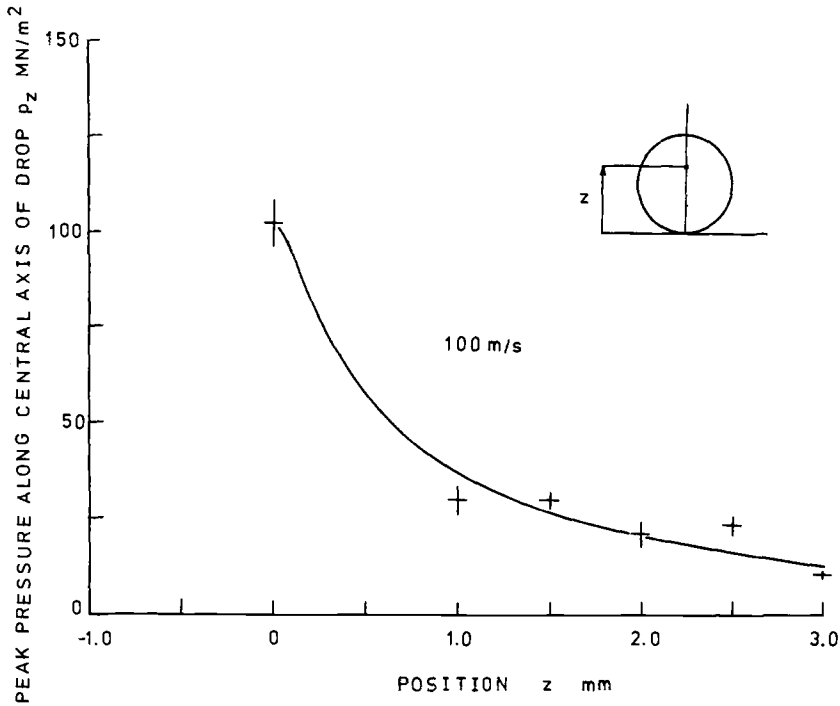


FIG. 8—*Peak pressure along the central axis of a water drop,* $p_z$, *versus position,* z,

by interactions with waves generated along the impact surface and waves produced by the reflection of these waves in the surface of the drop.

### *Effect of Velocity on Peak Pressure at the Center of Impact*

The measurements with the bullet probe of the peak pressure at the center of impact versus impact velocity are plotted in Fig. 9. The pressure varies linearly with impact velocity in the range examined and is about $0.7\rho_0 c_0 V$, a value in general agreement with the estimates of Huang et al[*13,14*], as mentioned previously.

It is interesting to relate this result to the measurements of erosion damage given earlier in the paper. For carbon tetrachloride a maximum pressure of $0.7\rho_0 c_0 V$ is approximately equal to the yield stress of nickel at an impact velocity of 210 m/s. It was found that Stage 1 in the erosion process is absent at this velocity, suggesting that each impact is sufficient to produce gross yielding of the surface, so that Stage 2 begins almost immediately. For mercury the maximum impact pressure is far in excess

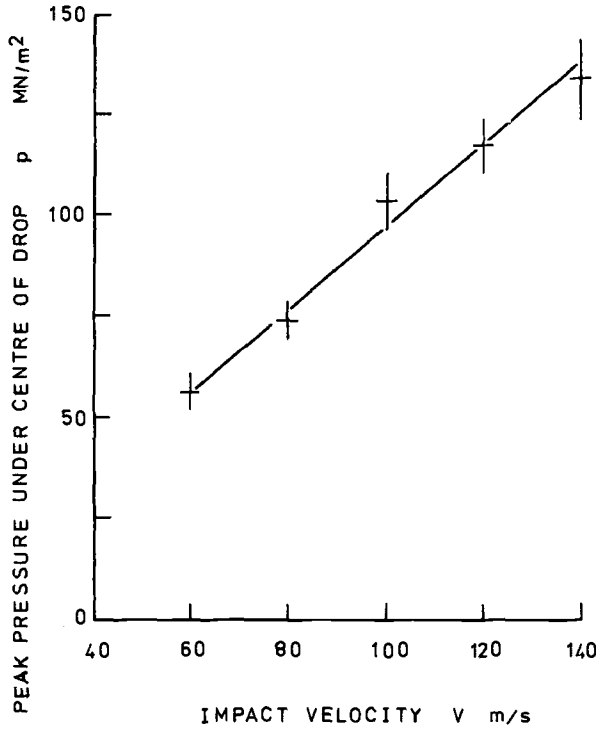


FIG. 9—*Peak pressure under the center of a water drop,* p, *versus impact velocity,* V.

of the yield stress and Stage 1 does not appear. For all the other liquids the maximum pressure calculated from $0.7\rho_0 c_0 V$ is below the yield stress and a well-defined Stage 1 is observed.

### *Shape of the Pressure Pulses*

Three typical pressure pulses are shown in Fig. 10. They have been traced from the originals, which were too faint for adequate reproduction. It can be seen that the pressure at the center of impact rises to a peak in a fraction of a microsecond and then falls to a much lower value in about 2 $\mu$s, a fact in broad agreement with the results of single-impact experiments[*10*] and high-speed photographic studies[*17*]. The oscillations on this pulse follow much the same pattern as those predicted by Huang et al[*13,14*]. The pressure away from the center rises more slowly to a peak and then oscillates erratically, suggesting that the flow at this point is very uneven. The shape of the pressure pulse at the center of

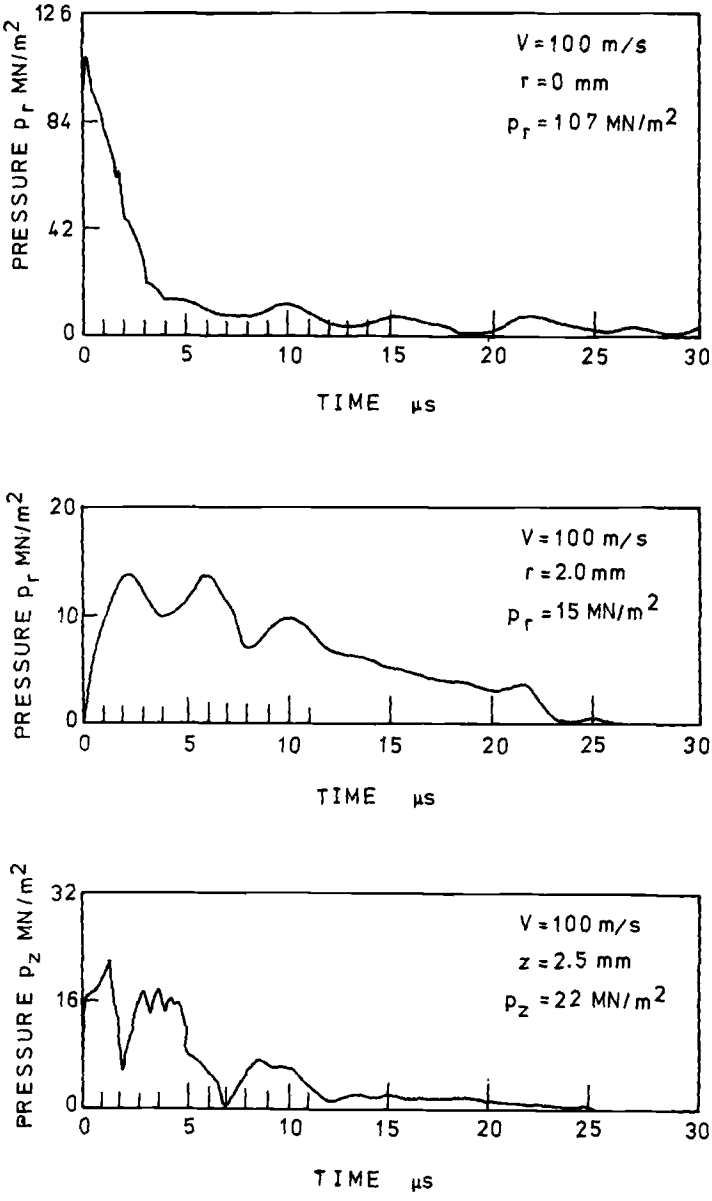


FIG. 10—*Typical pressure pulses produced during the impact.*

the drop suggests that complex interactions occur at this point between the initial pulse and waves reffected from the boundaries of the drop.

## Conclusion

It has been demonstrated that liquid properties have a marked effect on the erosion of nickel. Graphs of mean depth of erosion, $Y_e$, versus mean height of impingement, $H_i$, were found to have the same shape for most liquids. In general there were three well-defined stages. The exceptions were as follows: Stage 1 was not found with carbon tetrachloride at 210 m/s and Stages 1 and 3 were not found with mercury.

Measures of erosion damage were defined and related to the density, acoustic impedance, and viscosity of the fluid. Density was found to affect the parameters defining damage during Stages 2 and 3 but was not correlated with the Stage 1 parameter. Acoustic impedance was found to be related to the parameters defining damage during all stages of the process, as was viscosity. It was concluded that the physical processes occurring during Stage 1 are governed by the impact pressure and those during Stages 2 and 3 by both energy transfer from the impinging fluid and the forces generated during the impact.

It has been shown that the erosion rate during Stage 2, $Y_2'$, is proportional to about the fifth power of the impact velocity when carbon tetrachloride is used as the eroding fluid. This is similar to the relation found for water in other work. It was concluded that the physical properties of the liquid as they affect erosion are independent of flow velocity during impact.

Measurements of the impact pressure distribution under the surface of a 5.0-mm-diameter water drop at 100 and 140 m/s have shown that the pressure distribution is symmetrical about the center of impact and is a maximum at the center where it reaches a value of about $0.7\rho_o c_o V$. The maximum pressure was found to vary linearly with velocity in the range 60 to 140 m/s. The pressure distribution along the central axis of the drop was found to decrease rapidly with distance from the center of impact; it was not found to have a simple shape and this, considered with the shape of a typical pressure pulse, suggested that complex interactions occurred between initial and reflected waves within the drop.

*Acknowledgments*

We would like to thank the Science Research Council and the Steam Turbine Division of Westinghouse-Electric Corporation for financial support of the work described in this paper and the Science Research Council

for a grant to one of us (MCR). We would also like to thank Jim Hughes for his assistance with some of the erosion experiments and Alexander Duckham Ltd. for the mineral oils used in the work.

## References

[1] Honegger, E., *Brown Boveri Review*, Vol. 14, 1927, pp. 95–104.
[2] Thomas, G. P. and Brunton, J. H., *Proceedings of the Royal Society*, Series A, Vol. 314, 1970, pp. 549–565.
[3] Heymann, F. J., in *Characterization and Determination of Erosion Resistance, ASTM STP 474*, American Society for Testing and Materials, 1970, pp. 212–243.
[4] Hoff, G., Langbein, G., and Rieger, H., in *Erosion by Cavitation or Impingement, ASTM STP 408*, American Society for Testing and Materials, 1967, pp. 42–69.
[5] Thiruvengadam, A., in *Proceedings*, Second International Conference on Rain Erosion and Allied Phenomena, Royal Aircraft Establishment, Farnborough, England, 1968, pp. 605–653.
[6] Canavelis, R., *Journal of Basic Engineering, Transactions*, American Society of Mechanical Engineers, Series D, Vol. 90, 1968, pp. 355–367.
[7] Bowden, F. P. and Brunton, J. H., *Proceedings of the Royal Society*, Series A, Vol. 263, 1961, pp. 433–450.
[8] Bowden, F. P. and Field, J. E., *Proceedings of the Royal Society*, Series A, Vol. 282, 1964, pp. 331–352.
[9] Engel O. G., *Journal of Research*, National Bureau of Standards, Vol. 54, 1955, pp. 281–298.
[10] Hancox, N. L. and Brunton, J. H., *Philosophical Transactions of the Royal Society*, Series A, Vol. 260, 1966, pp. 121–139.
[11] Savic, P. and Boult, G. T., in *Proceedings*, Heat Transfer and Fluid Mechanics Institute, Stanford University Press, 1957, pp. 43–73.
[12] Heymann, F. J., *Journal of Applied Physics*, Vol. 40, 1969, pp. 5113–5122.
[13] Huang, Y. C., Hammitt, F. G., and Yang, W. J., "Impact of Spherical Water Drop on Flat Rigid Surface," Report No. UMICH 033710-10-T, University of Michigan, Ann Arbor, Mich., 1971.
[14] Huang, Y. C., Hammitt, F. G., and Yang, W. J., "Computer Simulation of High Speed Collision with Rain Drop (Combined Spherical-Cylindrical Shape)," Report No. UMICH 03371-12-T, University of Michigan, Ann Arbor, Mich., 1971.
[15] Crook, A. W., *Proceedings of the Royal Society*, Series A, Vol. 212, 1952, pp. 377–390.
[16] Heymann, F. J., in *Proceedings*, Second International Conference on Rain Erosion and Allied Phenomena, Royal Aircraft Establishment, Farnborough, England, 1968, pp. 98–157.
[17] Brunton, J. H. and Camus, J. J., in *Proceedings*, Third International Conference on Rain Erosion and Allied Phenomena, Royal Aircraft Establishment, Farnborough, England, 1970, pp. 327–352.

# DISCUSSION

*A. F. Conn*[1]—Once again the authors have, as we have come to expect from the laboratories at Cambridge, broken new ground and provided us with unique and valuable information pertaining to erosion by both cavitation and liquid impingement. My questions pertain to certain details of the dynamic properties of the piezoelectric crystal which was used to make the pressure measurements, and the similar properties of the plastic material which was used to imbed this crystal. Could the authors supply the values of the wave speed, density, and impedances of each of these materials? Also, would they provide some details of their techniques to calibrate this system for making these dynamic pressure measurements. The authors are to be congratulated for managing to continue to stay at the forefront of this difficult field of erosion, and for providing a clear path for many of us to follow.

*F. G. Hammitt,*[2] *J. B. Hwang,*[3] *and Y. C. Huang*[4]—The authors are to be congratulated for this most interesting study, particularly the experimental measurements of local pressure under the impacting drop as a function of time and position. We are of course especially grateful to note their statement that the results agree with our previous numerical calculations for the impact of spherical drops on rigid surfaces. This should help to end doubts which have been expressed concerning the accuracy of these numerical calculations, which in fact do not agree with previous simplified analyses of the same problem (as Messrs. Rochester and Brunton state).

We have made a specific comparison between our previous calculated results[*13*,*14*] and the present experimental results, and are happy to note that the agreement in terms of magnitude, time, and spatial distribution of maximum pressure is indeed very good. From Table 4 (data

[1] Principal research scientist and head, Material Sciences Division, HYDRONAUTICS, Incorporated, Laurel, Md. 20810.

[2] Professor, Department of Mechanical Engineering, Automotive Engineering Laboratory, University of Michigan, Ann Arbor, Mich. 48104.

[3] Doctoral candidate, Cavitation and Multiphase Flow Laboratory, University of Michigan, Ann Arbor, Mich. 48104.

[4] Nuclear Power Division, Combustion Engineering, Inc., Windsor, Conn. 06095.

TABLE 4—*Numerical values of normalized pressures at different impact velocities.*

| Reference | Impact Velocity, m/s | Liquid Mach No., $V_0/C_0$ | Maximum Normalized Pressure $\frac{p_{max}}{\rho_0 C_0 V_0}$ | $\frac{p_{max}}{\rho_0 C V_0}$ |
|---|---|---|---|---|
| Present paper | 60 | 0.040 | 0.62 | 0.575 |
| | 80 | 0.053 | 0.615 | 0.568 |
| | 100 | 0.066 | 0.686 | 0.646 |
| | 120 | 0.080 | 0.655 | 0.565 |
| | 140 | 0.093 | 0.64 | 0.542 |
| [14] | 300 | 0.200 | 0.69 | 0.495 |
| | | | 0.80[a] | 0.65[a] |
| | 750 | 0.500 | 1.07 | 0.52 |
| | | | 1.23[a] | 0.625[a] |

[a] No-slip boundary condition.

extracted from Refs *13* and *14* of paper, plus the present experimental data) we note that our calculated maximum pressure, if normalized to the corrected water-hammer pressure, is nearly independent of liquid Mach number, with a value slightly less than (but close to) the experimental values, which are also almost independent of liquid Mach number. The value ranges approximately between 0.5 and 0.6. The maximum pressure if normalized to "uncorrected" water-hammer pressure grows with Mach number, particularly as the Mach number becomes appreciable, for both calculated and experimental values.

Our previous calculations[*13*,*14*] were done for both nonslip and full-slip boundary conditions at the material-liquid interface, although the fluid was assumed to be inviscid in all cases. As shown in Table 4, the higher pressures are predicted for the nonslip boundary condition (as would intuitively be expected). Comparison with the experimental values indicates that tthe true value may be approximately a simple average between these extremes, that is, about 0.57 for low Mach numbers ($M \leqslant 0.5$) and spherical drops.

Another factor which can be compared with the present experiment and our previous calculations is the duration of the high initial pressure caused by the impact. Pressure versus time curves from both the present paper and Huang et al[*13*,*14*] have a peak after which the pressure drops to approximately the stagnation pressure. Huang's results show that this occurs at $(Ct/D) \cong 1.5$, where $C$ = sonic velocity in liquid, $t$ = time, and $D$ = droplet diameter. For a droplet of 5-mm diameter, we can then

predict that the duration of pressure before reaching stagnation pressure is

$$t \cong \frac{1.5D}{C} \cong \frac{(1.5)(5 \times 10^{-3}\ \text{m})}{1500\ \text{m/s}} \cong 5 \times 10^{-6}$$

This matches exactly the experimental result of the present paper.

We would also like to request from the authors further information on their experimental arrangements. What are the diameter, material, and response rate of the pressure transducer? What is its general form of construction?

The authors mention strain energy to fracture as a failure criterion. Is this engineering strain energy or ultimate resilience? Along with numerous other investigators (for example, refer to the discussers' paper in *Characterization and Determination of Erosion Resistance, ASTM STP 474*, 1970), we have found the former to give statistically a very poor correlation to damage rate, while the best correlation (still not good) is generally provided with ultimate resilience (perhaps combined with hardness).

*M. C. Rochester and J. H. Brunton (authors' closure)*—We should like to thank Dr. Conn and Professor Hammitt and his colleagues for their comments. Both discussers would like to know more about the properties of the piezoelectric ceramic and the material in which it was imbedded, and Professor Hammitt would like to know how the gage was constructed. Large sheets of the ceramic were obtained from Brush Clevite, Ltd. and ground on a polishing wheel to the dimensions given in the paper. The plastic bullet was made from a sheet of cloth-laminated plastic known in the U.K. as Tufnol and supplied by Tufnol, Ltd. The physical properties of the ceramic are given in Table 5.

The ceramic was electroded with conducting epoxy and glued with epoxy resin in a groove cut in the front surface of the Tufnol bullet. The response time of the gage was taken to be the time a stress wave takes to cross the ceramic, that is, about 0.2 $\mu$s.

Despite the excellent agreement between the results in the present paper

TABLE 5—*Physical properties of the piezoelectric ceramic used in the pressure gages.*[a]

| Material | Density, kg/m$^3$ | Sound Speed, m/s | Acoustic Impedance, kg/m$^2$-s |
|---|---|---|---|
| PZT 4 | $7.5 \times 10^3$ | 4600 | $34.5 \times 10^6$ |

[a] Piezoelectricity, Brush Clevite, Ltd. 1966.

and the calculations of Professor Hammitt and his colleagues, more recent experimental results[5] show an important difference in the pressure distribution over the central region of impact. Measurements of the impact pressure distribution for a 5.0-mm-diameter drop struck at a velocity of 100 m/s were obtained using a gage of much improved design. The impact pressure distribution was found to be symmetrical about the center of impact but the maximum pressure occurred 0.5 mm either side of the center. The pressure at the center was about 0.7 $\rho_0 c_0 V$ and at the edges about 1.8 $\rho_0 c_0 V$. The difference between these more recent results and the results presented in this paper is due to both an improvement in the design of the gage and a considerable reduction in the size of the piezoelectric ceramic. The ceramic used to obtain the results in this paper was 0.9 mm wide (about one fifth of the diameter of the drop) whereas the one used in the later paper was only 0.33 mm wide (about one fifteenth of the diameter of the drop). It is likely that the larger gage used in the aforementioned work missed the high edge peaks which were found to act over a very small area (for a 5.0-mm-diameter drop, it was less than 0.3 mm wide), and gave only an average value over the region measured.

[5] Rochester, M. C. and Brunton, J. H., "Surface Pressure Distribution During Drop Impingement," Report No. CUED/C—MAT/TR 15, Engineering Department, University of Cambridge, Cambridge, England, 1974; also, 4th International Conference on Rain Erosion and Allied Phenomena, Meersburg, West Germany, 1974.

*Kazimierz Steller,*[1] *Tadeusz Krzysztofowicz,*[2] *and Zdzislaw Reymann*[1]

# Effects of Cavitation on Materials in Field and Laboratory Conditions

**REFERENCE:** Steller, Kazimierz, Krzysztofowicz, Tadeusz, and Reymann, Zdzislaw, "**Effects of Cavitation on Materials in Field and Laboratory Conditions,**" *Erosion, Wear, and Interfaces with Corrosion, ASTM STP 567,* American Society for Testing and Materials, 1974, pp. 152–170.

**ABSTRACT:** The behavior of certain materials exposed to cavitation, in field as well as laboratory conditions, was observed. The investigations were aimed at uncovering differences as well as singularities occurring in cavitation damage processes and determining the efficiency of comparing "cavitational resistance" of material on the basis of testing specimens under various conditions. Observations of specimen surfaces geometric structure were made together with measurements of the specimen destruction rate, microscopic observations of upper layers of material surface, and hardness measurements.

**KEY WORDS:** cavitation erosion, cavitation resistance, tests, pitting, points (mathematics), positioning, cold-working, erosion

The existence of a variety of hypotheses to explain the phenomenon of cavitational erosion results first of all from the complexity of the phenomenon itself, which depends on physico-chemical properties of liquid and material as well as on other factors relevant to the initiation and progress of cavitation. The variety of hypotheses comes also as a result of differences in investigative methods used, that is, different ways and conditions of modeling cavitational erosion.

In spite of the lack of a unique description of cavitation damage kinetics and controversies about the influence of some parameters[*4*][3] on

[1] Doctor of engineering and mechanical engineer, respectively, Institute of Fluid-Flow Machinery, Polish Academy of Sciences, Gdańsk, Poland.

[2] Doctor of engineering and lecturer, Technical University, Gdańsk, Poland.

[3] The italic numbers in brackets refer to the list of references appended to this paper.

the process of cavitation development, the following opinions prevail[*1,3,5,8,11–13,15,17*] regarding this effect:

1. Cavitation damage occurs as the result of the collapse of cavitation bubbles—inside the material, on its surface, or near the wall—as well as of additional hydrodynamic effects (such as cavitation cloud separation and pulsing, instantaneous peaks of pressure changes in liquid, intensive turbulence in a boundary layer and collision of streams) which take place most often in unstable regions of cavitation zones.

2. Mechanical effects, namely collisions between the material surface and stream of the liquid, and dynamic loads due to shock waves are the main and direct cause of the material damage. However, the contribution of nonmechanical processes and, particularly, electromechanical ones, is not ruled out.

3. Physico-chemical and structural properties of materials as well as the properties of liquids are responsible for damage kinetics at a given form and intensity of cavitation. However, traces of cavitation are as a rule connected with strengthening of the upper layer due to plastic deformations.

4. Damage intensity depends first of all—for the given material and liquid and determined investigation method or cavitation form (distinguished as macro- or microscopic[*6*], constant or transient[*3*], flow- or pulse-type[*12*], volume or local[*8*], border, boundary, tear-off, stream, wave[*8,14*] etc.)—on the cavitation discriminant $\sigma$ and parameters which describe collisions between hydraulic pulses and solid body[*2,13*]. These are: bubble shape and dimensions, potential of a mircostream resulting from an implosion, impact velocity and frequency, run of pressure fluctuations, and pressure distribution.

The behavior of certain materials exposed to cavitation, in field as well as laboratory conditions, was observed with the foregoing statements taken for a start. The investigations were aimed at uncovering differences as well as singularities occurring in cavitation damage processes, and at determining the efficiency of comparing "cavitational resistance" of material on the basis of testing specimens under various conditions. Observations of the geometric structure of specimen surfaces were made together with measurements of the specimen destruction rate, microscopic observations of upper layers of the material surface, and hardness measurements.

## Investigations and Test Rigs

Armco annealed iron (99.3Fe), two-component brass (62Cu-38Zn), and cast steel (0.26C-5Mn-0.4Si-0.03S-0.03P-0.2Cr) were tested. Test specimens made of those materials (39 specimens total) were subject to damaging on a magnetostriction rig, a rig with rotating disk, and in the

impeller chamber of a water turbine. Initial surface conditions were equal for all the specimens; namely, polished surfaces.

Following are the main technical data of the test rigs:

| | |
|---|---|
| Magnetostriction Rig | |
| Vibration frequency | 8.5 kHz |
| Vibration amplitude | 55 $\mu$m |
| Input power (rated) | 250 W |
| Specimen diameter | 14 mm |
| Submersion depth of a specimen into a liquid | 3 mm |
| Liquid | tap water; temperature, 20°C ± 0.5 (68°F) |
| Rotating-Disk Rig | |
| Velocity of disk rotation | 2980 rpm |
| Specimen diameter | 30 mm |
| Type and dimensions of cavitation exciter | pins of 12 mm diameter and 8 mm length |
| Diameter of mounting of specimens and exciters | 270 mm |
| Driving motor power | 40 kW |
| Liquid | tap water in a closed cycle; temperature, 20°C ± 0.5 (68°F) |

Specimens subjected to tests in field conditions were of 30 mm diameter. They were kept by a holder inside the impeller chamber of a water turbine, in the region where near-wall cavitation occurs, in such a way that the front side of the holder was, together with the specimen surface, flush with the inner surface of the chamber. Operating conditions of the turbine (Kaplan type, specific speed $n_{sQ} = 148$) changed in a narrow range. The suction number $S_q = 0.82$ to 0.88 whereas the cavitation discriminant $\sigma = 0.4$ to 0.45.

Use is made of additional data collected in water power plants throughout Poland, as well as those obtained when testing other material specimens under laboratory conditions. The data refer to the macrostructure of cavitation damage.

### Geometric Structure of Surface Damage

A variety of geometric structures can be observed on material surfaces damaged by cavitation. Three typical arrangements of pits can be distinguished; namely, point arrangement (isolated pits), strip arrangement

(pits connected along a determined direction), and total one (pits connecting in one determined spot).

Arrangement type depends on the run of cavitation development and a particular stage of it[*14*], location of a specified part of the element in a cavitation zone, and type of material[*9*]. The arrangement of pits in a given region of cavitation damage is therefore not necessarily fixed.

The point arrangement (Fig. 1) is observed principally inside the region of the "stable" part of the cavitation cloud which developed either near the surface of the material element having large, even, and immovable surfaces, or in places behind an obstacle where pressure gradients are not large.

A similar pit arrangement is obtained in conditions of pulsed cavitation (such as obtained, for example, with a magnetostriction device). When cavitation is caused by ultrasounds, bubbles are of course smaller and their pulsation rate higher. The damage pattern is compact because of the absence of flow and pulse concentration.

Isolated pit distribution can be regarded as statistical; however, in many cases their appearance and development in certain places can be explained. For instance[*8*] alloys with well-defined heterogeneous structure and nonuniform physico-chemical properties are most susceptible to damaging. Heterogeneity of structural components and other material flaws lead to selective damaging, the weakest points being attacked. Moreover, in carbon steels corrosion takes place, resulting in a higher rate of pit penetration into the material.

The plasticity of materials also influences the arrangement of pits. Metals with a low yield point are being damaged more uniformly than those with a high yield point. This is caused by, among other things, the differences in energies required for plastic deformation to occur. As a result, different numbers of active impingements[*7*,*16*] capable of deforming a material surface are required for a unit area (Table 1).

The strip arrangement of pits (Fig. 2) corresponds to the flow direction of the liquid. It is observed most often for high-velocity elements and in

TABLE 1—*Number of hydraulic impingements of different values established on the basis of signs of the cavitation effect in venturi nozzle after 60 s (in accordance with* [18]).

| Flow Speed, m/s | Number of Hydraulic Impingements After 60 s | | | |
|---|---|---|---|---|
| | $p>10^7$ N/m$^2$ | $p>10^8$ N/m$^2$ | $p>2\times10^8$ N/m$^2$ | $p>3\times10^8$ N/m$^2$ |
| 22.2 | 300 | 100 | 0 | 0 |
| 30.4 | 1150 | 500 | 100 | 20 |
| 36.9 | 3200 | 1200 | 350 | 150 |

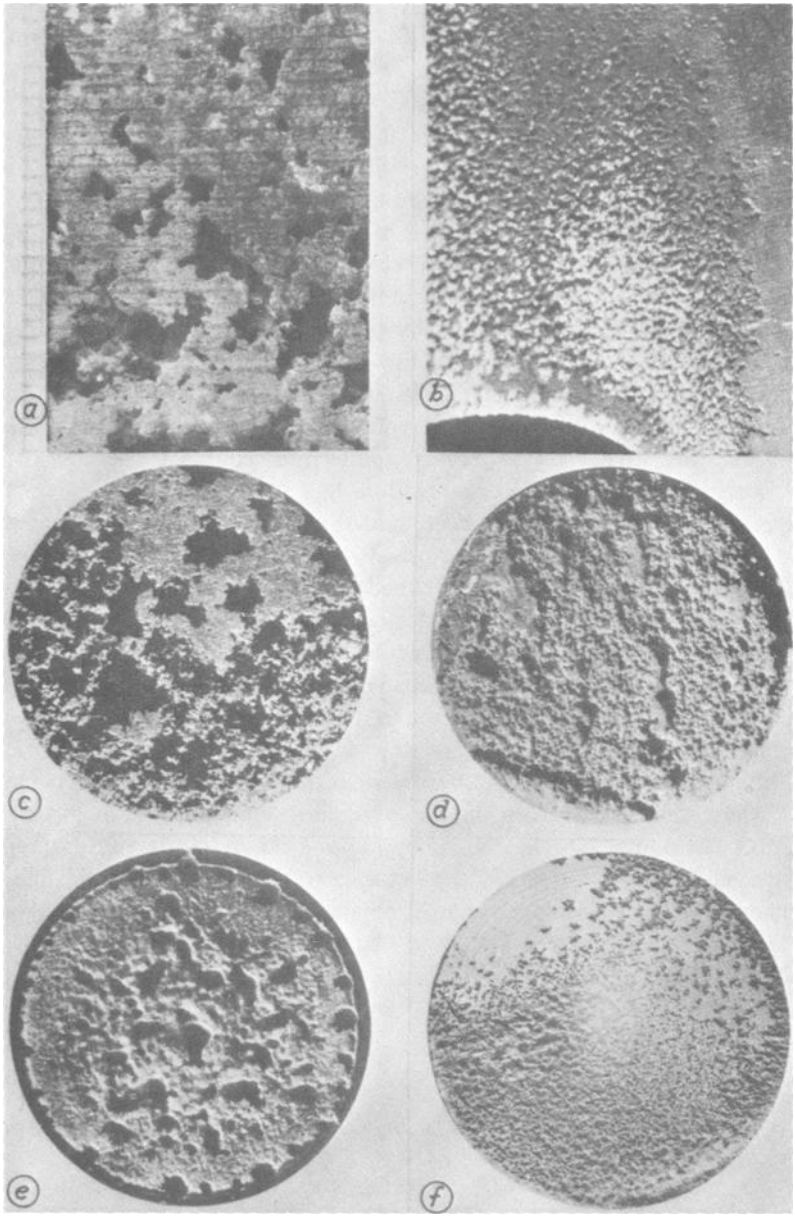


FIG. 1—*Examples of isolated cavitation pitting (point structure):* (a) *fragment of damaged runner casing of Kaplan turbine;* (b) *fragment of damaged nave of centrifugal pump runner;* (c) *surface of cast steel specimen after 1143 h exposure in natural conditions;* (d) *surface of Armco iron specimen after 850 h exposure in natural conditions;* (e) *surface of Armco iron specimen after 360 min exposure on magnetostriction rig;* (f) *surface of aluminum specimen after 18 h exposure on rotating-disk rig (rotating speed of disk twice less than nominal).*

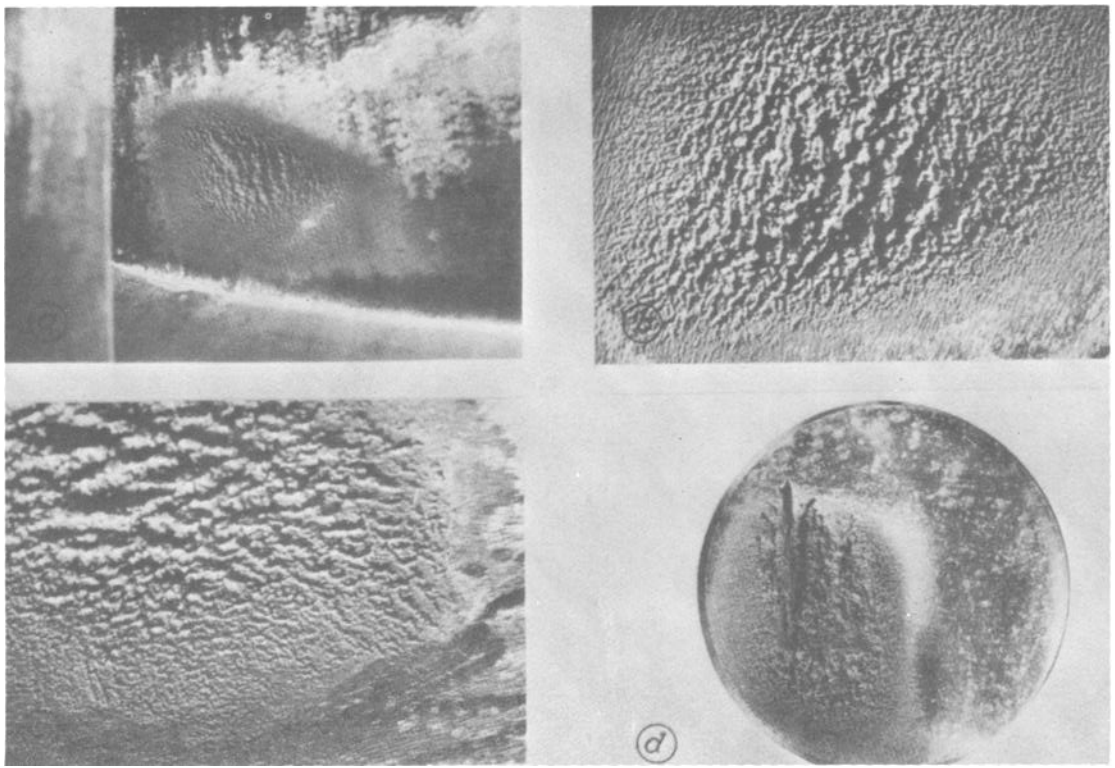


FIG. 2—*Examples of cavitation pitting in "strip" structure:* (a) *damaged blade of runner of the hydraulic reversible machine;* (b) *fragment of the damaged blade (material: chrome-nickel cast steel);* (c) *fragment of the damaged blade surface of the pump runner made from chrome cast steel;* (d) *surface of Armco iron specimen after 360 min exposure on rotating-disk rig.*

places where high-pressure gradients occur. Such are the conditions in the "unstable" part of a cavitation cloud, containing a dense bulk of bubbles, which moves downstream by vibrating motion. Extending and shortening of the cloud, and particularly transportation of its fragments (torn off the stationary part of the cloud) by flowing liquid, lead not only to collisions of material with pulses caused by bubble collapsing but also with those resulting from the flow turbulence (for example, from droplets separated from the stream which pass a highly turbulent region[*3*]).

The "total" arrangement (Fig. 3) appears as a result of high-intensity pulses directed, from a focused source, into a fixed area of the material surface. Hydraulic impingements generated by the conversion of the energy into pressure energy (for example, collisions between solid surface and liquid stream) or shock waves generated when liquid streams of high potential collide (for example, when burst cavitation cloud is being replaced by liquid) are responsible for such an effect. The total damage can be observed within the cavitation region in the end part of the cavitation cloud.

Materials with a low yield point are more liable to get damaged in such a way, total damage occurring here at relatively low intensity of the cavitation processes. Such effects were observed, for instance, for lead within the stationary part of the cavitation cloud.

FIG. 3—*Example of the lead specimen surface damaged totally.*

Various geometrical patterns of surface damage are thus characteristic for processes in the natural conditions and for those laboratory devices where a flow of liquid is involved in the cavitational erosion modeling. The surface pattern of cavitation damage obtained with the magnetostriction rig is characteristic (point arrangement) and always the same.

## Damage Rate

Diagrams of erosion rate versus time for materials tested are presented in Fig. 4. Weight losses of material are shown here as functions of reduced time $t/t_{tot}$, where $t$ denotes time and $t_{tot}$ a total time of test specimen exposition in the test rig. Comparison of damage rate for $t = t_{tot}$ leads to the conclusion that the ordering of examined materials with regard to cavitational resistance does not depend on the methods of modeling of cavitation processes. This conclusion did not prove strictly valid in all cases. Damage rates at $t = t_{tot}$ for cast carbon steel and the Armco iron are different, the differences depending on the test conditions. Slight differences (about 5 percent) were observed between the results of field tests carried out on the rotating-disk rig, and relatively large ones (about 50 percent) between them and those obtained with the magnetostriction rig.

Larger differences of the damage rate were observed for initial periods. It is easy to see that, apart from quantitative differences resulting mainly from differences in cavitation intensity, the relative incubation and accumulation times are longer in natural conditions than in laboratory conditions. At the same time, however, notice must be taken of the similiar character of damage rate changes for the rotating-disk rig and field tests. A velocity extremum can be shown in both the cases; such an extremum is not observed for the magnetostriction testing method.

The foregoing data lead to the conclusion that the modeling of cavitation damage by a rotating-disk rig is closer to the process occurring in natural conditions than is achieved with the magnetostriction method.

## Metallographic Examination

Metallographic examination consisted of microscopic observation of test specimen surfaces in the first stage of damaging as well as in examination of microsections of the upper surface layers (with and without etching) after a time duration equal to 0.3 to 1 $t_{tot}$. Some results of the observation are presented in Figs. 5–8.

Figure 5 shows fragments of Armco iron and brass specimen surfaces before testing and after 10 min on a test rig. Surfaces changes deepened in time, from small plastic deformations to larger ones, related to the growing of micro-irregularities of the surface and the forming of hollows.

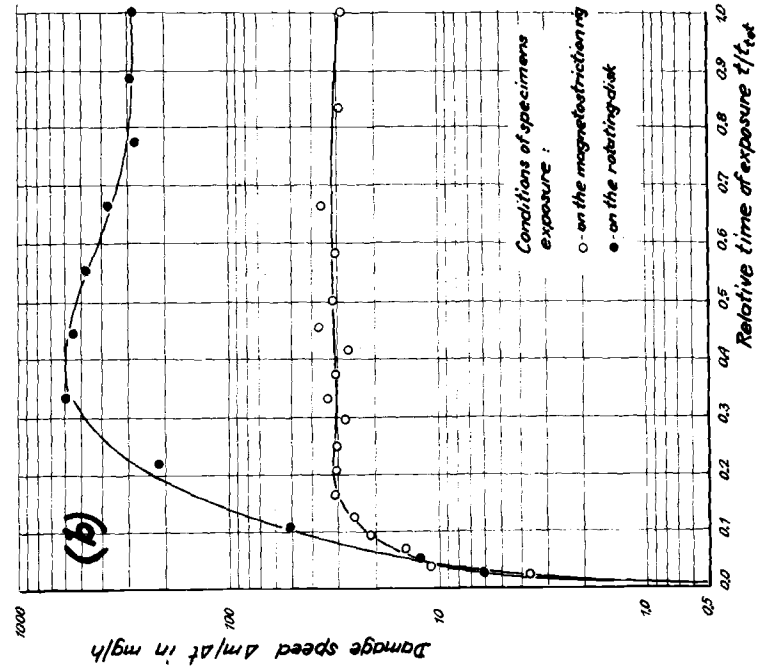
(b)
Conditions of specimens exposure :
○ - on the magnetostriction rig
● - on the rotating-disk
Damage speed Δm/Δt in mg/h
1000
100
10
1.0
0.5
0.0 0.1 0.2 0.3 0.4 0.5 0.6 0.7 0.8 0.9 1.0
Relative time of exposure t/t_tot

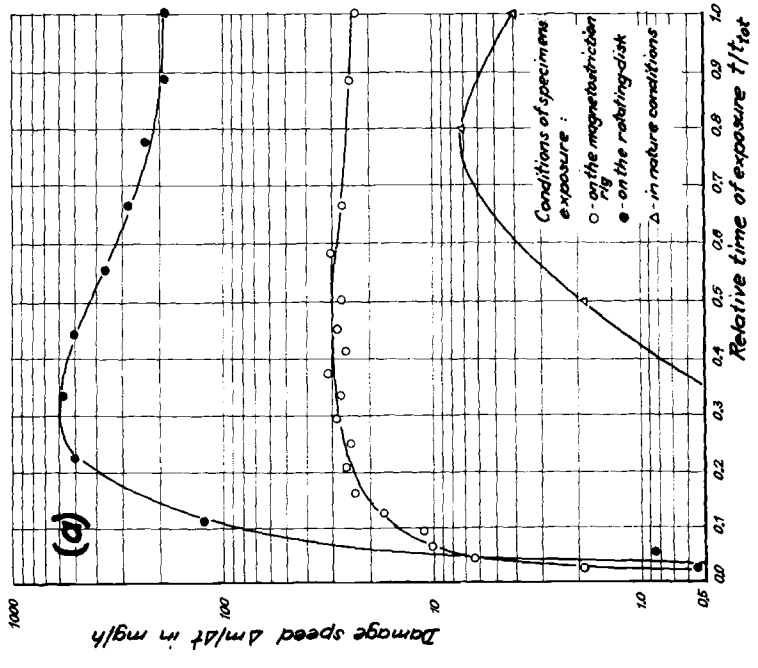
(a)
Conditions of specimens exposure :
○ - on the magnetostriction rig
● - on the rotating-disk
Δ - in nature conditions
Damage speed Δm/Δt in mg/h
1000
100
10
1.0
0.5
0.0 0.1 0.2 0.3 0.4 0.5 0.6 0.7 0.8 0.9 1.0
Relative time of exposure t/t_tot

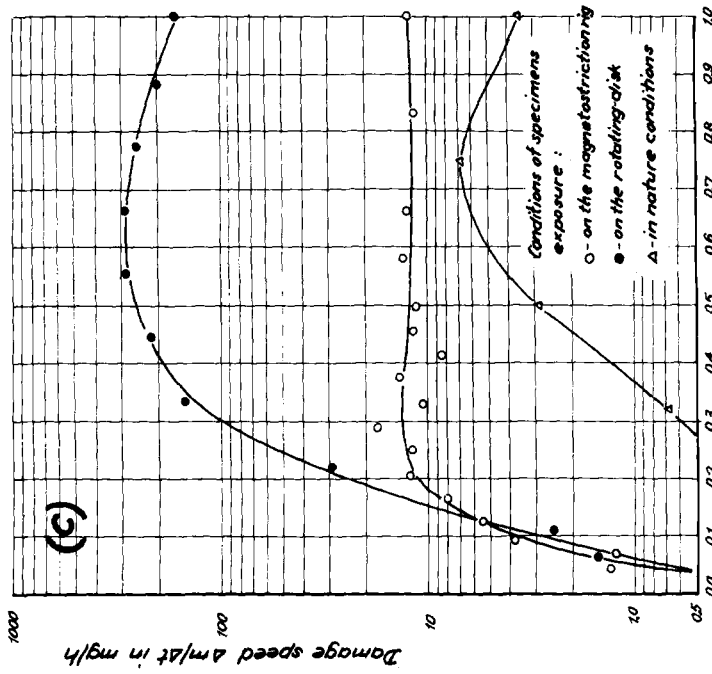


FIG. 4—*Process of damaging of the material specimens on three test rigs: (a) dependence* $\Delta m/\Delta t = f(t/t_{tot})$ *for the Armco iron; (b) for the brass; (c) for the cast steel.*

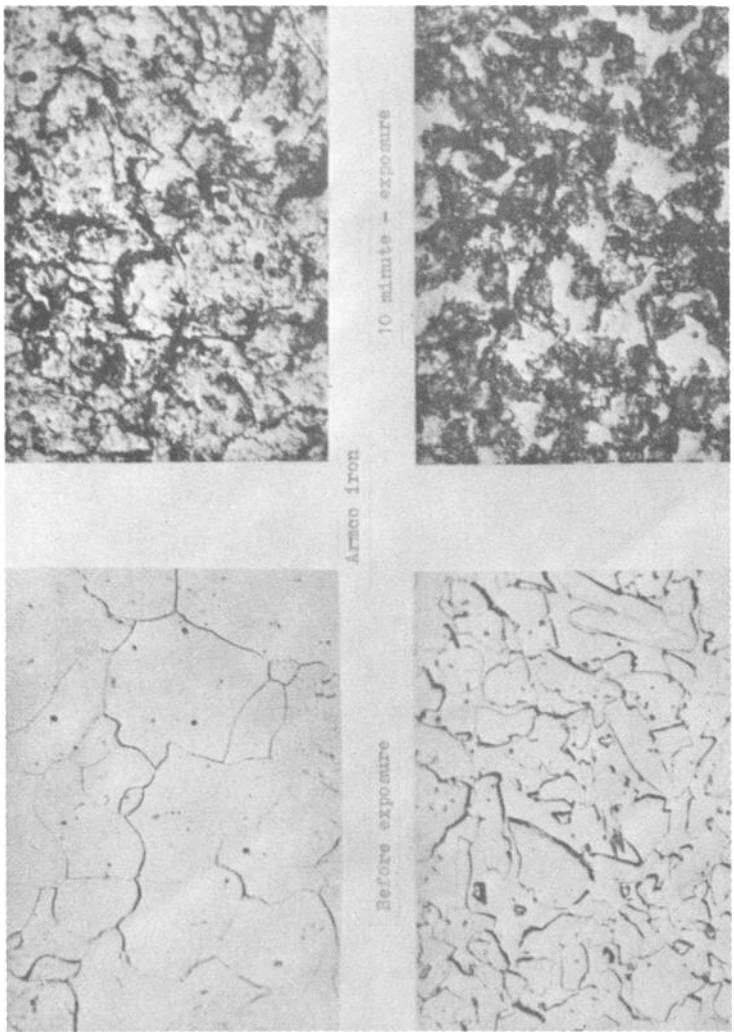


FIG. 5—*Changes on the specimen surfaces in the initial period of damaging.*

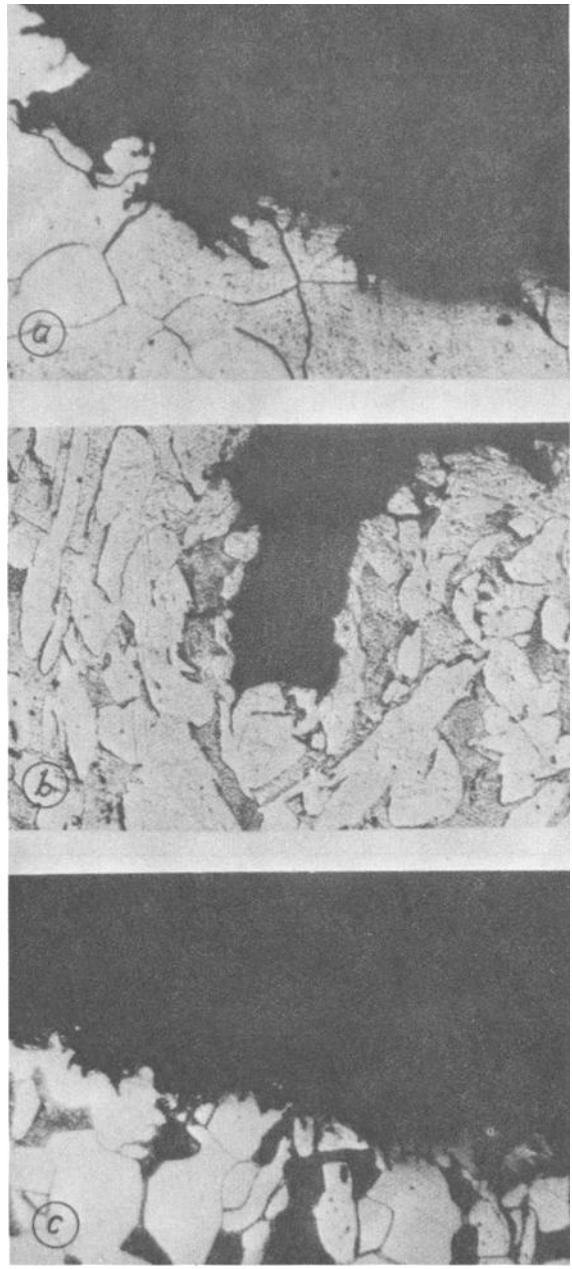


FIG. 6—*Structure of* (a) *Armco iron,* (b) *brass, and* (c) *cast steel in the area of cavitation damage developing on the magnetostriction rig.*

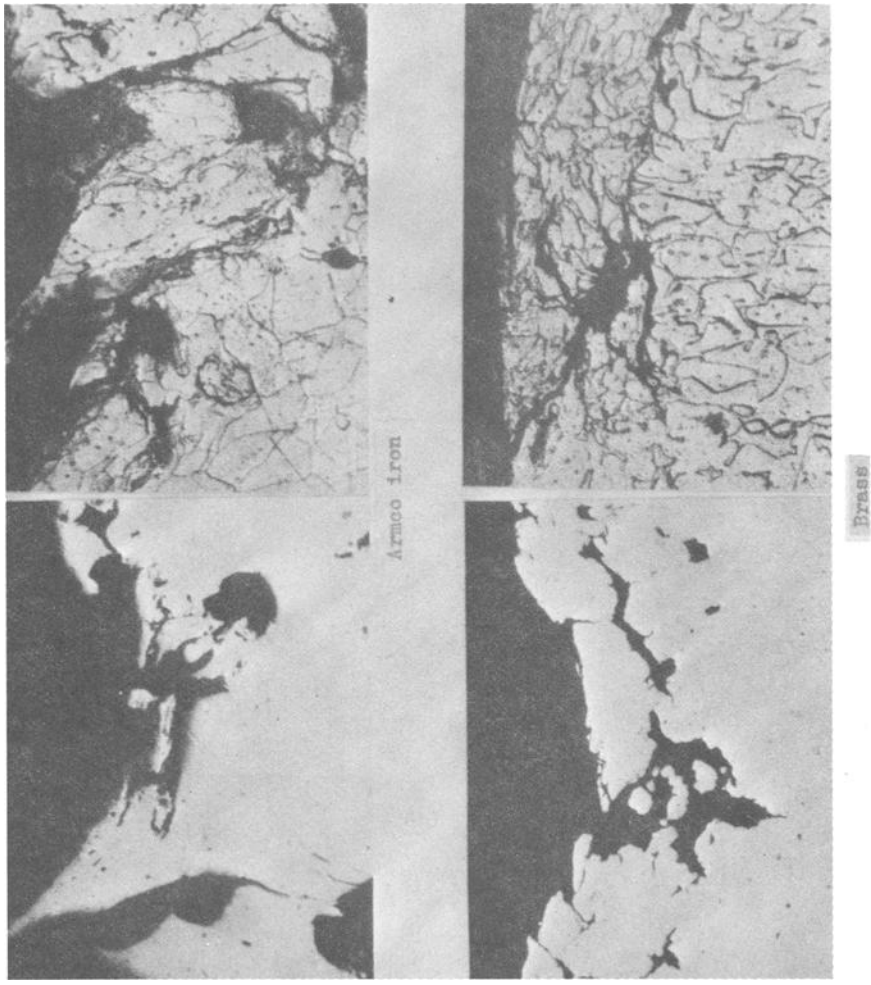
Armco iron
Brass

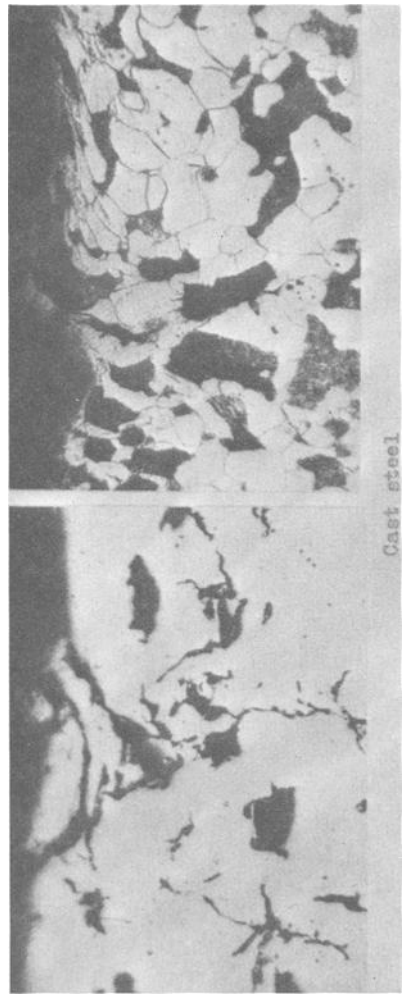


FIG. 7—*The etched and nonetched polished surfaces of material specimens damaged on the rotating-disk rig.*

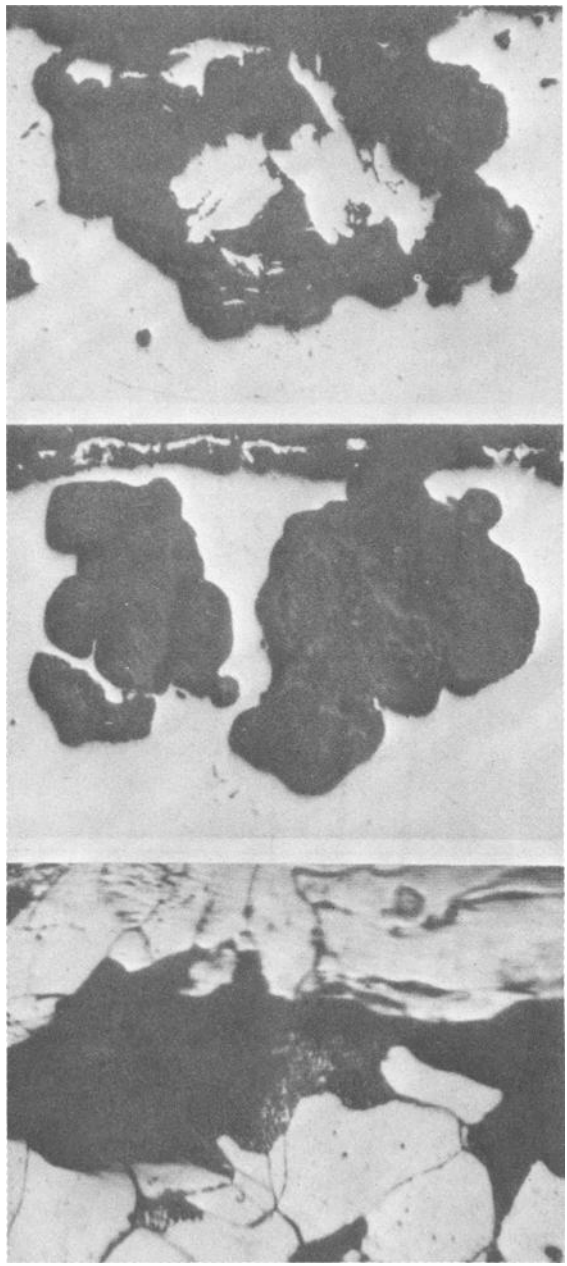

FIG. 8—*Pictures of cavitation damage revealed on the Armco iron specimens* (top), *and cast steel* (middle *and* bottom) *after testing in natural conditions.*

Extending of the hollows into the material and the connecting of neighboring damaged spots were observed. No regularity which could disprove the thesis stating statistical distribution of surface damages was observed. However, the progress of surface destruction seems to show that certain spots are particularly susceptible to damage, which suggests the influence of anisotropy on the damage process.

Cavitation pits in tested materials developed in a way that depended mainly on the conditions in which the materials were being exposed to cavitation. Examination of microsections has shown the following:

1. Tests on the magnetostriction device (Fig. 6) lead to surface destruction similar to pitting, without distinct penetration of the damage into the material. Microscopic observations did not show either plastic deformations or the translation inside the crystals. Damage progress did not show any dependence on crystal grain boundaries.

2. Damages which occur during tests with the rotating-disk rig (Fig. 7) are characterized by the extension of the pits into the material and the occurrence of microcracks. Pits are arranged in various ways. The effects of cold-working can be seen in some spots. Damage development did not depend uniquely on the material structure (leaving aside the influence of material flaws).

3. Pits irregular and developing in three dimensions are characteristic (Fig. 8) of specimens tested in natural conditions. They have the form of hollows, rather smoothly shaped, which shows the simultaneous influence of the cavitational erosion and corrosion. Microcracks are not typical for these tests. No evidence was obtained of the dependence of damage development on crystal grain boundaries. Plastic deformations, however, were observed on the surface as well as around the points of material loss.

The foregoing observations lead to the following conclusions:

1. The progress of cavitation development is responsible for the pit arrangement. Microcracks develop intensively for high-density cavitational erosion (rotating-disk rig) whereas corrosion (in natural conditions) leads to formation of smoothly shaped pits.

2. Despite the changes in the upper layers of material, plastic deformations are not always seen during microscopic examination. It is suggested that visual effects depend on the shape, value, and rate of pulses acting on material.

3. The supposition that the progress of damage development[*1*,*5*,*16*] does not depend in the first place on crystal grain boundaries was confirmed. This takes place in spite of the fact that the boundaries form a discontinuity in the regular lattice of atoms and that a certain excess of energy is stored there.

## Microhardness

The Hanemann and Khruschev methods were used for microhardness measurements.

The Hanemann method was used for measuring microhardness in spots not affected by cavitation as well as in those damaged. Comparison of results of the measurements (Table 2) shows that hardening of the material occurred in all cases, microhardness being increased by 30 to 50 percent. The test specimen subjected to cavitation on the magnetostriction device showed the least changes whereas the greatest changes were caused by cavitation in natural conditions. These results are a logical complement to the observations described earlier.

The Khruschev method was applied to microhardness measurements of specimen fragments at various depths. The results have shown that hardness changes penetrate the material in natural conditions more deeply than in laboratory conditions. The following are depths of a hardened layer measured for the Armco iron and cast carbon steel:

Magnetostriction device, 30 to 60 $\mu$m
Natural conditions, 250 to 500 $\mu$m

These differences result from the differences in loading of the material. The duration of the tests was undoubtedly a very important factor here (in natural conditions the specimens were exposed to cavitation hundreds of times longer than during the laboratory tests). It is believed that the gathering of energy carried by hydrodynamic pulses of different potentials, and the corresponding process of stress increase inside the material, affects not only the thickness of the layer which has the structure changed, but also the damage mechanism itself. Lattice deformations and cold-working are regarded as possible factors facilitating corrosion.

## Conclusions

The results of the investigations show limitations in the evaluation of the cavitational resistance of materials. For instance, relative cavitational resistance determined on the basis of tests carried out in certain conditions can differ from that obtained from tests carried out in other conditions. Cases are known[*10*]where material which proved resistant to cavitation in laboratory tests failed in natural conditions. For this reason, a way of modeling of the cavitation erosion should be applied such that disparities connected with the scale effect are as small as possible. Keeping the laboratory conditions as close as possible to natural conditions allows for

TABLE 2—*Change in microhardness of material after cavitation.*

| Material | Hardness, HB, kp/mm² | Conditions of Testing Specimens: Method of Inducing Cavitation | Conditions of Testing Specimens: Exposure Time | Microhardness, μHV( kp/mm²: Before Test | Microhardness, μHV( kp/mm²: In Cavitation Damage Area | Increase of Microhardness, % |
|---|---|---|---|---|---|---|
| Armco iron | 98 / 101 | magnetostriction | 360 min | 110 | 145 | 31.8 |
| | | rotating-disk | 300 min | 112 | 156 | 39.3 |
| | | natural condition | 723 h | 108 | 160 | 48.1 |
| Brass (μHV concern to phase α) | 126 / 128 | magnetostriction | 360 min | 116 | 166 | 43.1 |
| | | rotating-disk | 300 min | 118 | 176 | 49.2 |
| Cast steel (μHV concern to ferrit) | 156 / 159 | magnetostriction | 360 min | 164 | 214 | 30.5 |
| | | rotating-disk | 300 min | 170 | 229 | 34.7 |
| | | natural condition | 1143 h | 166 | 240 | 44.6 |

better evaluation of the material properties (as well as ordering them with regard to cavitational resistance) and for anticipating damage development in structural components.

## References


[1] Borbe, P. C., "Beitrag zur Werkstoffzerstörung durch Strömungskavitation in kalten und warmen Brauchwässern," dissertation, Technische Universität, Hannover, Germany, 1968.

[2] Canavelis, R., "Analyse du mécanisme de l'érosion de cavitation," *La Houille Blanche*, No. 2/3, Grenoble, France, 1968.

[3] Eisenberg, P., Preiser, H. S., and Thiruvengadam, A., "On the Mechanisms of Cavitation Damage and Methods of Protection," *Transactions*, Society of Naval Architects and Marine Engineers, Vol. 73, 1965.

[4] Eisenberg, P., *Characterization and Determination of Erosion Resistance, ASTM STP 474*, American Society for Testing and Materials, 1971.

[5] Erdmann-Jesnitzer, F. and Borbe, P. C., "Metalographische Untersuchungen zum Beginn der Zerstörung metallischer Werkstoffe durch Kavitation in Wasser von 50 bis 55 deg C," *Archiv für das Eisenhüttenwesen*, Heft 1, 1967.

[6] Kermeen, R. W., MacGraw, Y. T., and Parkin, B. R., "Mechanism of Cavitation Inception and the Related Scale Effects Problem," *Transactions*, American Society of Mechanical Engineers, Vol. 77, 1955.

[7] Knapp, R. T., "Further Studies of the Mechanics and Damage Potential of Fixed Type Cavities," *Cavitation in Hydrodynamics*, London, 1956.

[8] Kozyrjew, S. P., "Gidroabraziwnyj iznos mjetallow pri kawitacji," *Maszinostrojenije*, Moscow, USSR, 1964.

[9] Lichtman, J. Z., Kallas, D. H., Chatten, C. K., and Cochran, E. P., "Cavitation Erosion of Structural Materials and Coatings," *Corrosion*, 1961.

[10] Lazarkiewicz, S. and Troskolański, A. T., *Pompy Wirowe*, WNT, Warsaw, Poland, 1968.

[11] Plesset, M. S. and Chapman, R. B., "Collapse of an Initially Spherical Vapor Cavity in the Neighborhood of a Solid Boundary," *Journal of Fluid Mechanics*, Vol. 47, 1971.

[12] Piltz, H. H., *Werkstoffzerstörung durch Kavitation*, VDI-Verlag, Düsseldorf, Germany, 1966.

[13] Pjernik, A. D., "Probljemy Kawitacji," *Sudostrojenije*, Leningrad, USSR, 1966.

[14] Raabe, J., *Hydraulische Maschinen und Anlagen*, Teil 2, VDI-Verlag, Düsseldorf, Germany, 1970.

[15] Ratnjer, A. W. and Zjeljenskij, W. G., "Erozija Matjerialow," *Enjergija*, Moscow, Leningrad, USSR, 1966.

[16] Robinson, M. J. and Hammitt, F. G., "Detailed Damage Characteristics in a Cavitating Venturi," *Journal of Basic Enginering*, Vol. 89, 1967.

[17] Varga, J. and Sebestyén, G., "Beiträge zur Bestimmung der Energie der Kavitationerosion," *Problems of Fluid-Flow Machines*, PWN, Warsaw, Poland, 1968.

[18] Pylajew, N. I. and Sotnikow, A. A., "Udarnyje impulsy pri kawitacji w potokie," *Energomaszinostrojenie*, Vol. 5, 1971.

*F. Erdmann-Jesnitzer* [1] *and H. Louis* [1]

# Studies on Cavitation Damages

**REFERENCE:** Erdmann-Jesnitzer, F. and Louis, H., "**Studies on Cavitation Damages,**" *Erosion, Wear, and Interfaces with Corrosion, ASTM STP 567,* American Society for Testing and Materials, 1974, pp. 171–196.

**ABSTRACT:** Tests in a new chamber for flow cavitation led to damages which are characteristic of erosive destruction caused by imploding cavitation bubbles. To develop material of greater cavitation resistance, it is necessary to find out exactly the different stages of damage. To do this, we started to examine model materials in a special testing chamber.

In the case of soft aluminum, these damages, caused by single imploding bubbles, give an idea about the way of load that is the effect due to micro-liquid-jets which impact the specimen surface under special conditions. Typical stages of deformations, formation of cracks and fractures are described with regard to the structures of the model materials by scanning electron microscope.

To transfer the different stages of damages from one material to others of the same crystalline structure, changes at different stages caused by the different mechanical properties, for example, as in the case of copper, must be taken into consideration.

**KEY WORDS:** cavitation erosion, damage, erosion, cavitation resistance, crack propogation, ductile fractures, brittle fractures, deformation, mechanical properties, tests

Material damages resulting from imploding cavitation bubbles are an economic factor. Therefore a lot of research has been done in the field of cavitation, particularly regarding the formation of cavitation bubbles, the way of their implosion, and the resulting material damages.

These damages consist in aqueous solutions of an erosive and a corrosive part[*1*].[2] In the case of heavy destruction the erosive part, called cavita-

[1] Head of institute and head of Material Damages by Hydraulics Group, respectively, Institut (B) für Werkstoffkunde, Technische Universität Hannover, Federal German Republic.

[2] The italic numbers in brackets refer to the list of references appended to this paper.

tion erosion, in particular is most important. That is why it is the central theme of many research projects.

## Test Equipment

To simulate erosive cavitation damages we used a recently developed testing chamber for flow cavitation[2,3]. The chamber consists of a rectangular channel (30 × 40 mm²) in which two cylinder-shaped barricades, called "Wehr" and "Gegenwehr," form a narrowing in the cross section of the channel (30 × 3.5 mm²) which then leads to the release of bubbles.

Figure 1 describes the way of flow and the formation of two water-bubble streams in this cavitation chamber and gives an idea of the amount of damage on an aluminum specimen (Al-99.988) loaded for 15 min by imploding cavitation bubbles.

Special importance is attached to the barricades because only the

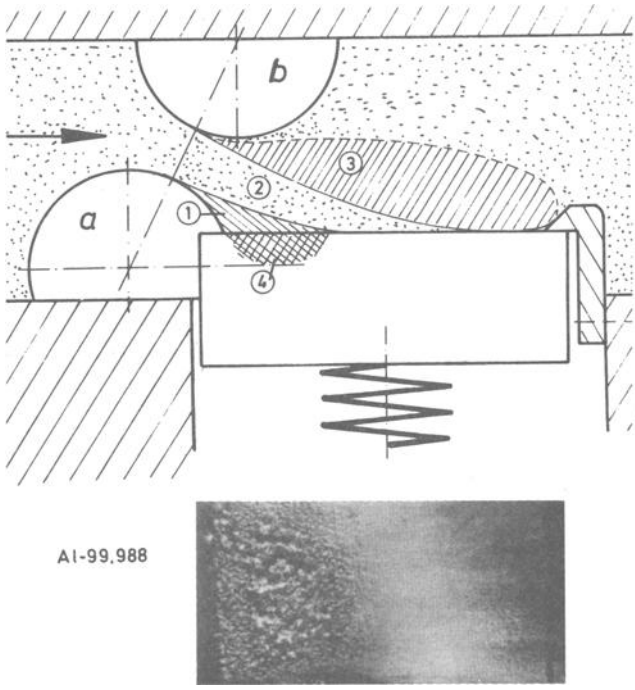


FIG. 1—*Way of flow (schematically) in the newly developed testing chamber for cavitation erosion and a damaged specimen (Al-99.988) after 15 min of cavitation load.* (1), (3) = *streams of bubbles;* (2) = *liquid, devoid of bubbles;* (4) = *main region of destruction;* (a) = *barricade I (Wehr);* (b) = *barricade II (Gegenwehr).*

cylindrical form can enable us to reproduce their micro- and macro-geometrical shapes. In addition to these special barricades, a maximum damage intensity is guaranteed by means of a significant combination of the geometrical and hydromechanical test parameters as shown in Fig. 2:

1. Inlet pressure $p_1$, that is, the maximum velocity in the throat.
2. Reverse pressure $p_2$, which influences the pressure field in the region of the imploding bubbles.
3. Deflection angle $\alpha$ of the water-bubble streams.
4. Distance $s$ between the barricades which form the throat of the channel.
5. Mean distance of the bubbles from the line of generation at the barricades to the place of implosion at the specimen surface by its positioning $h$.

A special combination of these test parameters leads to a maximum of the "damage intensity," the extent of which is not usually demonstrated

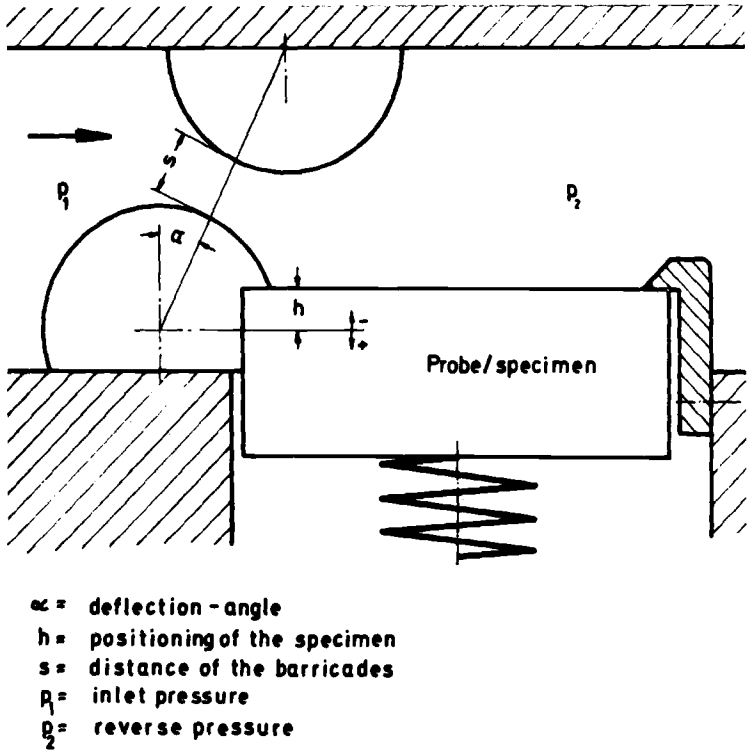


FIG. 2—*New chamber for testing flow cavitation damage (schematically), with geometrical and hydromechanical variations.*

by such test devices for flow cavitation. The damage intensity is described by means of the mass loss as a function of testing time of a special material (Al-99.988). Therefore differences in the running of the mass-loss/testing-time curves signal a change in the intensity of the bubbles in respect to the resulting damage.

The test conditions normally used are

[3] Inlet pressure, $p_1 = 10\text{-}13$ bar

[3] Reverse pressure, $p_2 = 1.25\text{-}1.75$ bar

Deflection-angle, $\alpha = 45$ deg

[3] Distance, $s = 3.5$ mm

[3] Positioning, $h = +4 - +6$ mm

The testing chamber is the main part of the cavitation apparatus, as shown in Fig. 3. A multistage centrifugal pump (1) sucks the test fluid,

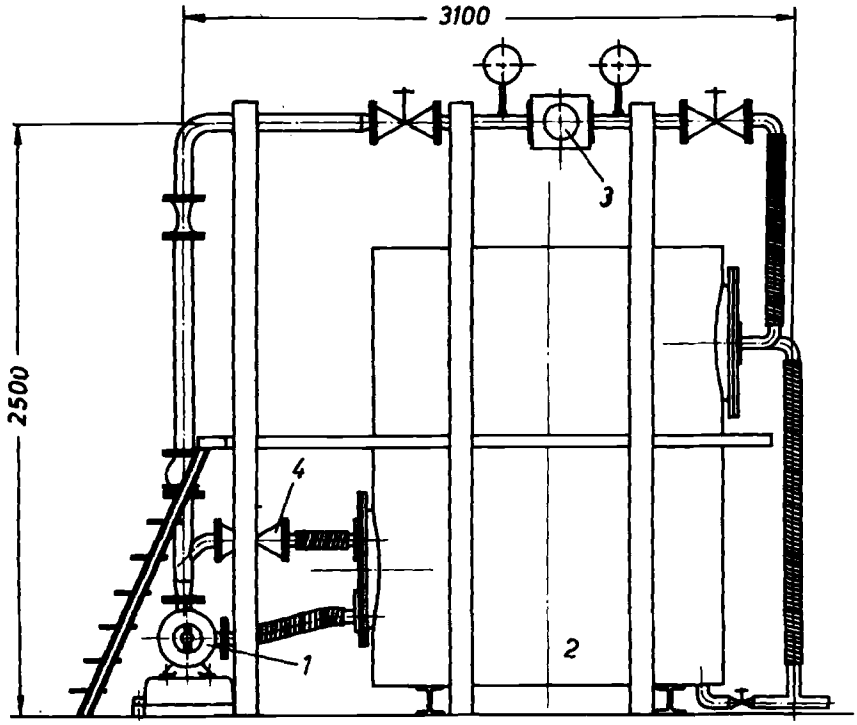


FIG. 3—*Test apparatus for erosive cavitation damage.* (1) = *multistage centrifugal pump;* (2) = *container* (~3 $m^3$); (3) = *testing chamber;* (4) = *slide valve in the bypass.*

[3] Parameters that can be varied in the testing chamber.

generally tap water, which has been partially degassed by its circulation. Taking it out of a container (2) lined with plastic material from the pump, the water reaches the test chamber (3). The insert pressure can be regulated by means of a slide valve (4) in a bypass. The reverse pressure within the area of the imploding bubbles can be regulated by the slide valve behind the test chamber. Then the water returns to the container in which are both a heating and cooling element to keep it at temperature. The liquid temperature normally used is 20°C (68°F).

## Measurements of Cavitation Erosion

One object of research during the past few years was the kinetics of destruction in materials caused by imploding cavitation bubbles. A knowledge of the kinetics of destruction is important in order to be able to produce successfully materials with a higher resistance to cavitation.

As a rule, when cavitation damages are simulated in laboratories the mass loss or the velocity of erosion as a function of testing time is determined. It is also useful to follow the changes in the profile of the surface as a result of the imploding bubbles. This can be done by means of a surface analyzer which gives us different results depending on the materials used. In the case of ductile materials the initial stage is characterized by a distinct increase in the surface roughness without any mass loss up to a certain value of testing time. In the case of brittle materials without plastic deformability there are no changes in the surface profile until parts of the material break away, which signifies the beginning of a mass loss. Figure 4 compares typical changes in the surface profiles of a ductile (Al-99.988) and a brittle (Plexiglas)[4] material.

Such test methods, namely, which change the surface profiles or mass of the specimen as a function of testing time, are able to describe macroscopically the behavior of the material when it is loaded by imploding cavitation bubbles. These test methods—in particular the determination of the mass-loss/testing-time curve—contribute only to a small extent to the knowledge of the *kinetics of destruction*. This results from the fact that the method encompasses the entire damaged area which is anisotropic in its load due to the imploding bubbles and in its mechanical properties.

If we consider a microscopically small "element" of the surface of a ductile material, imploding bubbles with sufficient damage energy will deform this element plastically. This happens first of all without any detectable erosion, behavior that corresponds to the incubation period of a mass-loss/testing-time curve[*4,5*]. After reaching a certain stage of

[4] Plexiglas 240 from Fa. Röhm u. Haas, Darmstadt, FGR.

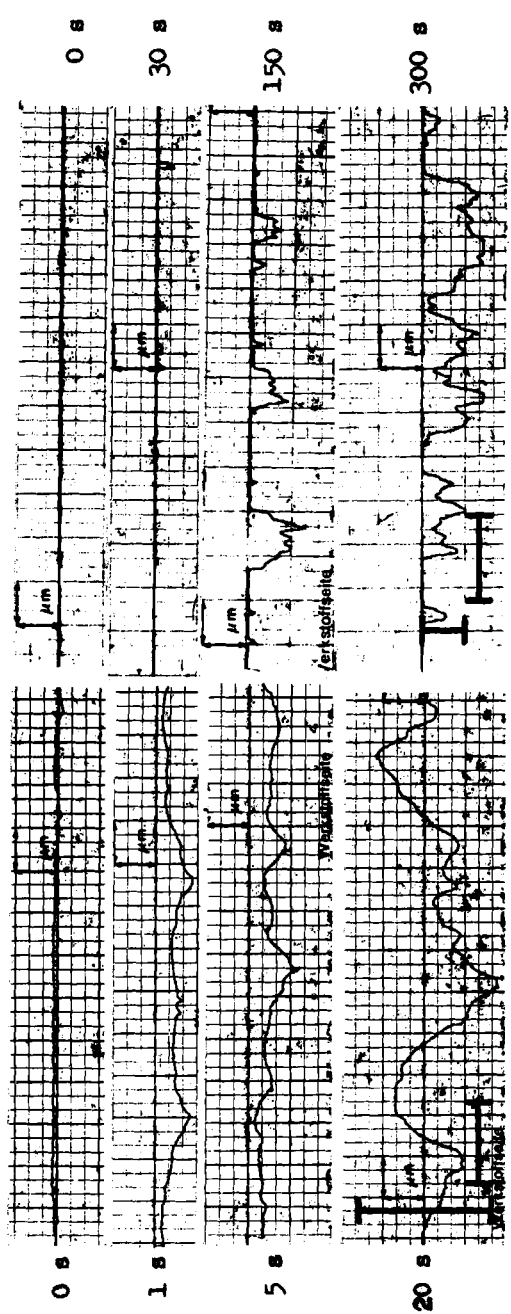


FIG. 4—*Surface profiles after different periods of cavitation.* (a) = *aluminum;* (b) = *Plexiglas. (Horizontal scale mark indicates 600 μm; vertical scale mark indicates 100 μm.)*

deformation the imploding bubbles lead to the fatigue of the material, and cracks begin to form. These cracks spread and finally cause erosion of the whole or in parts of the elements. In a theoretical mass-loss/testing-time curve, erosion begins right at this point, Fig. 5. This theoretical curve

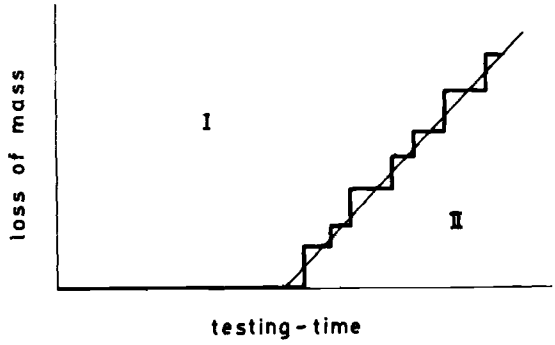


FIG. 5—*Theoretical mass-loss/testing-time curve.* (I) = *incubation period;* (II) = *period of advanced erosion.*

suddenly rises to a certain value and remains at this value. The erosion of parts of the specimen forms a new surface. In contrast to the surface of the specimen when the test started, the new surface is already deformed plastically and cracks are also present. Thus the underlying areas of the eroded surface element will show the same damaging process as mentioned before but with an *extremely shortened* incubation period; that is, the formation of cracks, their spreading and final erosion all take place in a shorter space of time. This behavior of the material is characterized by steps in the theoretical curve whereby the separate steps will not necessarily be constant.

In the usual test, the mass-loss/testing-time curves will not show this theoretical shape. Some reasons are:

1. The material is not homogeneous in its mechanical and physical properties, even if a metal of high purity or a single crystal is used.

2. The effect of the imploding bubbles differs from bubble to bubble because of the different energy of the bubbles, as a result of, for example, the spectrum of nuclei and the different conditions of implosion, which are a result of, again as an example, the different distances from the surface to be damaged.

3. The deformation of the surface by the imploding bubbles is not

homogeneous but leads to craters. These craters change the intensity of loading of the specimen surface.

For these reasons, we do not obtain more knowledge about the kinetics of destruction from the macroscopical observation of the material loaded by imploding bubbles. Besides this, a distinct transition from the incubation period without mass loss (I) to the period (II) with loss of mass (see Fig. 5) and a discontinuous run of the curve only be detected by analytical balance with very high accuracy of measurement. Normally, the analytical balance will only detect a loss of mass greater than 1 mg or 0.1 mg.

In the case of aluminum a mass of 0.1 mg means a volume of 0.04 $mm^3$. We only get a shape of the curves like the theoretical one if the eroded volume is greater than 0.04 $mm^3$ (in the case of aluminum) and we use very small time intervals. In practice, you may get this stepwise shape of the curve only in the state of great destruction. Nevertheless, if we add together many of these theoretical curves in which the length of incubation period and the amount of the average rate of erosion may differ, we will arrive at a curve which is similar to the macroscopic one. But there is no connection between the shape of this macroscopic curve and the respective changes in the surface. This may only be possible if we observe minute surface elements and their changes as a function of testing time by means of a microscope or scanning electron microscope (SEM).

That is why this way of testing was chosen in order to demonstrate the kinetics of destruction of metallic materials by imploding cavitation bubbles.

## Materials and Test Procedure

To demonstrate the behavior of metallic materials, we took model materials such as

1. aluminum, as an example of a face-centered cubic material with its ductile behavior;
2. zinc, as an example of a close-packed hexagonal material with moderate plasticity and with extremely anisotropic behavior; and
3. iron, as a body-centered cubic material, the basic material of many iron-alloys.

Table 1 gives a summary of material compositions and some of their mechanical properties.

In order to demonstrate the kinetics of destruction of materials loaded by imploding bubbles, the first period of change in the surface corresponding to the incubation period of the mass-loss/testing-time curve is of great importance. In this period the specimen surface will be prepared for a subsequent high rate of erosion.

TABLE 1—*Chemical compositions and mechanical properties of test materials.*

| | Material Composition, Impurities, weight % | Yield Strength, N/mm² | Ultimate Tensile Strength, N/mm² | Elongation % | Hardness |
|---|---|---|---|---|---|
| Al-99.988 | 0.003 Si; 0.002 Zn<br>0.004 Fe; 0.002 Cu<br>0.001 Mg | 9–10 | 55–60 | 55–45 | 14–16 HV 1[a] |
| Zn-99.99 | 0.003 Cd; 0.002 Fe<br>0.003 Pb; 0.001 Sn | ... | 25–40 | O.5–0.3 | 28–33 HB 30–30[b] |
| Armco iron | 0.02 C; 0.002 Si<br>0.04 Mn; 0.02 P<br>0.015 S | 200–250 | 340–380 | 28–22 | 92–96 HV 10[a] |

[a] DIN 50 133.
[b] DIN 50 351.

The changes in the material from its *undamaged state* to a state of *starting erosion* can only be observed during the incubation period.

If we continue further development of the damages we will only find a spreading of the cracks and different kinds and shapes of fractures which recur time and time again. To demonstrate the microscopical changes of the specimen surface, we used a SEM, model JSM-U3 of the Japan Electron Optics Laboratory.

The specimens were loaded with imploding cavitation bubbles for a certain time under test conditions normally used; then the surface changes were observed and afterwards loaded again, etc.

## Results

### *Aluminum*

In general, the energy of one imploding bubble in the case of our apparatus and the chosen test conditions does not lead to an erosion. However, only very few of the bubbles have sufficient energy to cause some visible changes in the surface. In the case of annealed aluminum they have the form of depressions which are partially surrounded by plastic deformation waves[*6*]. Depressions without plastic deformation waves represent as a rule the majority of these initial damages. Besides these visible changes we can note a strengthening of surface areas which do not show traces of plastic deformation. The strengthening can be detected on almost plain surface spots by microhardness measurements as a function of testing time[*1*,*7*].

All these kinds of characteristic surface changes, namely, depressions sometimes surrounded by plastic deformation waves, and strengthening without any visible traces of plastic deformation, can be explained by means of micro-liquid-jets resulting from collapsing bubbles. The different shapes of the damages are caused by two factors: (1) the bubbles, and the jets resulting from these bubbles, possess different amounts of energy; and (2) a thin liquid film of different thicknesses between the surface and the jet influences the damage.

In the case of very thin liquid films, depressions are surrounded by plastic deformation waves. An increase in the thickness of the film would prevent firstly any deformation waves and lastly any depressions in the surface.

Figure 6 shows the initial damages by imploding bubbles that will be found in annealed aluminum. The ratio thickness of a liquid-film/jet diameter describes the condition of the surface when the bubble implodes.

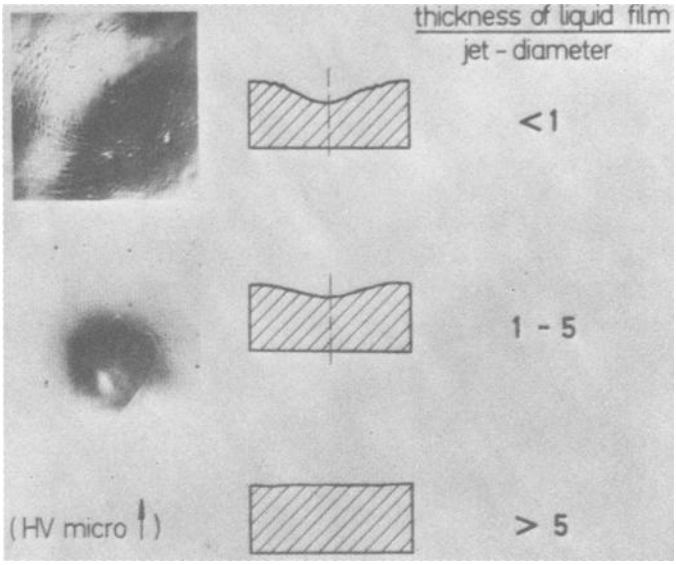


FIG. 6—*Surface damages caused by individual bubble implosions and their conditions with regard to different surface-liquid films, obtained from comparative tests with macroscopic liquid-jet attacks* [3].

The given factors are only approximate values because of the chosen test conditions and the extent of the initial damages, which differs from bubble to bubble.

The results have been obtained by making comparative experiments on damages caused by macro-liquid-jets[3]. The characteristic changes in the surface, known as initial damages, can be observed on the plain surface, but only as long as an irregular collapse of bubbles takes place at undeformed areas of the surface. In the case of the chosen material and test conditions, this period was less than 10 s. If the specimen is experimented on for a longer period, more and more cavitation bubbles implode in already deformed and therefore work-hardened surface areas. This strengthening by work hardening, however, does not impede any further deformation. On the contrary, greatly deformed surface areas, for example, large depressions, form specially favored places for imploding cavitation bubbles. This leads to a favored growth in some depressions, evidently caused by the increased effect of cavitation bubbles imploding at this point. Figure 7 gives an idea of the changes in the specimen surface loaded by imploding cavitation bubbles. The times of loading of this aluminum specimen are 30, 45, 60, and 70 s. These increasing depressions do not appear

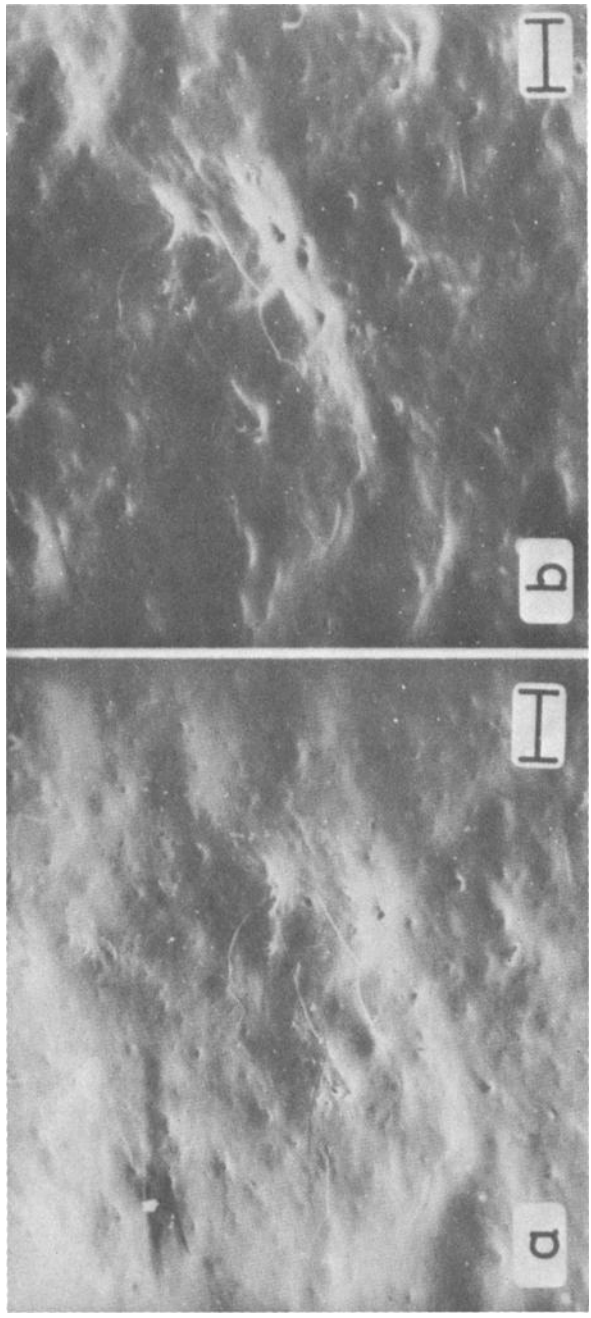
a
b

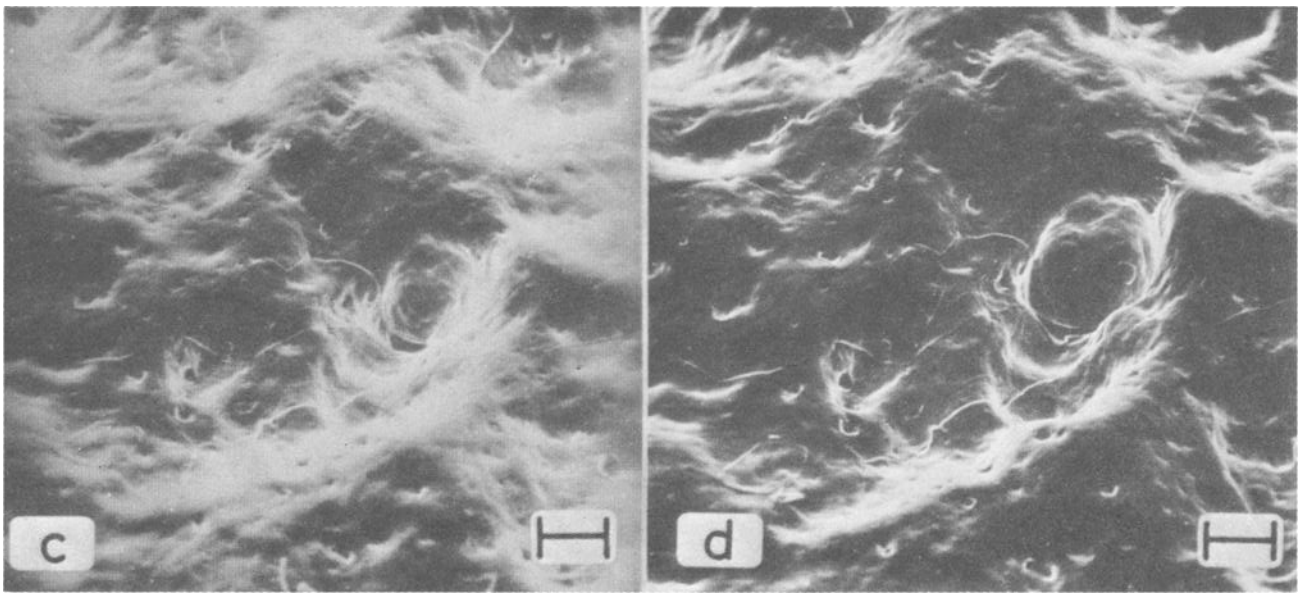


FIG. 7—*Surface changes in an aluminum specimen (taken by SEM) loaded for a period of 30, 45, 60 and 70 s by imploding bubbles. Period of increasing surface deformation. (Scale mark indicates 200 μm.)*

to depend on, for example, the orientation of the crystals or on a special behavior of the grain boundaries.

A further loading of imploding bubbles leads to an even higher rate of deformation of some depressions, forming craters. This in its turn leads to a further subsection of the incubation period where, among other things, distinct phenomena of flow appear at particular craters. These craters give the impression that the crystalline aluminum behaves like a viscous liquid, Fig. 8, after 70 s of cavitation load.

At the initial stage of loading the resulting damages in the surface are characterized by the implosion of single bubbles, which form the jets. In this following period, characterized by plastic deformations of the whole surface and a viscous-like flow of some of the craters, the loading of the specimen is the combined effect of all the imploding bubbles. They cause a quasi-static loading which is superimposed by an alternating stress of high frequency. That results in a favorable flow of the crystalline material, which has been a well-known fact for many years; for instance, in the case of lead and lead-alloys[*8,9*]. The effect of the individual bubble-implosion cannot be seen at this stage of the surface changes. At the beginning the deformation corresponds to the cohesion strengthening up to a maximum. A continued loading would lead to even greater deformations, resulting in bizarre shapes. These deformations lead to a fatigue in the material after which cracks begin to form. The appearance of the whole specimen surface is characterized by areas which are greatly deformed and areas which are less deformed, found next to each other, Fig. 9.

The spreading cracks, Fig. 10, lead to ductile fractures, which initiate a mass loss. The cracks may result from a shearing fatigue, or in the case of many imploding bubbles to an alternating shearing fatigue. It has not been proved whether the well-known accumulation of dislocations leads to the formation of the cracks, or, which could be possible, whether vacancies resulting from the alternating load of jets at high velocity contribute to the crack formation.

The appearance of dislocations loops resulting from condensed vacancies caused by deformation at high velocities, has been demonstrated by several authors[*10,11*]. The high deformation velocity of surface regions is given in the case of imploding bubbles by impacting micro-liquid-jets. Due to the erosion of the specimen by the imploding bubbles and the breakaway of material, new surfaces are formed which already contain initial cracks. These cracks then grow rapidly, resulting in a further mass loss without a noticeable incubation period.

Figure 11 gives an idea of the great differences in the kind of damage

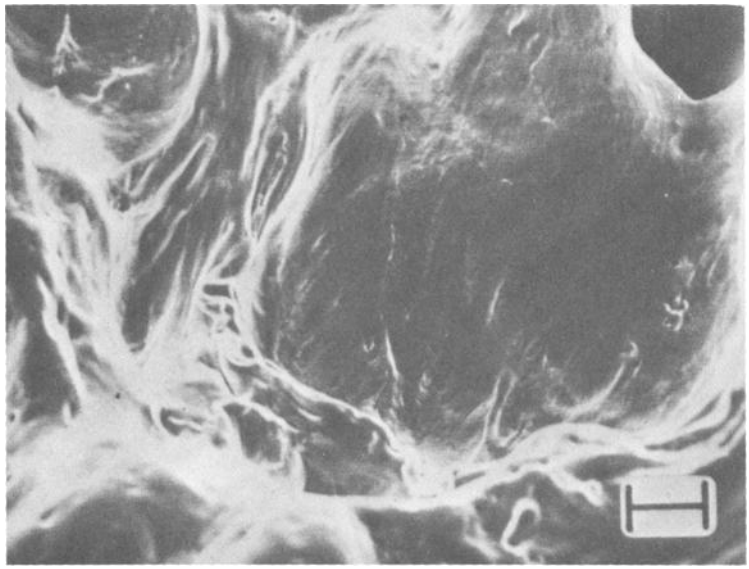

FIG. 8—*Viscous-like flow of a crater in aluminum, testing time 70 s (by SEM). (Scale mark indicates 100 μm.)*

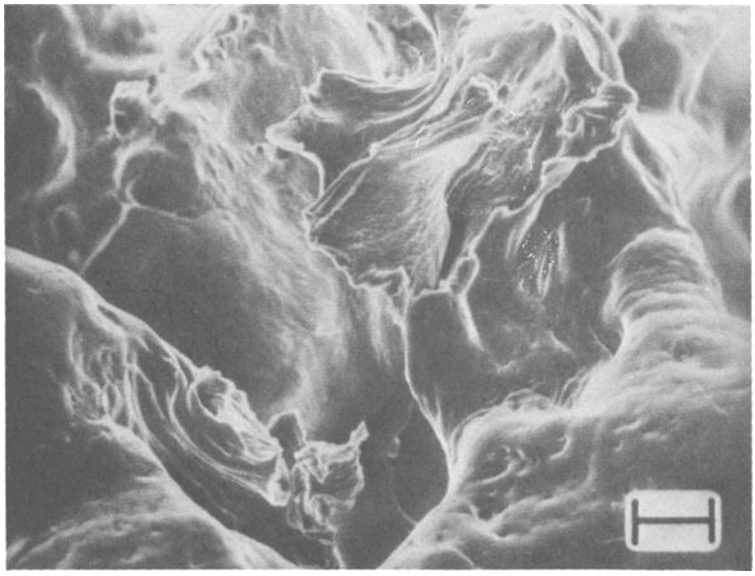

FIG. 9—*Aluminum specimen after 70 s of cavitation load, showing great differences in the rates of surface deformation (by SEM). (Scale mark indicates 100 μm.)*

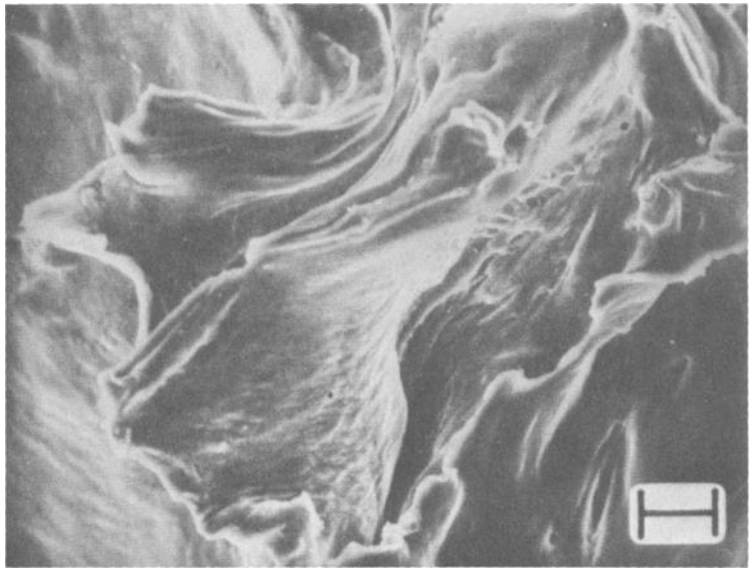

FIG. 10—*Growing cracks after 70 s of testing time (by SEM). (Scale mark indicates 50 μm.)*

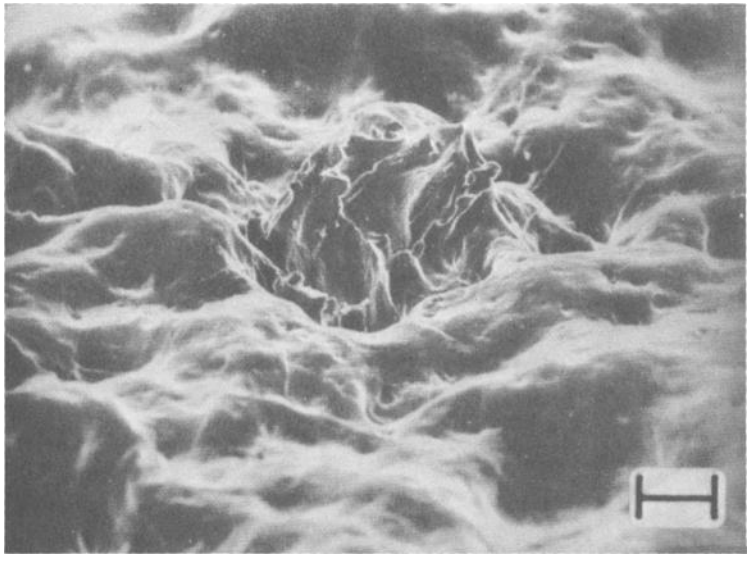

FIG. 11—*The same surface region as shown in Fig. 9, changed direction of view. Erosion starts only at one single area of the surface (by SEM). (Scale mark indicates 200 μm.)*

of an aluminum specimen, loaded 70 s by imploding cavitation bubbles. This picture demonstrates that an overall examination of the specimen, for example, as in the case of a mass-loss/testing-time curve, can tell us nothing about the actual behavior and the different stages of damage of individual surface areas. Therefore, only an examination of the changes in individual surface area, for example, by SEM, can provide us with particular information about the kinetics of destruction.

*Zinc*

The behavior of zinc (see Table 1) during implosion of cavitation bubbles is determined by its excessively anisotropic properties. As in the case of aluminum, the energy of *individual* bubbles does not lead to any erosion, due to the chosen test conditions.

In general, the material will be plastically deformed. This deformation can be caused by an individual imploding bubble or by many bubbles which implode both locally and one after the other. One individual energy-bearing bubble implosion may lead to an impression which, in contrast to aluminum, is not surrounded by plastic deformation waves. Within and closely around the impression, minute deformation twins can be observed. The second noticeable surface change is the appearance of macroscopic deformation twins which are caused not by single-bubble implosion but by a lot of imploding bubbles. The number and size of these macroscopic twins increase with testing time. The formation of these twins is not homogeneous in each individual grain because the material is so anisotropic that the grains differ in their lattice orientation.

Figure 12 shows initial damages in the kind of depressions and an increasing size and number of deformation twins after 30 s of cavitation load (*b*), which can be compared with the undamaged surface (*a*). The pictures were taken by a microscope with polarized light. With increasing time of loading, the size and the number of the deformation twins also increase. That means the amount of deformation grows. Some depressions even increase, but to a much smaller extent than they do in the case of aluminum.

The anisotropic behavior of the disorientated grains has visible effects in the regions of the grain boundaries, which sometimes form steps. These steps, however, lead to a favorable implosion of the bubbles. Therefore, as has often been proved, cracks start in the region of these grain boundaries. In that case they are not intercrystalline but transcrystalline in direct proximity to the grain boundaries. Sometimes, cleavages are detectable in grains that do not show a great amount of deformation. This is caused by a special lattice orientation of the grain which does not allow

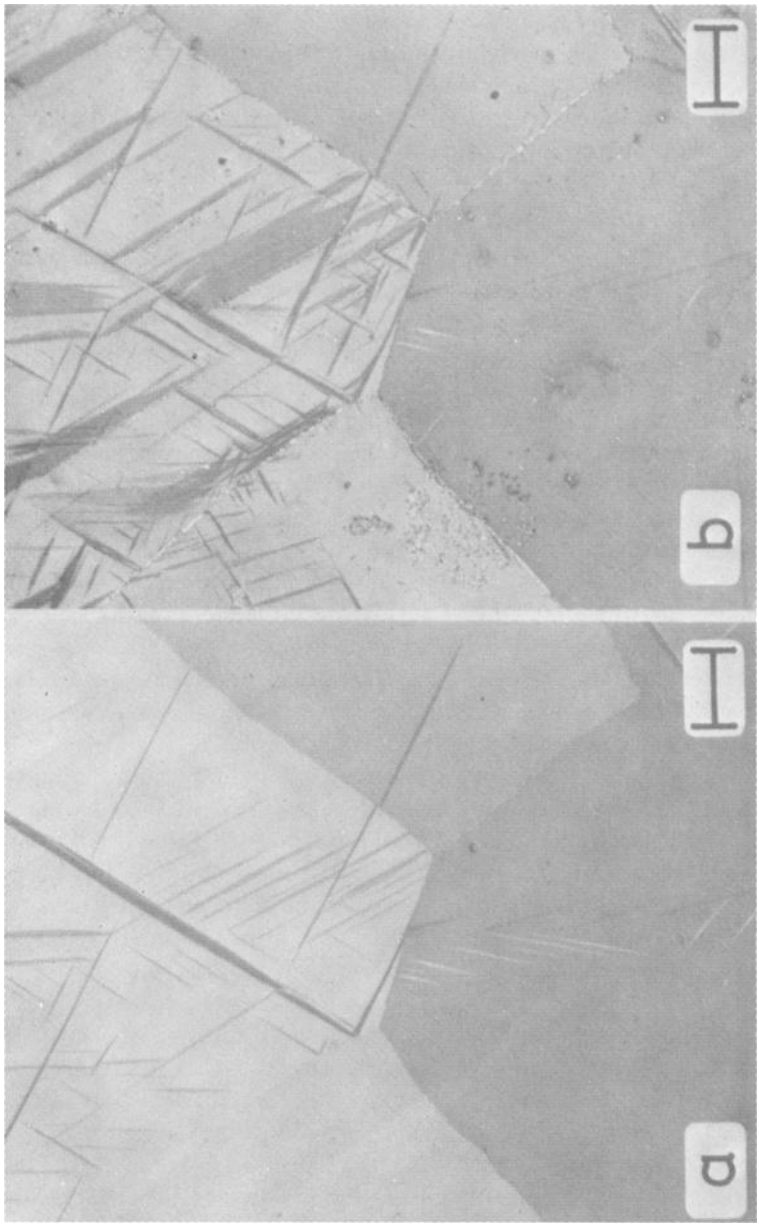


FIG. 12—*Initial damages and increasing size and number of deformation twins in a cavitated zinc surface under polarized light.* (a) = *undamaged surface;* (b) = *surface after 30 s of cavitation load. (Scale mark indicates 50 μm.)*

any plastic deformation due to the load. The implosions of the cavitation bubbles result in an enrichment of energy in parts of the crystalline material. This can suddenly lead to the formation of new surfaces by the formation of cracks. The spreading of the cracks then cause a mass loss. The destruction of this material is brought about by cleavages in special crystallographic planes. This can be proved by Fig. 13, which shows cracks and cleavage faces in grains of a large diameter. The same effect can also be seen in zinc with a small grain size. The cleavages are formed in the basic planes of this material. Sometimes cracks are found running in different but special directions, as shown in Fig. 14. In this case the regions of the cracks are former deformation twins, which have a particular connection with the surrounding parts in their crystallographic directions.

As in the case of aluminum, this state of knowledge could only be

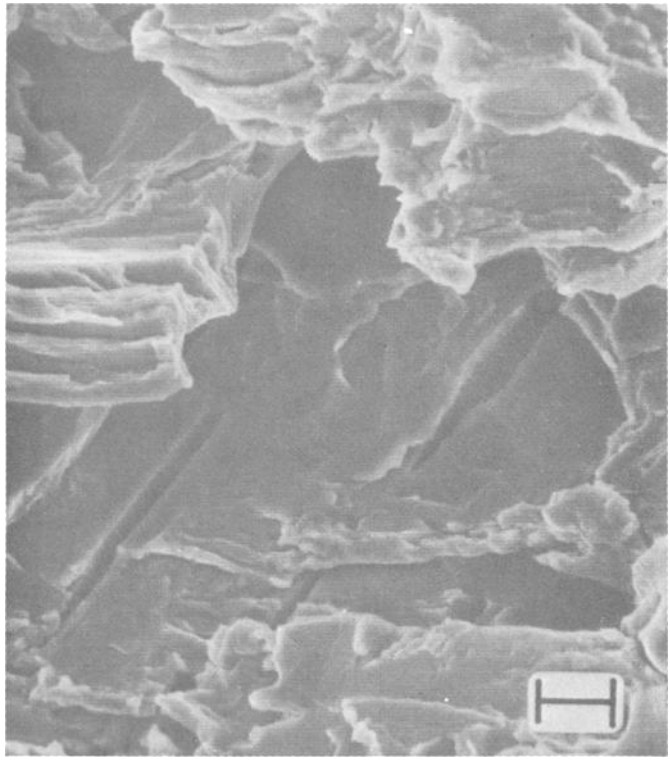

FIG. 13—*Cracks and cleavage faces in a zinc specimen after a long period of cavitation load (by SEM). (Scale mark indicates 10 μm.)*

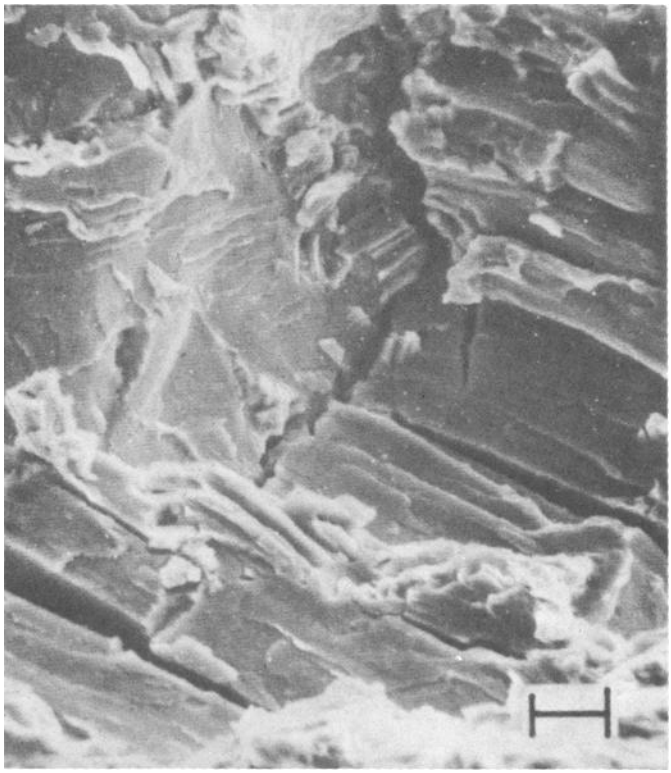

FIG. 14—*Eroded zinc specimen with cracks running in different directions (by SEM). (Scale mark indicates 10 μm.)*

reached by observing the changes of cavitated surface regions and not, for example, by taking a mass-loss/testing-time curve.

### *Iron*

Iron (see Table 1) in respect of its body-centered cubic structure takes on a middle position between aluminum and zinc; that is, it is more ductile than zinc but less deformable than aluminum. This fact leads to a behavior sometimes similar to aluminum, sometimes similar to zinc, when loaded by imploded bubbles.

As a result of its greater resistance to flow, initial damages caused by only one imploding bubble are to be seen in a smaller amount and in a smaller size than in the case of aluminum. These depressions in general do not have any surrounding plastic deformation wave. In addition to

these visible plastic deformations, an increasing hardness of the surface demonstrated by X-ray photographs or microhardness measurements can be determined.

The period of time in which initial damages can be proved is longer for iron than for aluminum or zinc. When continually loaded by imploding bubbles, some of these depressions grow. They do not reach the same size as in the case of aluminum. Distinct viscous flow in the formed craters is not to be seen. Impurities like manganese sulphide (MnS) in the surface, Fig. 15, have no important influence on the velocity of destruction. Although some of them break away after short periods of loading, the formed craters do not initiate positively a further destruction at this point.

The behavior of the regions of the grain boundaries is somewhat similar

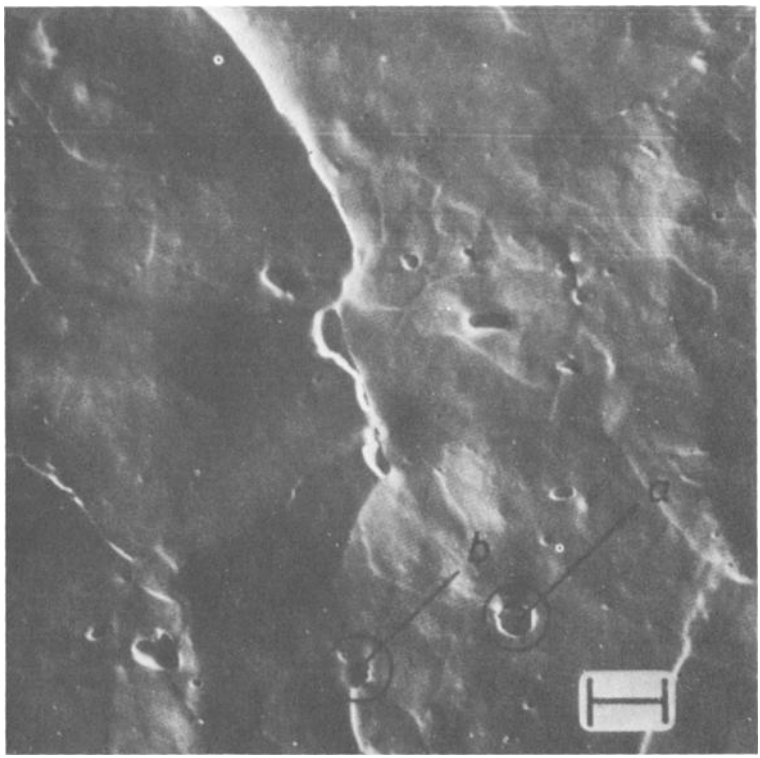


FIG. 15—*Armco iron specimen after 9 min of cavitation load (by SEM), showing impurities like manganese sulphide in the surface* (a) *and holes after breaking away of the MnS* (b). *(Scale mark indicates 33 μm.)*

to that in the case of zinc. All the imploding bubbles deform the whole surface of the specimen, Fig. 16. This deformation is unequal particularly near the grain boundaries, which are influenced in their mechanical behavior by the neighboring grains. Therefore, similar to the case of zinc, steps were found at the grain boundaries which are specially favored areas of imploding bubbles. The cracks resulting from this enforced loading run transcrystalline, often in direct proximity to the grain boundaries, Fig. 17. The increasing deformation of the surface, which is less pronounced than in the case of aluminum, leads to a fatigue of the iron[*12*].

In general the first initial fractures, resulting in a detectable mass loss, seem to be ductile. A continued loading of the specimen by imploding bubbles leads to an increasing rate of erosion. At this stage, cleavage planes demonstrating a brittle fracture are often to be seen, Fig. 18.

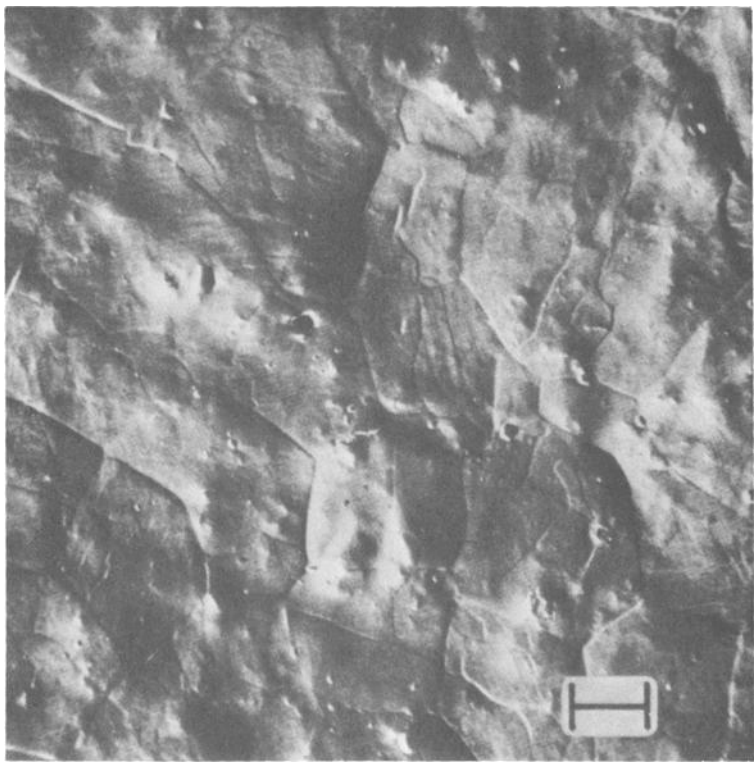

FIG. 16—*Plastic deformations of an Armco iron specimen after 4 min of cavitation load (by SEM). (Scale mark indicates 50 μm.)*

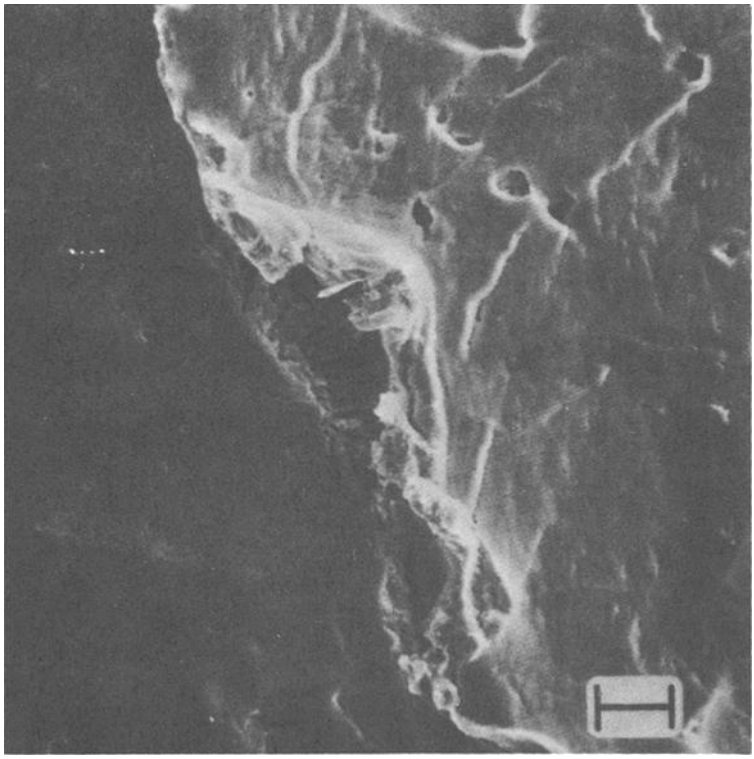

FIG. 17—*Transcrystalline cracking near a grain boundary in Armco iron after 20 min of cavitation load (by SEM). (Scale mark indicates 20 μm.)*

## Conclusions

To find out more about the kinetics of destruction of materials caused by imploding cavitation bubbles, you have to observe the changes of minute surface elements. An overall examination, that is, changes in surface profiles or in the mass of the specimen as a function of testing time, is only able to describe macroscopically the behavior of materials.

Studies on cavitated specimens by SEM provide us with more information about the kinetics of destruction, though some special mechanisms are not completely identified.

When transferring the results from one material to another, we must not only take into consideration the structure, which surely influences the behavior of the material under this special loading, but also the changed mechanical properties. This fact is of great importance especially if we

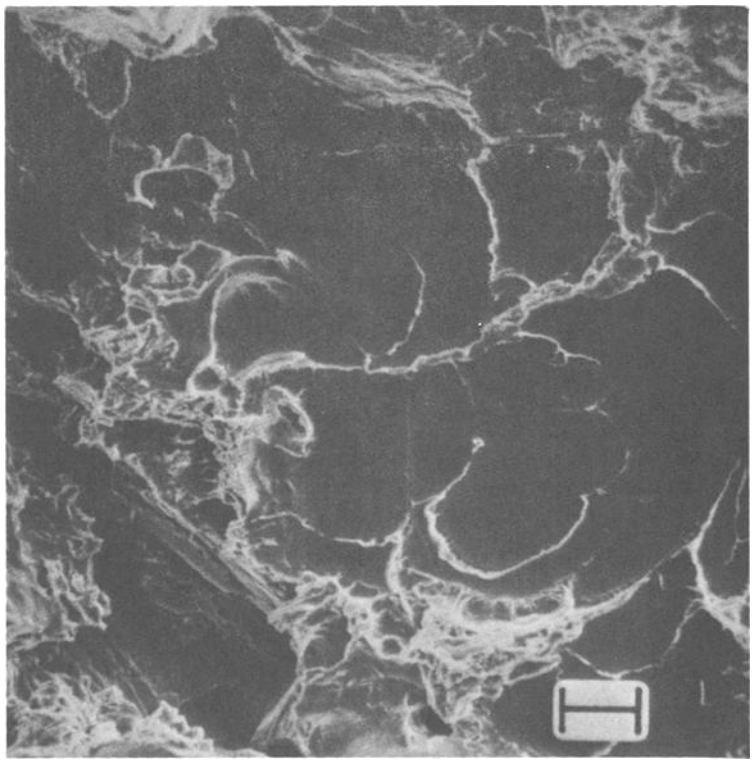

FIG. 18—*Cracks and fractures in iron (by SEM). (Scale mark indicates 60 μm.)*

want to estimate the cavitation resistance of heterogeneous materials with different mechanical properties in individual phases. However, knowledge of the kinetics of destruction enables us to produce successfully materials with a higher resistance to cavitation[*13*].

*Acknowledgment*

We would like to express our gratitude for the support given to us by our colleagues and assistants. We would also like to thank the German Research Association, which sponsored this research program.

## References

[*1*] Borbe, P. C., "Beitrag zur Werkstoffzerstörung durch Strömungskavitation in kalten und warmen Brauchwässern," dissertation, Technical University of Hannover, Hannover, Germany, 1968.

[2] Erdmann-Jesnitzer, F. and Louis, H., *Proceedings* of the 3rd International Congress on Marine Corrosion and Fouling," Oct. 1972, Gaithersburg, Md., pp. 454–461.

[3] Louis, H., "Erosive Zerstörungen durch Strömungskavitation," dissertation, Technical University of Hannover, Hannover, Germany, 1973.

[4] Eisenberg, P., Preiser, H. S., and Thiruvengadam, A., *Transactions*, Society of Naval Architects and Marine Engineers, Vol. 73, 1965, pp. 241–279.

[5] Canavelis, R., *La Honille Blanche*, Vol. 23, 1968, pp. 189–196.

[6] Erdmann-Jesnitzer, F. and Louis, H., *Jahrbuch der Schiffbautechnischen Gesellschaft*, Vol. 66, 1972, pp. 185–205.

[7] Rieger, H., *Zeitschrift für Metallkunde*. Vol. 58, 1967, pp. 821–827.

[8] Bernhardt, E. O. and Hanemann, H., *Zeitschrift für Metallkunde*, Vol. 30, 1938, pp. 401–409.

[9] Friedrich, R., Kaiser, G., and Pechhold, W., *Zeitschrift für Metallkunde*, Vol. 60, 1969, pp. 390–398.

[10] Imura, T., private communication.

[11] Hornbogen, E. and Keller, K., *Mitteilungen Forschungsgesellschaft Blechverarbeitung*, 1965, pp. 92–96.

[12] Erdmann-Jesnitzer, F., Louis, H., and Matsumura, M., "Erosive Kavitationszerstörungen an Armco-Eisen," to be published in *Archiv für das Eisenhüttenwesen*, Vol. 45, 1974.

[13] Erdmann-Jesnitzer, F. and Louis, H., "Werkstoffe hoher Kavitationsfestigkeit," to be published in *Metall*, Vol. 28, 1974.

# DISCUSSION

*A. F. Conn*[1]—From the oral presentation of this paper, I had the impression that cracks were observed in the aluminum specimens. Do these cracks imply the presence of a fatigue mechanism during the cavitation erosion of this aluminum? If so, this would conflict with the observations stated earlier in this symposium, during the paper presented by C. M. Preece. Or, as Dr. Preece has described the process, are these cracks merely the result of large ductile deformations?

*C. M. Preece*[2]—Are you suggesting that cracks are initiated in the aluminum by cavitation, and proceed to propagate during subsequent exposure, or that material removal is by ductile rupture of the protruding edges of deformation craters, as we observe in our experiments with the vibratory probe?

*F. Erdmann-Jesnitzer and H. Louis (authors' closure)*—Cracks observed in damaged aluminum specimens were mainly the result of large ductile deformation of the soft material. But in respect to the loading of the specimen, there can be observed also a quasi-static pressure superimposed by an alternating stress which results from the single-bubble-implosions fatigue phenomena.

In opposition to zinc, where cracks can be found without plastic deformation, the aluminum specimen shows large ductile deformation before cracks will be formed. The formation of cracks without plastic deformation is not to be seen in aluminum. This fact accords along general lines with the result C. M. Preece obtained in vibratory tests.

[1] Principal research scientist and head, Materials Sciences Division, HYDRONAUTICS, Incorporated, Laurel, Md. 20810.

[2] Associate professor, Materials Science Department, State University of New York at Stony Brook, Stony Brook, N. Y. 11790.

*F. G. Hammitt,*[1] *E. E. Timm,*[1] *J. B. Hwang,*[1] *and Y. C. Huang*[2]

# Liquid Impact Behavior of Various Nonmetallic Materials

**REFERENCE:** Hammitt, F. G., Timm, E. E., Hwang, J. B., and Huang, Y. C., "Liquid Impact Behavior of Various Nonmetallic Materials," *Erosion, Wear, and Interfaces with Corrosion, ASTM STP 567*, American Society for Testing and Materials, 1974, pp. 197–218.

**ABSTRACT:** Detailed photographs of liquid jet impact against elastomeric surfaces are presented and compared with impact and also cavitation erosion resistance. Two correlations between erosion resistance and material properties are presented.

**KEY WORDS:** cavitation erosion, velocity, deformation, mechanical properties, impact tests, liquid metals, erosion

Liquid droplet impact at high velocities upon materials is of importance in several applications. For instance, the low-pressure stages of large steam (or other vapor) turbines where moisture droplets form and impact rotating blading; high-speed military and civil aircraft where rain erosion of components such as radome surfaces is an important problem; and cavitation damage where the damage mechanism appears to include a major contribution from microjet impact induced by asymmetries such as an adjacent wall and pressure, or velocity gradients or both. In recent years, much theoretical and experimental work has been done upon liquid droplet or jet impingement or both upon material surfaces, including some at the authors' laboratory. However, most of this work, involving the details of the collision process, has been concentrated upon impacts on rigid surfaces rather than on surfaces for which substantial deformation takes place during

[1] Professor-in-charge and research assistants, respectively, Cavitation and Multiphase Flow Laboratory, College of Engineering, Department of Mechanical Engineering, University of Michigan, Ann Arbor, Mich. 48105.

[2] Combustion Engineering, Inc., Windsor, Conn.; formerly research assistant and doctoral candidate at coauthor's lab.

the impact, thus importantly influencing the collision process itself. The present paper reports upon photographic and theoretical studies of the impact process upon elastomeric and other nonmetallic materials.

High-speed motion picture sequences taken at about 0.6 million frames per second of short liquid jets of ~1.2 mm diameter and 500-mph (223 m/s) velocity, upon various elastomeric materials,[3] Epon-828 and Plexiglas, are presented. The water slugs result from our automatic water gun device[*1*],[4] and resemble closely those produced by the type of momentum exchange device pioneered by Brunton [*2*], for example. Since the jets have an approximately hemispherical leading edge, the resultant flow and pressure upon the target during the initial part of the impact are very similar to those obtained from a spherical drop of the same diameter. Previous theoretical work[*2*], including our own recent numerical studies[*3–5*], shows this is the case, and also that only the very initial part of the impact is likely to be important to the damage process.

The high-speed photographs indicate the large differences in splash patterns resulting from the different materials, which are then compared with the erosion resistance of some of the same materials as measured with the same automated water gun device, by cavitation, and by a propeller arm. In addition, quantitative data on the axial and radial velocities resulting from the impacts upon the various materials are presented, and comparison with the observed splash pattern is possible. It is hoped that this information may help to improve understanding of the relations between the mechanical properties of the materials and erosion resistance, and may perhaps also allow the eventual prediction of erosion resistance from splash patterns which can be observed fairly easily with suitable photographic equipment.

To further assist the understanding of the detailed mechanism of damage from droplet or jet impact upon elastomeric materials, we have performed numerical calculations showing surface deformation for such materials as well as velocities and pressures along the surface[*5*] during impact with spherical droplets. These preliminary results, using a somewhat restricted mathematical model, are discussed.

Since it is generally agreed today that cavitation damage includes a strong contribution from liquid microjet impact, but that detailed differences certainly exist between jet impact per se and cavitation damage mechanisms, including that of scale, it is useful to compare the cavitation and jet impact damage resistance of a group of materials. This has been done for

[3] Supplied by B. F. Goodrich Company.

[4] The italic numbers in brackets refer to the list of references appended to this paper.

the present material group, using a relatively standard vibratory cavitation test to be compared with the water gun tests, and also with tests from the Goodrich propeller-arm rain erosion test facility. The detailed results are presented. For this particular group of materials it was found that often an almost inverse relationship exists between liquid impact and cavitation damage resistance.

Correlations of both impact and cavitation damage resistance with Shore hardness are shown. Shore hardness was found to be reasonably successful in this respect, particularly for cavitation resistance, for the particular group of materials here tested.

## Experimental Results Obtained

### *Experimental Facilities Utilized (Figs. 1, 2)*

*Water Gun Device*—While the water gun device has been described elsewhere[*1*], the most important points are included here for convenience. The device is shown schematically in Fig. 1. Elongated jets of about 1.2 mm diameter are produced with velocity adjustable up to ~600 m/s, and with a repetition rate of about 30 per minute by the impact of a spring-driven steel bolt upon a hardened steel diaphragm, the opposite side of which is in contact with a small quantity of water within a closed chamber, itself opening into an orifice of suitable diameter from which the impacting jet emerges. This device is patterned after a similar unit developed by Kenyon[*6*] at Associated Electrical Industries in the UK. The appearance of the jet at the velocity used for these tests (223 m/s, or 500 mph) is as

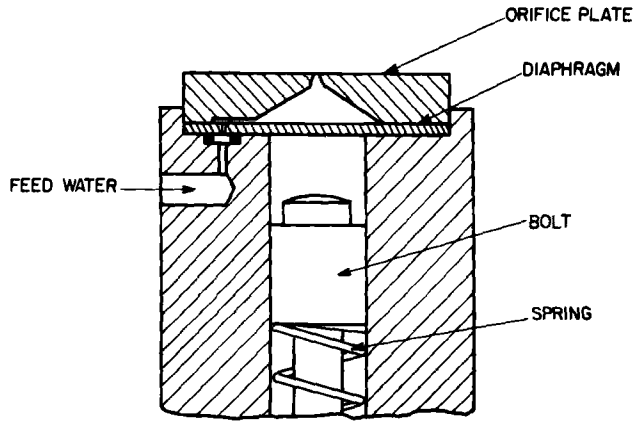


FIG. 1—*Schematic of water gun device.*

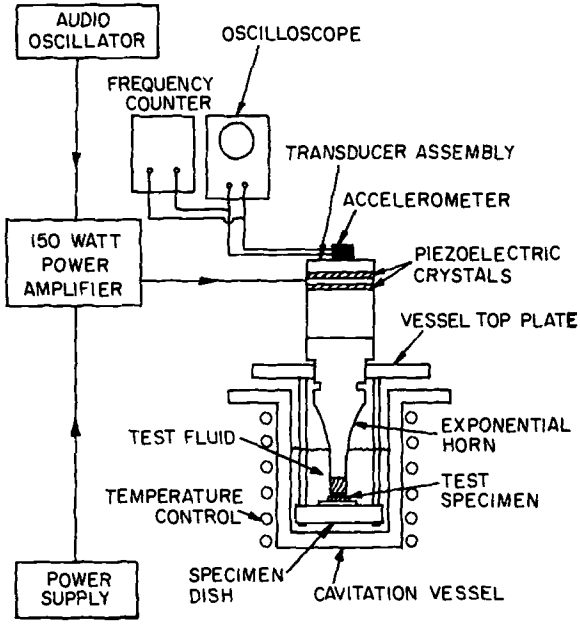


FIG. 2—*Schematic of stationary specimen vibratory cavitation test facility.*

shown in Figs. 3–6. The portion of the impact shown (up to 80 $\mu$s) is with a "precursor jet" of ~1/3 mm diameter, only about 1/4 the diameter of the main jet which follows. It is generally believed, and verified by numerical calculations ([*3–5*] etc.) as well as basic theory, that the damaging part of the impact is the initial part during which very high transient pressures and velocities exist. The pressure and velocity across the surface of a "steady-state" jet of the impact velocity here used would be much smaller and probably not damaging during the short-time duration of collision. It is still virtually beyond the state of the art to accurately measure pressures under such jets, though work at Cambridge under Brunton is progressing in this direction.

*High-Speed Motion Picture Facility*—The motion picture sequences of the water jet impacts (Figs. 3–6) were made with a Beckman-Whitley framing camera capable of a maximum framing rate of 2 million frames per second, with a total of 80 frames per run. To obtain maximum information per run, rates of between 0.5 and 0.66 million frames per second were used for the present tests. A laser-photocell arrangement interrupted by the water jet is used to trigger the camera light source.

*Cavitation Damage Facility*—Cavitation damage tests on many of the

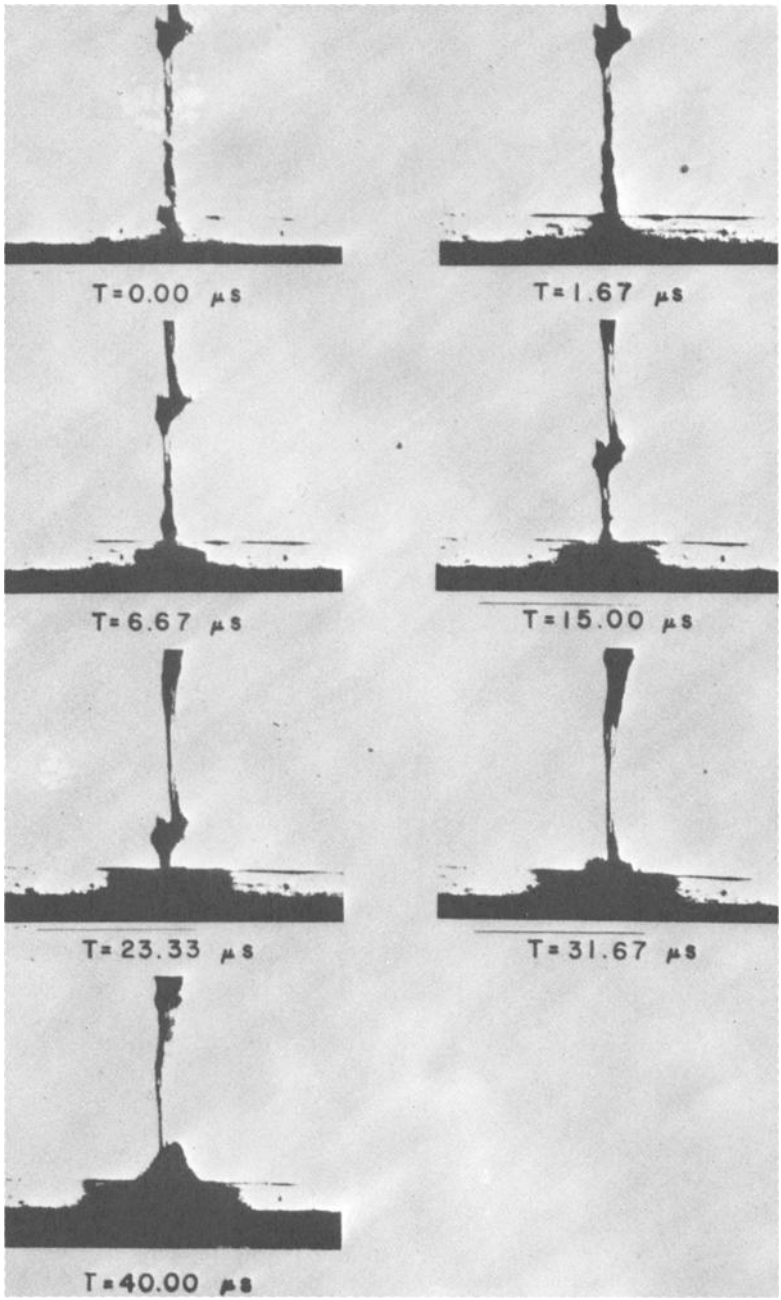


FIG. 3—*High-speed motion picture sequence of jet impact—Goodrich No. 1 (natural rubber).*

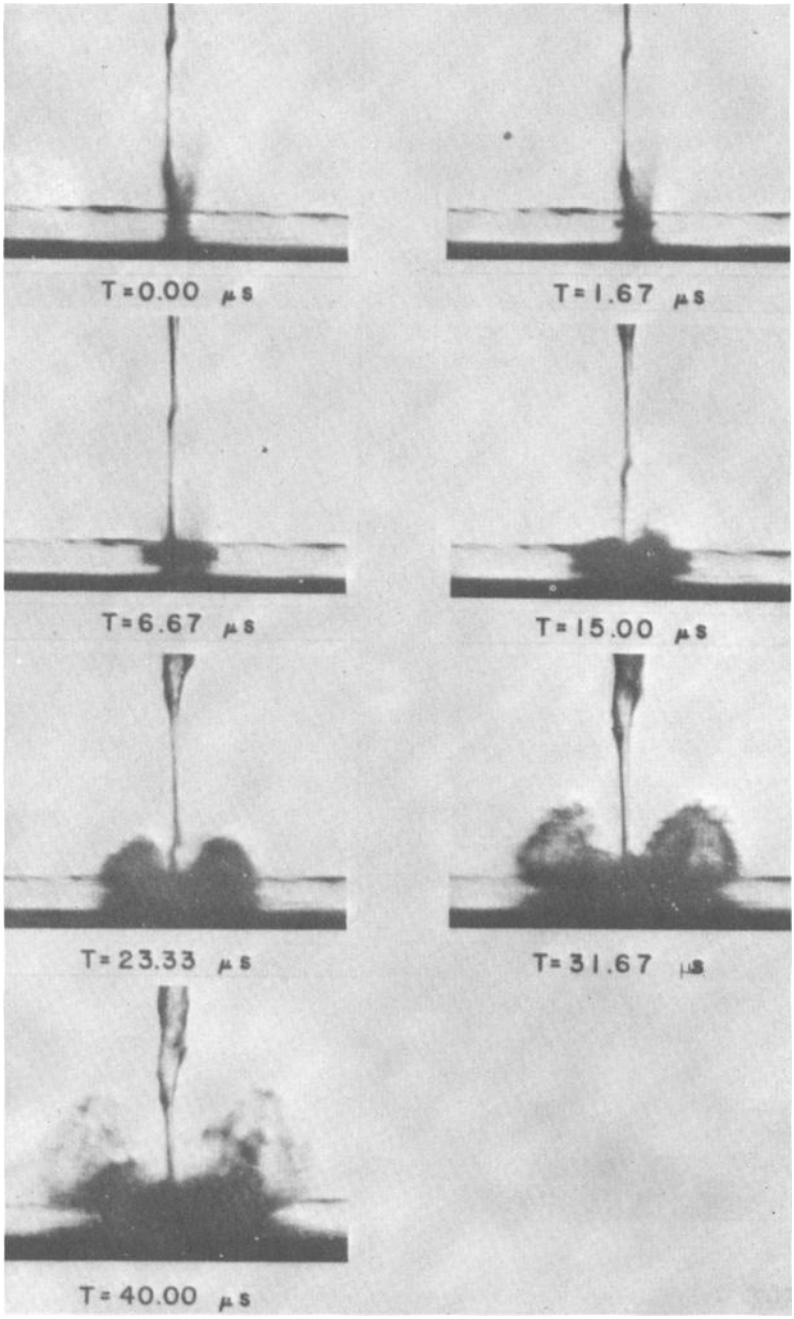


FIG. 4—*High-speed motion picture sequence of jet impact—Goodrich No. 10.*

materials were made in a vibratory-horn, stationary specimen setup (Fig. 2), described in more detail elsewhere[*1*]. The specimen is held 20 mils (0.51 mm) from the 20-kHz vibratory horn of 2-mil (0.051 mm) double amplitude.

*Photographic Results Obtained*

*General Observations*—Figures 3–5 are high-speed motion picture sequences of water-jet impacts at 500 mph (223 m/s ≅ 0.67 Mach at STP) upon various elastomeric materials supplied by Goodrich; Fig. 6 is for Plexiglas. The times in microseconds from the start of impact are shown in each frame. Although approximately 80 frames were exposed per run, only selected frames are shown, chosen to indicate the significant features of the impact. The portion of the impact shown is that with the "precursor" portion of the main jet, having a diameter of ~1/3 mm and persisting for ~80 $\mu$s. The main jet of about 1.2 mm follows, but since this latter portion is roughly steady-state impingement, it is not believed important to the damage process. Our numerical calculations ([*5–7*] etc.) indicate that damaging pressures persist for only about the first microsecond after start of impact, steady-state pressure being rapidly approached thereafter.

Although the impact phenomenon is quite similar for all the materials tested, there are significant differences in the velocity and direction of the splashback. The splashback was minimal for the more rigid materials such as Plexiglas, but quite pronounced for most (but not all) of the rubber-coated[5] materials. Presumably the larger splash patterns for the elastomeric materials are due to the increased surface deformation, which would no doubt result in a directing of the outflow away from the surface, causing a "splashback." Why these splash patterns differ as much as they do for the different elastomerics is not known at this time.

The axial and radial velocities as a function of time after collision have been estimated for some of the materials from the known time increment and leading-edge displacements in the photos. The flow patterns are well developed during the first 40 $\mu$s, and there are considerable differences in flow patterns between materials. Unfortunately, it is not possible from these photos to observe the deflection of the specimen surface during impact, and this is in fact a very difficult parameter to measure. However, from the steep angle of splashback, it appears that in some cases the surface deformation is considerable.

As is well known, the radial velocities of the splash component can be

[5] Coating thickness = 0.033 in. bonded to ¼-in. stainless steel substrates in all cases.

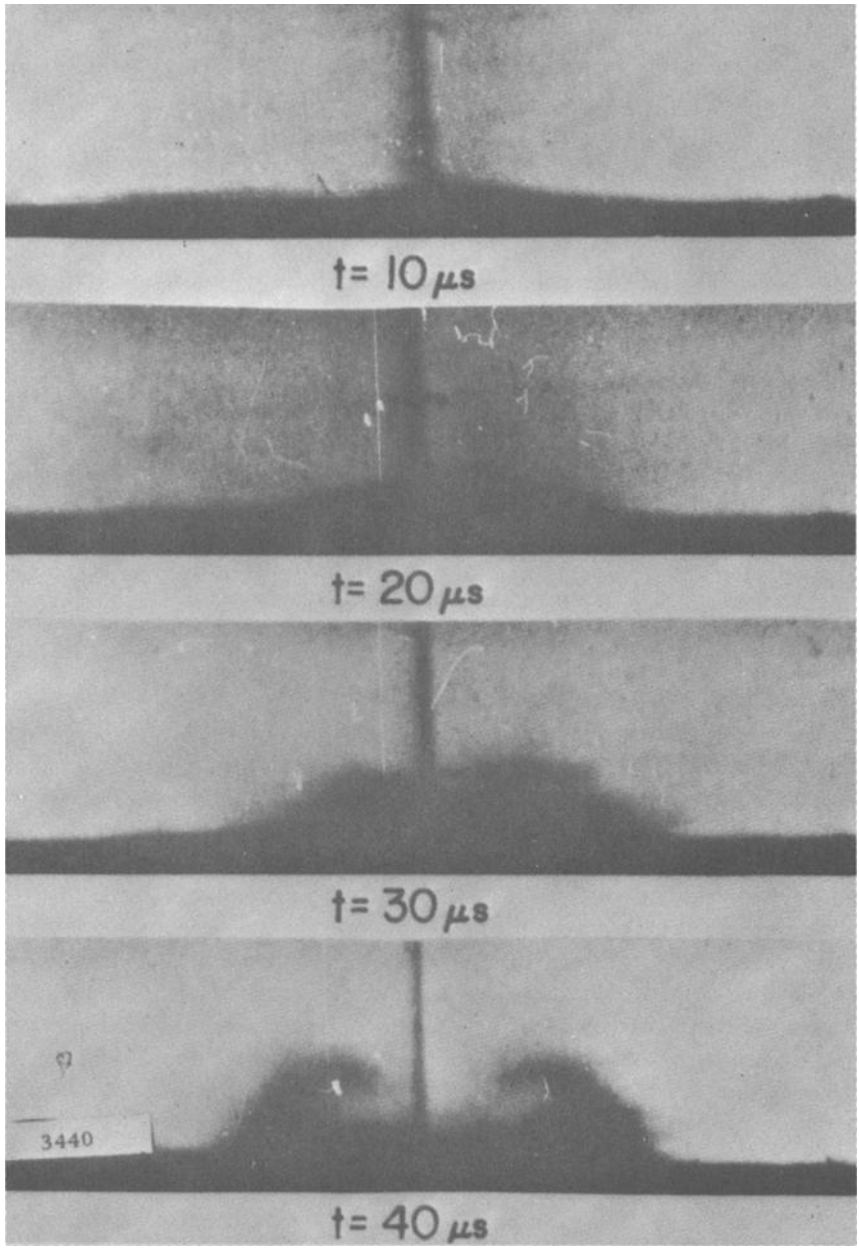


FIG. 5—*High speed motion picture sequence of jet impact—Goodrich No. B.*

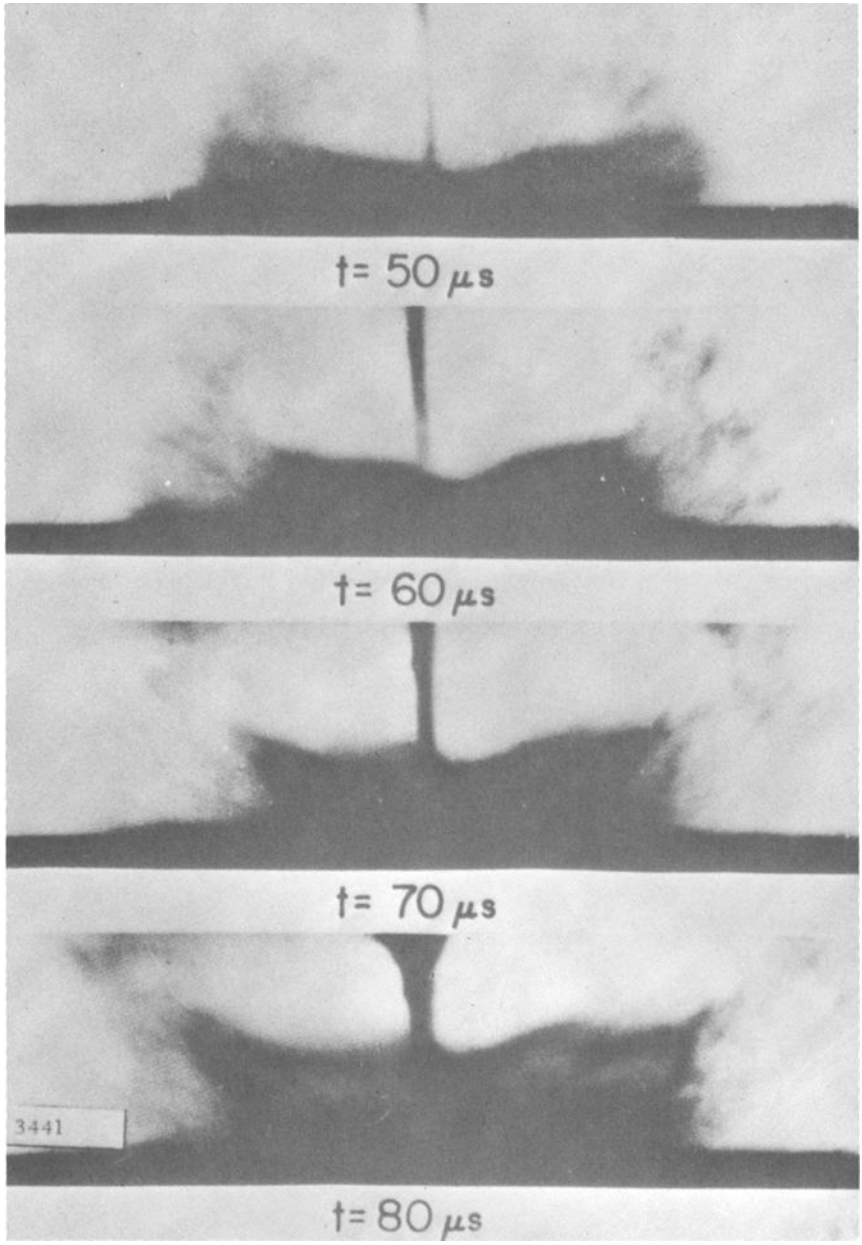


FIG. 5—*(Continued).*

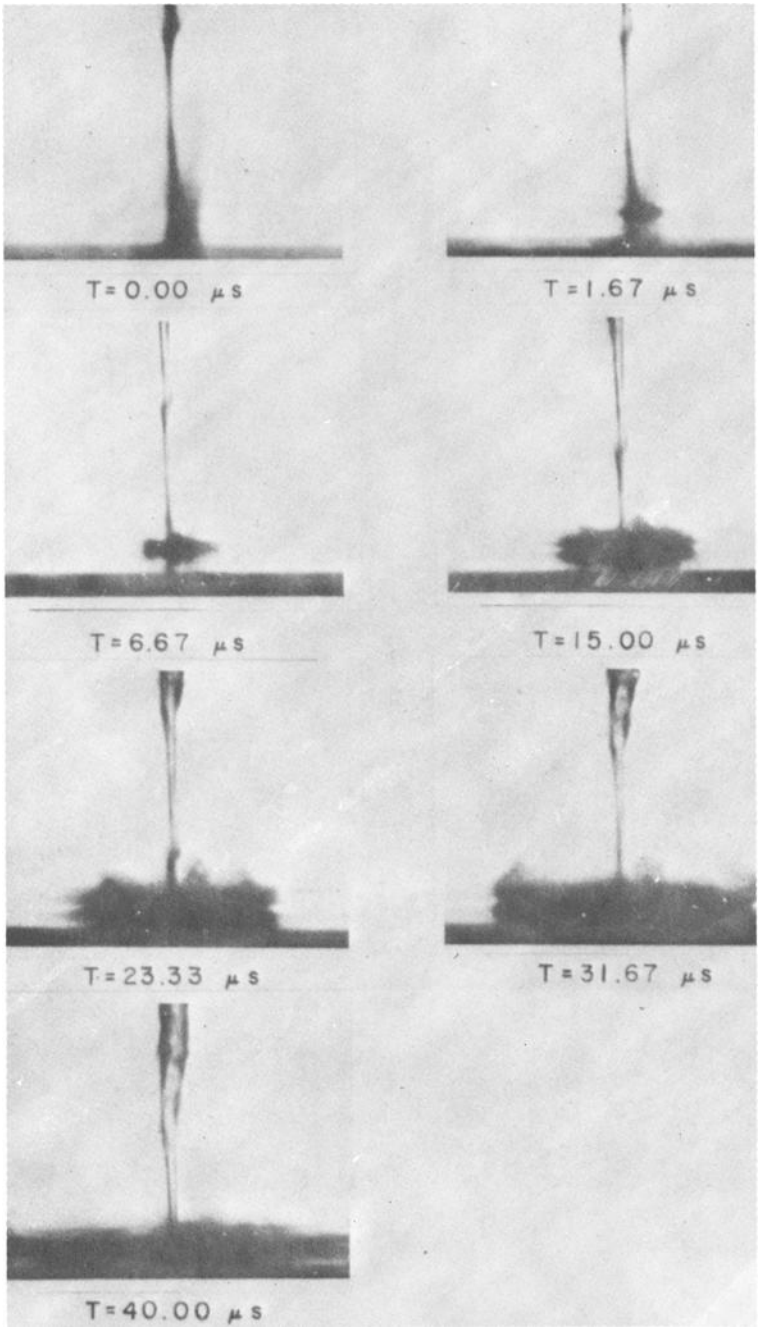


FIG. 6—*High speed motion picture sequence of jet impact—Plexiglas.*

considerably greater than the impact velocity, (~6.5 × impact velocity) for Goodrich No. 10 being the greatest ratio observed in these tests (Table 2). A more common ratio here observed was ~1.3, but in all cases the radial splash velocity attains higher values than the impact velocity. Thus it has often been assumed that the shear stress with the surface caused by this outward-flowing liquid sheet could contribute importantly to the damage. This certainly remains a possibility, but these tests appear to indicate that much of the splash liquid is directed upward and away from the surface with resilient materials of this type, so that contact with the surface may not be maintained except very close to the center of impact. The photos also appear to suggest that the splashback is not in the form of a continuous sheet, but rather is fragmented into individual rays and jets. If so, the erosion due to the radially outward-flowing liquid would certainly be affected by the actual flow geometry, and no actual shear stress could be computed. In addition, the various roughnesses and asperities found on an actual surface will affect the flow and stresses in different ways for different properties of the base material.

*Specific Photographic Results*—The photographic sequences of Figs. 3–5 illustrate differing splashback patterns for three of the elastomeric materials supplied by Goodrich. Figure 3 shows the minimum type of splash pattern observed in these tests upon an elastomeric material, natural rubber in this case. Figure 4 shows a maximum splashback pattern and Fig. 5 an intermediate splashback, but with more radial spreading than in the other cases shown. Figure 6 shows results with Plexiglas, which produces little splashback (much like the natural rubber tested) but considerable radial spreading. In Table 1 the Shore hardnesses and tensile strengths of various materials are listed with other material properties, along with the erosion results from the cavitation and impact tests. Table 2 lists the radial and axial maximum splash velocities as well as the plume heights obtained. Table 3 provides comparative erosion data as well as a relative ranking of erosion resistances for the materials in the impact and cavitation tests.

According to Table 2, Goodrich materials Nos. 3, 4, 6, and 10 show relatively large splash activity, while Goodrich Nos. 1 and 5, Epon-828, and Plexiglas show relatively small splashes. From the data of Table 3, the relative ranking in all tests of each of these groups of materials averages about 4. Hence, from the present results, the splashback parameters cannot be used as a reliable indication of erosion resistance. They do, however, indicate something of the surface deformation behavior which is at present otherwise extremely difficult to measure. Eventual comparison of the splash data with numerical calculations for the overall impact phenomenon,

TABLE 1—*Material damage and mechanical properties.*

| Material | Hardness, Shore A | Tensile Strength, psi | Elongation, % | Density, gm/cm³ | Gun WLR, mg/imp | Caviation WLR, 3 mg/h | Impacts to mm³ Volume Loss | Impacts to 1 mm³ Volume Loss | Incubation Period—Gun,[a] impacts | MDPR Cavitation, mils/h |
|---|---|---|---|---|---|---|---|---|---|---|
| Goodrich No. 1 (natural rubber) | 36 | 4 190 | 740 | 0.976 | 0.039 | 0.026 | 81 | 61 | 10 | 0.0695 |
| Goodrich No. 3 (neoprene) | 62 | 2 830 | 710 | 1.359 | 0.059 | 0.15 | 120 | 1 000 | 1 000 | 0.0192 |
| Goodrich No. 4 (neoprene) | 55 | 3 090 | 580 | 1.321 | 0.081 | 0.80 | 300 | 71 | 20 | 0.158 |
| Goodrich No. 5 (neoprene) | 37 | 2 440 | 1 000 | 1.229 | 0.05 | 1.10 | 630 | 143 | 0 | 0.244 |
| Goodrich No. 6 (neoprene) | 45–48 | 2 730 | 1 080 | 1.574 | 0.029 | 0.44 | 218 | 86 | 55 | 0.075 |
| Goodrich No. 10 (estane) | 75–80 | 3 000 | 900 | 1.215 | 0.013 | 2.4 | 2 490 | 1 370 | 4 730 | 0.517 |
| Epon-828 Laminate | 99.5 | ... | ... | 1.60 | 0.125 | 52.00 | 860 | 600 | 880 | 11.4 |
| Plexiglas | 99.5 | ... | ... | 1.19 | 0.29 | 27.00 | 810 | 460 | 1060 | 4.4 |
| Goodrich No. 11 | 65 | ... | ... | 1.10 | 0.004 | 3.20 | 13 500 | 12 900 | 12 666 | 0.75 |

Goodrich No. B—Proprietary elastomeric material

[a] Defined here as intersection between abscissa and tangent to maximum damage rate portion of volume loss versus number of impacts. Hence the impacts to a fixed (small) volume loss may be less than the "incubation period" so defined.

TABLE 2—*Liquid impact collision parameters.*

| Specimen | Max $V_{ax}$, m/s | Max $V_{rad.}$, m/s | Max Radial Velocity of Splashback Plume, m/s (impact velocity = 223 m/s) | Max Plume Height (40 μs) mm | | |
|---|---|---|---|---|---|---|
| | | | | left | right | avg |
| Goodrich No. 1 | 180 (0–1.7 μs) | 299 (0–1.7 μs) | 28 | 1.8 | 2.2 | 2.0 |
| Goodrich No. 3 | 299 (0–1.7 μs) | 539 (0-1.7 μs) | 108 | 3.3 | 3.7 | 3.5 |
| Goodrich No. 4 | 120 (0–1.7 μs) | 240 (0–1.7 μs) | 110 | 3.8 | 5.4 | 4.6 |
| Goodrich No. 5 | 240 (0–1.7 μs) | 299 (0–1.7 μs) | 37 | 2.8 | 2.7 | 2.7 |
| Goodrich No. 6 | 180 (0–1.7 μs) | 299 (0–1.7 μs) | 63 | 4.1 | 4.5 | 4.3 |
| Goodrich No. 10 | 180 (0–1.7 μs) | 1170 (0–1.7 μs) | 80 | 4.6 | 4.5 | 4.6 |
| Epon-828 | 240 (0–1.7 μs) | 299 (0–1.7 μs) | 170 | 2.0 | 2.2 | 2.1 |
| Plexiglas | 180 (0–1.7 μs) | 240 (0–1.7 μs) | 180 | 1.8 | 2.3 | 2.1 |

TABLE 3—*Relative rankings for erosion resistance.*[a]

| Material | Goodrich Propeller Arm | | | U-M Water Gun, impacts to 1 mm³ | | U-M Cavitation, mils/h | |
|---|---|---|---|---|---|---|---|
| | 10 mm³ | 100 mm³ | 60 min | | | | |
| Goodrich No. 1 | 1 | 1 | 1 | 1 | 1[b] | 5 | 8[b] |
| Goodrich No. 5 | 2 | 4 | 4 | 4 | 4 | 2 | 5 |
| Goodrich No. 3 | 3 | 3 | 3 | 5 | 7 | 6 | 9 |
| Goodrich No. 6 | 4 | 5 | 5 | 3 | 3 | 4 | 7 |
| Goodrich No. 4 | 5 | 2 | 2 | 2 | 2 | 3 | 6 |
| Goodrich No. 10 | 6 | 6 | 6 | 6 | 8 | 1 | 4 |
| Epon-828 | ... | ... | ... | ... | 6 | ... | 1 |
| Plexiglas | ... | ... | ... | ... | 5 | ... | 2 |
| Goodrich No. 11 | ... | ... | ... | ... | 9 | ... | 3 |

[a] Highest value = greatest resistance.

[b] This column includes Epon-828, Plexiglas, and Goodrich No. 11 in the rankings.

such as Ref 5 and our ongoing work[7], will be possible and will contribute, we hope, to an understanding of the overall phenomenon.

Figure 7 shows our calculated surface deformation[5] for a rubberlike material (inertial but zero-strength properties were assumed, and specimen represents an infinite planar half-surface) for impact with a spherical water drop at about 270 m/s. The sharp deformation of the surface under this condition indicates the mechanism for the generation of splashback, though it is not clear why the intensity of splashback differs so greatly between materials, since the properties of the materials do not differ very widely (Table 1).

Figures 8 and 9 indicate the type of surface failure encountered with typical materials, Fig. 8 being one of the elastomeric materials, and Fig. 9, Plexiglas. In those cases (Fig. 9) where the cavitation and impact damage are compared directly, it is noted that the cavitation attack is on a much finer scale due no doubt to the large diameter ratio between impacting jet and microjet. The large-scale brittle nature of the impact Plexiglas failure compared with that of the other materials is also evident.

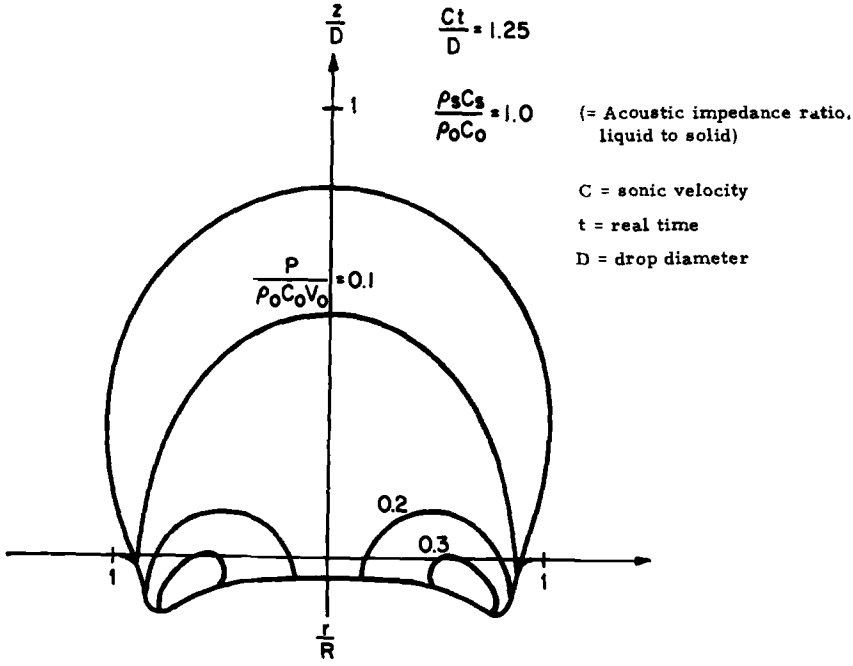


FIG. 7—*Calculated profiles for liquid impact on flexible surface.*

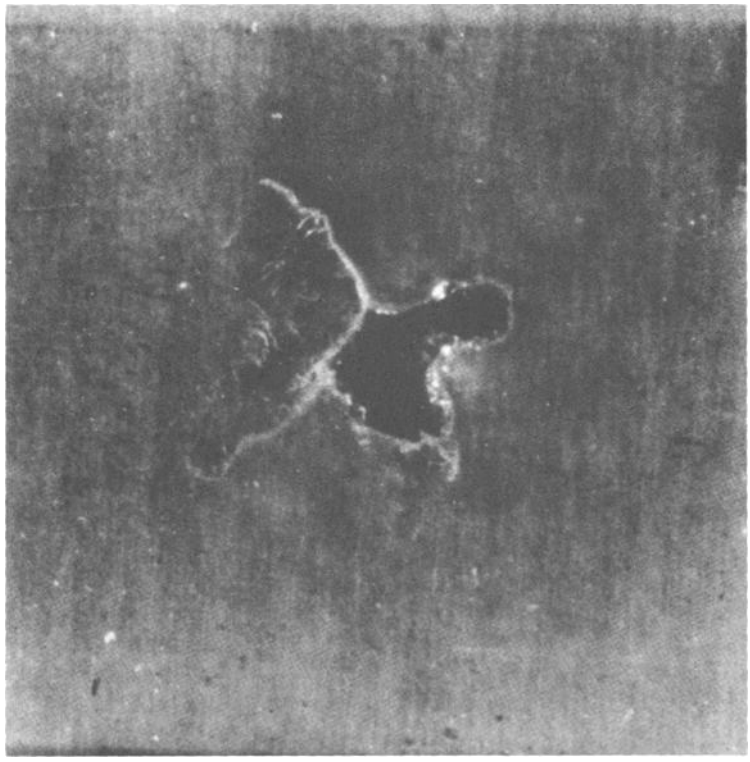

FIG. 8—*Typical failure of elastomeric specimen from water gun test.*

### *Comparative Erosion Results*

Both impact and cavitation erosion tests were conducted on most of the materials for which photographic results were obtained, and in addition some erosion results were also available from the Goodrich propeller-arm rain erosion test facility. Figure 10 shows the correlation of our gun impact results with Shore hardness, and Fig. 11 cavitation erosion resistance with Shore hardness. Table 2 compares erosion resistance as measured by water gun, cavitation, and propeller arm, and Table 3 provides relative ranking of materials in all these devices according to erosion resistance, as already discussed. It is noted that the relative ranking of materials (Table 3) is often in strong disagreement for the different types of materials. This tends to emphasize the increasingly apparent fact that erosion tests of all kinds, even for relative rankings, depend very heavily on the particular test, and test geometry, used. This was made evident even for the recently completed ASTM Committee G-2 Cavitation Round Robin[*8*] and also

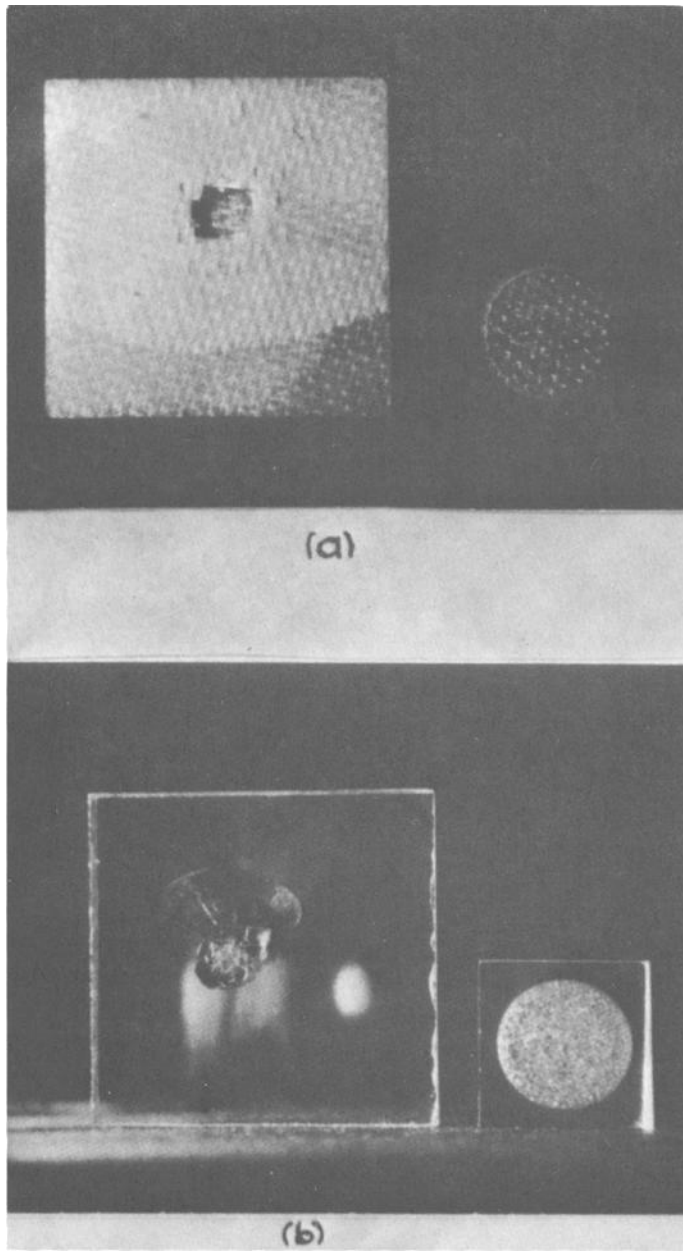


FIG 9—*Damaged specimen photos:* (left) *impact specimen,* (right) *cavitation specimen.* (a) *Epon-828,* (b) *Plexiglas.*

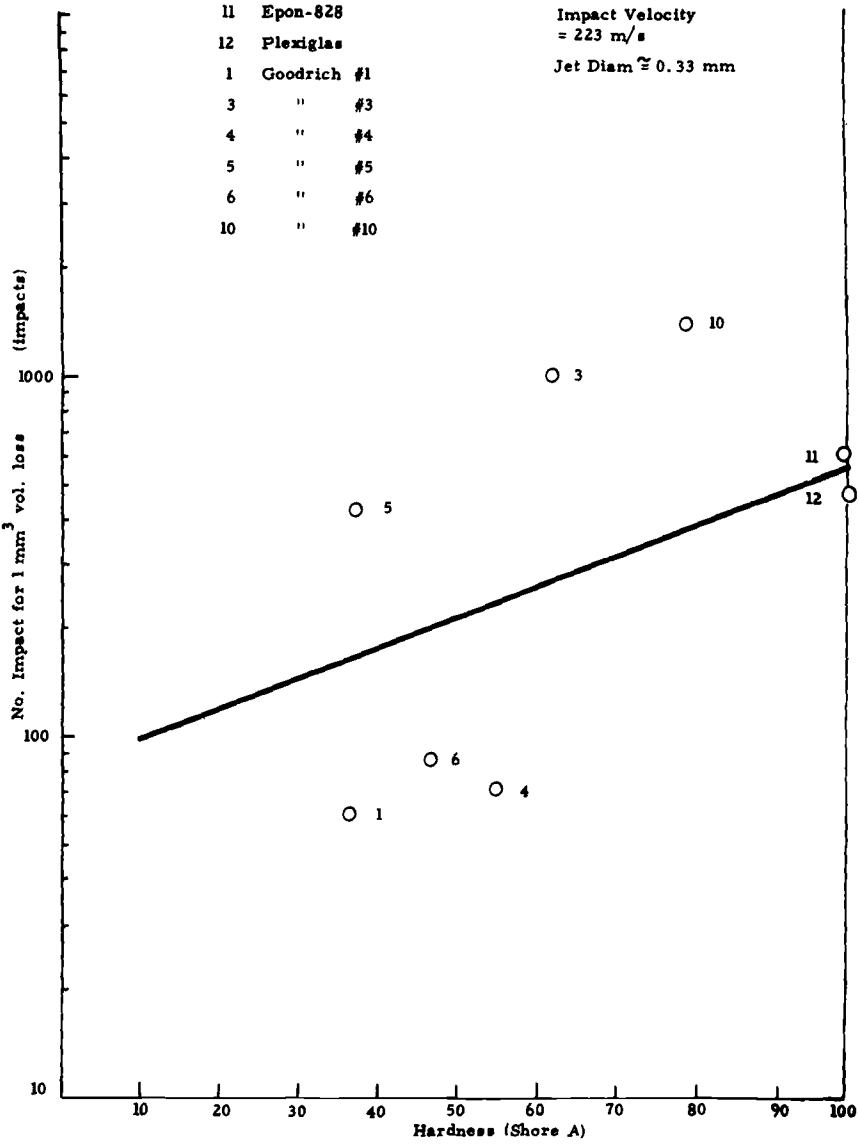


FIG. 10—*Impact erosion data correlated with hardness.*

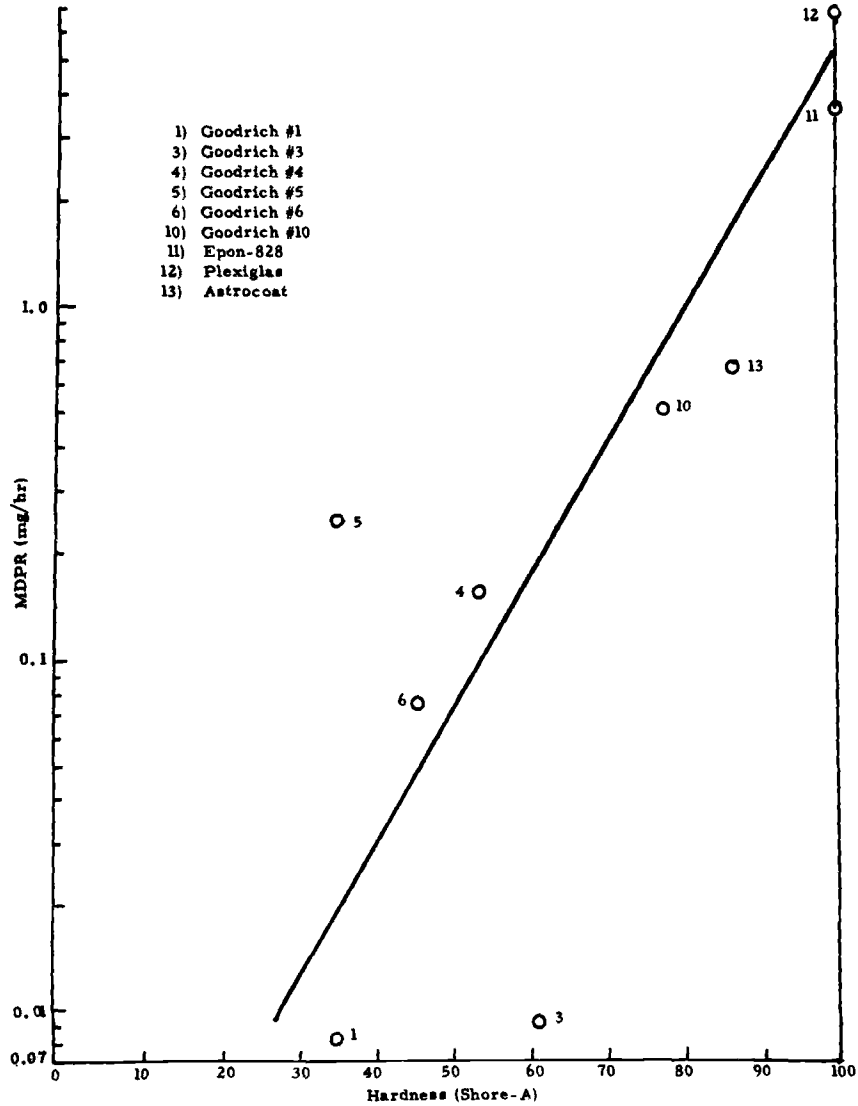


FIG. 11—*Cavitation erosion data correlated with hardness.*

from the preliminary results of the ongoing Liquid Impact Round Robin. With regard to the present comparison between cavitation, water gun impact (elongated slugs), and rotating arm (round drops) erosion rates, it is apparent that the size, shape, and impact velocity differences have importantly influenced the results. It appears possible that nonmetallic materials of the type here tested are more sensitive to these influences than are usual metallic materials. It thus appears that only round droplet impact as provided by a rotating arm can be used to evaluate such materials for the aircraft rain erosion application.

Figures 12 and 13 indicate respectively that with the present group of materials there is at least a trend indicating increasing erosion resistance with increasing hardness for both the impact and cavitation tests. The correlation appears much closer for the cavitation than for the impact

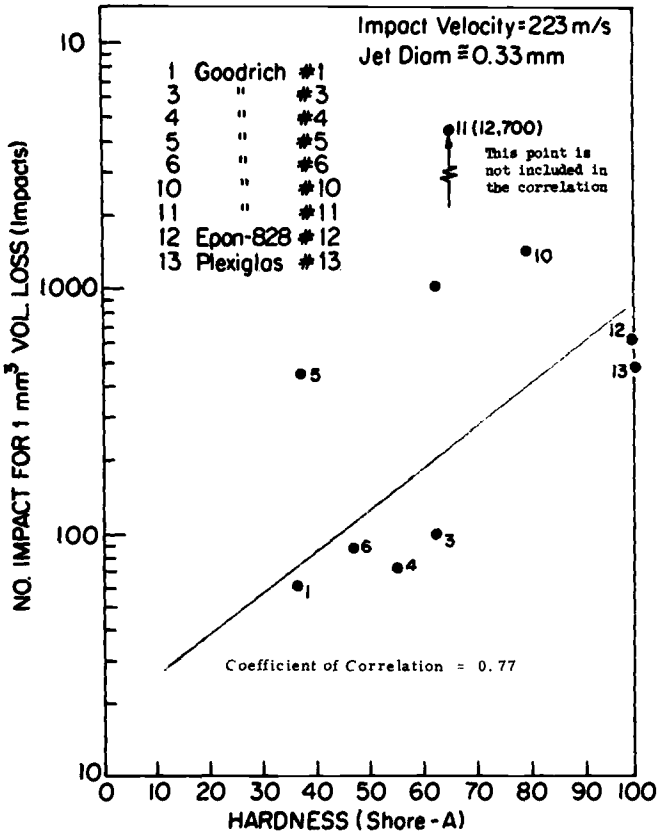


FIG. 12—*Impact data correlation with hardness.*

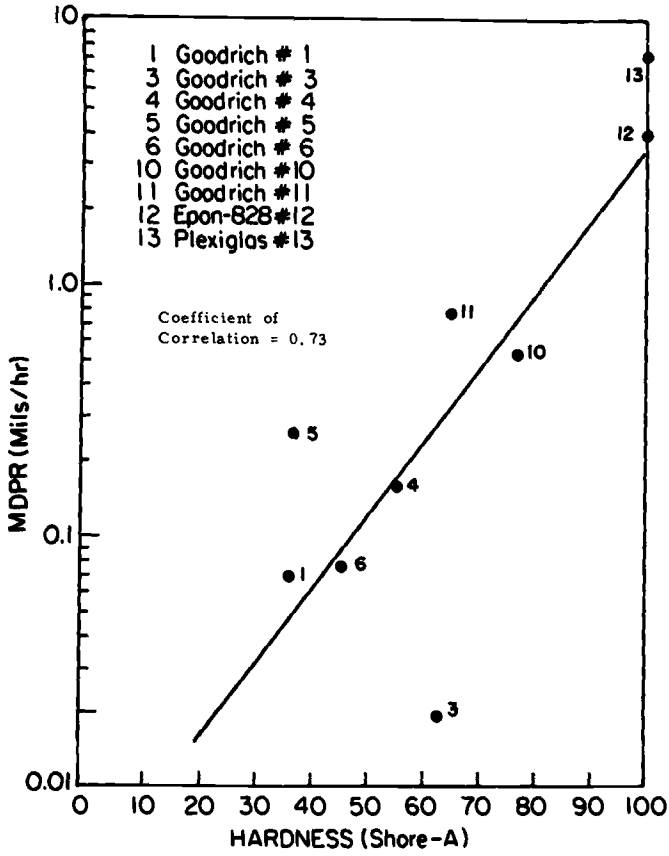


FIG. 13—*Cavitation data correlations with hardness.*

tests, but there are some "bad" points involved for this as well as for the other. The hardness correlations are in general better than those obtained with tensile strength[9]. Admittedly these correlations are probably not general, but apply only to this rather limited group of materials in these particular devices. The utility of quasi-static mechanical properties to evaluate cavitation or impact erosion resistance is no doubt questionable because of the strong dependence of mechanical properties on rate of loading. In addition, the situation for cavitation is different from and more complex than that for impact, since the bubble trajectory (in approaching or being repelled from the surface) is strongly influenced by the surface elasticity[*10*].

## Conclusions

Detailed photographs of the splash behavior in liquid impact against elastomeric and other nonmetallic materials are presented. No direct correlation between these patterns and erosion resistance seems possible from these results. However, detailed information on the splash is obtained that can hopefully be correlated with the on-going numerical studies of the impact phenomenon, thus improving overall understanding.

A rough correlation between Shore hardness and erosion resistance for both liquid impact and cavitation tests is presented.

*Acknowledgments*

Financial support for this work was provided primarily by the B. F. Goodrich Company. Special thanks are due to Michael Hall, who provided the broad technical direction for the work from the side of B. F. Goodrich. In addition, financial support for the numerical impact studies was derived from NSF Grant GK 730, and a grant from the Alcoa Foundation.

## References

[1] Hammitt, F. G., et al., "Cavitation and Droplet Impingement Damage of Aircraft Rain Erosion Materials," *Proceedings*, 3rd International Conference, Rain Erosion and Associated Phenomena, Farnborough, England, 1970; also available as ORA Report UMICH 02643-5-I, University of Michigan, Ann Arbor, Mich. May 1970.

[2] Brunton, J. H., *Philosophical Transactions of the Royal Society*, Series A, No. 1110, Vol. 260, July 1966, pp. 78–85.

[3] Huang, Y. C., "Numerical Studies of Unsteady, Two-Dimensional Liquid Impact Phenomena," Ph.D. thesis, Mechanical Engineering Department, 1971; also available as ORA Report UMICH 03371-8-T, University of Michigan, Ann Arbor, Mich., July 1971.

[4] Huang, Y. C., Hammitt, F. G., and Yang, W-J., *Transactions*, American Society of Mechanical Engineers, *Journal of Fluids Engineering*, 1, Vol. 95, No. 2. 1973, pp. 276–294.

[5] Huang, Y. C. and Hammitt, F. G., "Liquid Impact on Elastic Solid Boundary," 11th Symposium, Georgia Institute of Technology, July 1972; also available as ORA Report UMICH 03371-12-I, University of Michigan, Ann Arbor, Mich., Feb. 1972.

[6] Kenyon, P., personal communications with F. G. Hammitt, 1967.

[7] Hwang, J. B., "Liquid Impact on Elastic Materials," Ph.D. thesis (in progress), Mechanical Engineering Department, University of Michigan, Ann Arbor, Mich.

[8] Hammitt, F. G., et al., *Materials Research and Standards*, Oct. 1970, pp. 16–23.

[9] Hammitt, F. G., et al., "Liquid Impingement and Cavitaion Studies of Erosion Resistance of Rubber-Coated Materials for B. F. Goodrich," ORA Report UMICH 324490-1-T, University of Michigan, Ann Arbor, Mich., Dec. 1970.

[10] Timm, E. E. and Hammitt, F. G., "Bubble Collapse Adjacent to a Rigid Wall, Flexible Wall, and a Second Bubble," *1971 ASME Cavitation Forum*, American Society of Mechanical Engineers, pp. 18–20.

# DISCUSSION

*A. F. Conn*[1]—The authors are to be congratulated on developing and performing a most difficult series of experiments in order to photographically capture considerable detail of the impact and splash from a jet of water on elastomers. However, I feel that if the objective of using such splash data to understand either the impingement or cavitation erosion behavior of such materials is to be met, one must utilize their dynamic properties and not the static values cited during the oral presentation of this paper. Our tests at HYDRONAUTICS with such elastomers have shown that their dynamic response differs greatly from the static properties. Due to the extremely high rates of loading associated with either droplet impingement or cavitation, one should not expect static mechanical property test results to shed light on these dynamic phenomena.

*F. G. Hammitt (authors' closure)*—The authors would like to thank Dr. Conn for his kind remarks concerning our high-speed photography used in this study. We agree with him that the dynamic properties of the materials should certainly be used, rather than the static properties, to correlate damage resistance, provided these are available. However, as far as we know they are not at present available for the materials here tested.

[1] Principal research scientist and head, Materials Sciences Division, HYDRONAUTICS, Incorporated, Laurel, Md. 20810.

*G. F. Schmitt, Jr.,*[1] *W. G. Reinecke,*[2] *and G. D. Waldman*[2]

# Influence of Velocity, Impingement Angle, Heating, and Aerodynamic Shock Layers on Erosion of Materials at Velocities of 5500 ft/s (1700 m/s)

**REFERENCE:** Schmitt, G. F., Jr., Reinecke, W. G., and Waldman, G. D., "Influence of Velocity, Impingement Angle, Heating, and Aerodynamic Shock Layers on Erosion of Materials at Velocities of (5500 ft/s (1700 m/s)," *Erosion, Wear, and Interfaces with Corrosion, ASTM STP 567*, American Society for Testing and Materials, 1974, pp. 219–238.

**ABSTRACT:** The dependence of materials erosion in rain at supersonic velocities up to 1700 m/s (5500 ft/s) has been determined as a function of velocity, impingement angle, and aerodynamic heating. The erosion rate of materials has been found to vary with the 4.5 to 6.5 power angle. Coupled heating and erosion effects are highly significant for polymeric composites. The effects of shock layer breakup, acceleration, deflection, and deformation of the droplets have been quantitatively assessed, and damage gradients in materials are shown to be a function of primarily droplet distortion and breakup resulting from drop traversal of the shock layer around the vehicle.

**KEY WORDS:** rain erosion, velocity, cavitation erosion, impingement angle, heating, shock layer breakup, distortion, deflection, deceleration, mean depth of penetration, erosion

## Erosion Rate-Velocity Impingement Angle Dependence

Rain erosion of ceramic, graphite, and plastic composite materials at supersonic speeds of 450–1700 m/s has been extensively investigated by the Air Force Materials Laboratory over the past five years utilizing the

[1] Materials engineer, Air Force Materials Laboratory, Wright-Patterson AFB, Ohio 45433.

[2] Senior consulting scientists, Avco Corporation, Wilmington, Mass. 01887.

Holloman AFB rocket sled track[*1*].[3] Shock layer effects on droplets have likewise been investigated by Avco Corporation[*2*].

For runs up to 1300 m/s (4500 ft/s) a wedge-shaped holder which accommodated forty-eight 1.25 × 1.25-in. material specimens (16 each) at 13.5-, 30-, 45-, and 60-deg angles (measured from surface) was used. For 1700 m/s velocities, two pyramidal shapes with half angles of 13.5 deg (holding 32 specimens) and 30 deg (holding 16 specimens) were developed. These fixtures are mounted on the front of a rocket sled and, by proper choice of rocket motors, various velocity profiles were achieved.

In these experiments weight loss is determined on the specimens after exposure. In the analysis, a mean depth of penetration rate (MPDR) in centimeters per second has been defined in which edge effects or uneven erosion on the specimen have been eliminated by assuming uniform erosion across the entire specimen area. This MDPR is calculated from the weight loss, density, known surface area, and time of exposure as obtained from microsecond readings on the Holloman instrumentation.

A relationship was developed relating *MDPR* as determined from the weight loss per unit area to the impact and the impingement angle $\theta$, as follows:

$$\text{MDPR} = KV^{a} \sin^2\theta$$

where

MDPR = mean depth of penetration rate,
$V$ = velocity,
$K, a$ = constants for a particular material, and
$\theta$ = impingement angle.

The foregoing expression with the $\sin^2\theta$ term differs from a previously developed relationship[*1*], namely:

$$\text{MDPR} \sin\theta = K\,(V \sin\theta)^{a}$$

which correlated experimental data up through 1300 m/s. The $V \sin\theta$ term or normal component of the velocity governs the impact pressure up through 1300 m/s at impingement angles of 30 deg or greater. However, at 1700 m/s it was found that the tangential component of the velocity which influences the flow of an impinging water drop along the surface in a low-angle (less than 30 deg), high-velocity impact is as damaging as the impact pressure associated with the normal component of the velocity. This effect had not been isolated in any previous erosion investigations and

[3] The italic numbers in brackets refer to the list of references appended to this paper.

is highly significant for shallow-angle cone shapes at high supersonic velocities.

The erosion rate (surface recession due to particle impingement) of composite materials varies with the 4.5 to 6.5 power of the velocity and the sine squared of the impact angle at speeds from 450 to 1700 m/s. This dependence is determined by computer analysis of weight loss data as a function of velocity and impingement angle. Computer-determined plots of $MDPR/\sin^2\theta$ versus velocity are shown in Figs. 1 and 2. Values of velocity exponents, $a$, the value $K$ in the equation, and the correlation coefficient, $r$, describing degree of fit for various materials and the number of data points are given in Table 1.

The tangential component of the velocity, that is, the component associated with flow of the droplet along the surface after impact, is significant at velocities of 1700 m/s or above. The depth-of-penetration rate obtained for low-angle (13.5 deg) exposures at 1700 m/s is a full order of magnitude higher than that predicted from the normal velocity component and

TABLE 1—*Rain erosion equation constants:* $MDPR = KV^a \sin^2 \theta$.

| Class | Material | $a$ | $K$ | $r$ | No. of Data Points |
|---|---|---|---|---|---|
| | | BULK CERAMICS | | | |
| A-8 | 7941 Fused silica | 4.480 | $9.22 \times 10^{-17}$ | 0.797 | 36 |
| A-13 | Isotropic pyrolytic boron nitride | 4.643 | $6.05 \times 10^{-17}$ | 0.902 | 28 |
| A-16 | Silicon carbide (0.020 in.) on bulk graphite | 5.243 | $1.11 \times 10^{-19}$ | 0.910 | 29 |
| | | PLASTIC LAMINATES AND COMPOSITES | | | |
| C-2 | Furane B265 epoxy-glass | 6.526 | $1.32 \times 10^{-24}$ | 0.981 | 32 |
| C-3 | Epon 828 epoxy-glass | 7.574 | $3.49 \times 10^{-28}$ | 0.970 | 41 |
| C-10 | Polyphenylene oxide (531-801)-glass | 5.756 | $8.90 \times 10^{-22}$ | 0.958 | 35 |
| C-13 | Low-void polyimide-glass | 6.247 | $7.81 \times 10^{-24}$ | 0.956 | 25 |
| M-2 | Perpendicular glass-epoxy composite | 4.795 | $1.28 \times 10^{-18}$ | 0.863 | 19 |
| I-1 | Polyphenylene oxide 531-801 | 8.721 | $9.80 \times 10^{-33}$ | 0.983 | 29 |
| I-2 | Plexiglas (Type II-UVA) | 6.402 | $5.54 \times 10^{-24}$ | 0.959 | 28 |
| I-3 | Trifluoroethylene (TFE) resin | 4.642 | $1.13 \times 10^{-17}$ | 0.978 | 55 |

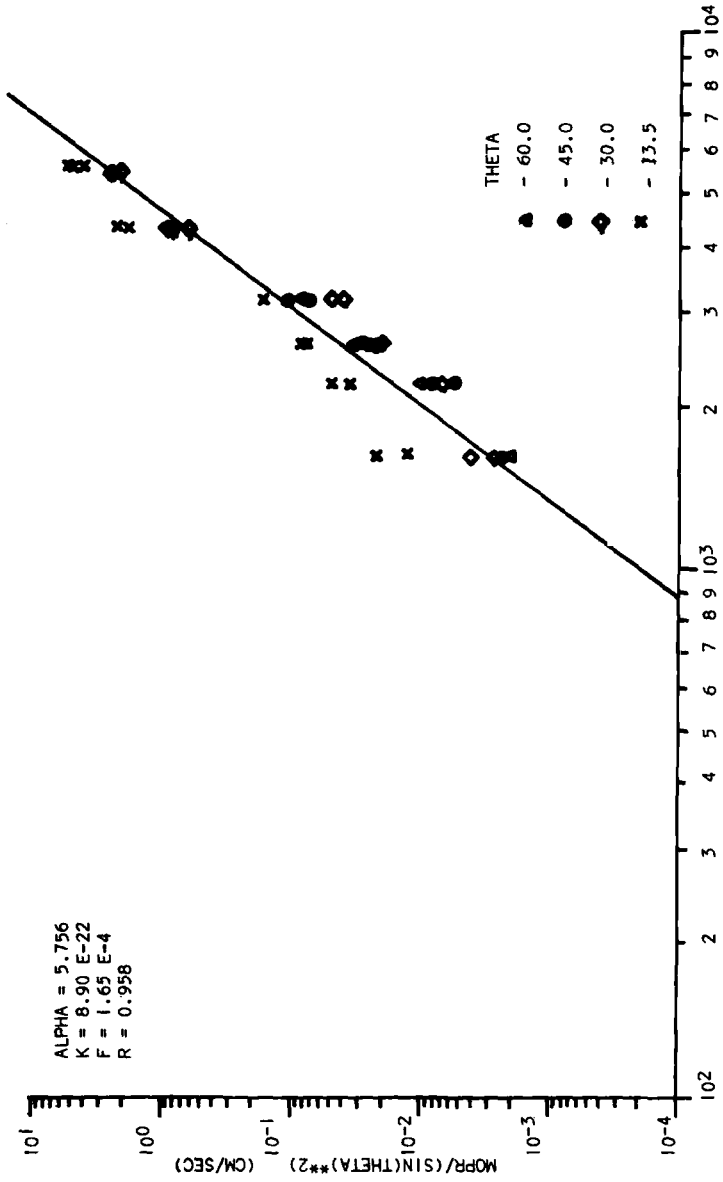


FIG. 1—*C10 PPO glass laminate.*

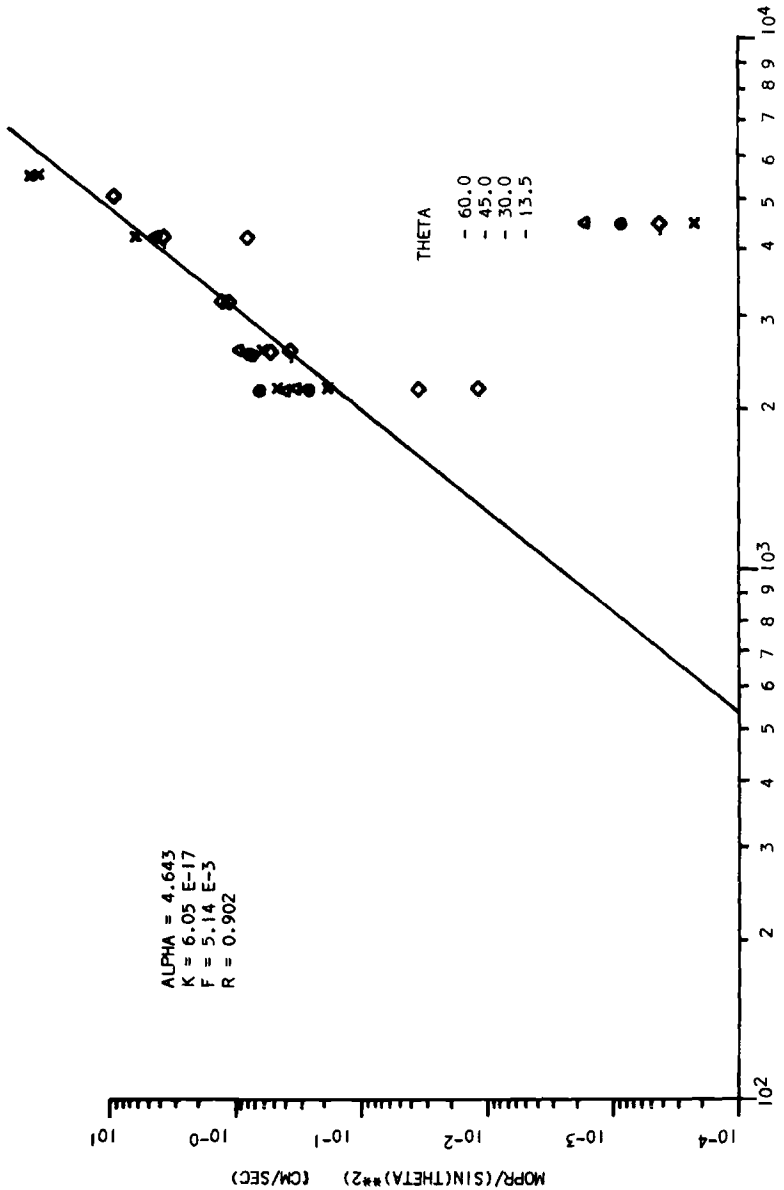


FIG. 2—*A13 boron nitride.*

erosion rate-velocity dependence based upon supersonic speed relationships. This increased penetration is partially due to combined-particle erosion effects but its magnitude is much greater than would be predicted from higher-angle data.

This finding is significant because no studies have been conducted at a combination of this high a velocity and this low an impingement angle before, such that the tangential velocity component effect could have been determined.

The traditional technique for mitigating the damaging effects of erosion at high velocity has been to protect the 90-deg angle area with a metal or ceramic tip and reduce the impingement angle to as low a value as possible consistent with transmission, drag, and other requirements. The results of this high-speed low-angle erosion investigation indicate that considerable damage can still occur in a supersonic rain exposure even at low angles.

### Influence of Materials Construction Variables

The failure of bulk brittle materials, including dense ceramics such as alumina, beryllia and Pyroceram and bulk graphites, is the result of impact fracture. These materials do not erode as such. The erosion rate-velocity relationships for some isotropic ceramics could not be meaningfully developed because breakage of these materials under droplet impact was so severe that true erosion could not be measured. Only fused silica and isotropic pyrolytic boron nitride eroded rather than fractured, and the erosion rate of these two ceramics varied with the 4.5 power of the velocity.

The coupled heating from the high-speed sled run and the erosion from rain droplets produces a high degree of charring and material removal of reinforced plastic composite materials, thus graphically demonstrating their limitations in this environment.

Reinforced laminates and composites cannot be used in an unprotected form because of their poor erosion resistance. The erosion of uncoated laminates was remarkably uniform and consistent. Heating effects at Mach 5 exert a considerable influence over the erosion behavior of polymeric-based materials as a function of their thermal stability. The low-void polyimide glass laminate retains its strength better at elevated temperature and hence was less eroded than other laminates at 1700 m/s, where thermal effects seriously degraded the epoxy-glass and polyphenylene oxide-glass laminates. However, all composites evaluated exhibited relatively poor erosion resistance and must be coated for erosion protection. The use of a three-dimensional fiber construction did not yield improved rain erosion resistance in a multiple-particle environment compared with

more conventional two-dimensional layups. A composite construction which incorporates the one-dimensional orientation of fibers in the direction of the impinging drop exhibits potential for supersonic erosion resistance.

## Shock Layer Effects on Droplets and Their Resulting Influence on Materials Erosion

When a vehicle passes through a rain storm at high speed, the vehicle surface may experience erosion from drop impingement. However, the flow field around the vehicle provides some protection to the surface—(1) by shattering the drops into smaller droplets that conform to streamlines and do not reach the vehicle surface; (2) by accelerating the drops away from the vehicle and thus reducing their impact speed and impact angle[*2*]; and (3) by deforming the drops and thus reducing the stresses at impact[*3*]. We will discuss these effects as they apply to data obtained at the Holloman Air Force Base sled facility.

Two right-octagonal cone models (of 30- and 13½-deg inscribed circular cone half angles) as described earlier were used in the experiments. The test specimens were located on the test cone faces flush with the surfaces at slant locations 5.8 and 8.1 in. from the tip of the 30-deg model, and 12.2, 14.9, 17.5 and 20.2 in. from the tip of the 13½-deg model. Measurements of the mass removed from the test specimens (homogeneous and reinforced plastics), resulting from passage through the rain field nominally at Mach 5, are shown in Figs. 3 and 4, in which the average (over all materials) of the mass eroded at each station has been divided by the mass eroded from the first station and plotted versus distance aft of the first station. Each point shown represents the mean of from 7 to 13 measurements and is bracketed by the rms variation. Although there is substantial scatter, a decrease in damage with distance aft is clearly exhibited. Because of the way the data were averaged and normalized, this gradient in damage cannot result from variations in rainfield concentration during a test or from test to test. Thus shock layer shielding effects appear to be the most likely cause.

## Drop Breakup

The reduction in mass impinging the test cone surface resulting from the shock layer effects can be calculated from the results of Ref *2*. In order to make this calculation the rainfield characteristics must be known, as well as the test speed and geometry. The Holloman rainfield has been calibrated in detail as reported in Ref *5*. Figure 3 is reproduced from that report and

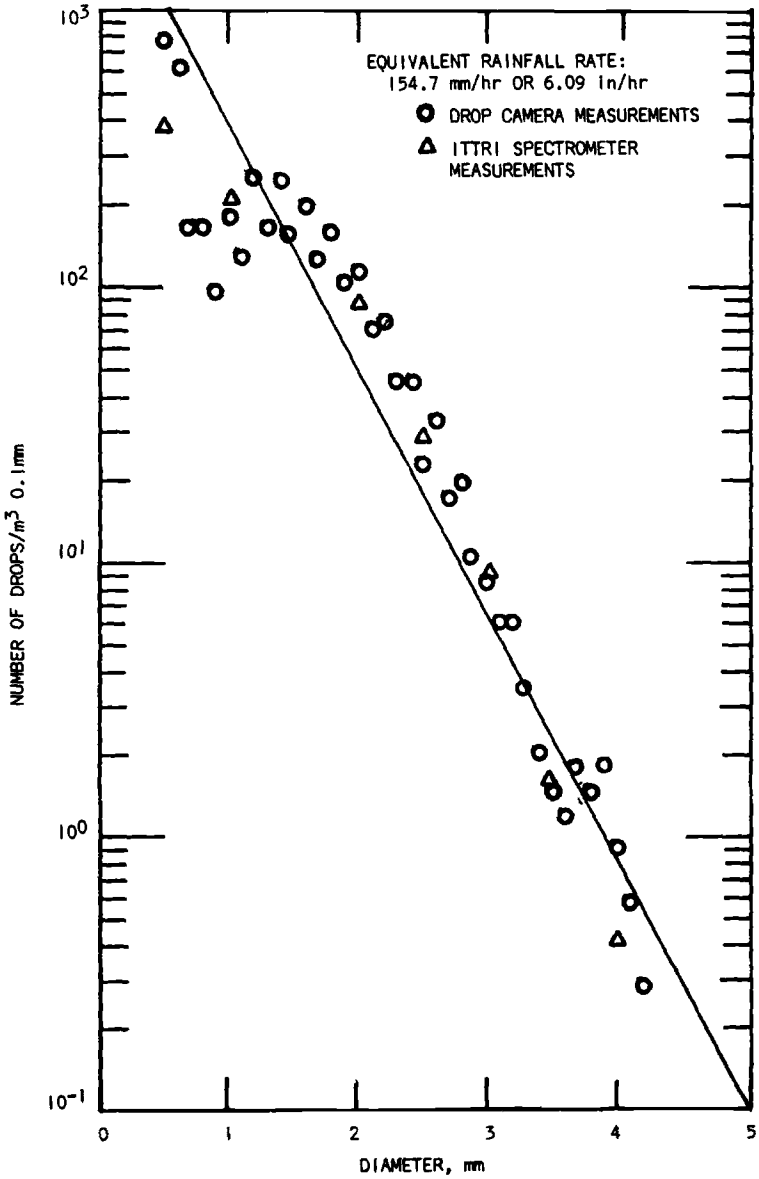


FIG. 3—*Drop spectra for Sept. run 1 as determined by the drop camera and by the IITRI spectrometer.*

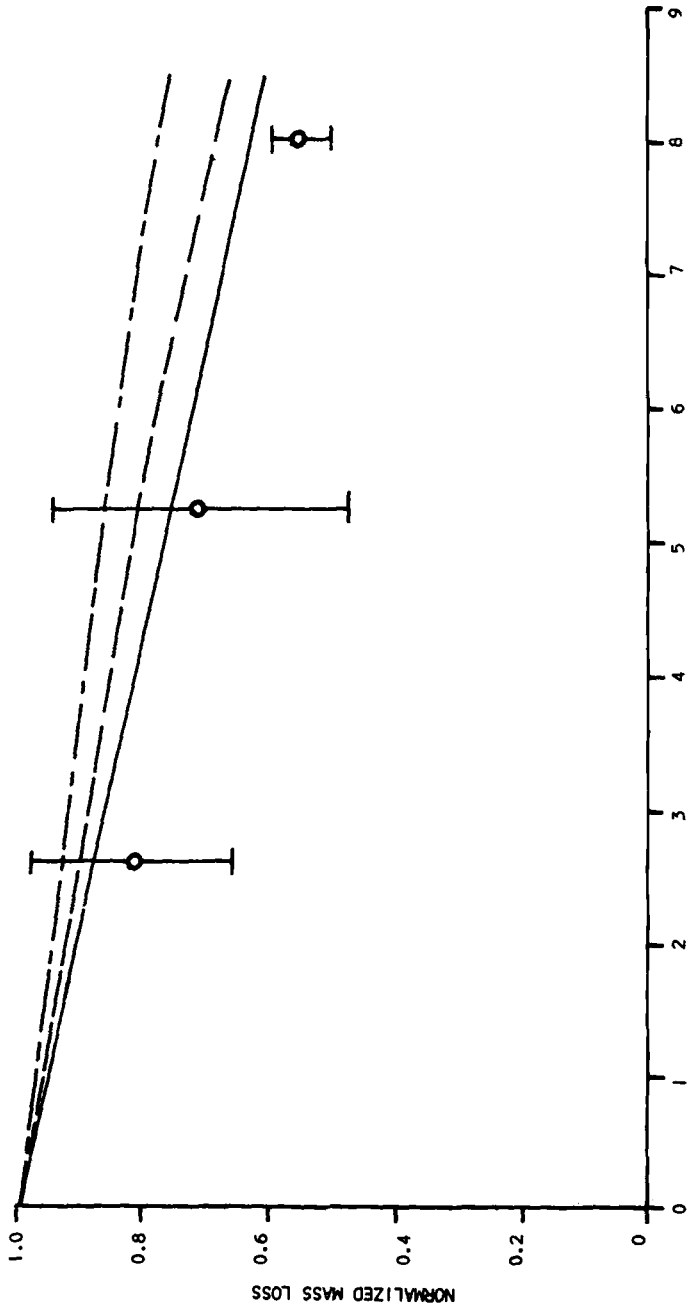


FIG. 4—*13½-deg cone results.*

shows the drop size distribution. The straight line in Fig. 3 is the analytical representation of the drop size used in the calculation discussed in the following (In the terminology of Ref *4*, $D_R = 0.489$ mm).

In Ref *4* it is shown that the Mach number corresponding to the component of velocity normal to the sled bow shock determines (along with ambient density) the time required for drops to be shattered by the air in the shock layer. This Mach number is 1.6 for the 13½-deg cone and 2.9 for the 30-deg cone. Thus based on the experiments and discussion in Refs *2* and *6*, dimensionless times to breakup of 2.0 and 3.5 were used in the shattering calculations for the 13½- and 30-deg cones respectively.

Table 2 is a summary of the drop breakup calculations pertaining to the 30- and 13½-deg, Mach 5 sled tests. The rain mass impinging the first station divided by the mass that would reach that station in the absence of the shock layer is 0.820 for the 13½-deg cone and 0.933 for the 30-deg cone, indicating a nonnegligible shock layer drop shattering effect on the absolute erosion measurement even at the most forward stations. Since a reduction in mass impinging would lead to a proportional reduction in mass eroded, the data in the last column of Table 2 are plotted as the interrupted lines in Figs. 4 and 5. Note that while the drop shattering should cause a measurable reduction in the experimentally determined mass removal (up to 37 percent at the 13½-deg cone after station), the drop breakup effect is too small to account for the actual decrease in erosion with distance aft.

## Drop Deceleration and Deflection

The calculation discussed in the foregoing section also yields the trajectories of the water drops in the conical flow fields. In particular, the reduction in the velocity component normal to the surface is calculated along with the reduction in impact angle. In the absence of the shock layer, the normal velocity at impact is simply $u \sin\theta$ (where $u$ is the test speed and $\theta$ the cone half angle) and the impact angle is $\theta$. In Table 3 the effects of the shock layer in decelerating and deflecting drops of 1.5 mm diameter are given. This diameter represents the peak of the rain mass distribution function. At the first station the impact angles for the 30- and 13½-deg cones were determined to be 29.0 and 12.8 deg, respectively, indicating that drop deceleration and deflection are not significant effects in these tests. Furthermore, we note from Table 3 that even if the erosion damage varies as the fifth power of the normal velocity component, the drop deflection would only result in a 10 percent reduction in damage at the last station relative to the first station. Thus drop deflection effects cannot account for the experimental results.

TABLE 2—*Reduction in impinging rain mass due to drop stripping in shock layer:* $M = 5$, $D_R = 0.489$ *mm*, $h = 0$ *(sea level).*

| Cone Half Angle, deg | Dimensionless Time to Drop Breakup | Slant Distance of Specimen from Tip, in. | Mass of Rain Impinging Divided by Value in Absence of Shock Layer | Mass of Rain Impinging Divided by Mass Impinging First Sample Location |
|---|---|---|---|---|
| 13½ | 2 | 12.2 | 0.820 | 1.000 |
| | | 14.9 | 0.759 | 0.925 |
| | | 17.5 | 0.695 | 0.848 |
| | | 20.2 | 0.631 | 0.769 |
| 30 | 3.5 | 5.8 | 0.933 | 1.000 |
| | | 8.1 | 0.877 | 0.940 |

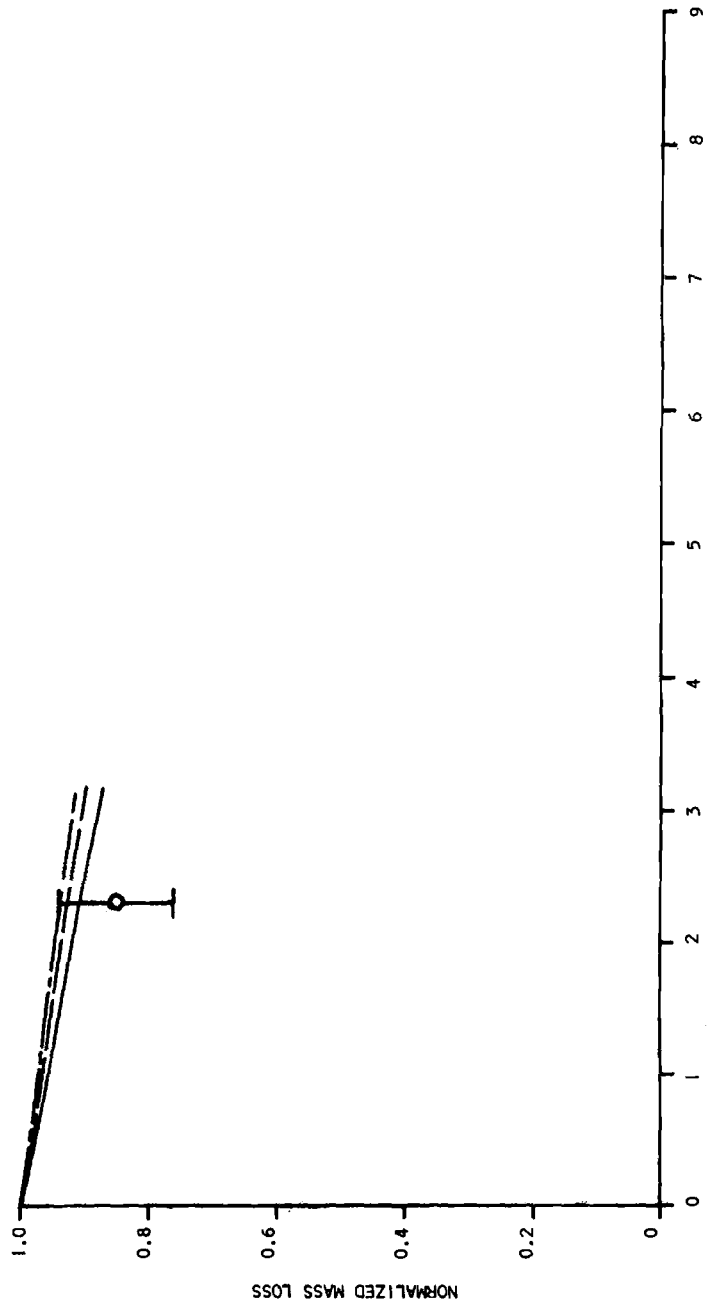


FIG. 5—*30-deg cone results.*

TABLE 3—*Deflection and deceleration of rain due to shock layer:* $M = 5$, $D_R = 0.489$ *mm*, $h = 0$ *(sea level)*, $D_0 = 1.5$ *mm*.

| Cone Half Angle, deg | Distance of Specimen from Tip, in. | Normal Impact Velocity Component Divided by Value in Absence of Shock Layer | Normal Impact Velocity Component Divided by Value at First Station | Impact Angle, deg | Impact Angle Divided by Value at First Station |
|---|---|---|---|---|---|
| 13½ | 12.2 | 0.953 | 1.000 | 12.8 | 1.000 |
| | 14.9 | 0.947 | 0.993 | 12.7 | 0.992 |
| | 17.5 | 0.941 | 0.987 | 12.6 | 0.988 |
| | 20.2 | 0.934 | 0.980 | 12.6 | 0.981 |
| 30 | 5.8 | 0.961 | 1.000 | 29.0 | 1.000 |
| | 8.1 | 0.941 | 0.980 | 28.5 | 0.984 |

### Water Layer

Is it possible that the encountered rain water forms a layer on the cone surface and provides protection for the test specimens? We can estimate this effect by calculating the thickness of the water layer on the model. Assuming all the encountered water stays in a circumferentially uniform layer on the model surface, that the mean speed of this layer is half the external air speed (that is, half the drops' initial relative tangential speed), and that the aerodynamic shock layer is fairly thin, it is easy to show that the water layer thickness $t$ at a distance $R$ from the tip is given by

$$\frac{t}{R} = \frac{w}{d} \tan\theta$$

where $w$ is the rainfield liquid water concentration, $d$ the water density, and $\theta$ the cone half angle. Using $w = 7.8 \times 10^{-6}$ g/cc, the water layer thicknesses were calculated to be 0.58 to 0.96 $\mu$m. Since the characteristic rain drop diameter in the tests is about 1.5 $\mu$m (1500 $\mu$m), these values of $t$ make it clear that water layer buildup cannot have any appreciable effect on the test results. Even if all the eroded material were also confined to this layer, it would be less than doubled in thickness (since the measured mass loss ratios were of order one and only a small fraction of the cone surface consisted of eroding specimens) and this conclusion would be unaltered.

### Drop Deformation

Experiments reported in Ref *4* indicated that an aerodynamic shock layer can provide significant rain erosion protection at transonic speeds (up to 1260 ft/s) even when the drops are neither significantly reduced in mass nor significantly decelerated. The reduction in erosion damage in this case appears to be the result of the deformation of the initially spherical drop into an oblate spheroid by the relative air flow. This deformation results in the energy of the drop being dissipated over a larger area of the impacted material through either lower average stress levels or shorter loading time.

Since the impact velocity component normal to the surface in the subject 13½-deg-cone, Mach 5 tests was about 1300 ft/s, it is of interest to determine if the drop distortion effects reported in Ref *4* can result in the decrease in erosion damage measured. We will also extrapolate these distortion results and apply them to the 30-deg cone tests, where the normal component is about 2800 ft/s. The calculations in this case, however, are of very uncertain applicability and accuracy.

The relevant data in Ref *4* consist of only two classes of results: those in which the test surface was damaged, and those in which it was not. Since shock layer shielding is least effective against large drops, the damage threshold of Ref *4* must be associated with the largest drop encountered by the vehicles tested. This is explicitly recognized in Ref *4* and the "distortion parameter" therein computed is based on the largest drop existing in the rain field as determined by oil suspension sampling. At test speeds of 1260 ft/s, the damage threshold "distortion parameter" was between 1 and 1.5, corresponding to dimensionless times of between 0.82 and 1.00. Since recent rain field calibration work at Holloman AFB[*5*] indicates that rain drop samples obtained from static samplers significantly underestimate the actual population of large drops present as determined by photographs of the falling drop field, we feel that the lower value of dimensionless time in Ref *2* is probably more nearly correct than the upper value (and still may be too high). At this time ($T = 0.82$) the drop has flattened such that its diameter in the plane normal to the relative wind or parallel to the target surface is 2.4 times the original diameter[*2*], resulting in a nearly sixfold increase in projected area. Extrapolating the results of Ref *4* to 2800 ft/s yields a lower bound on the threshold "distortion parameter" of 2.2 and a corresponding dimensionless time of 1.21.

To apply these results to the cone tests, we simply exclude from the calculation of impinging mass those drops whose dimensionless time to impact is greater than 0.82 on the 13½-deg cone and 1.21 on the 30-deg cone, that is, those smaller drops which flatten sufficiently to cause no damage upon impact. The results in the data shown in Table 4. The result of this phenomenon is that the mass effectively impinging the first station on the 13½-deg cone is 0.87 of the mass that would impinge in the absence of the shock layer. Since the mass eroded at each station is proportional to the effective impinging mass, the relative damage at each after station can be equated to the effective impinging rain mass divided by the effective mass reaching the first station. This calculation yields the dashed lines shown in Figs. 4 and 5. As noted, the distortion effects given in Table 4 and Fig. 5 for the 30-deg cone should be viewed with skepticism since they represent more than a twofold extrapolation in normal impact speed over the test reported in Ref *4*. Nevertheless, it appears that shock layer-induced drop distortion effects are a partial cause of the measured reduction in damage with distance aft. Note at this point that, first, the tests in Ref *4* were for normal impact on glass, not oblique impact on plastic (which almost certainly erodes by a different mechanism); and second, the flow yield experienced by the drops in the tests of Ref *4* was

TABLE 4—*Reduction in effective impinging mass due to drop distortion in shock layer:* $M = 5$, $D_R = 0.489$ *mm*, $h = 0$ *(sea level).*

| Cone Half Angle, deg | Dimensionless Time to Threshold Distortion | Distance of Specimen from Tip, in. | Effective Mass of Rain Impinging Divided by Value in Absence of Shock Layer | Effective Impinging Mass Divided by Value at First Station |
|---|---|---|---|---|
| 13½ | 0.82 | 12.2 | 0.870 | 1.000 |
| | | 14.9 | 0.789 | 0.907 |
| | | 17.5 | 0.699 | 0.803 |
| | | 20.2 | 0.603 | 0.693 |
| 30 | 1.21 | 5.8 | 0.957 | 1.000 |
| | | 8.1 | 0.890 | 0.930 |

nonsteady, and a superpositional computational method was used to determine the appropriate values of "distortion parameter" and dimensionless time. Nevertheless, since the other possible modes of shock layer protection alone cannot account for the measured damage reduction, while (as will be seen in the following) a combination of drop distortion and drop breakup effects can, it appears that the distortion phenomenon is, indeed, a significant contributor to the gradient in measured damage.

### Combined Deformation and Breakup

The preceding discussion makes clear that both drop stripping and drop distortion induced by the aerodynamic shock layer contribute significantly to the measured damage gradient. Using the methods of Ref *4*, we have calculated the combined effects of stripping and distortion by excluding from the calculated mass impinging all drops whose dimensionless time to breakup is greater than 0.82 and 1.21 on the 13½- and 30-deg cones, respectively, and subjecting the remaining drops to mass reduction due to stripping. As before, dimensionless times to breakup of 2 and 3.5 were used for the 13½- and 30-deg cones, respectively. The results are shown in Table 5 and as the solid lines in Figs. 4 and 5. The mass impinging the first location divided by the mass that would impinge in the absence of shock layer is 0.78 and 0.92 for the 13½- and 30-deg cones, respectively. Figure 4 indicates that the calculated combined effects of the shock layer in distorting and breaking the drops result in an accurate prediction of the measured damage gradient in the 13½-deg tests. However, Fig. 5 suggests that the calculated damage reduction is too small to explain the experimental gradient on the 30-deg cone. Since the calculation of the drop breakup is rather well understood and based on directly applicable experiments, it appears that the drop distortion effects on the Mach 5, 30-deg test data are more important than we have postulated. To illustrate this point, we have repeated the 30-deg calculations using a threshold distortion time of 0.82. The results are shown in Fig. 5, where, as before, the datum is compared with calculated drop breakup effects only (interrupted line), drop distortion effects only (dashed line), and a combination of both (solid line). The agreement of the combined calculation with the experimental gradient is good. We do not imply by presenting Fig. 6 that we have quantitatively explained the 30-deg data; almost nothing is known about drop distortion effects in this speed regime. Rather we wish to make the point that the distortion-induced phenomenon is causing damage reduction in addition to drop breakup effects at test speeds as high as Mach 5.

In summary, a significant damage gradient exists in the subject experiments. This gradient cannot be accounted for solely by the effects of the

TABLE 5—*Reduction in effective impinging mass due to combined drop breakup and distortion in shock layer:* M = 5, $D_R$ = 0.489 *mm*, h = 0 *(sea level).*

| Cone Half Angle, deg | Dimensionless Time to Drop Breakup | Dimensionless Time to Threshold Distortion | Slant Distance of Specimen from Tip, in. | Mass of Rain Impinging Divided by Value in Absence of Shock Layer | Mass of Rain Impinging Divided by Value at First Station |
|---|---|---|---|---|---|
| 13½ | 2 | 0.82 | 12.2 | 0.777 | 1.000 |
| | | | 14.9 | 0.681 | 0.876 |
| | | | 17.5 | 0.585 | 0.753 |
| | | | 20.2 | 0.488 | O.628 |
| 30 | 3.5 | 1.21 | 5.8 | 0.916 | 1.000 |
| | | | 8.1 | 0.833 | 0.910 |

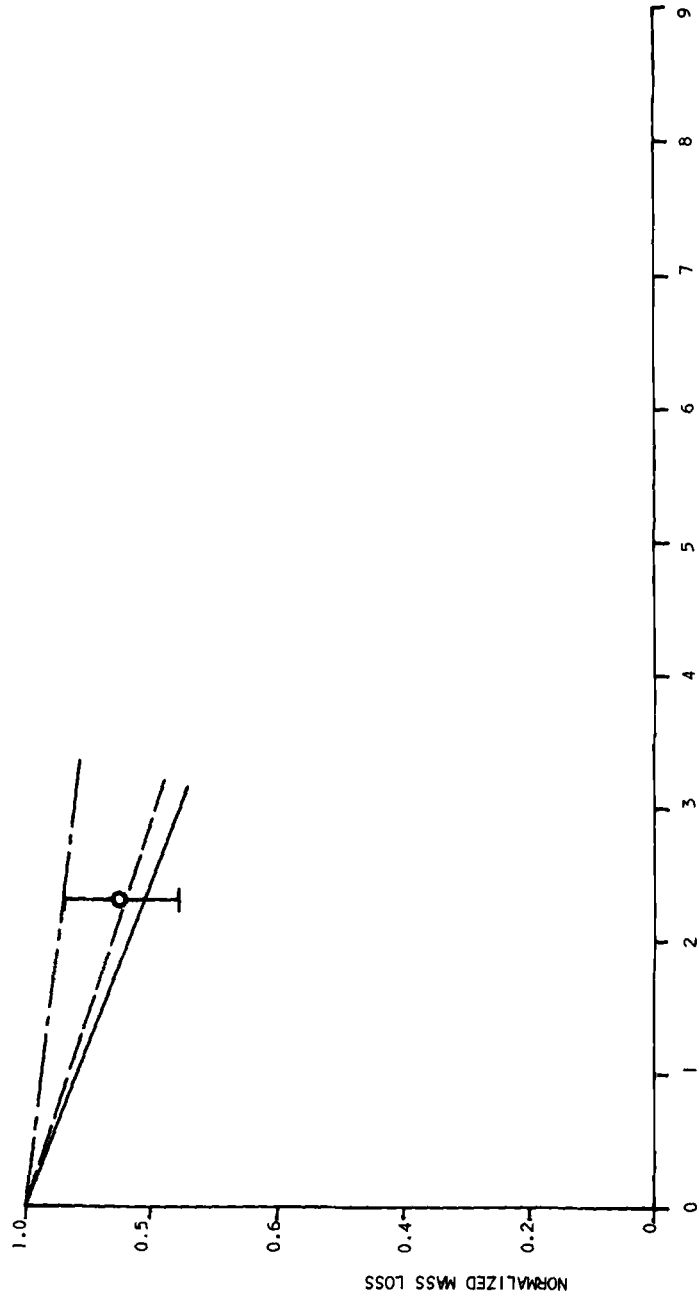


FIG. 6—*Improved 30-deg cone results.*

shock layer in shattering and deflecting the raindrops; drop distortion effects are significant even at Mach 5. The gradient apparently results from the combined effects of raindrop distortion and breakup resulting from drop traversal of the shock layer around the vehicle. Moreover, distortion effects are more important than shattering, and both effects are more important than deflection. Using existing theory and experimental data, the gradient, as well as the absolute reduction, in damage can be accurately calculated for the 13½-deg cone tests, and can be approximately calculated for the 30-deg cone tests. These shock layer effects reduce the damage experienced by the test samples by about 10 to 50 percent, depending on the sample location and cone half angle.

## References

[1] Schmitt, G. F., Jr., in *Characterization and Determination of Erosion Resistance, ASTM STP 474*, American Society for Testing and Materials, 1970, pp. 323–352.

[2] Reinecke, W. G. and Waldman, G. D., *Proceedings* of the Third International Conference on Rain Erosion and Associated Phenomena, Royal Aircraft Establishment, Farnborough, England, Vol. 2, Aug. 1970, pp. 629–658.

[3] Waldman, G. and Reinecke, W., *Journal*, American Institute of Aeronautics and Astronautics, Vol. 9, No. 6, June 1971.

[4] Hill, J. and Smith, M., *Proceedings* of the Third International Conference on Rain Erosion and Associated Phenomena, Royal Aircraft Establishment, Farnborough, England, Vol. 2, Aug. 1970, pp. 935–958.

[5] Mueller, E. and Sims, A., "Measurement of the Simulated Rainfall at the Holloman Track Test Facility," AFCRL-70-0282, University of Illinois, Urbana, Ill., April 1970.

[6] Engel, O., *Journal of Research*, National Bureau of Standards, Vol. 60, No. 3, March 1958.

*A. F. Conn* [1] *and S. L. Rudy* [1]

# Effects of Fatigue and Dynamic Recovery on Rain Erosion*

REFERENCE: Conn, A. F. and Rudy, S. L., "Effects of Fatigue and Dynamic Recovery on Rain Erosion," *Erosion, Wear, and Interfaces with Corrosion, ASTM STP 567*, American Society for Testing and Materials, 1974, pp. 239–269.

ABSTRACT: The latest results from a study of the dynamic behavior of rain erosion-resistant coating and substrate materials are described. The correlations between rocket sled erosion data and fracture stresses determined from single-impact tests with a split Hopkinson pressure bar facility have been extended to include polyurethane. The results of tests within a small-scale erosion facility, and analyses of large whirling-arm studies, have shown that a fatigue type of behavior, already found to be applicable for an acrylic plastic, may also be used to describe the rain erosion resistance of elastomeric coatings such as polyurethane, and the glass fiber-reinforced epoxy composite substrates which are frequently utilized for radome construction. The importance of the "dynamic recovery rate" or relaxation time, and stress wave interactions, in understanding the rain erosion phenomenon is described in this paper. The applicability of the elastic-plastic, uniaxial stress wave theory for making rain erosion predictions is also discussed.

KEY WORDS: coatings, composites, rain erosion, dynamic properties, fatigue, recovery rate, stress waves, erosion

This paper describes the most recent phase of an investigation of fundamental aspects of the rain erosion phenomenon. The damage to components of high-speed aircraft and missiles has motivated extensive research, both

* The contents of this paper are based on research projects at HYDRONAUTICS, Incorporated, Laurel, Md., sponsored by the Materials and Processes Branch, Naval Air Systems Command, Washington, D. C., under Contract Nos. N00019-70-C-0276 and N00019-71-C-0297, with S. Kaplan as technical director.

[1] Principal research scientist and head, and associate research scientist, respectively, Materials Sciences Division, HYDRONAUTICS, Incorporated, Laurel, Md. 20810.

basic and applied, toward understanding rain impact erosion and developing improved methods for minimizing its effects. In particular, much attention has been focused on the protection of nonmetallic components such as reinforced plastic radomes, which are particularly susceptible to erosion from raindrop impacts. This led to the creation of various elastomeric coating systems with dynamic, that is, impact stress-strain, relations which were vastly different from those measured by traditional static techniques.

This program at HYDRONAUTICS, Incorporated began with a study of the dynamic properties of various candidate coating and substrate materials which have been developed for improved resistance to the erosion caused by raindrop impact[*1*,*2*].[2] Using the split Hopkinson pressure bar (SHPB) facility, the properties of a wide variety of elastomeric and rigid polymers were determined, including their dynamic fracture strength[*3*,*4*]. It was found that this dynamic fracture strength, as measured in our laboratory, could be correlated with rain erosion observations in large whirling-arm and rocket sled test facilities[*4*,*5*]. Study of an acrylic plastic (polymethylmethacrylate) has shown[*4*,*5*], that a fatigue-like behavior may be successfully used to characterize rain erosion response.

In this paper we describe an extension of our earlier investigation, with emphasis on the rain erosion behavior of polyurethane coatings and glass fiber-reinforced epoxy substrates[*6*]. This particular coating-substrate system has received considerable attention in the literature (see Refs 7 to *14*). Measurements made within our small multiple-impact erosion facility have been correlated with the results from large whirling-arm tests, demonstrating that fatigue-like behavior is also the unifying factor in these tests. The "dynamic recovery rates" of these materials were measured and shown to be another important factor in rain erosion[*6*].

The SHPB test involves a uniaxial stress measurement within the elastic-plastic deformation range. Although these tests were expected to simulate dynamic rates of loading created by the raindrop impact, they were not intended to completely simulate either the geometrical or temporal aspects of this impact. Hence, we had originally planned to use the SHPB test results only to provide a relative assessment of the impact resistance of various materials, and did not expect the successful quantitative predictions of rain erosion behavior which have been obtained. These predictions have been the subject of considerable discussion[*5*,*6*,*8*,*13*,*14*], mainly centering on two conflicting points of view: (*a*) the uniaxial stress, elastic-plastic theory utilized in our studies[*1–6*]; and (*b*) the uniaxial strain,

[2] The italic numbers in brackets refer to the list of references appended to this paper.

shock-wave theory proposed by Morris[*8,13,14*]. A brief discussion is given of the observations that can be correctly explained by the uniaxial stress, elastic-plastic theory, particularly in predicting the initiation of rain impact erosion. Further details are contained in Ref *6*.

## Dynamic Property Measurements

### *Split Hopkinson Pressure Bar Facility*

This dynamic property measurement facility has been described in detail in earlier reports[*1–4*]. The facility as shown in Fig. 1 consists of an air gun for accelerating an impact projectile, two long elastic bars with strain gages affixed, and electronic equipment to record the projectile velocity and the strain waves created in the elastic pressure bars. A furnace allows testing at elevated temperatures. The test specimen, which is sandwiched between the two pressure bars, receives an extremely high rate of deformation, at strain rates on the order of $10^3 s^{-1}$, which is caused by the transmission of a strain-wave pulse through the first pressure bar after impact by the projectile. In addition to the strain-time records in each pressure bar, which are used to derive the dynamic stress-strain behavior of the test specimen, high-speed photographic records of the dynamic deformations of the specimen have been made[*4–6*].

### *Test Results*

The dynamic properties for a number of materials have been reported earlier[*1–5*]. The two materials that are the main subject of this paper are an epoxy resin which has been reinforced with glass fiber fabric, to be hereafter referred to as "epoxy laminate"; and a polyurethane material specifically developed for its ability to resist rain erosion, to be hereafter referred to as "AFML polyurethane." The dynamic stress-strain curves for these two materials are shown in Fig. 2. Also shown are multilinear approximations for each of these stress-strain curves. These linearized approximations are used in the impact stress calculations and wave interaction analyses which were performed. Also shown in Fig. 2 are the corresponding relationships between dynamic stress and particle velocity as derived from the stress-strain measurements and the dynamic impedances required for these calculations. The dynamic impedance $Z = (\rho d\sigma/d\epsilon)^{1/2}$, where $\rho$ is the mass density, $\sigma$ the dynamic stress, and $\epsilon$ the dynamic strain.

## Correlation of Impact Stress Predictions with Rocket Sled Erosion Data

A valuable collection of rocket sled data has been reported by Schmitt and Krab ll[*9*]. Among the extensive list of materials tested is a series on

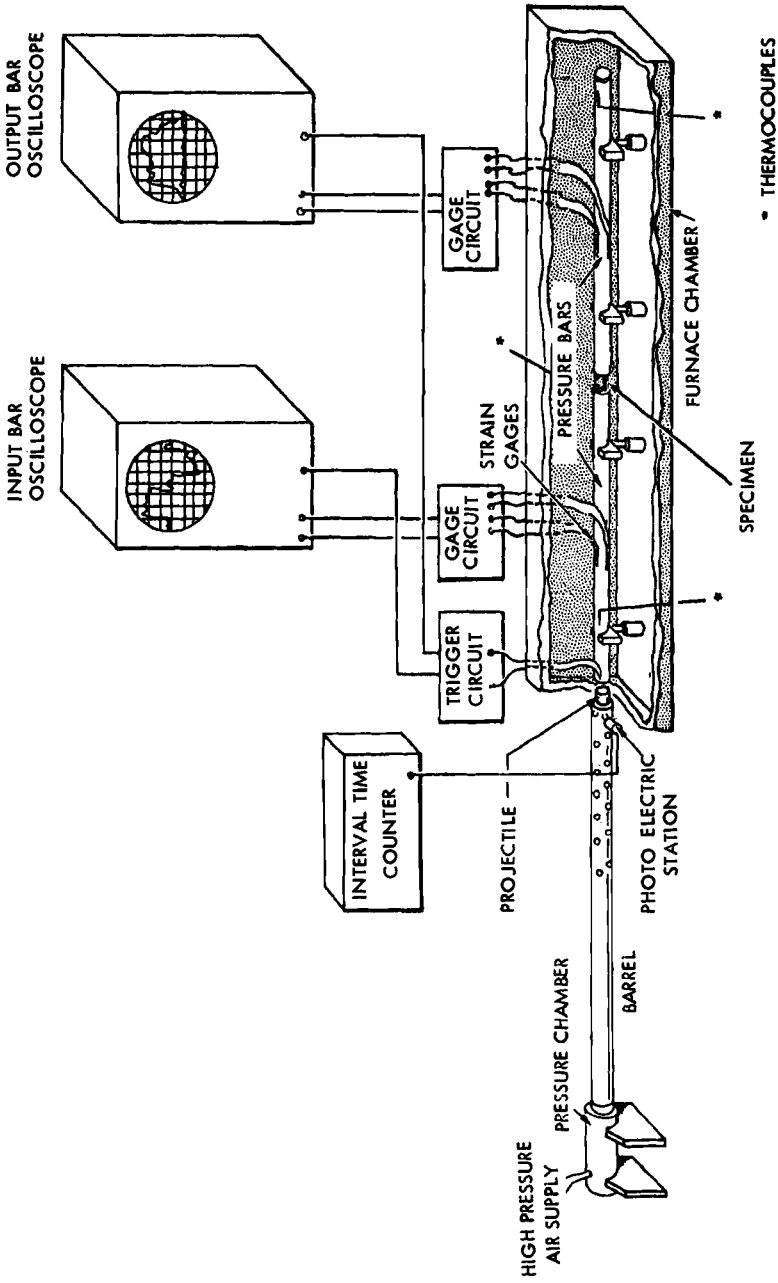


FIG. 1—*Schematic of SHPB test facility.*

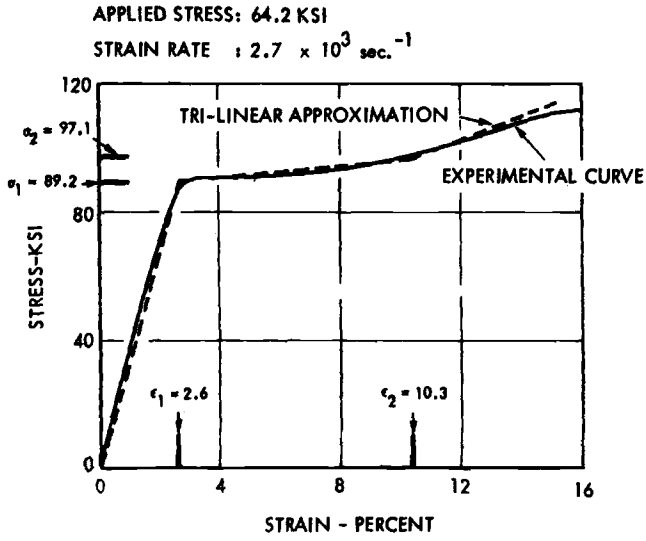


(a) STRESS-STRAIN CURVE AND TRI-LINEAR APPROXIMATION

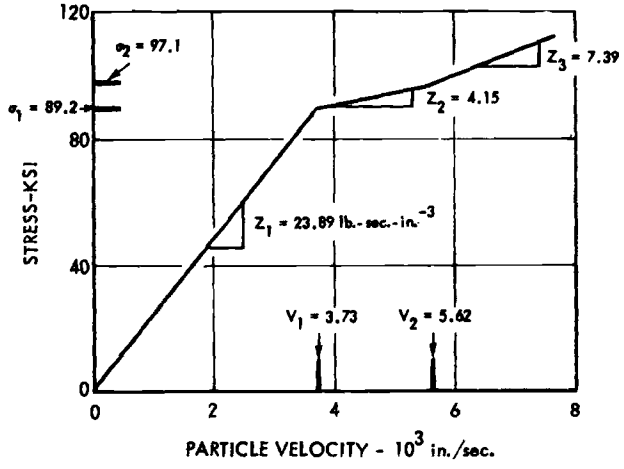


(b) TRI-LINEAR STRESS-VELOCITY RELATION

FIG. 2a—*Dynamic properties of fiber glass-reinforced epoxy resin.*

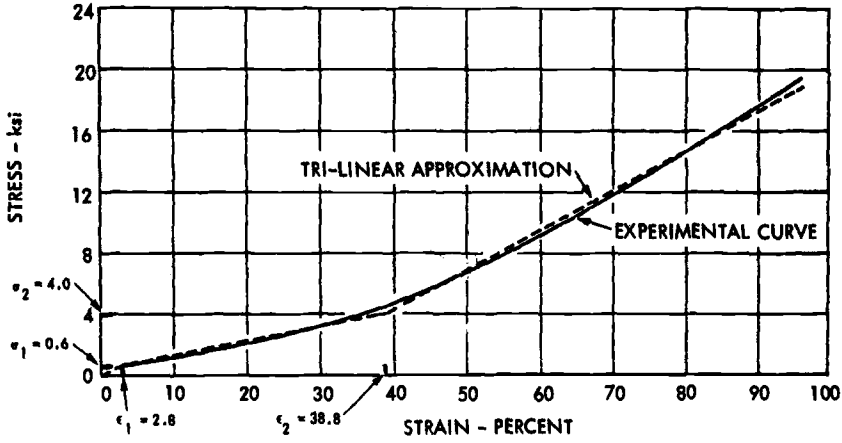


(a) STRESS - STRAIN CURVE AND TRI-LINEAR APPROXIMATION

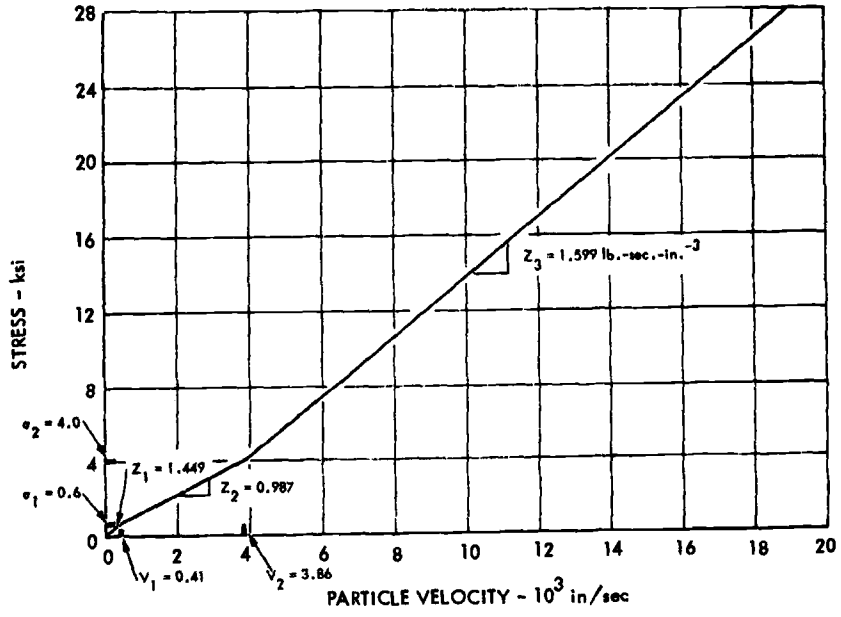


(b) TRI-LINEAR STRESS-VELOCITY RELATION

FIG. 2*b*—*Dynamic properties of clear AFML polyurethane.*

everal versions of the same AFML polyurethane which we have studied with the SHPB technique, namely, a compound containing Polymeg 650 polyols. Using the method[*4*] for predicting the stress created by a raindrop striking a surface at various velocities, we calculated impact stresses for many of the materials studied with the rocket sled technique. The resulting stresses are plotted in Fig. 3 versus the equivalent dynamic impedance for the material at that impact velocity. Also shown in this figure are the dynamic fracture stress amplitudes for these materials, as determined with the SHPB.

It has been estimated[*3,4*] that each 2 mm-diameter area of these rocket sled specimens receives on the average only about three impacts during the run. This 2 mm diameter of an "average" raindrop has been used to define the impact area for all of our calculations. Hence, it seems reasonable to ignore fatigue effects and treat sled studies as essentially single-impact tests, with dynamic fracture stress as the essential factor in erosion initiation. For each of the rigid plastics shown in Fig. 3, the datum point indicating its dynamic fracture stress lies between the curves which bracket the onset of measurable weight loss.

A summation of some results from rocket sled testing of AFML polyurethane is shown in Fig. 4. It is seen that the specimens which suffered "slight" and "some" weight losses were struck by raindrops which created stresses in the polyurethane within the range of measured dynamic fracture. However, the tests causing "considerable" weight loss involved impact stresses well above the fracture range for this elastomer. Thus, the fracture stress for this type of polyurethane, as determined within the SHPB facility, can be correlated with the rain impact erosion behavior of such materials in a rocket sled test, where only a few impacts may be expected.

## Multiple Impact Observations

Water impact erosion tests were conducted on both the AFML polyurethane and the epoxy laminate using the HYDRONAUTICS multiple-impact erosion facility[*15,16*]. This device, shown in Fig. 5, consists of a rotating disk driven by a 2½-hp variable-speed motor, capable of sustained operation at 20 000 rpm. Impact velocities in excess of 733 ft/s (500 mph) may be achieved without evacuating the test chamber. The rotating disk shown in Fig. 5 is capable of holding up to six specimens. The lighter disk used in these tests supports only two specimens, allowing higher speeds for less power. The disk rotates in the horizontal plane, causing the specimens to cut two 1/32-in.-diameter vertical columns of water during each revolution, as shown schematically in Fig. 6.

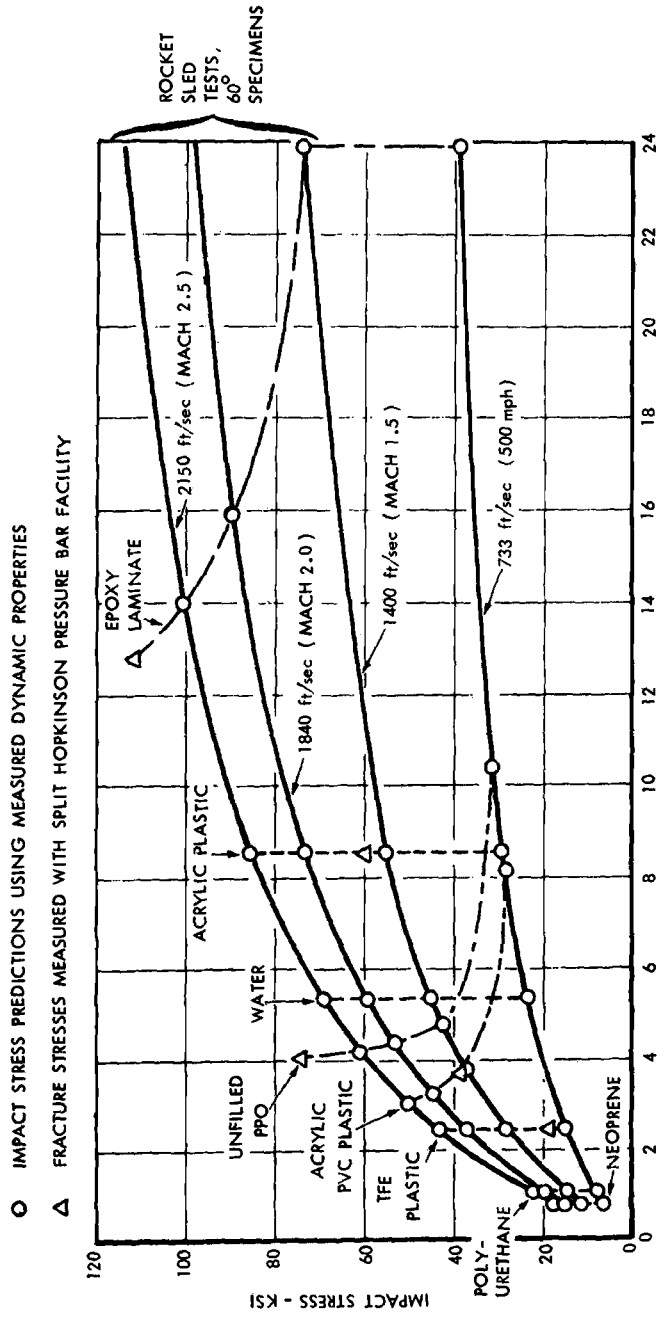


FIG. 3—*Comparison of impact stress predictions with single-impact fracture stress.*

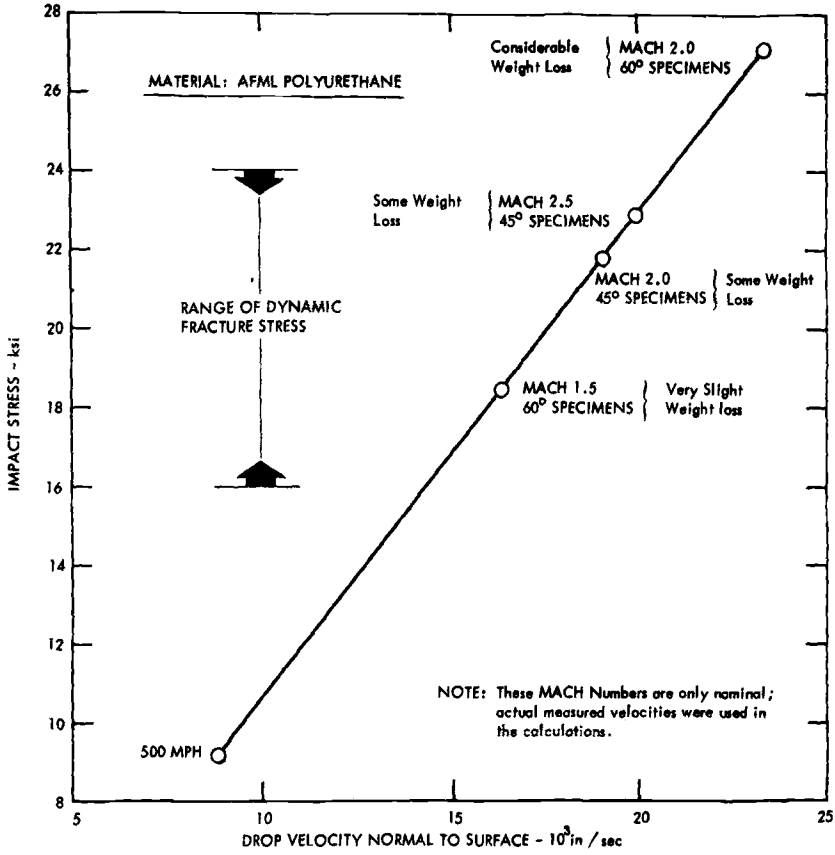


FIG. 4—*Comparing rocket sled rain erosion tests with impact stress calculations and dynamic fracture stress measurements.*

An electronically controlled solenoid valve permits very brief and precisely controlled durations of the water column down to a minimum of about 20 ms. The test requires bringing the disk up to the required speed, turning the water on for the desired time duration, and then stopping for specimen examination. Our failure criterion, in order to relate to dynamic fracture stresses, differed from the usual one of complete coating erosion down to the substrate, which is the criterion in large whirling-arm tests. We defined failure to be when initial fractures were seen in the middle area of the specimen.

The result of eroding considerably beyond this initial fracture is seen in Fig. 7. In this case the test was continued until the coating was completely torn away, exposing the red primer. In the large photograph the lower half

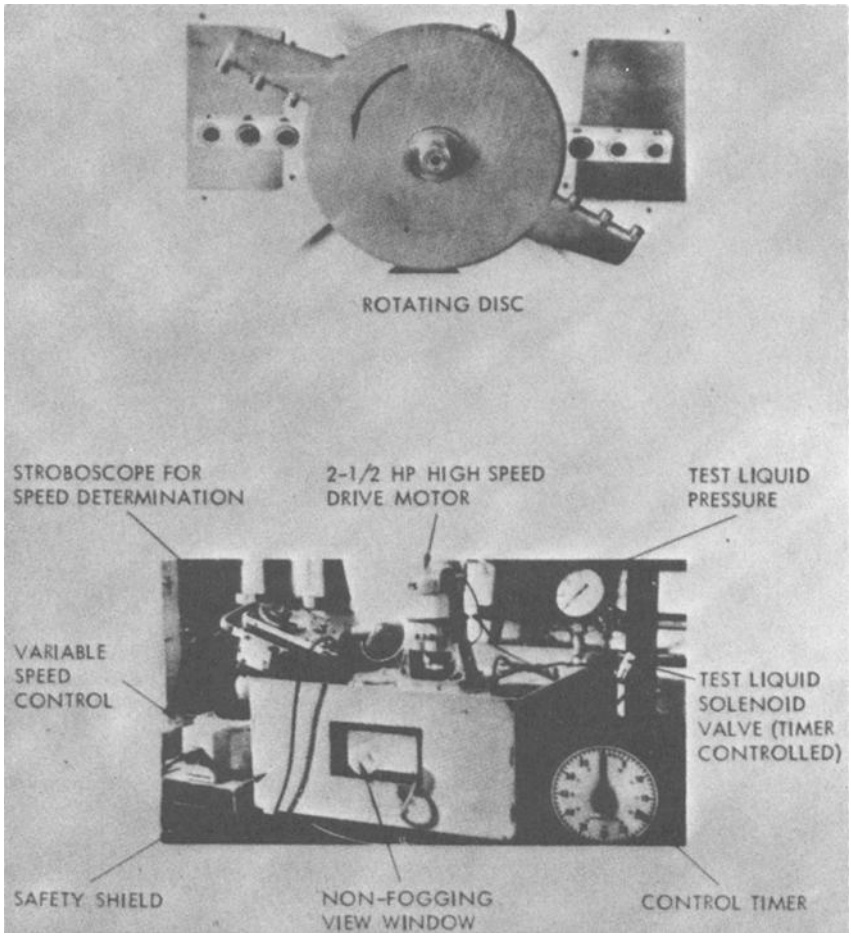


FIG. 5—*General view of multiple liquid impact erosion facility.*

of the specimen was cleaned down to the epoxy laminate substrate after the test, in order to determine whether any damage had occurred to the substrate. It is seen, even after the relatively long exposure of 200 impacts at 650 ft/s (443 mph), that there is virtually no damage to the epoxy laminate. A small spot may be seen in the lower right-hand quadrant of the specimen. This lightly frosted area was made by gently scraping with a knife to artificially establish the visibility of damage. The scraped area clearly shows up on the test specimen. Thus the protection offered by this white-pigmented AFML polyurethane has been graphically demonstrated.

For contrast, the smaller photograph in Fig. 7 shows the epoxy laminate

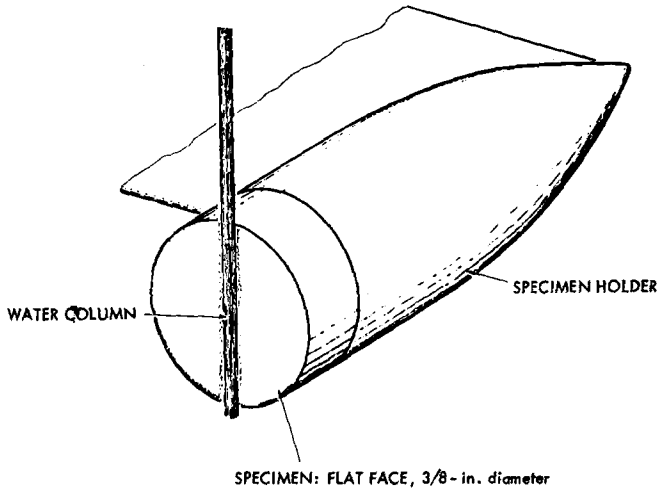


FIG. 6—*Impact of water column by test specimen in multiple-impact erosion facility.*

substrate after testing without a coating at the same velocity of 650 ft/s. With only half as many impacts, there has been severe damage to this composite. Delaminations, fracture of the glass fibers, frosting, and chipping out of the epoxy matrix are observed. These results, as discussed later, provide additional experimental support of the applicability of the uniaxial stress, elastic-plastic theory for describing rain erosion observations.

A summation of the erosion data obtained for the AFML polyurethane and the epoxy laminate is shown in Fig. 8. Also in Fig. 8 are erosion observations from large whirling-arm tests by Moraveck and Clarke[7] on thicker coatings of the same white-pigmented AFML polyurethane. It is seen that their tests involved considerably larger numbers of impacts before failure. It should be emphasized that their failure criterion was not merely the initiation of fracture, but complete erosion through to the substrate. Rainfield analyses developed earlier[2,3] were used here to determine the number of impacts in those whirling-arm tests[7] and an average of about 2½ s between impacts was calculated for 500 mph.

Part of the reason for the more rapid failure of these coatings within our smaller device is the much shorter time between impacts with each of the columns of water, which is, at 500 mph, only about 2 ms. As discussed in the following, this brief time duration does not permit the AFML coating to fully recover from the prior impact before receiving the subsequent one. Thus, the damage to this coating is accumulative, and deformation sufficient to cause fracture is rapidly achieved.

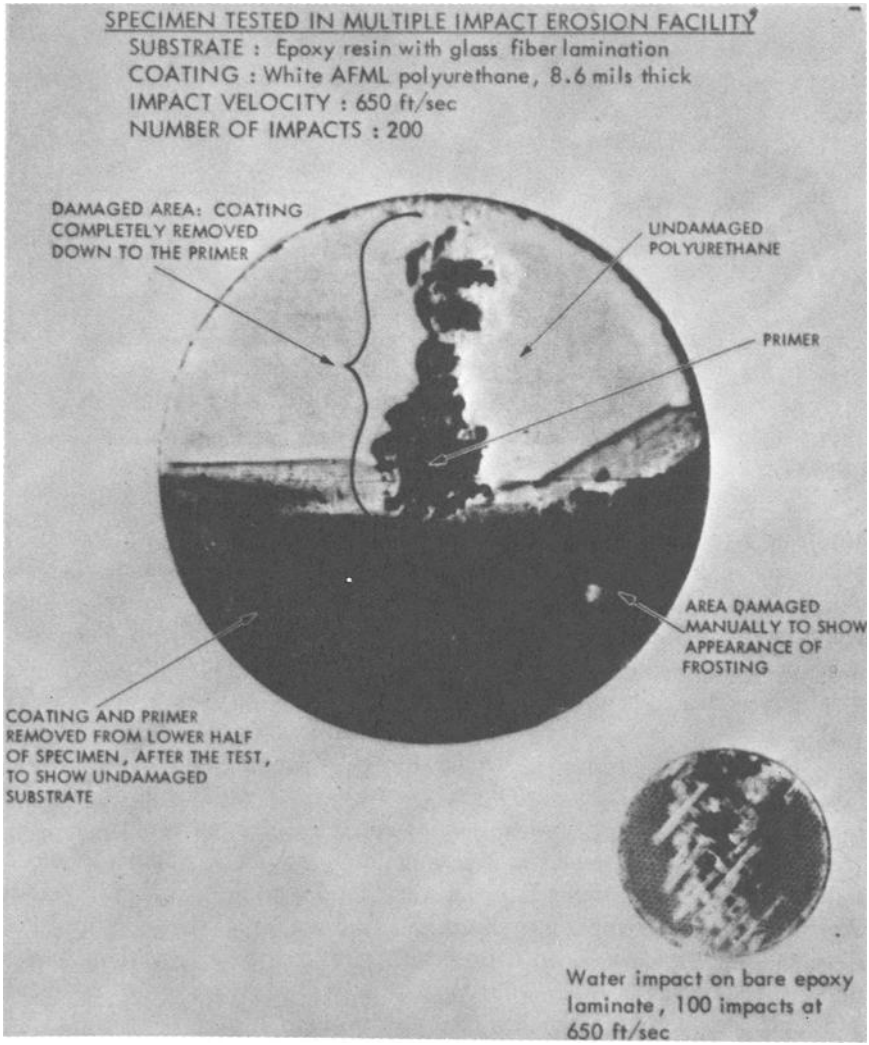


FIG. 7—*An experimental demonstration of the applicability of the uniaxial stress, elastic-plastic stress wave theory to describe rain erosion observations. This observed absence of substrate damage shows the lack of validity of the shock-wave, uniaxial strain theory, which predicts stresses in a coated substrate that are larger than the stresses predicted for direct water impact on bare substrate.*

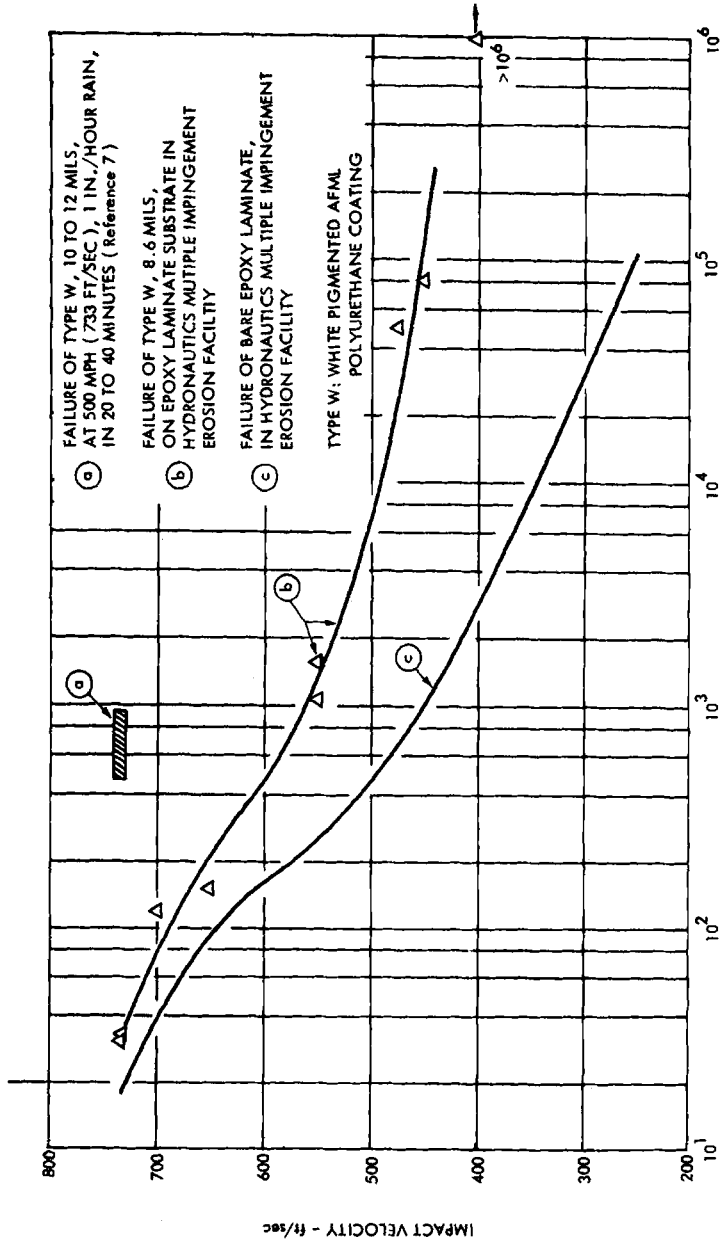


FIG. 8—*Fatigue curves for the water impingement erosion of polyurethane epoxy laminate.*

The curve in Fig. 8 for the epoxy laminate indicates the considerable protection provided by the AFML polyurethane at any given impact velocity; considerably shorter lifetimes are observed for direct water impact on the epoxy laminate. In addition, it should be emphasized that virtually no damage occurred to the epoxy laminate substrate beneath the AFML polyurethane coating until the coating was entirely torn away; then direct impact could occur upon the epoxy laminate.

### *Analyses of Whirling-Arm Erosion Tests of AFML Polyurethane*

The same techniques used to demonstrate that fatigue behavior could describe the rain erosion observations for polymethylmethacrylate[*4,5*] have now been applied to two types of AMFL polyurethane. These results for the white-pigmented and black-pigmented types are summarized in Fig. 9. The data reported by Moraveck and Clarke[*7*] and Morris and Wahl[*11*] can be related to observations by Schmitt[*12,13*]. Schmitt has reported that the lifetime of these AFML polyurethanes and other elastomeric coatings is, at 600 mph, only about 2/3 of their rain erosion lifetimes at 500 mph. The calculated ranges of lifetime at 880 ft/s (600 mph) are based on 2/3 of the measurements at 500 mph, and are seen to fall on the lines connecting the tests at 733 and 1120 ft/s. Details of these calculations are given in Ref *6*.

A portion of the data obtained with the HYDRONAUTICS multiple-impact erosion facility, shown in Fig. 8, are repeated for reference in Fig. 9. Here again the effect of recovery time is clearly seen, with the very short time between impacts in our small erosion facility causing accelerated accumulative damage histories at each of the test velocities for the white-pigmented AFML polyurethane.

### *Erosion Testing of Epoxy Laminate*

The results of tests on bare epoxy laminate in our small erosion facility are plotted in Fig. 10. Schmitt's observations[*12,13*], wherein failure after 1 or 2 min was seen at 500 mph, were analyzed and the resulting span of impacts is plotted in Fig. 10. These large whirling-arm results are seen to agree very well with our small-scale tests. The rapid recovery of the epoxy laminate, as discussed in the next section, apparently accounts for this agreement despite the brief interval between impacts in our facility.

Another interesting correlation has also been derived, and is plotted at 365 ft/s in Fig. 10. This is the result of calculating the stress imparted to the epoxy laminate substrate through an AFML polyurethane coating at 500 mph. Schmitt[*13*] reported up to 5 h before failure for the clear version

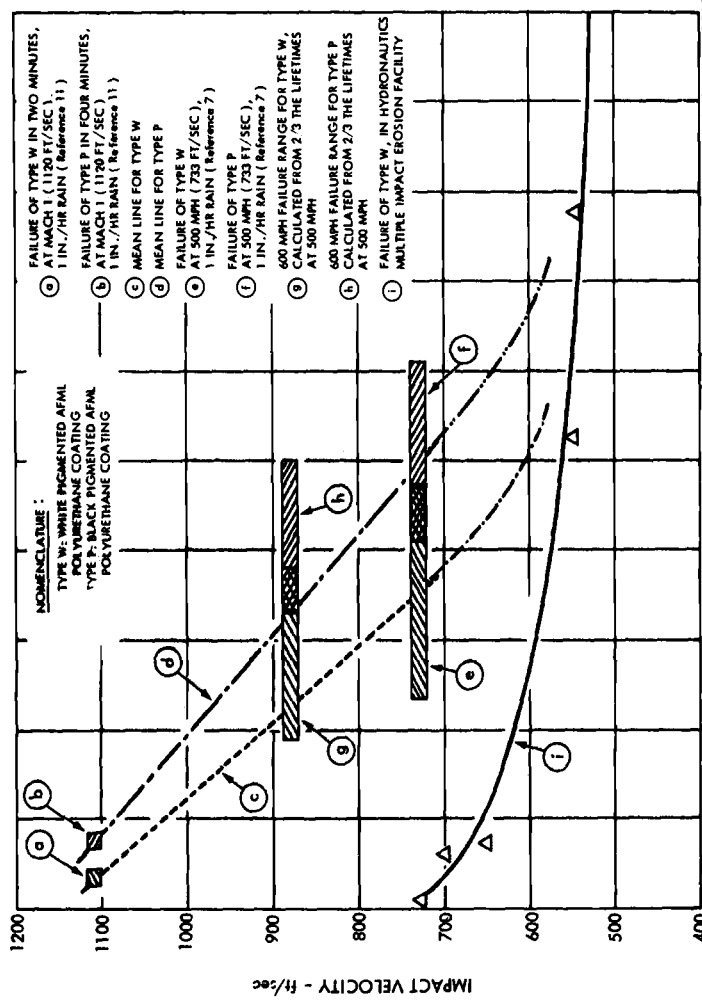


FIG. 9—*Fatigue representation for the rain erosion failures of two AFML polyurethanes.*

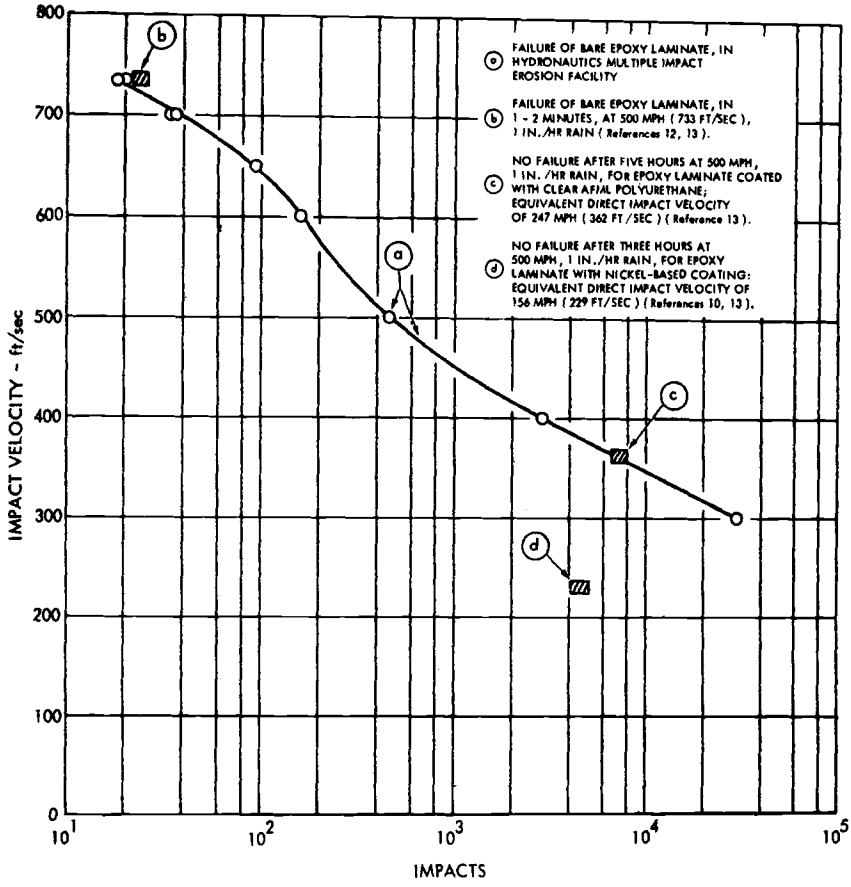


FIG. 10—*Fatigue curve for the water impingement erosion of epoxy laminate.*

of AFML polyurethane when tested within his whirling-arm facility at 500 mph in a 1-in./h simulated rainfall. The typical mode for failure, however, has not been tearing and erosion of the coating, but a secondary failure initiated within the substrate. Schmitt reports[*13,14*] that the epoxy laminate substrate was observed to frost, powder, and break up, thus destroying the bond between the substrate and the coating, which allows flexing and tearing of the coating to occur, leading to eventual failure. Thus beneath an intact coating, failure of the substrates was seen when using these highly effective, clear types of AFML polyurethanes, which are capable of resisting rain erosion at 500 mph for extremely prolonged periods.

An explanation of these observations has been offered[*4*] using an

analysis based on the uniaxial stress, elastic-plastic dynamic properties measured for these materials, AFML polyurethane and epoxy laminate. With the dynamic properties given in Fig. 2, and using a nonlinear technique[*6,17,18*] to analyze the stress-wave interactions at the interface, we calculate that a stress of 19.2 ksi is transmitted to the epoxy laminate substrate. This stress, on bare epoxy laminate, would occur at a 362-ft/s raindrop impact. A 5-h exposure in Schmitt's facility[*13*] is equivalent to about $7 \times 10^3$ impacts on the average 2-mm circle used in our calculations. This result, plotted at Point *C* on Fig. 10, is seen to agree with the erosion tests of bare epoxy laminate in our facility. It should be noted that the transmitted stress of 19.2 ksi for an AFML polyurethane-coated epoxy laminate substrate is only one half of the 38.7 ksi, which is the calculated amplitude for direct raindrop impact on this composite at 500 mph.

The use of a nickel-based coating on an epoxy laminate substrate has been reported[*10,13*] to provide extremely long rain erosion lifetimes. Failures, when they did occur, were not due to powdering or crushing of the epoxy laminate but were described as initiating at either voids in the substrate or spots of adhesion loss. Utilizing elastic-plastic, uniaxial stress theory, a transmitted amplitude of 12.1 ksi has been calculated as the stress received by an epoxy laminate substrate under a nickel-based coating when tested at 500 mph.

Analogous to the "equivalent direct raindrop impact velocity" calculation performed for an AFML polyurethane coating on epoxy laminate, a velocity of 229 ft/s (156 mph) has been computed from the series of 12.1 ksi. Using a testing time of 3 h, an equivalent number of impacts of about $4 \times 10^3$ was derived. This point has been plotted in Fig. 10, and is seen to lie well below the rain erosion fatigue-type curve for epoxy laminate.

Therefore, very high fatigue lifetimes would be expected at this velocity of only 156 mph, perhaps in excess of $10^5$ impacts before fracturing of the substrate would be initiated. At 500 mph, in simulated 1-in./h rainfall, this would require a testing time of at least 70 h and perhaps considerably longer. Thus this fatigue-type analysis, utilizing uniaxial stress, elastic-plastic considerations, provides a means of predicting the performance of both hard and soft coating systems.

### Dynamic Recovery Rate

High-speed photography has been used to record the dynamic deformations of materials while undergoing impact within the SHPB facility[*4,5*]. These photographs record lateral and longitudinal deformations as a function of time. From these measurements we have determined the

"dynamic recovery rate," that is, the initial rate at which a material tends to relax toward the undeformed state after suffering large-amplitude elastic impact stresses. For instance the AFML polyurethane, after receiving a raindrop impact at 500 mph, which would produce strains of over 90 percent, has an initial dynamic rate of recovery of 50 percent per millisecond. These photographic data indicate that rate of recovery for elastomers is dependent on the amplitude of the dynamic strain. As with a typical highly damped system at lower strains, the rate of recovery is considerably smaller. Although sufficient data were not obtained to fully define the relaxation curve for this polyurethane, the relaxation time (to recover down to the $e^{-1}$ of the peak strain) from a maximum compression of 90 percent was found to be over 2 ms. Thus, complete recovery from a raindrop impact at 500 mph would be considerably longer than 2 ms. Since the time between impacts in our small erosion facility is only about 2 ms, incomplete recovery, and hence accumulative accelerated damage is created in the AFML polyurethane at 500 mph.

Similar measurements for the epoxy laminate showed a dynamic rate of recovery of about 170 percent per millisecond. Thus, the maximum recovery rate for the epoxy laminate is on the order of three times larger than the maximum rate for the AMPL polyurethane. Also, at 500-mph raindrop impact, the peak strain in the epoxy laminate is only about 2 percent. The relaxation time, from a peak of 2 percent, is about 7 $\mu$s. Hence, the time required to fully recover should be on the order of 0.01 ms. Therefore, the epoxy laminate specimens tested in our erosion facility were fully capable of recovery between impacts. This explains the agreement of our data with the results from large whirling-arm tests of epoxy laminates, and why the polyurethane measurements do not agree.

## Discussion

A question which has received considerable attention during the past few years[*5,6,8,13,14*] pertains to what models, mechanical and material, should be used to describe the response of coatings and substrates when subjected to raindrop impacts at velocities in the range of 500 mph (733 ft/s) to about Mach 1 (1120 ft/s). Specifically, we have been trying to determine whether one should use either (*a*) the uniaxial stress, elastic-plastic theory, or (*b*) the uniaxial strain, shock-wave (Rankine-Hugoniot) theory to describe the erosion observations in this velocity range.

Without attempting to recreate these discussions, as the details may be found in the cited references, we shall briefly indicate how the newest experimental observations and analyses tend to support the uniaxial stress, elastic-plastic theory.

*Prediction of Rocket Sled Erosion Results*

From the SHPB uniaxial stress, elastic-plastic measurements, with corresponding calculations, predictions have been made for the erosion observations of a wide variety of materials (see Figs. 3 and 4).

*Circular Damage Patterns*

The actual dynamic loading, that is, those stresses which create fracture and initiate the damage process in a material undergoing raindrop impact, arises from a complex hemispherical stress wave situation. Fyall[*19*] has observed these waves, and a recent paper by Peterson[*20*] may begin to provide an understanding of the three-dimensional aspects of this problem. Eventually, one hopes a complete theory will be derived that will define a dynamic deformation process between the extremes of the uniaxial stress and the uniaxial strain concepts.

However, we have found that the uniaxial stress SHPB tests create circular fracture patterns analogous to those observed in materials subjected to both raindrop and jet impacts[*21–27*]. The fractures[*4,5*] observed in specimens tested within the SHPB occur from circumferential strains—created by lateral deformations originally caused by the longitudinal compressive loading of the specimen—analogous to the stress field analytically described by Peterson[*20*] though by no means the same as the hemispherical three-dimensional stress field described in his theory. Therefore, although it should be emphasized that the SHPB test is not intended to be a simulation of the complete three-dimensional stress-strain dynamic wave pattern created by a raindrop impact, it is clear that this test does provide an empirical method for predicting the fracture of materials when subjected to the kind of dynamic loading created by a raindrop impact.

*Multiple-Impact Observations*

Using uniaxial stress, elastic-plastic material properties, and stress wave interaction analyses based on these measurements, we have provided explanations for the erosion observations of epoxy laminate, bare and while coated with either an elastomeric or nickel-based material. As shown in Figs. 7, 8, and 10, and as predicted by the uniaxial stress, elastic-plastic theory, an AFML polyurethane coating protects the epoxy laminate substrate by reducing the amplitude of the compressive stress transmitted, relative to the amplitude created by direct raindrop impact on this composite.

The compressive stresses transmitted to an epoxy laminate substrate that is protected by a nickel-based coating are smaller than the stresses

from a low-modulus elastomeric coating. Thus, the larger compressive stress amplitude transmitted to the epoxy laminate by the AFML polyurethane coating, along with the tensile stresses[*4–6*] which may be achieved near the interface between the polyurethane coating and epoxy laminate because of wave reflections and interactions, may both contribute to the relatively shorter survival time of epoxy laminate beneath AFML polyurethane compared with its ability to resist damage when tested beneath a nickel coating[*10,12*].

## Conclusions

1. Small-scale testing within the HYDRONAUTICS multiple-impact erosion facility may be used to provide valuable insight into the rain erosion resistance of coating and substrate materials.

2. The fatigue-like failure mechanism shown to be applicable to the rain erosion behavior of an acrylic plastic (polymethylmethacrylate)[*4,5*] is also the mechanism for the failure initiation of elastomers, such as the AFML polyurethane, and composites such as glass fiber-reinforced epoxy resin. Analyses of the densities of rainfalls[*3*] are applicable for development of this fatigue failure concept.

3. The uniaxial stress, elastic-plastic theory for determining impact stress amplitudes, and as the basis for wave interaction analyses, is capable of predicting experimental observations relevant to the initiation of the rain erosion process. Predictions from the uniaxial strain, shock-wave theory do not agree with these experimental results in the velocity range of 500 to 750 mph.

4. The "dynamic recovery rate" of materials is an important factor in understanding the rain erosion process. This rate, measured within the SHPB facility by high-speed photography, indicates how fast a material returns toward a state of zero strain after receiving a large dynamic load.

5. In addition to the results reported earlier for rigid plastic materials[*4,5*], similar correlations can be made between the dynamic fractures measured for AFML polyurethane in the SHPB facility and the response of this elastomer during rocket sled rain erosion testing.

*Acknowledgments*

The authors wish to express again their sincere appreciation to A. Thiruvengadam for continuing to provide his consultation, valuable advice, and discussions during the progress of this work. The support of E. W. Russell, Jr., Stephen Howard, and Michael Lewis with the experimental work and data analyses is also gratefully acknowledged.

## References


[1] Conn, A. F., "Research on Dynamic Response and Adhesion Failures of Rain Erosion Resistant Coatings," Technical Report 811-1, HYDRONAUTICS, Incorporated, Jan. 1969.

[2] Conn, A. F. and Thiruvengadam, A., "Dynamic Response and Adhesion Failures of Rain Erosion Resistant Coatings," Symposium on the Characterization and Determination of Erosion Resistance, American Society for Testing and Materials Annual Meeting, Atlantic City, N. J., June 1969; *Journal of Materials*, Vol. 5, 1970, pp. 698–718.

[3] Conn, A. F., "Relating Dynamic Properties of Materials and Resistance to Damage by Rain Impact," Technical Report 905-1, HYDRONAUTICS, Incorporated, Jan. 1970.

[4] Conn, A. F. and Rudy, S. L., "Research on Techniques to Predict the Resistance of Materials to Rain Erosion," Technical Report 7011-1, HYDRONAUTICS, Incorporated, May 1971.

[5] Conn, A. F., *Proceedings*, Third International Conference on Rain Erosion and Associated Phenomena," Aug. 1970, pp. 353–403.

[6] Conn, A. F. and Rudy, S. L., "Further Research on Predicting the Rain Erosion Resistance of Materials," Technical Report 7107-1, HYDRONAUTICS, Incorporated, May 1972.

[7] Moraveck, J. F. and Clarke, G. H., "Rain and Sand Erosion Resistant Polyurethane Protective Coatings," Technical Report AFML-TR-67-227, Part II, Olin Mathieson Chemical Corporation, New Haven, Conn., July 1969.

[8] Morris, J. W., Jr., "Supersonic Rain and Sand Erosion Research—Part II—Mechanistic Investigation of Rain Erosion," Technical Report AFML-TR-69-287, Part II, Textron's Bell Aerosystems Co., Buffalo, N. Y. Sept. 1969.

[9] Schmitt, G. F., Jr. and Krabill, A. H., "Velocity-Erosion Rate Relationships of Materials in Rain at Supersonic Speeds," AFML-TR-70-44, Air Force Materials Laboratory, Oct. 1970; see also Schmitt, G. F., Jr. et al., AFML-TR-67-164, Dec. 1967.

[10] Weaver, J. H., "Electrodeposited Nickel Coatings for Erosion Protection," AFML-TR-70-111, Air Force Materials Laboratory, July 1970.

[11] Morris, J. W., Jr. and Wahl, N. E., "Supersonic Rain and Sand Erosion Research: Erosion Characteristics of Aerospace Materials," AFML-TR-70-265, Textron's Bell Aerospace Company, Nov. 1970.

[12] Schmitt, G. F., Jr., "Materials Parameters that Govern the Rain Erosion Behavior of Polymeric Coatings and Composites at Subsonic Velocities," AFML-TR-71-197, Air Force Materials Laboratory, Dec. 1971.

[13] Schmitt, G. F., Jr., *Proceedings*, Third International Conference on Rain Erosion and Associated Phenomena, Aug. 1970, pp. 107–145.

[14] Morris, J. W., Jr., Bates, C. H., and Wahl, N. E., *Proceedings* Third International Conference on Rain Erosion and Associated Phenomena, Aug. 1970, pp. 261–301.

[15] Thiruvengadam, A. and Rudy, S. L., "Experimental and Analytical Investigations on Multiple Liquid Impact Erosion," Technical Report 719-1, HYDRONAUTICS, Incorporated, June 1968 (also NASA CR-1288).

[16] Thiruvengadam, A., Rudy, S. L., and Gunasekaran, M., in *Characterization and Determination of Erosion Resistance, ASTM STP 474*, American Society for Testing and Materials, 1970, pp. 249–287; also Technical Report 719-2, HYDRONAUTICS, Incorporated, Aug. 1969; also NASA CR-1638, Sept. 1970.

[17] Conn, A. F., "On Impact Testing for Dynamic Properties of Metals," Ph.D. thesis, The Johns Hopkins University. Baltimore, Md., 1964.

[18] Conn, A. F., *Journal of the Mechanics of Physics and Solids*, Vol. 13, 1965, pp. 311–327.

[19] Fyall, A. A., work in progress at the Royal Aircraft Establishment, Farnborough, England, exhibited during the Third International Conference on Rain Erosion and Related Phenomenon, Aug. 1970.

[20] Peterson, F. W., "Some Considerations of Material Response Due to Liquid-Solid Impact," ASME Paper No. 72-WA/FE-27, to be published in *Journal of Basic Engineering, Transactions*, American Society of Mechanical Engineers, (presented at ASME Winter Annual Meeting, Nov. 1972).

[21] Engel, O. G., *Journal of Research*, National Bureau of Standards, Vol. 54, No. 1, Jan. 1955, pp. 51–59.

[22] Engel, O. G., *Journal of Research*, National Bureau of Standards, Vol. 61, No. 1, July 1958, pp. 47–52.

[23] Engel, O. G., *Journal of Research*, National Bureau of Standards, June 1959, pp. 229–246.

[24] Engel, O. G., *Journal of Research*, National Bureau of Standards, Vol. 64A, No. 6, Nov.-Dec. 1960, pp. 499–512.

[25] Bowden, F. P. and Brunton, J. H., *Proceedings of the Royal Society*, London, Series A, Vol. 263, 1961, pp. 433–450.

[26] Field, J. E., Camus, J. J., and Gorham, D. A., *Proceedings*, Third International Conference on Rain Erosion and Associated Phenomena, Aug. 1970, pp. 303–325.

[27] Rochester, M. C. and Brunton, J. H., *1st International Symposium on Jet Cutting Technology*, April 1972, pp. A1–1 to A1–24.

# DISCUSSION

*W. F. Adler*[1]—I would like to make a few comments regarding the relation between the one-dimensional momentum balance equations for the propagation of plane waves in laminated materials and the relations used by Dr. Conn and co-workers to evaluate the magnitude of the impact and transmitted stresses for polymeric coatings. First, it is my belief that simple one-dimensional analyses[*3,4,6,8*] are not general enough to describe the failure mechanisms which actually prevail in coated materials. I also acknowledge that statements appear repeatedly in reports from HYDRONAUTICS that more general approaches are required, but the simplified approach is justified by the fact that the results from the uniaxial plane stress analysis appear to correlate well with the data obtained from erosion tests. After a general development of the governing equation for stress waves propagating in laminated materials, I will discuss certain aspects of the approach used at HYDRONAUTICS in the context in which it was presented.

Consider the one-dimensional shock-wave analysis of laminated materials. The equations for the purely mechanical theory for a water drop striking a coated substrate are given in Fig. 11 for the various plane wave fronts which develop as the pressure pulse propagates into the laminate.

The water drop strikes the coated material with an impact velocity $V_0$. A shock wave is transmitted into the drop at a velocity $U_w$, and a second shock wave is propagated into the coating at a velocity $U_c$ across the water/coating interface. The conditions at the interface between the compressing water drop and coating are that the pressures and particle velocities are continuous; that is, $p_c = p_w$ and $V_c = V_w$. The equation in Fig. 11 corresponds to the balance of mass and momentum as a shock wave is transmitted into the new layer and a second wave is reflected back into the previous layer. Continuity of the pressures and particle velocities also prevails at the coating substrate interface: $p_s = p_c'$ and $V_s = V_c'$. The notation $U[\,]$ is used to denote that the shock velocity is a function of the particle velocity. This information is available for water. If the relation

[1] Principal scientist, Advanced Materials Research Department, Bell Aerospace Company, Buffalo, N. Y. 14240.

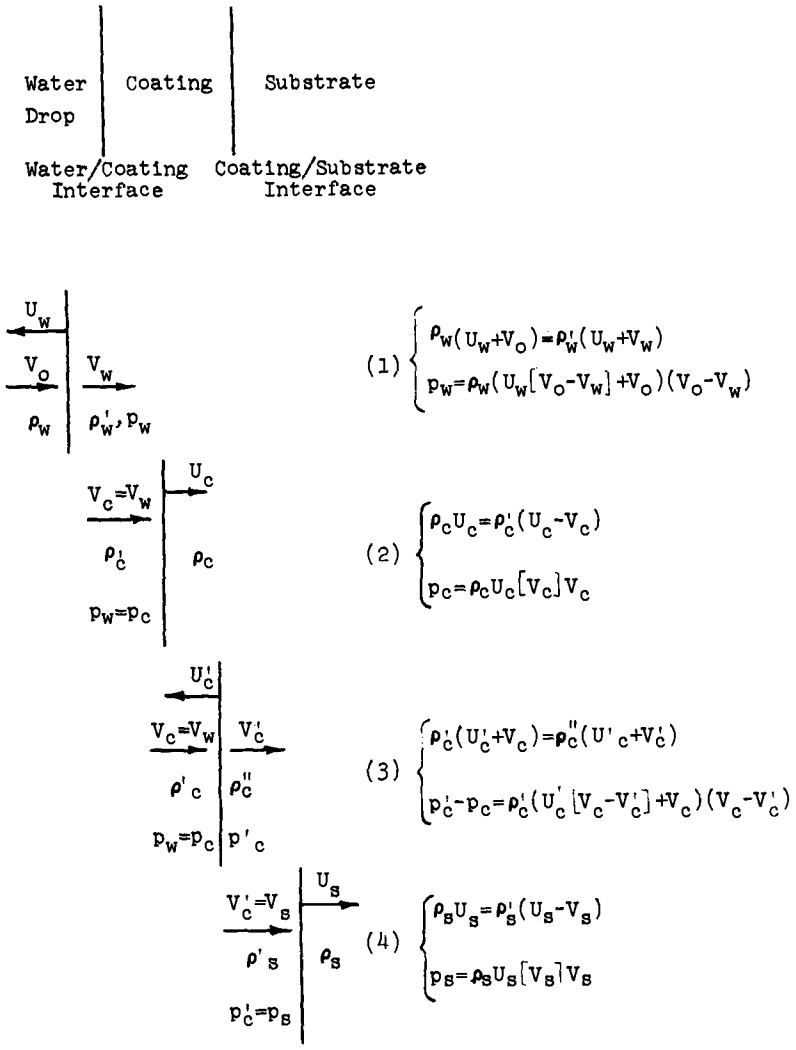


FIG. 11—*Mass and momentum balance equations for shock-wave fronts in coated materials.*

between the shock velocity and the particle velocity is known for the coating and substrate, the equations provided in Fig. 11 can be solved graphically[*8*]. Only momentum Eqs 1 and 2 are required to obtain the magnitude of the pressure pulse applied to the coating. The solution of Eqs 3 and 4 can be obtained from the momentum equations in conjunction with the balance of mass from Eq 2 in order to express the density of the

compressed coating, $\rho_c'$, in terms of its unstressed density, $\rho_c$. Then:

$$p_s = p_c^* + \frac{\rho_c U_c[V_c^*]}{U_c[V_c^*] - V_c^*} (U_c'[V_c^* - V_s] + V_c^*)(V_c^* - V_s) \quad (5)$$

where $p_c^*$ and $V_c^*$ denote the specific values of $p_c$ and $V_c$ obtained from the solution of Eqs 1 and 2.

The approach described in the foregoing was adopted by Morris[8] in estimating the pressure pulse transmitted to the coating and substrate by an impacting water drop. Now consider the form of momentum Eqs 1 to 4 when the droplet impact velocity is small in comparison with the acoustic velocities of the coating and substrate materials. When this condition prevails, the respective particle velocities are also negligible with respect to the acoustic velocities. The shock velocities in Eqs 1 to 4 become the constant dilatational wave speeds for an elastic medium. Momentum Eqs 1 to 4 become

$$p_w = \rho_w C_w (V_0 - V) \quad (6)$$

$$p_c = \rho_c C_c V \quad (7)$$

where $V = V_c = V_w$ and $p_w = p_c$, and

$$p_s - p_c = \rho_c C_c (V_c - V_s) \quad (8)$$

$$p_s = \rho_s C_s V_s \quad (9)$$

Using the condition that $p_w = p_c$, the unknown velocity $V$ can be eliminated from Eqs 6 and 7 to obtain

$$p_c = \frac{\rho_w C_w V_0}{1 + \frac{\rho_w C_w}{\rho_c C_c}} \quad (10)$$

Similarly, eliminating $V_s$ from Eqs 8 and 9 yields

$$p_s = \frac{2p_c}{1 + \frac{\rho_c C_c}{\rho_s C_s}} \quad (11)$$

The relations given in Eqs 10 and 11 are precisely the expressions used by Dr. Conn and his co-workers[3,4,6] in evaluating the impact stress, $\sigma_I$ in their notation, and the transmitted stress, $\sigma_T$, respectively. The derivation of Eqs 10 and 11 from the momentum equations for uniaxial shock-

wave propagation in a laminated system clearly points out the relation between the governing equations for droplet impacts adopted by Morris[*8*] and those used in the experimental program at HYDRONAUTICS.[*3,4,6*]

The assumption that the impact velocities are small in comparison with the speed of propagation of a dilatational wave in the coating or substrate is an inherent limitation on Eqs 10 and 11. We further note that Eq 11 is the same result obtained from the theory of elasticity for a dilatational wave, or a distortional wave, striking the interface between two different media of finite extent at normal incidence.[2] The quantity $\rho C$, where $C$ is the propagation velocity of an elastic wave, will be referred to as the characteristic impedance of the medium. For an elastic medium and low droplet impact velocities, the only difference in the uniaxial strain theory[*3,4,6*] is the propagation velocity for an elastic wave (corresponding to a dilatational wave in an extended medium). The wave velocity is given by

$$C^2 = \frac{(1-\nu)}{(1+\nu)(1-2\nu)} \frac{E}{\rho} \tag{12}$$

for uniaxial strain, and by

$$C^2 = \frac{E}{\rho} \tag{13}$$

for the uniaxial stress theory, where $E$ and $\nu$ are Young's modulus and Poisson's ratio, respectively.

For large-amplitude pressure pulses, Dr. Conn replaces Eqs 10 and 11 by

$$p_c = \frac{Z_w V_0}{1 + \dfrac{Z_w}{Z_c}} \tag{14}$$

$$p_s = \frac{2p_c}{1 + \dfrac{Z_c}{Z_s}} \tag{15}$$

where $Z$ denotes the dynamic impedance and the subscript denotes the medium to which it is applicable. This notation will be used only to signify the evaluation of the dynamic impedance based on the dynamic stress-strain curve obtained experimentally at HYDRONAUTICS using the SHPB.

[2] Knott, C. G., Reflection and Refraction of Elastic Waves," *Philosophical Magazine*, Vol. 48, 1899, pp. 64–97.

I would now like to make some observations regarding the use of Eqs 14 and 15 in the evaluation of polymeric materials using the data supplied in a number of HYDRONAUTICS reports[*3,4,6*]. First of all, I agree with Dr. Conn that the dynamic response of a material specimen should be considered in describing its behavior when subjected to an erosive environment, unless adequate justification can be provided for considering the process in simpler terms. However, very little consideration has been given to the constitutive behavior of the materials being investigated. In general, polymeric materials will exhibit nonlinear, viscoelastic behavior, which is referred to as elastic-plastic in the context of the uniaxial stress analysis. The viscoelastic nature of polymers subjected to short-duration pulses will not be described here; instead, the discussion provided will follow along the lines developed at HYDRONAUTICS.

On the basis of uniaxial, elastic-plastic stress wave theory:

$$Z = \left(\rho \frac{d\sigma}{d\epsilon}\right)^{1/2} \tag{16}$$

Dr. Conn replaces the dynamic stress-strain curves for polymeric materials by a trilinear approximation which simplifies the evaluation of Eq 16. In his notation

$$Z_1 = \left(\rho \frac{\sigma_1}{\epsilon_1}\right)^{1/2} \qquad \text{for } \sigma \leqslant \sigma_1 \tag{17}$$

$$Z_2 = \left(\rho \frac{\sigma_2 - \sigma_1}{\epsilon_2 - \epsilon_1}\right)^{1/2} \qquad \text{for } \sigma_1 < \sigma \leqslant \sigma_2 \tag{18}$$

$$Z_3 = \left(\rho \frac{\sigma - \sigma_2}{\epsilon - \epsilon_2}\right)^{1/2} \qquad \text{for } \sigma_2 < \sigma \tag{19}$$

Now the propagating wave front is no longer plane but for $\sigma_2 < \sigma$ is composed of three plane fronts propagating at wave velocities corresponding to Eqs 17, 18, and 19 such that according to the HYDRONAUTICS data, $C_1 > C_3 > C_2$. This implies that at the higher stress levels (above $\sigma_2$) the disturbance will propagate faster than the plane wave corresponding to the range $\sigma_1 \leqslant \sigma \leqslant \sigma_2$. I believe that the nonlinear stress-strain relations should possibly be expressed in terms of equivalent stress-equivalent strain plots instead of the engineering stress-strain curves. The equivalent strain measure would be a better representation of the finite strains which develop in the tests on polymers using the SHPB.

Data for the polymers considered at Hydronautics are given in Table 1. I have added a column which provides the values of the wave velocities

TABLE 1—*Acoustic and dynamic impedances for polymeric materials.*

| Material | Density, $\rho$, $\frac{\text{lb-s}^2}{\text{in.}^4 \times 10^{-4}}$ | Elastic Modulus, $E$, psi | $C = \sqrt{\frac{E}{\rho}}$, in./s $\times 10^{+4}$ | $C$ (experimental), in./s $\times 10^{+4}$ | $\rho C$, $\frac{\text{lb-s}}{\text{in.}^3}$ | $Z$, $\frac{\text{lb-s}}{\text{in.}^3}$ |
|---|---|---|---|---|---|---|
| Acrylic plastic | 1.12 | $4 \times 10^5$ | 5.98 | 7.65 | 6.70 | 8.54 |
| Acrylic PVC plastic | 1.22 | $3 \times 10^5$ | 4.96 | 9.15 | 6.05 | 11.1 |
| Unfilled PPO | 1.00 | $4 \times 10^5$ | 6.32 | 10.9 | 6.32 | 10.9 |
| Epoxy laminate | 1.70 | $3 \times 10^6$ | 13.29 | 14.1 | 22.6 | 23.9 |
| Polyurethane (Hill AFB) | 0.93 | $3 \times 10^3$ | 0.57 | 1.08 | 0.53 | 1.00 |
| Polyurethane (AFML) | 1.00 | $9 \times 10^2$ | 0.30 | 1.45 | 0.30 | 1.45 |
| TFE plastic | 2.00 | $9 \times 10^4$ | 2.12 | 1.22 | 4.24 | 2.44 |

evaluated from Eq 13 corresponding to the quasistatic value of Young's modulus. Now consider a water drop impacting a deformable surface at 1000 mph ($1.76 \times 10^4$ in./s). Referring to Table 1, it is readily seen that the impact velocity, $V_0$, is quite close to the magnitude of the stress wave velocities calculated in terms of either the quasistatic or dynamic Young's moduli for the polymeric materials listed. This condition violates the fundamental assumption used in obtaining Eqs 14 and 15 from the more general momentum balance Eqs 1 to 4. While I definitely question the applicability of the data obtained using the SHPB for the erosion of polymeric materials, I would like to suggest that the evaluation of the impact and transmitted stress be given more careful consideration.

A second point along these lines is that while Dr. Conn and his co-workers have devoted considerable attention to incorporating a dynamic elastic modulus in the evaluation of the stress generated in laminated material systems, they have neglected the compressibility of the water drop, which at moderate impact velocities can have a significant influence on the magnitude of the stress computed from Eq 14. The characteristic impedance of water at an impact velocity of 1000 mph is 8.86 lb-s/in.[3] instead of the 5.39 lb-s/in.[3] used in the evaluations of coating materials at HYDRONAUTICS. Figure 12 illustrates the relative difference that can occur in the evaluation of the impact stress using Eq 14 with the trilinear approximation to the dynamic stress-strain curve and a number of alternative solutions to momentum Eqs 1 and 2 that can be found in the literature on liquid particle erosion. The solid curves originating at the origin are the trilinear approximation to the stress-particle velocity relations for selected polymers based on experimental data from HYDRONAUTICS. The dashed lines originating at the origin signify the linear stress-particle velocity relations for the same polymers based on the constant values of the acoustic impedance recorded in Table 1. The lines originating at point $A$ are the stress-particle velocity relations for water using different values for the impedance. Line $\overline{AB}$ denotes the stress-particle velocity relation used by Conn based on a constant acoustic impedance of 5.39 lb-s/in.[3]. The line $\overline{AC}$ is the linear stress-particle velocity relation accounting for the compressibility of water at an impact velocity of 1000 mph; the curve $AC$ is the nonlinear form of this relation based on the data of Rice and Walsh.[3] The line $\overline{AD}$ includes the correction to the dynamic impedance of water as dictated by the form of momentum Eq 1. The corresponding nonlinear form of stress-particle velocity relation is omitted in this case for clarity in Fig. 12.

[3] Rice, M. H. and Walsh, J. M., "Equation of State of Water to 250 Kilobars," *Journal of Chemical Physics*, Vol. 26, 1957, pp. 824–830.

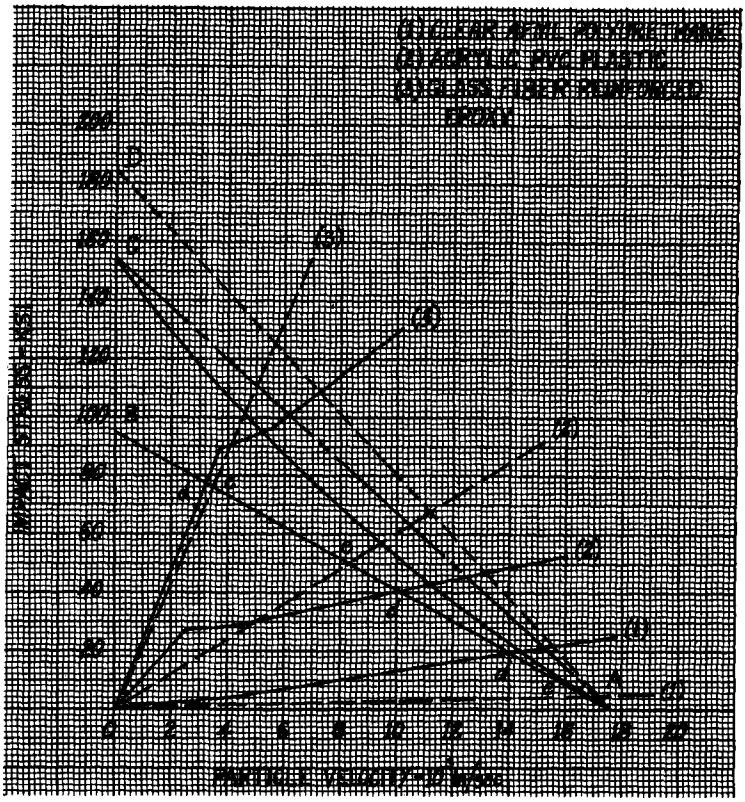

FIG. 12—*Impact stress evaluation for a water drop impacting polymeric materials at 1000 mph.*

The intersection points in Fig. 12 denoted by *d* are the evaluation of the impact stress as compared by Conn using Eq 14. The points denoted by *e* are the straightforward solution of Eq 10. The other points of intersection correspond to various assumptions which can be introduced in the form of the stress-particle velocity relations for water.

The intersection of the nonlinear relation corresponding to line $\overline{AD}$ in Fig. 12, and the nonlinear stress-strain relations for the polymers at strain rates corresponding to the duration of the peak impact pressure for a water drop, would be about the best one-dimensional approximation for the evaluation of the impact stress that could be obtained from Eqs 1 and 2. However, due to the extremely short duration of the peak impact pressure (on the order of 1 $\mu$s), the applicability of Eqs 1 and 2 would certainly be questionable since the long wavelength approximation would not be valid under these conditions. The graphical solutions of Eqs 1 and 2 provided in Fig. 12 indicate that the magnitude of the impact stress com-

puted from the dynamic stress-strain curves for polymeric materials can exhibit positive and negative variations from the popular de Haller equation, Eq 10. Figure 12 is also used to demonstrate the large differences which can occur in the results upon introducing the correct form of the momentum balance equations and accounting for the compressibility of water at high impact velocities. The graphical solutions provided for Eqs 1 and 2 can also be carried out for Eqs 3 and 4.

In summary, I feel the following points should be considered in future research employing the uniaxial stress approach:

1. The expressions for evaluating the impact stress and transmitted stress for polymeric materials should be generalized on the basis of the momentum balance equations when the drop impact velocity approaches the wave propagation velocity in the material.

2. Since finite strains are involved in the tests on polymeric materials using the SHPB, the equivalent strain or some other finite strain measure should be used.

3. At droplet impact velocities above 500 mph a more accurate evaluation of the impact stress and transmitted stress can be made within the scope of the one-dimensional analysis if the nonlinear relation between the wave speed and particle velocity for water is taken into account.

*A. F. Conn and S. L. Rudy (authors' closure)*—The authors are quite flattered and appreciative of the time and effort spent by Dr. Adler in his detailed analysis and commentaries on the experimental (and rather limited analytical) research on rain erosion which has been conducted at HYDRONAUTICS over the past five years. As the main emphasis of our work has been to provide data on the dynamic behavior of the various elastomeric and composite materials encountered in rain erosion situations to our fellow researchers and engineers, it is nice to see that at least one person has indeed read, understood, and begun to use our results.

We want to emphasize that the concern of the sponsor of our studies, the Naval Air Systems Command, is for relatively low-speed rain encounters, that is, up to 500 mph. Thus, we felt that the many other approximations justified using the equations as indicated, and the ambient value for the impedance of water. We fully agree with Dr. Adler in the use of shock wave concepts for the supersonic impacts which torment the aircraft and missile systems traveling at such velocities.

Again, we want to congratulate and thank Dr. Bill Adler for using our research results as the basis for carrying forward by one more step mankind's understanding of this area of rain erosion, and we envy him the time he has available to continue to dig more deeply into this fascinating problem.

*R. C. Tucker, Jr.* [1]

# Wear Characteristics of Modified Plasma-Deposited Aluminum Bronze

**REFERENCE:** Tucker, R. C., Jr., "Wear Characteristics of Modified Plasma-Deposited Aluminum Bronze," *Erosion, Wear, and Interfaces with Corrosion, ASTM STP 567*, American Society for Testing and Materials, 1974, pp. 270–293.

**ABSTRACT:** Plasma-deposited aluminum bronze coatings (Cu-10 Al) have been shown to be superior to wrought aluminum bronze (AMS 4640) when mated against steel with a hydraulic oil lubricant. In this study a series of compositional changes of the plasma-deposited aluminum bronze resulted in another order-of-magnitude reduction in wear rate. This was achieved without an increase in the hardness of the material so the embeddability and conformability of the materials were not degraded. The coefficients of friction of the plasma-deposited materials were much lower than their wrought counterpart, but there was little further change in the coefficients as a function of compositional changes in the plasma-deposited materials.

The coating parameters and compositional studies were based on unidirectional wear tests with the Dow Corning Alpha Wear Test Machine LFW-1 using hydraulic fluid Mil H5606A at loads from 30 to 450 lb at constant speed. The wear scars and debris were examined using scanning electron microscopy and microprobe analyses, and these observations correlated with the microstructures of the deposits. Differences between the various plasma deposits were correlated with microstructural and compositional variations.

**KEY WORDS:** wear, friction, plasma-deposited, materials, aluminum-bronze, coatings, erosion

In a previous study the wear behavior of plasma-deposited aluminum bronze and beryllium copper coatings was compared with their wrought counterparts.[2] The superior wear resistance of the plasma-deposited mate-

[1] Manager, Materials Development, Union Carbide Corporation, Linde Division, Indianapolis, Ind. 46224.

[2] Tucker, R. C., Jr. and Traub, P. W., "Wear Behavior of Wrought and Plasma-Deposited Aluminum Bronze and Beryllium Copper," presented at The Metallurgical Society Spring Meeting, American Institute of Mining, Metallurgical and Peroleum Engineers, 19 May 1971.

rials was thought to be due to their structure and perhaps influenced by the amount of oxide present. In this study the influence of oxides and other hard phases was specifically explored by modifying both the amount of oxygen added during plasma deposition and by adding several volume fractions of hard particles to the powder being sprayed. Although most of the work was done with an aluminum-bronze matrix and alumina additions, similar results have been obtained with other matrices (for example, nickel, aluminum, and steel) and other additives (for example, chromia and chromium carbide).

## Experimental Procedure

All of the wear tests were run on an LFW-1 Alpha Wear Test Machine according to the ASTM Test for Calibration and Operation of the Alpha Model LFW-1 Friction and Wear Testing Machine (D 2714-68). In this test 0.635-cm-wide (0.25 in.) blocks were held against the top of 3.4925-cm-diameter (1.375 in.) steel rings with a surface hardness of HRC 58 to 63 and a surface finish of 0.20 to 0.25 $\mu$m (8 to 10 $\mu$in.) CLA. The bottom portion of the rings was immersed in Mil H5606A hydraulic fluid. The blocks were either the wrought alloy of interest or blocks coated with 0.0508-cm-thick (0.020 in.) plasma coatings. In either case, just before testing, the wear surfaces of the blocks were finished with 2:0 emery paper with the residual scratches parallel to the direction of rotation. This left a surface finish of 0.15 to 0.20 $\mu$m (6 to 8 $\mu$in.) CLA measured perpendicular to the direction of rotation. A constant rotation speed of 33 cm/s (65 ft/min) for a distance of 594 m (1950 ft) was used. The friction force, block temperature, and depth of wear were continuously recorded and the lubricant temperature periodically measured. No correction of the block temperature was made for the minor differences in thermal conductivity caused by the coatings. The depth-of-wear recordings were used only to monitor the rate of wear, because it was inconvenient to correct for thermal expansion of the ring and block as they expanded due to the heat of friction.

Scar volumes rather than weight changes were used to characterize the block wear because the inherent porosity of the plasma coatings absorbed an unknown amount of lubricant. The block scar volumes were calculated from measurement of the projected scar area. Conversely, weight changes were used with the rings since they were solid and residual lubricant could easily be removed. Because of errors in weighing and the random transfer of aluminum bronze to the rings, the accuracy of the wear scar on the rings is estimated to be approximately $\pm 50 \times 10^{-6} \text{cm}^3$.

## Materials

The materials used are shown in Table 1. The AMS 4640 aluminum bronze was chosen because of its common use as a bearing material. The standard plasma-deposited aluminum bronze is a commercially available coating.[3] The "oxidizing" deposition was achieved by modifying the coating parameters. Photomicrographs of the cross sections of the plasma-deposited coatings are shown in Fig. 1. Standard deposition conditions were used for all of those materials that contained hard particles with the exception of one containing 11 percent alumina. The latter was made with slightly oxidizing conditions.

The oxide volume fractions were calculated from neutron activation analyses for oxygen in the plasma-deposited material. These calculations corresponded quite closely to oxide contents determined by chemical extractions of alumina.

The mechanical properties of wrought aluminum bronze are well known. Those of several of the plasma-deposited materials were determined in compression by machining rectangular cylinders out of very thick coatings with their long axes (axes of loading) either perpendicular or parallel to the surface of the coating. Bonded strain gages were used to measure strain. The results are shown in Table 2.

TABLE 1—*Aluminum bronze materials.*

| Type | Volume % $Al_2O_3$ | $DPH_{300}$[d] | $R_{30T}$[d] |
|---|---|---|---|
| Wrought AMS 4640[a] | | 252 | 81 |
| Plasma-deposited Al-10 Cu[b] | | | |
| Unmodified | 2.36 | 246 | 69 |
| Oxidizing deposition | 3.20 | 200 | 64 |
| Alumina added | 7.26 | 170 | 75 |
| Alumina added | 12.4[c] | 202 | 72 |
| Alumina added | 21.0 | 246 | 75 |
| Alumina added | 40.5 | 186 | 61 |

[a] Cu-10.3Al-5.0Ni-2.8Fe nominal composition by weight.
[b] Cu-10Al-1.5Fe nominal composition by weight.
[c] Based on extraction of $Al_2O_3$ rather than neutron activation.
[d] In direction of deposition (that is, on wear surface), standard deviations varied from 12 to 22 on six readings for DPH and 1 to 3 for $R_{30T}$.

[3] UCAR LCU-2, Union Carbide Corp.

TABLE 2—*Mechanical properties in compression of plasma-deposited aluminum bronze.*

| | Perpendicular to Surface | | | Parallel to Surface | | |
|---|---|---|---|---|---|---|
| | Elastic Modulus, $10^6$ psi | 0.2% Yield Strength, $10^3$ psi | Ultimate Strength, $10^3$ psi | Elastic Modulus, $10^6$ psi | 0.2% Yield Strength, $10^3$ psi | Ultimate Strength, $10^3$ psi |
| Unmodified | 7.1 (0.89)[a] | 58 (6.2) | 95 (1.4) | 8.4 (0.41) | 62 (2.6) | 91 (5.3) |
| Oxidizing deposition | 2.9 (0.14) | 47 (6.5) | 140 (9.6) | 7.0 (1.2) | 42 (5.0) | 71 (5.1) |
| 12.4 volume/0 $Al_2O_3$ | 8.5 (0.77) | 73 (1.2) | 125 (1.3) | 9.7 (1.24) | 89 (11.2) | 101 (3.9) |
| Oxidizing deposition + 10.8 volume/0 $Al_2O_3$ | 7.6 (0.61) | 57 (3.1) | 128 (5.7) | 10.9 (2.76) | 70 (6.3) | 91 (2.0) |

[a] Standard deviation for three to five specimens.

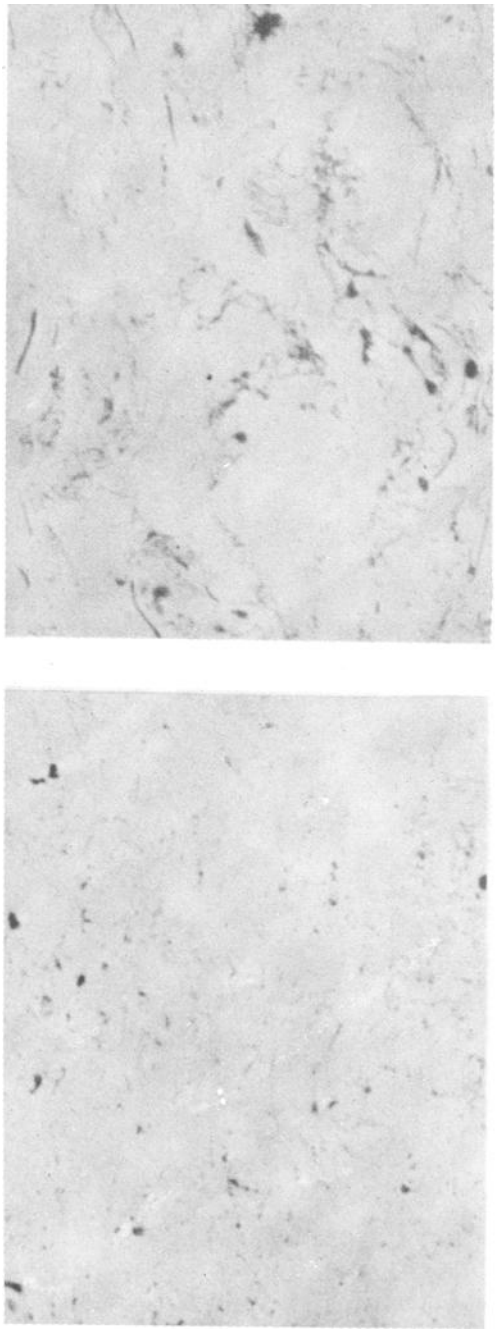
Slightly oxidizing deposition
Standard, unmodified

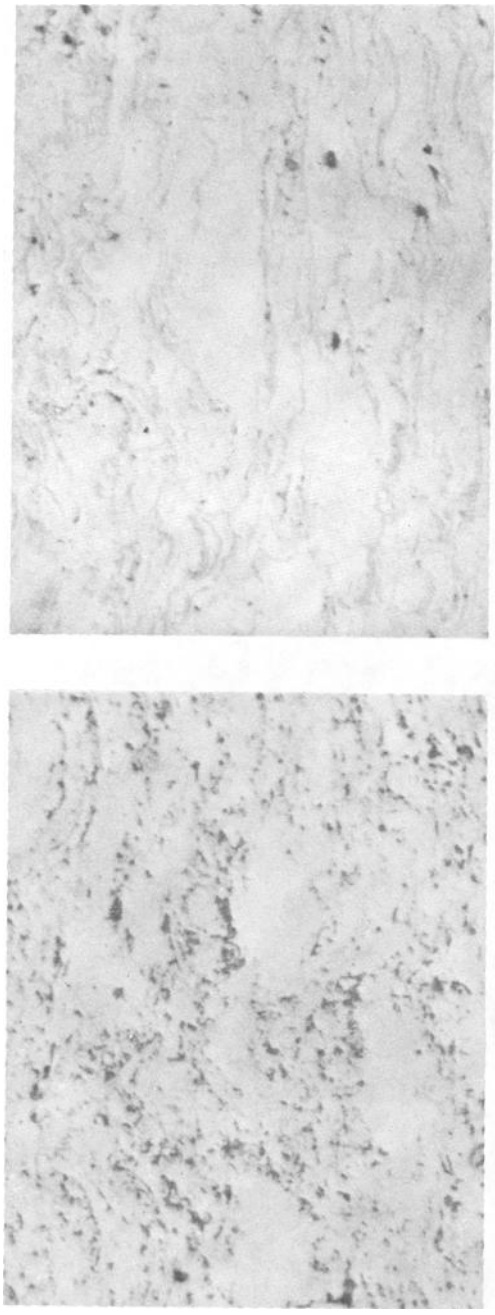


FIG. 1a—*Microstructures of aluminum bronze coatings with and without additions as shown (as polished).*

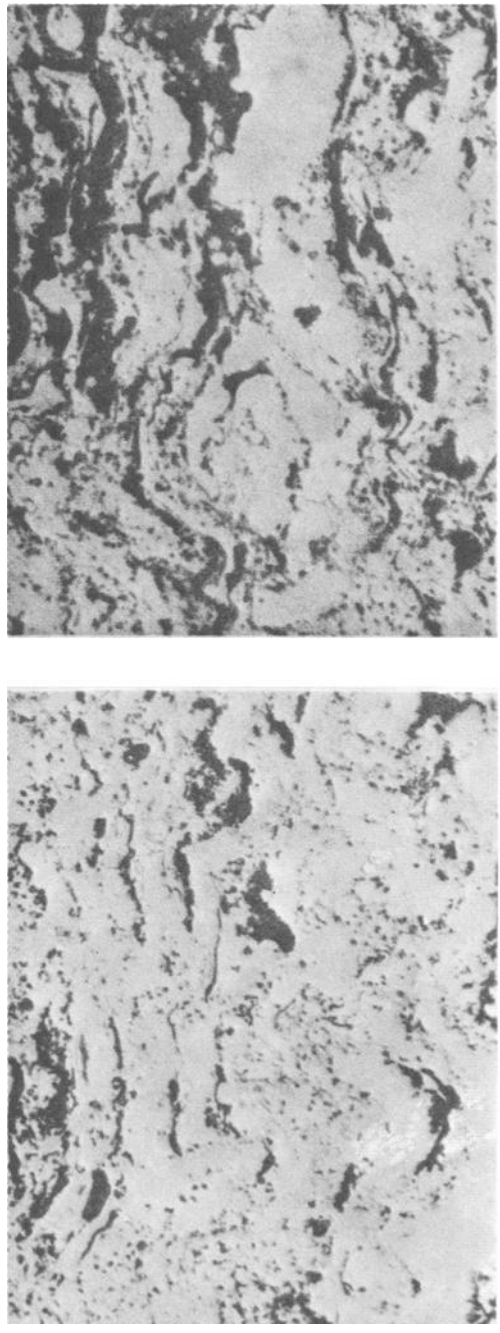
12% Alumina
7% Alumina

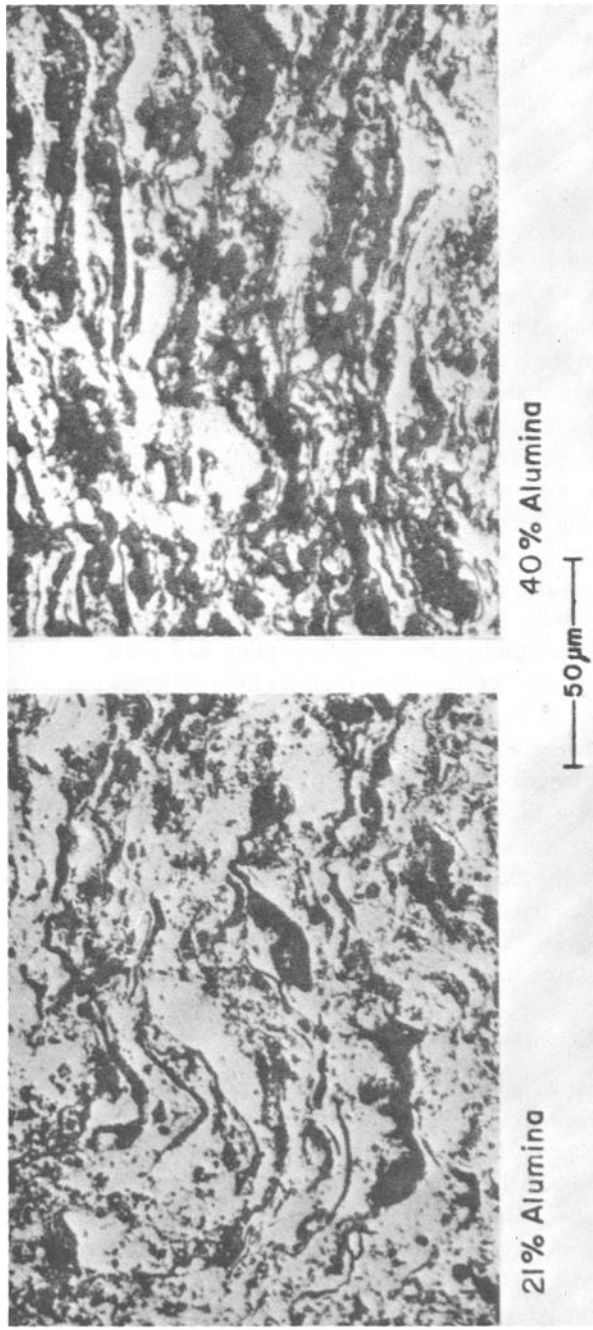


FIG. 1b—*Microstructures of aluminum bronze coatings with additions as shown (as polished).*

The compressive properties measured perpendicular to the surface are of the greatest interest since that is the usual direction of loading. It should be noted that the ultimate compressive strength in service would be higher than that shown in Table 2 because the measured value is a function of the specimen geometry and these materials are normally used as relatively thin coatings rather than the tall, thin columns used here.

The compression specimens loaded perpendicular to the coating surface ultimately failed by cracking with a classical diagonal or triangular pattern on a macro-scale. Microscopic examination revealed that the crack propagation occurred in short steps, predominantly along splat boundaries. Specimens loaded in a direction parallel to the surface, on the other hand, failed only after extensive barreling, with the predominant cracks occurring as long segments along splat boundaries parallel to the loading direction.

It is particularly interesting to compare the mechanical properties of plasma-deposited materials containing oxides introduced as a result of oxidizing coating conditions with the properties of plasma-deposited materials containing oxides intentionally added as discrete particles. Plasma deposition with oxidizing conditions significantly weakens the structure because the oxides are formed on the molten particles in transit and on the cooling surface layers immediately after deposition. These oxide films prevent metallic bonding between the splats and reduce the splat-to-splat bond strength. Therefore, while there is little difference in strength in the two directions of testing for the standard coating, there is a drastic reduction in the strength of the oxidized material when loaded parallel to the predominant layering planes of the oxides (that is, parallel to the surface) as compared with its strength when loaded perpendicular to the predominant layering. As previously noted, failure in the former case is due to splitting along the oxide layers.

On the other hand, if the oxide additions are made as discrete particles a high percentage of the splat-to-splat interface area remains metallic and the strength of the material is actually increased rather than decreased.

## Wear Test Results

The average wear scar volumes of the bronze blocks and the steel mating rings are shown in Fig. 2. The ring weight losses for the wrought and unmodified plasma-deposited aluminum bronzes are not shown because the losses were within the range of experimental error. Standard, unmodified plasma-deposited aluminum bronze has a much lower wear rate than wrought aluminum bronze (footnote 2). The wear of wrought aluminum bronze at 204 kg (450 lb) exceeded the capacity of the machine in less than the normal test duration used here; thus it is not shown in Fig. 2.

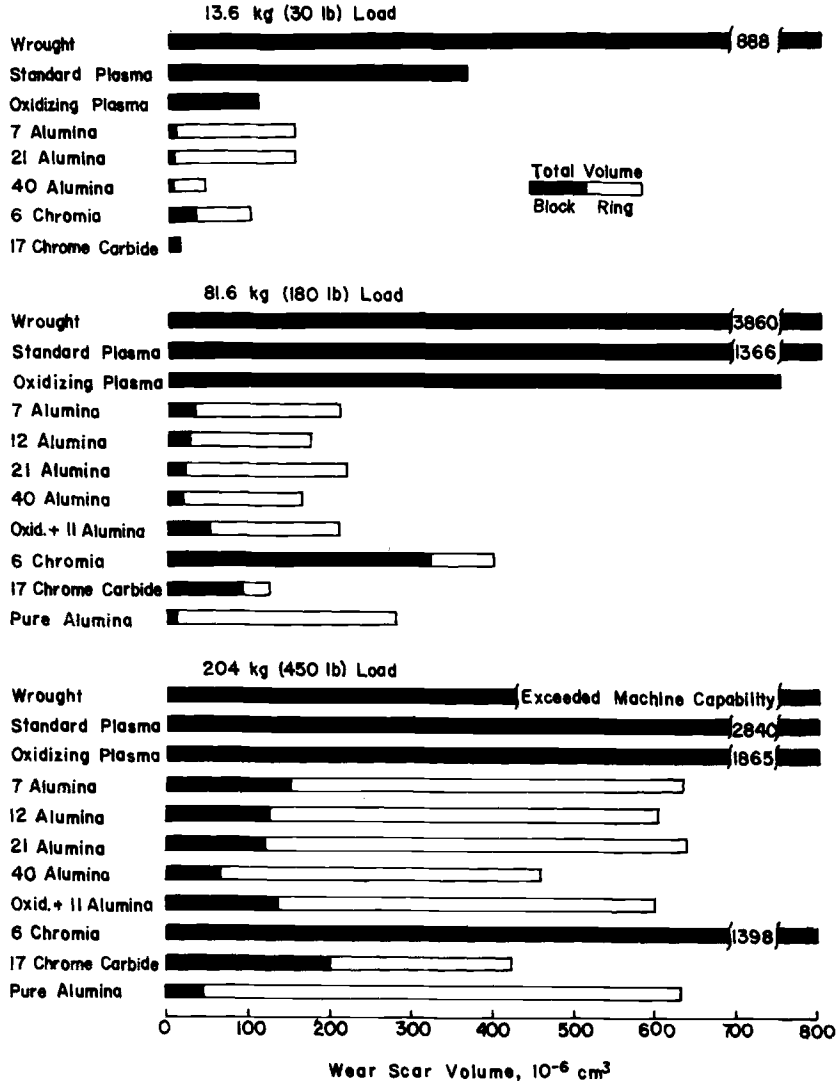


FIG. 2—*Average scar volumes of the aluminum bronze and the total system (aluminum bronze plus steel) after 5400 revolutions in Mil H5606A in LFW-1 wear test.*

At all three loads the plasma-deposited bronze made with slightly oxidizing conditions was more wear resistant than the standard material.

The precipitous effect of small volume fractions of oxide additions on the wear rate of plasma-deposited aluminum bronze is very evident when wear volumes are plotted as a function of oxide content as in Figs. 3, 4,

and 5. The lines are an approximate fit to the data. Volume fractions as low as 7 per cent result in wear resistance almost as high as the pure plasma-deposited alumina[4] coating shown on the right of Figs. 4 and 5, even though the composite hardness of the material is not significantly different from that of the unmodified aluminum bronze.

Weight losses were within the experimental error of measurement for those rings mated against the wrought and unmodified plasma-deposited aluminum bronze (that is, both weight gains and losses of up to $50 \times 10^{-6}$cm$^3$ were recorded). However, in spite of the fact that the weight losses of those rings mated against the modified materials were significant, the total system wear for the modified materials was much lower than for the unmodified, particularly at 81.0 to 204 kg (180 to 450 lb), Figs. 2 through 4. The rather large scatter in total system wear at 13.6 kg (30 lb) is probably due for the most part to the errors in the measurement of ring losses.

An approximately linear relationship for scar volume as a function of load was found for the wrought and unmodified plasma-deposited bronzes (footnote 2). However, as shown in Fig. 6, this linearity apparently did not hold for the modified bronzes. It should also be noted that, if all the materials are considered as a single class, an inverse linear relationship between scar volume and hardness was not found. Because of this it was earlier found convenient (footnote 2) to use a bearing performance factor (BPF) rather than a wear constant[5,6] to characterize the material:

$$\text{BPF} = \frac{\text{Load-velocity-time}}{\text{Scar volume}} = \frac{Lx}{V}$$

Figure 7 compares the BPF values for some of the various materials studies herein at several loads. The areas are bounded by extreme values in each case.

The difference in wear behavior between wrought and unmodified plasma-deposited bronzes, although not yet explicitly explained, is undoubtedly due to the unique microstructure that results from plasma deposition. The possibility of an increase in lubrication efficiency due to porosity in the plasma deposit seems unlikely since no difference was found between sealed and unsealed plasma-deposited aluminum bronze in an earlier study.

Examination of the blocks with scanning electron microscopy (SEM) showed a significant amount of plastic deformation for both wrought and

[4] UCAR LA-6, Union Carbide Corp.
[5] Archard, J. F., *Journal of Applied Physics*, Vol. 24, 1953, pp. 981–988.
[6] Rabinowicz, E., *Friction and Wear of Materials*, Wiley, New York, 1965, p. 168.

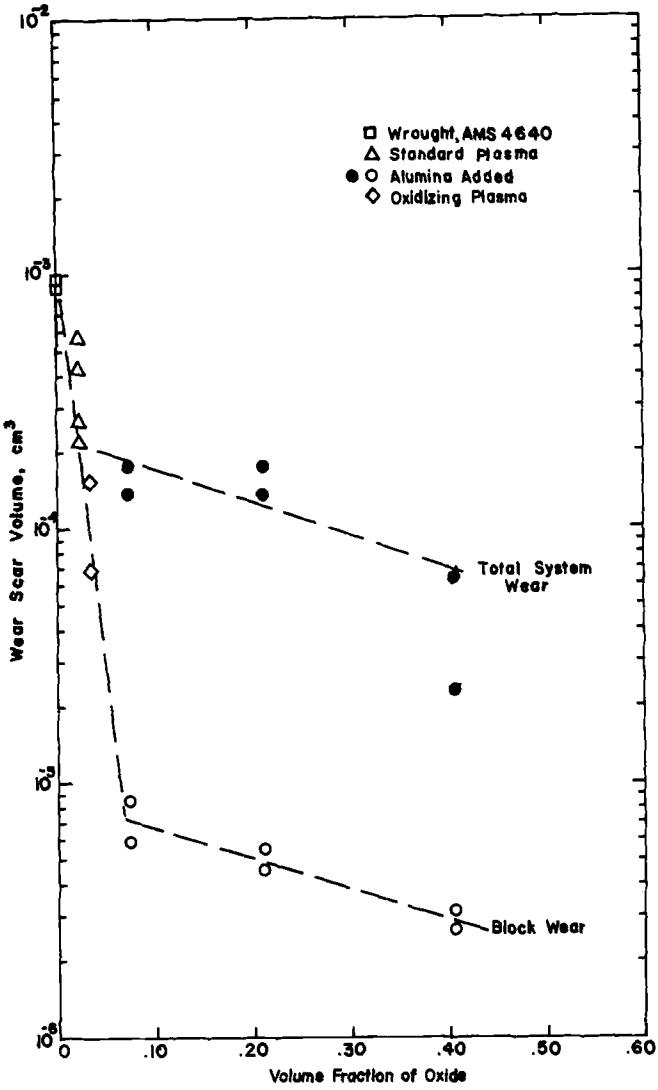


FIG. 3—*Aluminum bronze block wear and total system wear after 5400 revolutions in Mil H5606A at a 13.6-kg (30 lb) load in an LFW-1 wear test.*

unmodified plasma-deposited bronze (footnote 1), with all signs of splat boundaries in the plasma-deposited materials obliterated and ridges of smeared metal formed. However, since the splat boundaries of the modified bronzes remained visible in secondary electron images, and the appearance of smeared metal was far more limited, the extent of plastic deformation was apparently lower. Part of the splat boundary visibility

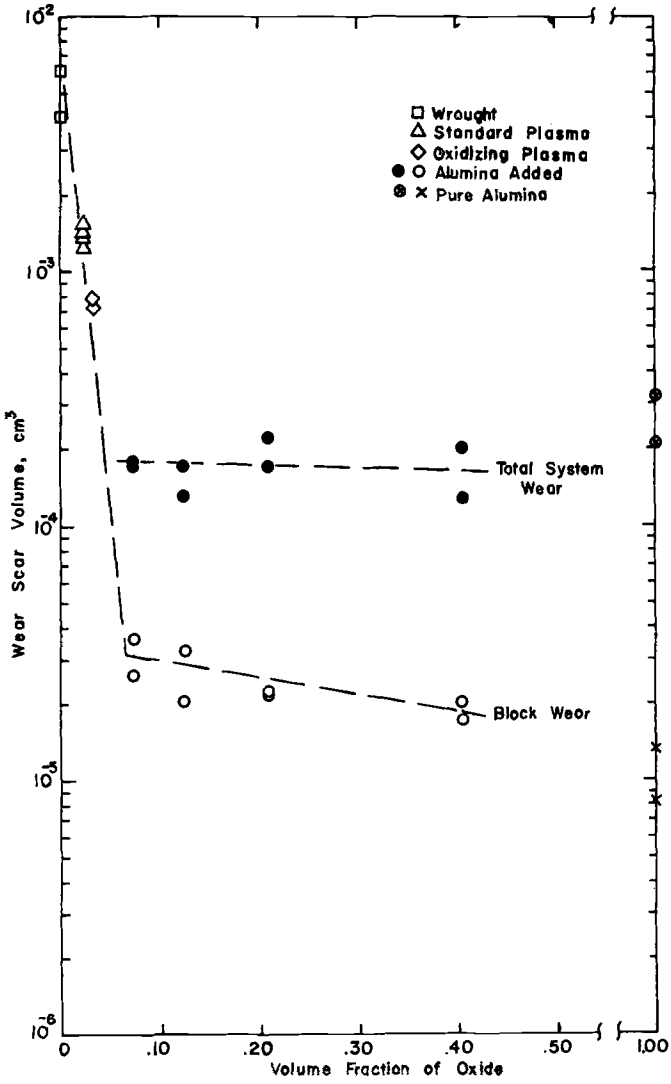


FIG. 4—*Aluminum bronze block wear and total system wear after 5400 revolutions in Mil H5606A at an 81.6-kg (180 lb) load in an LFW-1 wear test.*

in the SEM must, of course, be attributed to the compositional variation in the as-deposited material itself. The wrought aluminum bronze alloys developed large collections of compacted wear debris at the trailing edge of the wear scar. This appeared to be due to the release of relatively large particles of bronze adhered to the steel mating surface when the contact stress was released (footnote 2). The wear particles from the unmodified

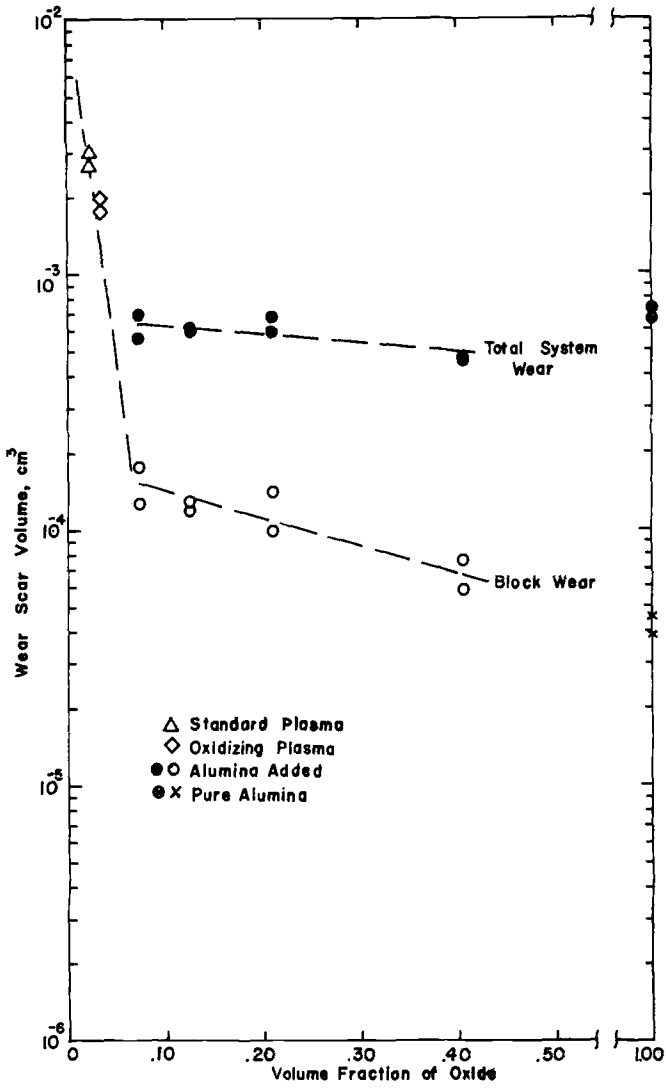


FIG. 5—*Aluminum bronze block wear and total system wear scar volume after 5400 revolutions in Mil H5606A at a 204-kg (450 lb) load in an LFW-1 wear test.*

plasma-deposited bronze were apparently smaller and did not tend to collect and compact at the trailing edge of the wear scar. This characteristic was also true of the modified bronze.

The transfer of bronze to the steel rings was very evident, visually and in electron microprobe X-ray images, for the wrought and, to a lesser extent, for the unmodified plasma-deposited bronzes. Conversely, the

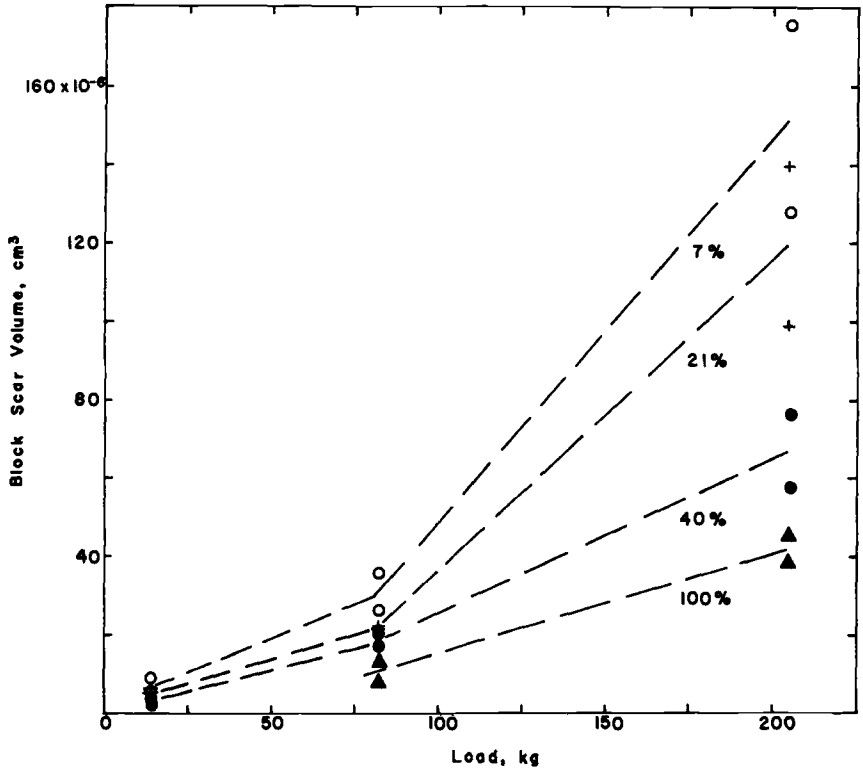


FIG. 6—*Block scar volumes as a function of load for plasma-deposited aluminum bronze with alumina additions as shown and pure plasma-deposited alumina after 5400 revolutions in Mil H5606A in an LFW-1 wear test.*

transfer of steel to the blocks for these materials was negligible. However, when mated against plasma-deposited modified bronzes, ring losses became measurable and iron was detected on those blocks examined in the microprobe (those modified with 7 and 21 volume percent alumina).

The X-ray images showed that the iron on plasma-deposited bronze + 7 alumina wear scars at 13.6-kg (30 lb) loads was randomly distributed in small particles or areas on the block. There seemed to be an association between high densities of iron and alumina. The major portion of the surface was covered with somewhat smeared copper. Very little copper or aluminum was detected on the ring at 13.6 kg (30 lb) and none at higher loads or higher oxide content. At 81.6-kg (180 lb) loads, higher-density patches of iron that were slightly elongated in the direction of rotation and about 10 $\mu$m long developed on the block. The patches were very dense, about 50 to 100 $\mu$m long, and covered roughly half the surface on the 204-kg (450 lb) blocks, Fig. 8.

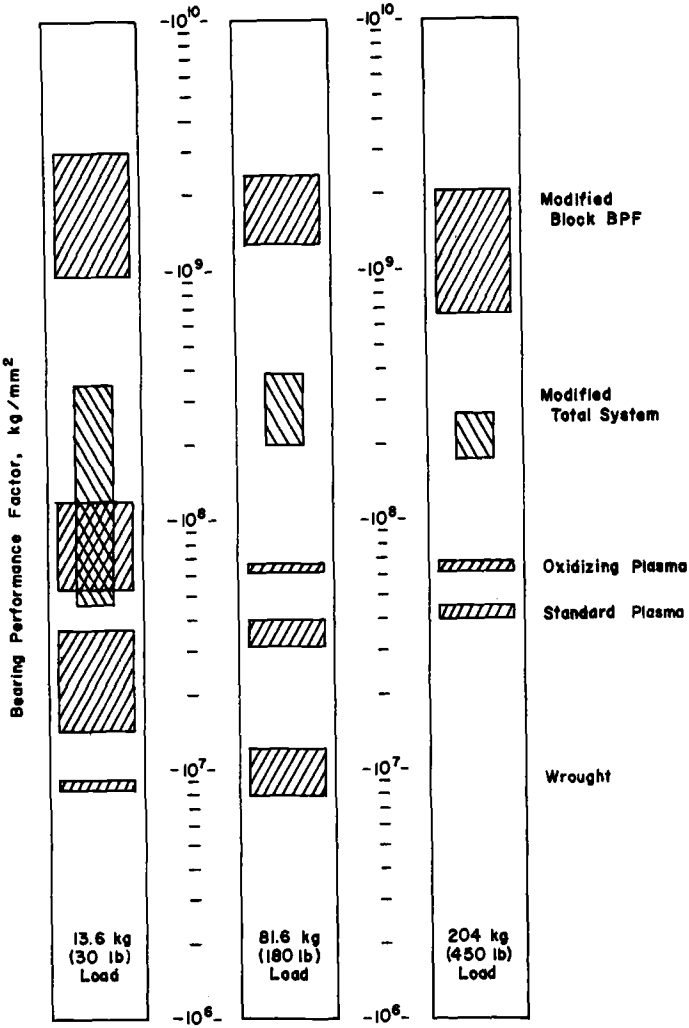


FIG. 7—*Bearing performance factors as a function of load. The blocks are bounded by extreme values. The blocks for modified coatings include all the volume fraction alumina additions.*

A similar pattern of iron transfer was exhibited by the bronze + 21 alumina specimens, but was more advanced at each load level. Thus at 13.6-kg (30 lb) loads, small patches, arranged in streaks in the direction of rotation, had already developed, Fig. 9. Extensive areas were covered with a high density of iron at 81.6 kg (180 lb), Fig. 10. Although no X-ray images were made of the 204-kg (450 lb) specimens, the secondary electron and specimen current images suggested that somewhat larger areas

Fe

-S.C.

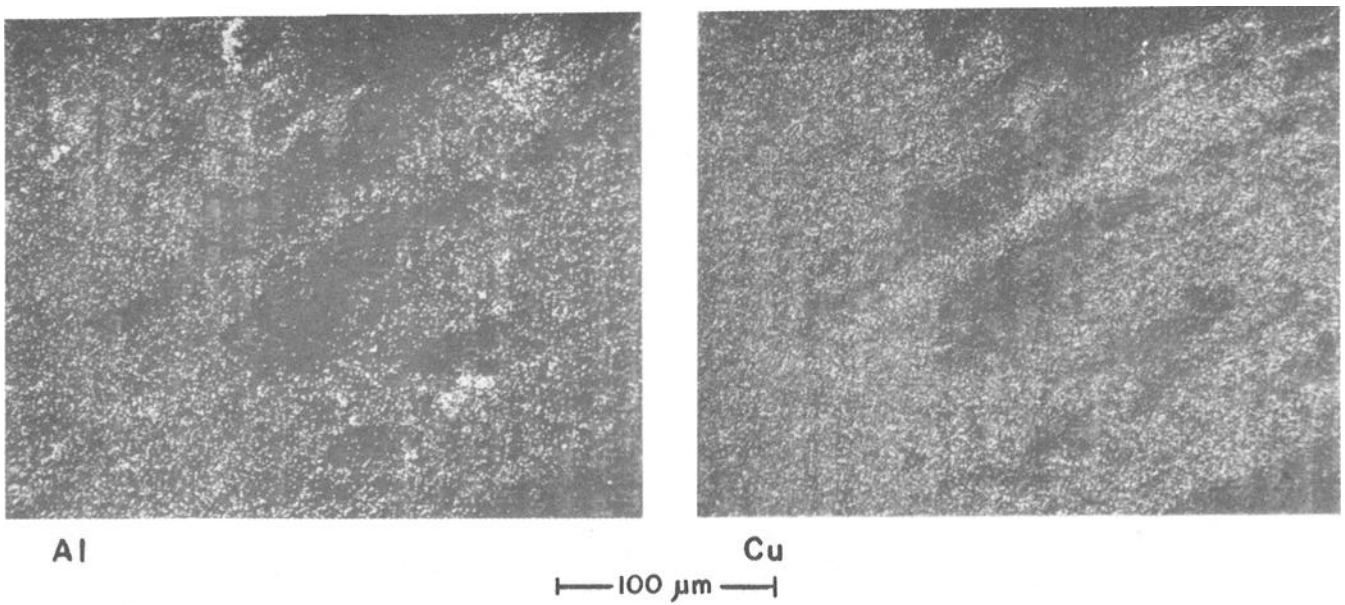


FIG. 8—*Electron microprobe inverse specimen current and X-ray rasters of the edge of the block scar of aluminum bronze + 7 alumina after 5400 revolutions in Mil H5606A at 204 kg (450 lb).*

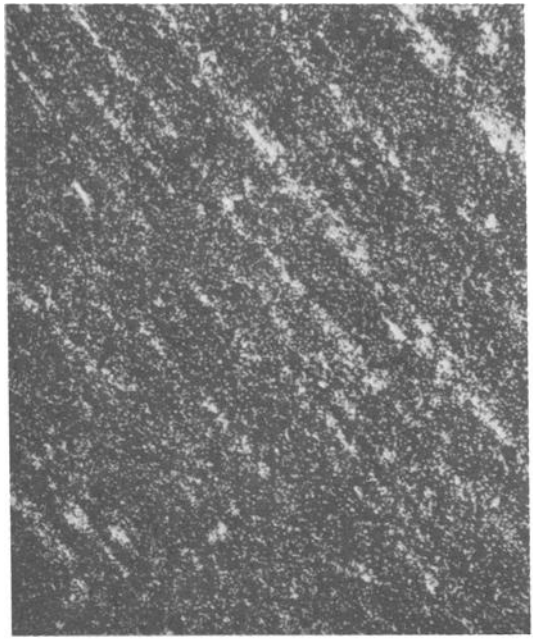

Fe

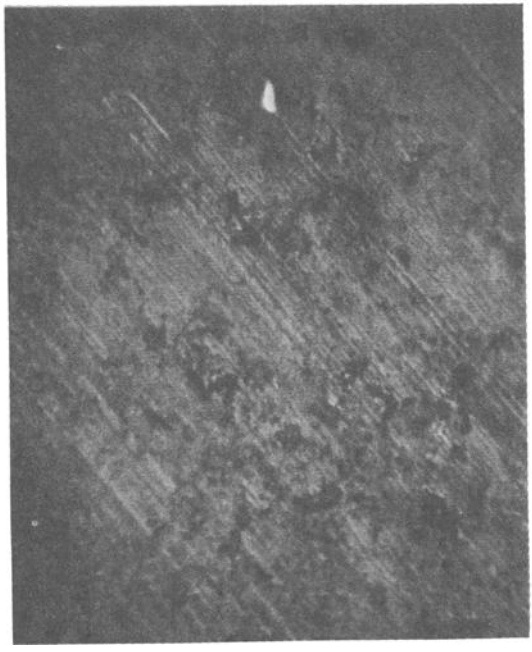

– S.C.

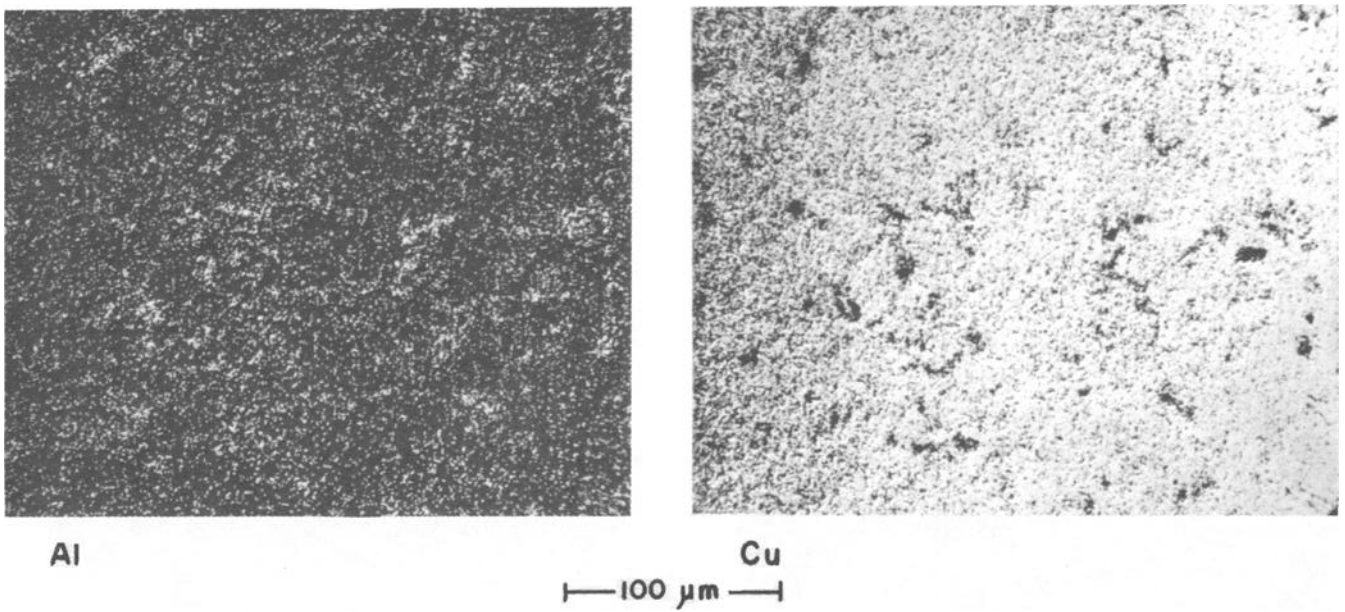


FIG. 9—*Electron microprobe inverse specimen current and X-ray rasters of the center of the block scar of aluminum bronze + 21 alumina after 5400 revolutions in Mil H5606A at 13.6 kg (30 lb).*

Fe

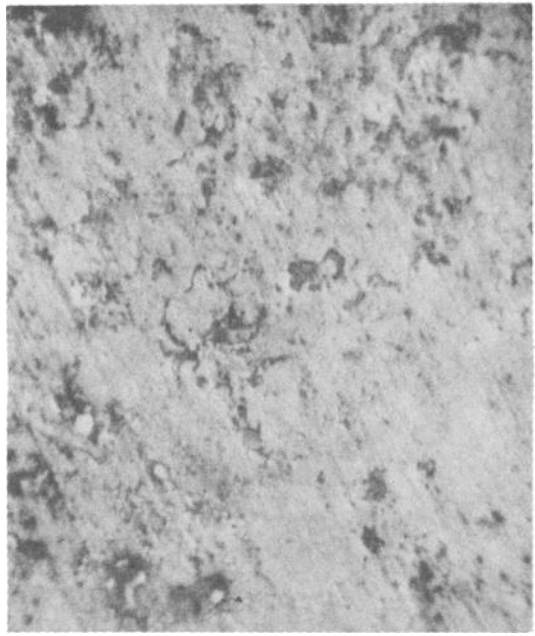

– S.C.

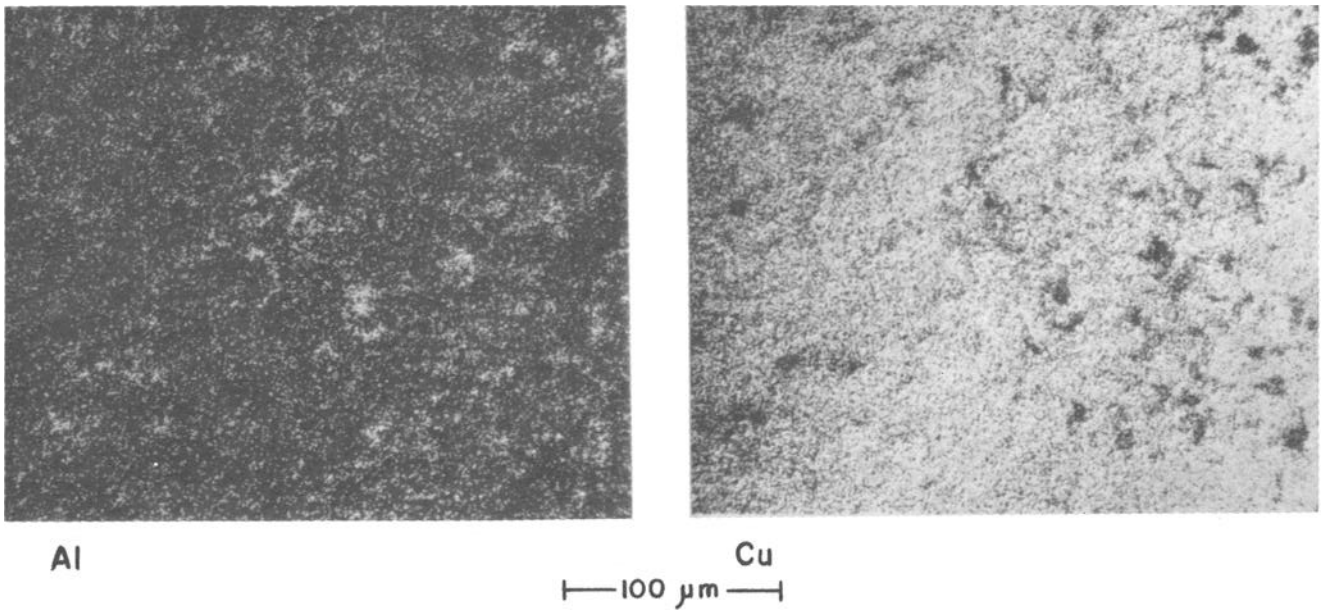


FIG. 10—*Electron microprobe inverse specimen current X-ray rasters of the center of the block scar of aluminum bronze + 21 alumina after 5400 revolutions in Mil H5606A at 81.6 kg (180 lb).*

were covered with iron than for the aluminum bronze + 7 alumina. Again there was no buildup of debris at the edges.

### Miscellaneous Additions

Among several additional types of hard-particle modifications, chromium carbide appears particularly interesting, Fig. 2. At test loads of 13.6 kg (30 lb), aluminum bronze specimens with chromium carbide additions exhibited not only very low wear scar volumes (only slightly higher than with alumina additions), but no measureable steel mating ring losses. The wear scar volumes of the aluminum bronze with chromium carbide additions were three to four times higher than with the alumina additions at 81.6-kg (180 lb) loads, but the total system loss was lower for the chromium carbide additions than for any of the alumina additions. The same pattern holds at 204-kg (450 lb) loads, although the wear was about evenly distributed between the two mating surfaces.

In addition to the systems shown in Fig. 2, oxide additions to nickel, aluminum, and steel matrices have been studied and show similar improvement in wear resistance.

### Friction Data

The oxide additions do not significantly affect the friction behavior of the plasma-deposited materials. For the most part they all fall between 0.13 and 0.15 and are significantly lower than the wrought alloy, which had values between 0.21 and 0.26 at the end of the test. Owing to space limitations, the friction behavior during the test is shown schematically in Fig. 11 in lieu of detailed tables. The plasma-deposited materials exhibited much less fluctuation in friction force during the test than the wrought aluminum bronze and rapidly declined to a constant value. The friction force of the modified bronzes usually dipped slightly below the final value within the first 100 to 200 revolutions. The coefficients of friction were virtually independent of load.

### Conclusions

The addition of less than 10 volume percent alumina (or some other hard particles) to plasma-deposited aluminum bronze reduces the wear scar volume by at least an order of magnitude compared with the same plasma-deposited material without such additions, and at least two orders of magnitude compared with its wrought alloy counterpart in an LFW-1 wear test with Mil H5606A hydraulic fluid as a lubricant. Although the hard-particle additions caused some wear of the mating steel surface, the

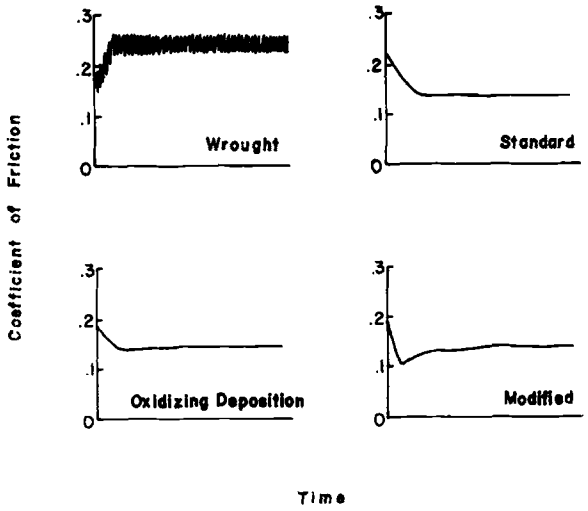


FIG. 11—*Typical friction behavior for wrought aluminum bronze AMS 4640 and modified and unmodified plasma-deposited aluminum bronze.*

total system wear was still less than that for the wrought alloy by more than an order of magnitude and significantly less than for the unmodified plasma-deposited bronzes. This increase in wear resistance was achieved without an increase in bulk hardness so that the embeddability and conformability of the bronze would not be impaired. The significant reduction in the coefficient of friction of the plasma-deposited bronze compared with the wrought alloy was not changed by the hard-particle additions.

The addition of alumina as discrete particles strengthens the compressive mechanical properties of the plasma-deposited structure, but the addition of oxides by deposition with oxidizing conditions tends to weaken it. Therefore, in spite of the fact that some increase in wear resistance can be achieved by deposition with oxidizing conditions, it is more advantageous to obtain even greater wear resistance and an increase in load-carrying capacity by the addition of discrete particles.

Similar improvements in wear resistance can be obtained with other hard-particle additions, such as chromium carbide, and with other matrices, such as nickel, aluminum, and steel.

## *Acknowledgments*

The assistance of P. W. Traub, J. W. Arthur, R. L. Meunier, W. J. Runkle, and M. W. Brooks in the collection and reduction of the data is greatly appreciated.

*W. F. Adler* [1]

# Erosion of Fused Silica by Glass Beads

**REFERENCE:** Adler, W. F., "Erosion of Fused Silica by Glass Beads," *Erosion, Wear, and Interfaces with Corrosion, ASTM STP 567*, American Society for Testing and Materials, 1974, pp. 294–315.

**ABSTRACT:** An analytical approach to particle erosion of brittle material surfaces is being developed based on a statistical model of erosion pit nucleation and growth[*1,2*].[2] For solid-particle erosion the Hertzian theory of impact is being considered in order to introduce the kinematic and material parameters into the general statistical formulation of the erosion process. In order to minimize the number of unknown factors in the initial development of a predictive erosion theory, the particular case of spherical glass beads impacting directly on the plane surface of relatively flaw-free fused silica (Corning 7940) has been investigated.

The erosion mechanisms in fused silica have been identified for both 70- and 290-$\mu$m glass beads impacting at 61 and 91.5 m/s. The experimentally observed erosion mechanisms could be correlated with the measured erosion rates, and it was substantiated that the solid-particle erosion of fused silica could be modeled in terms of preferential pit nucleation and growth. The controlled erosion tests provided evidence for the applicability of the Hertzian relations to the impact conditions associated with solid-particle erosion.

**KEY WORDS:** erosion, solid particle erosion, impact, glass, fused silica, weight loss, microscopy, evaluation, tests

The erosion of brittle materials by multiple, solid-particle impacts has been idealized as a process of pit nucleation and growth on the surface of the eroding solid[*1*].[2] An analytical model is being developed based on the assumption that the erosion pits are uniform in depth during the initial stages of growth and that typical pits undergo appreciable lateral growth before conjoining with other growing pits[*1,2*]. The eroding solid is con-

[1] Principal scientist, Advanced Materials Research Department, Bell Aerospace Division of Textron, Buffalo, N. Y. 14240.

[2] The italic numbers in brackets refer to the list of references appended to this paper.

sidered to be a laminate of plates whose individual thickness is determined by the depth of propagation of typical impact fractures.

The mathematical formulation requires the specification of a time-dependent pit nucleation probability function and growth rate for each layer of the laminate model of the eroding solid. The value of the theory as a predictive tool in the development of erosion-resistant materials depends on how much information pertaining to the kinematics of the erosive environment and the material characteristics of the eroding solid can be incorporated into the explicit analytical representations of the pit nucleation and growth rate functions. It would be satisfying to prescribe these functions on a purely analytical basis; however, this is not possible at the present time.

The pit nucleation concept is dependent on the manner in which the material's surface is fractured by the multiple solid-particle impacts. The nucleation of an erosion pit may occur through one of several processes whose relative probabilities are difficult to assess without evaluating a detailed model. This information was obtained through microscopic observations of the erosion mechanisms in a series of controlled experiments using the AFML-Bell erosion apparatus. These experiments involved the direct impact of small, spherical glass beads on the plane face of relatively flaw-free fused silica (Corning 7940) specimens in order to minimize the number of unknown factors pertaining to the kinematic and material parameters. The impact conditions were selected so that results from the Hertzian theory for the impact of a spherical elastic body on an elastic half-space could be used.

The experimental program is designed to evaluate the damage to the eroded surface of fused silica specimens after incremental exposures to the direct impact of spherical glass beads in the AFML-Bell erosion apparatus. The research reported here concentrates on identifying the fundamental mechanisms responsible for the nucleation and growth of pits in fused silica and correlating the nucleation process with the Hertz-Huber theory of impact[1].

## Experimental Procedure

Due to the low-impact velocities used in this study, it was possible to design specimens with a sizable flat surface exposed to the eroding particles. This geometry eliminated the effect of the variable angles of attack associated with the aerodynamic shapes usually employed in the AFML-Bell erosion apparatus. A special specimen holder was fabricated for the rotating arm so that these flat-faced specimens could be used. Fused silica (Corning 7940) was selected for the erosion targets. The general specimen

dimensions are indicated in Fig. 1. The diameters of the glass beads (impacting particles) were selected so that they would be small in comparison with lateral dimensions of the specimen. Under these conditions the effects of the impacts will be quite localized; the influence of the finite boundaries of the specimen will be minimized and the central region of the specimen would approximate a mathematical half-space as required in the Hertzian analysis. In order to provide an accurate appraisal of the model, spherical glass beads (3M Superbrite-Knoop Hardness No. 525) with average diameters of 70 $\mu$m and 290 $\mu$m were used. The beads showed some variation in size from these dimensions, but the sizes were quite narrowly distributed around the mean diameters. The mechanical properties of the fused silica (Corning 7940) and the glass beads are provided in Table 1.

The test conditions for the fused silica specimens are given in Table 2. Particle impact velocities of 61 and 91.5 m/s were selected on the basis

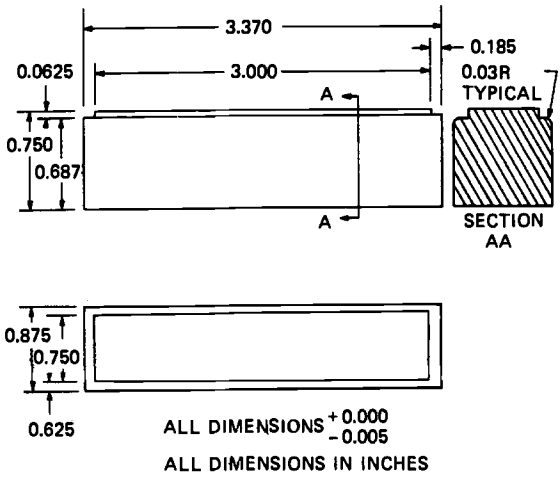


FIG. 1—*Glass erosion test specimen.*

TABLE 1—*Mechanical properties of fused silica and soda lime glass.*

| | Soda Lime Glass | Fused Silica |
|---|---|---|
| Density (kg/m$^3$) | 2400 | 2180 |
| Poisson's ratio | 0.22 | 0.17 |
| Young's modulus (N/m$^2$) | $68.95 \times 10^9$ | $73.50 \times 10^9$ |

TABLE 2—*Erosion test schedule.*

| Specimen | Bead Size, $\mu$m | Bead Flow Rate, g/s | Impact Velocity, m/s |
|---|---|---|---|
| G1 | 70 | 15.1 | 61.0 |
| G2 | 290 | 7.55 | 61.0 |
| G3 | 290 | 7.55 | 91.5 |

of adjunct experimentation using borosilicate glass specimens. Impact velocities were required which would be capable of producing ring fractures on the surface of the fused silica, but not of a magnitude such that the initial and intermediate stages of the erosion process would be complete before the various erosion mechanisms operative during different periods of the total exposure time could be identified.

In the erosion experiments conducted in the AFML-Bell erosion apparatus shown in Fig. 2, the glass beads are taken from the sand hopper by a screw-type feeder and fall down the 1⅜-in.-diameter (3.49 cm) blast tube which is approximately 7 ft (2.14 m) long. They are dropped through the plane of the rotating arm from an elliptical nozzle which has a major axis of 1⅞ in. (4.76 cm) and a minor axis of 7/8 in. (2.22 cm).

The rate of flow of the beads was calibrated by weighing the beads which fall from the tube for a number of settings on the feed mechanism. Although it was not possible to ascertain directly the actual number of beads striking the surface of the specimen, a theoretical calculation of the maximum number of impacts is possible.

The number of 290-$\mu$m beads in 0.454 kg was determined to be $1.5 \times 10^7$. There are $10^9$ 70-$\mu$m beads in 0.454 kg. The calculated number of impacts per revolution of the rotating arm was 49 000 for the 70-$\mu$m beads and 740 for the 290-$\mu$m beads at a flow rate of 7.55 g/s. The velocity, $v$, of the specimen near its midpoint on the rotating arm is related to the rotational speed of the arm, $\Omega$, measured in revolutions per minute by

$$\Omega = 3.48v$$

when $v$ is measured in m/s.

The specimens were handled with cotton gloves, weighed, and carefully mounted in the specimen holder on the blade. They were exposed to the direct impacts of the glass beads for time periods which increased with the increase in the cumulative time of exposure. The damage process in each specimen was monitored microscopically after each time increment

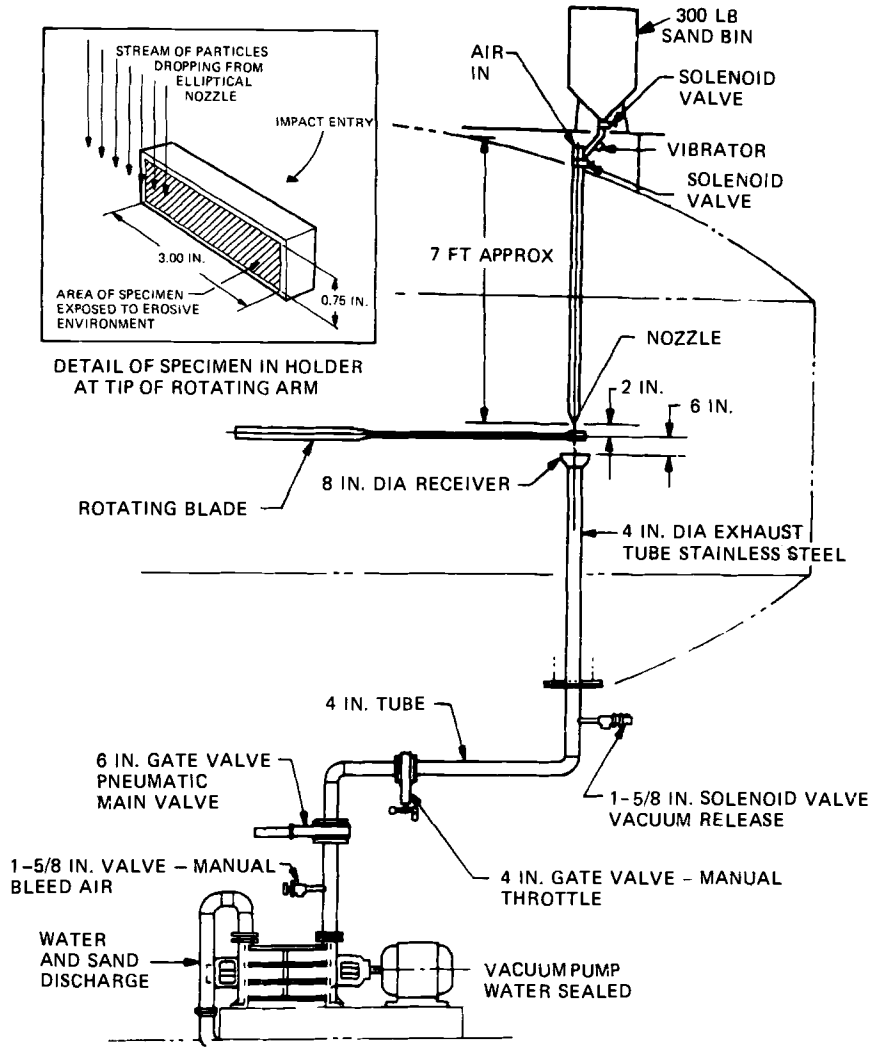


FIG. 2—*Sand injection and exhaust system for AFML-Bell erosion apparatus.*

in order to determine the erosion mechanisms responsible for the nucleation of pits in the eroding surface and their subsequent growth patterns. The scale of the damage was such that optical microscopy could be used to make the necessary observations. A special staging plate designed and fabricated for the optical microscope made it possible to return consistently to within a few mils of a particular location on the surface of a specimen.

The experimental procedure for recording the extent of the erosion

damage after each incremental exposure on the rotating arm was first to survey the entire surface for any unusual feature produced by the particle impacts. Then a total of 75 sites, approximately 1.5 mm diameter, located in the central region of the specimen was investigated in detail. In the initial stages of the erosion process the number of ring fractures was counted for each site along with the number of double, triple, and more complex ring fracture interactions. The depth of a particular feature on the surface can be measured to within a few microns using the optical microscope. By setting the focus at a level below the surface, it is possible to note the extent of the damage at this level based on areas which are in focus as the surface of the specimen is scanned.

## Erosion Mechanisms in Fused Silica

Although inorganic glasses have been used in erosion studies reported in the literature[*3–6*], no information could be found on the operative erosion mechanisms associated with the various stages of the weight-loss data for glasses subjected to multiple solid-particle impacts. The erosion data for solid particles impacting brittle materials are generally reported in terms of plots of the mass of specimen loss per unit mass of eroding particles (or an equivalent measure of erosion) as a function of the particle impingement angles. Such an approach only provides the steady-state erosion rate for a prescribed particle size (or distribution of particle sizes), particle shape, and impact velocity.

The fracture surface produced in a large glass plate by a spherical indenter appears as a circular ring on the surface of the plate and penetrates the interior of the plate to form a conical frustrum. The depth of penetration increases with increasing load. The production of ring fractures on the surface of the glass specimens by multiple particle impacts is the elemental fracture mechanism in this study; however, a single ring fracture may or may not be the nucleus for a growing erosion pit. Described in the following are detailed observations of the evolution of the material removal process in fused silica by glass bead impacts from its inception to the establishment of a steady-state removal rate.

Specimen *G1* (Table 2) was exposed to impacts by 70-$\mu$m glass beads at 61 m/s (or the equivalent of 212 rpm on the rotating arm). The bead flow rate was 15.1 g/s, so according to our analysis of the erosive environment the maximum number of bead impacts should be on the order of 98 000 impacts per revolution.

The erosion test for Specimen *G1* was exploratory. During the early stages of erosion, under 8 min, microscopic examination of the eroded surface at $\times$110 showed that it was composed of a distribution of ring

fractures, small pitted areas less than 25 $\mu$m diameter, and a distribution of very small imprints, less than 2.5 $\mu$m, due to collisions which did not produce measurable damage. The average diameter of the ring fractures was 76 $\mu$m with very little deviation from this value. The formation of these rings on the surface and their interaction were assumed to be the primary mechanism for material removal. However, this assumption proved to be false. The investigation of these large ring fractures is described elsewhere[1] and represents anomalous behavior which contributes little to the overall material removal process.

At higher magnification, $\times$440, it was seen that the small pits in the range of slightly less than 2.5 $\mu$m to approximately 25 $\mu$m were in essence material removal on the periphery of incomplete ring fractures whose average diameter was 22.8 $\mu$m. Complete ring fractures were also found, but usually only a portion of the material along the circumference is removed. These fractures were single rings, so the force imparted by the particles to the surface must have been just sufficient to create the ring fractures. The rings are formed preferentially and seem to congregate in the neighborhood of existing rings. The depth of the material removal is only 5 to 10 $\mu$m per impact.

Specimen *G2* (Table 2) was exposed to the 290-$\mu$m glass beads at a velocity of 61 m/s and a bead flow rate of 7.55 g/s. The specimen experiences a maximum of 740 particle impacts per revolution of the rotating arm according to the theoretical estimate. The arm rotates at 212 rpm to attain a linear velocity of 61 m/s at the center of the specimen. Specimen *G3* was impacted by the 290-$\mu$m beads at 91.5 m/s (or 318 rpm) at the same bead flow rate of 7.55 g/s. The erosion process for both specimens is described in the following, since the erosion mechanisms were the same, differing only in the quantitative aspects of the process.

The form of the ring fractures produced on the glass surfaces at very short exposure times was observed optically using Nomarsky phase interference and with transmission electron microscopy (TEM) using surface replicas. The optical micrographs in Fig. 3 show that the central region of the inner ring is not damaged by the impacts. It was not possible to see the cone fractures extending into the interior of the specimens at this point; however, subsurface interactions between the transient stress fields produced by particles impacting in the vicinity of already existing fracture surfaces could be observed by the reflection of light from these surfaces. A good example of this effect is seen in Fig. 3*c*, where a number of interactions have taken place. The ring fractures at 91.5 m/s have outer rings which are approximately 30 percent larger than the outer rings for the ring fractures at 61 m/s. The average diameter of the inner rings for

the fractures formed at 61 and 91.5 m/s is approximately 63.5 $\mu$m; however, the range of the inner ring sizes at 91.5 m/s is fairly broad (45 to 84 $\mu$m), whereas the range of inner ring sizes at 61 m/s is relatively narrow.

Figure 4 shows TEMs of the ring fracture formed in the early stages of the erosion process. Since the stress components are symmetrical about the contact area, the initial cracks will tend to be arcs of circles. However, the relaxation brought about by these fractures will produce a redistribution of stress with the tendency for the crack to propagate in a direction perpendicular to local trajectories of the maximum tensile stress. If the loading is continued, circular fractures will be produced at other flaws in the same manner as these initial cracks. If the crack is able to follow the trajectories dictated by the maximum tensile stress, it will not be circular. If, however, for any reason it is prevented from doing so, it may follow a more nearly circular outline for a short time and then branch off so as to bridge the distance between its present position and that of another circular crack. If fractures have begun at several places, development of each crack in this manner is to be expected, giving rise to the complicated figures found in practice. The composite micrograph in Fig. 4 is indicative of this process.

The observations of the specimen surfaces using Nomarsky phase intereference and surface replication do not provide information pertaining to the characteristic subsurface conical fracture. The extent of the conical fracture surfaces extending into the interior of the specimen could not be seen around isolated ring fractures occurring in the very early stages of the erosion process. The features of the subsurface fracture surface did become evident when a second ring fracture occurred in the vicinity of an existing one. Interactions between the dynamic stress field of an impacting particle which results in a new cone fracture and the flawed surface of a preexisting ring fracture were rarely found at separation distances greater than 300 $\mu$m. This effect was seen repeatedly in the microscopic observations. In nonoverlapping rings the interaction generally produced a short cracked boundary representing the intersection of the conical fracture associated with each ring fracture. This clearly visible demarcation is perpendicular to the line between the centers of the two adjacent ring fractures. Overlapping ring fractures show surprisingly little influence on each other as seen in the Nomarsky intereference micrographs, Fig. 3. The significance of a particle impacting just outside the periphery of an existing ring fracture is explained next in relation to the process of material removal.

As more particles impact the neighborhood of the preexisting ring frac-

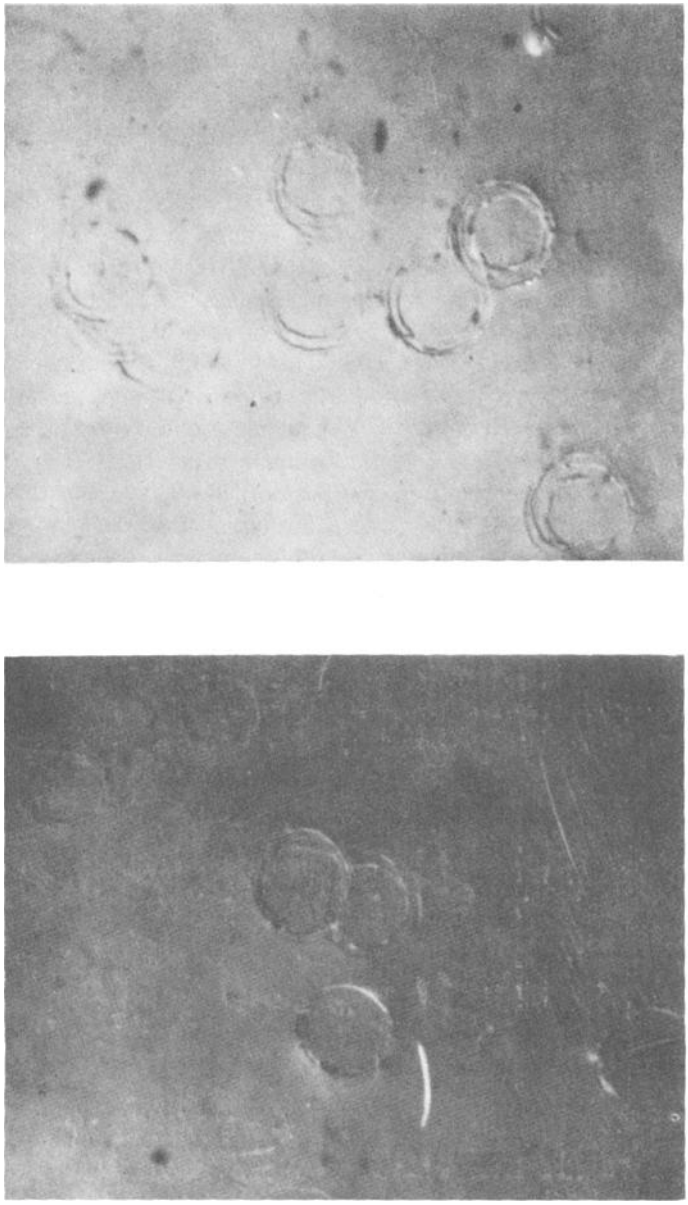

(a) IMPACT VELOCITY 61 m/s (b)

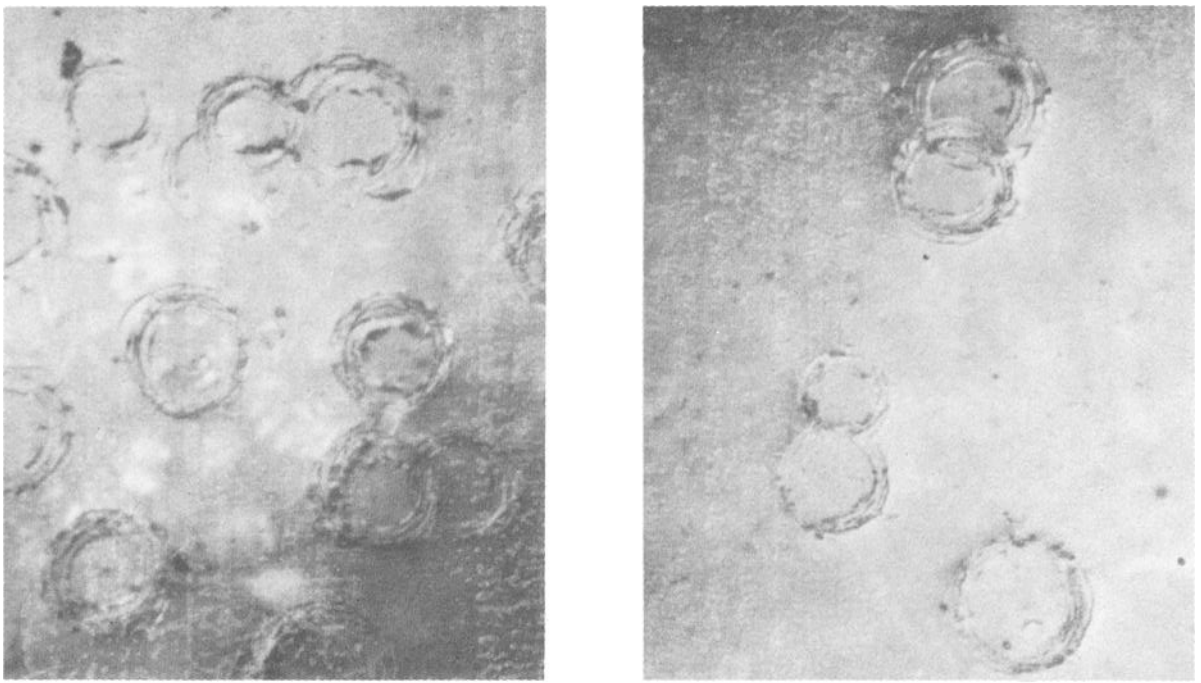


FIG. 3—*Ring fracture on the surface of glass specimens after impact with 290-μm beads for 1 s (~ ×125).*

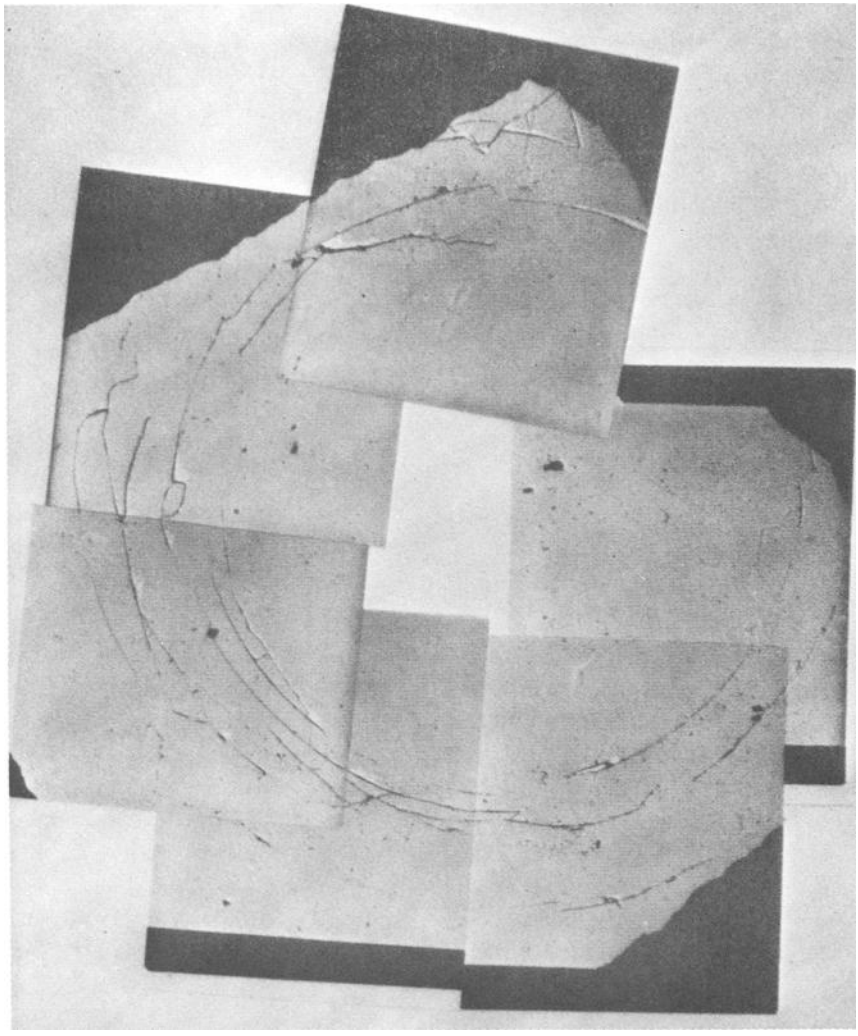

FIG. 4—*Ring fracture on Specimen* G2 *after an exposure time of 1 s (~ ×1200).*

tures, a complex pattern of subsurface fractures develops. The subsurface fracture process continues without any significant material removal from the surface. Subsequent impacts on the interstitial regions between cone fractures produce an increasingly complex network of fracture surfaces, but no new cone fractures are produced in the highly flawed interstitial areas. The general appearance of the surface of Specimen *G2* at 15 and 60 s is indicated in Fig. 5. The small white spots on the micrograph are

evidence of collisions which did not result in ring fractures. The particle bombardment has relatively little influence on the interior surface region of the ring fractures. The interstitial regions after an exposure time of 60 s are still intact over most of the surface area of Specimen *G2* with very little material being removed from the specimen as seen from the weight-loss data in Fig. 6.

The distribution of diameters of the inner rings of the ring fracture produced in Specimens *G2* and *G3* is shown in Fig. 7. These data were obtained at an intermediate stage of the overall exposure for each specimen and are based on measurements of 200 rings on the surface of each specimen. The average diameter for the inner rings of Specimen *G2* is 66.8 $\mu$m, while it is 63.9 $\mu$m for Specimen *G3*. This result is consistent with the average diameter of the inner rings evaluated in the very early stage of the erosion process.

Surveying the central region of Specimen *G2*, it was found that the density of ring fractures per square centimeter was 515 at 15 s, 640 at 60 s, and 455 at 130 s. Similar data for Specimen *G3* shows that the ring fracture density (rings per square centimeter) is 282 at 3 s and 304 at 18 s, reaching a maximum value within the given time range. The probability for the formation of ring fractures is quite high under these impact conditions. From these data it is seen that the maximum number of ring fractures is established quite early in the erosion process and that a majority of the rings formed survive the subsequent bombardment of particles as the erosion process continues. The reason for the decrease in the cone density as the exposure time increases is associated with the early removal of certain cones from the bulk specimen. The explanation established from the experimental observations of particles impacting just outside of existing ring fractures is illustrated in Fig. 8. The top surface appears as in Fig. 8*a*. A cross section of the conical fracture surfaces indicates that Cones *A* and *C* intersect below Cone *B* within the range of interaction described earlier. Such conditions have been observed microscopically. Cone *B* is only partially attached to the bulk material while Cones *A* and *C* are firmly anchored. The colliding particles are capable of producing fractures around Cone *B* which weaken its existing support, and ultimately it breaks loose.

The depth of the conical fracture surface is found to be fairly constant over the entire eroded area. For Specimen *G2* the cone depth is approximately 50 to 60 $\mu$m while for Specimen *G3* the fracture surface penetrates 80 to 90 $\mu$m below the surface. The larger depths in Specimen *G3* are attributed to the higher velocity of approach.

Following the erosion process in Specimen *G2* it was found that around

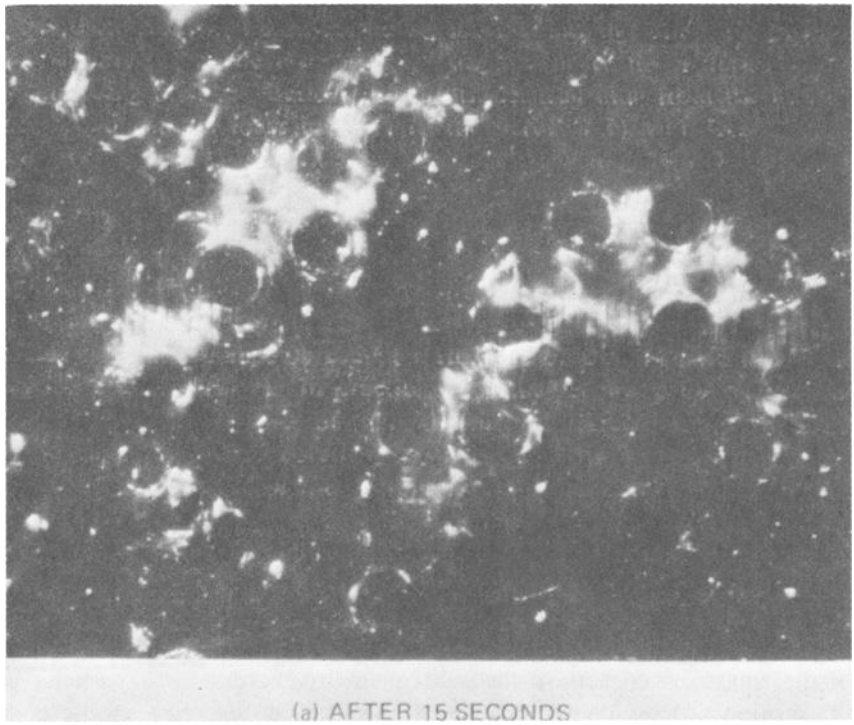


FIG. 5—*Appearance of the surface of Specimen* G2 (~ ×100).

an exposure time of 90 s large-scale removal of material from the interstitial regions between the firmly anchored truncated cones is the primary erosion mechanism. The accelerated rate of material removal is quite evident in Fig. 6. The glass in the interstitial areas is severely fractured and sizable areas are removed during each time increment. The micrograph in Fig. 9 illustrates this process. Just above the center of Fig. 9 there is a triplet of cones from which the interstitial glass has been removed. In the vicinity of the triplet the imprint of two cones which did not survive the impact loadings is also clearly visible. The conditions for their disintegration correspond to that shown schematically in Fig. 8. A number of other cones which are going to be removed with the interstitial glass can also be seen in Fig. 9. Only the interstitial material is being removed up to an exposure time of 130 s for Specimen *G2* as indicated by the microscopic observations. The firmly anchored cones are relatively unaffected by the particle impacts during this phase of the erosion process. A number of

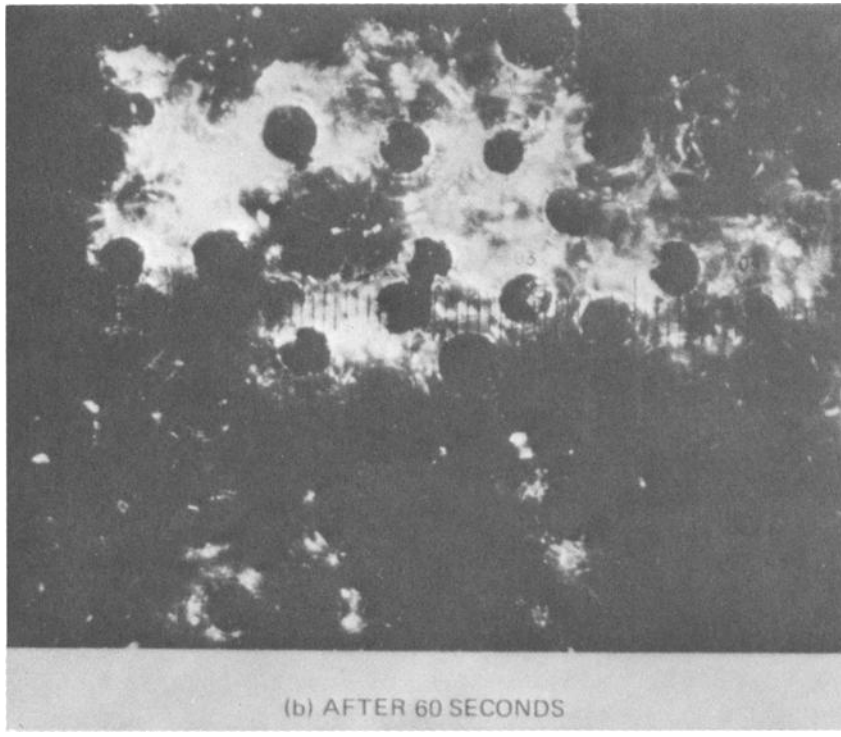


FIG. 5—*(Continued).*

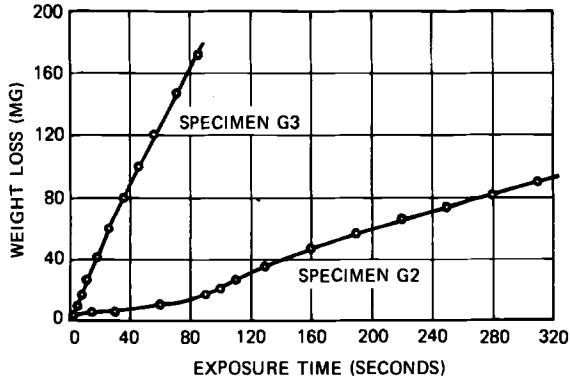


FIG. 6—*Weight-loss data for Specimens* G2 *and* G3.

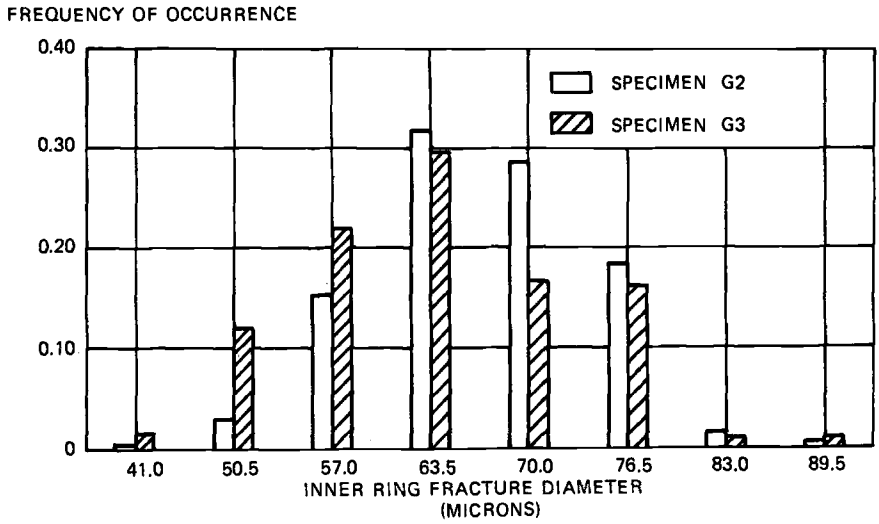


FIG. 7—*Distribution of diameters of ring fractures in Specimens* G2 *and* G3.

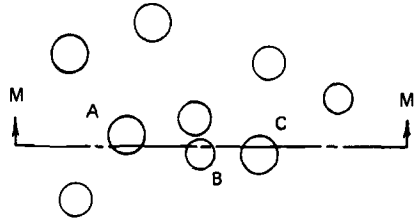


(A) RING FRACTURES ON GLASS SURFACE

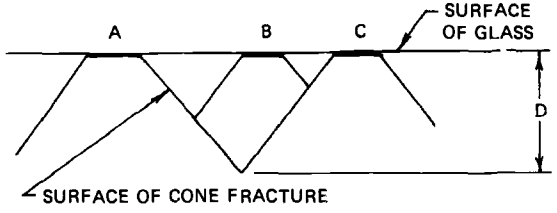


(B) ENLARGEMENT OF SECTION MM

FIG. 8—*Mechanism for removal of cone fractures from surface.*

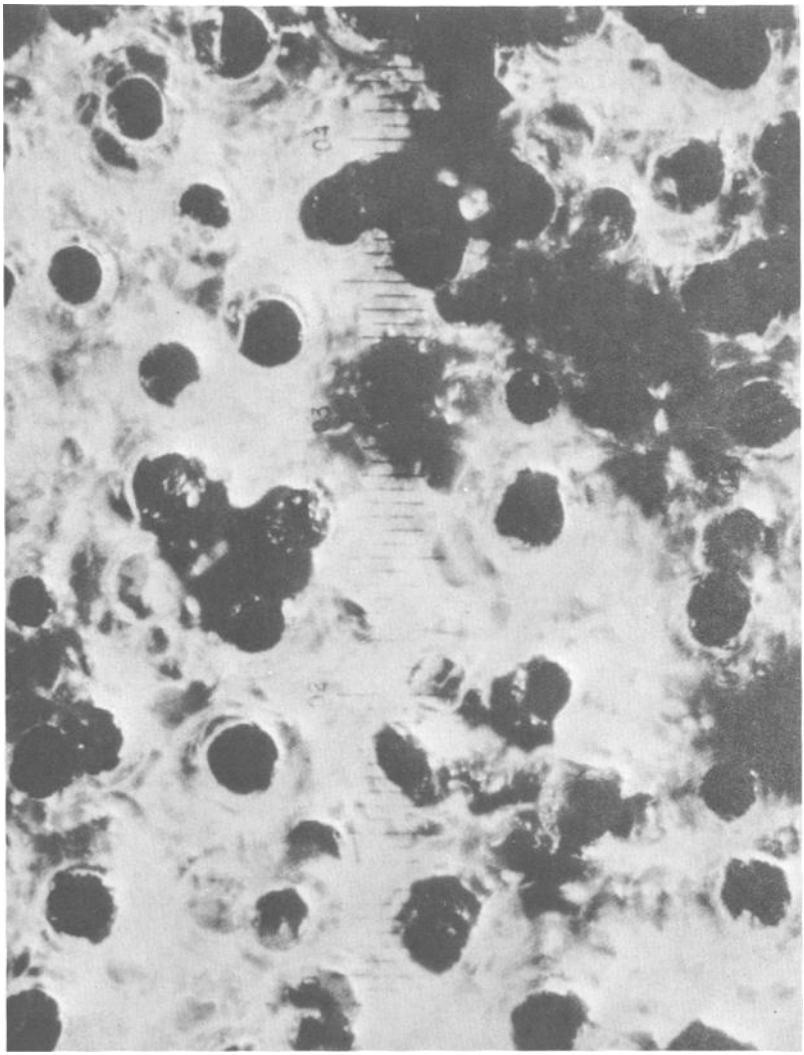

FIG. 9—*Removal of fractured glass from interstitial regions on surface of Specimen* G2 (~ ×110).

areas on the specimen's surface were observed microscopically during this period of the erosion process, and it was found that the growth behavior of nucleated regions was quite irregular. At 130 s most of the interstitial material was removed from the primary erosion area on the specimen's surface. The form of the weight-loss data for Specimen *G2* (Fig. 6) shows the accelerated rate of material removal which occurs between exposure times of 90 and 130 s. The removal of the interstitial material completes another stage of the erosion process which overlaps with the final stage.

The general appearance of the eroded surface is now comparable to a waffle iron. Dense arrays of solid conical frustrums are protruding from the surface and are generally still intact. The impacting particles do little damage in a single impact. The sides of the cones and common points of intersection are highly resistant to material removal. The particles can only chip small pieces from the protruding frustrums, beginning at the plateau and slowly working down to the bulk material. This chipping process eventually removes the frustrums from the surface and continues into the bulk material.

The same sequence of events occurred during the erosion of Specimen *G3* (Table 2) except that the initial phases of the material removal process are greatly accelerated. The distinct phases illustrated here for Specimen *G2* have a greater tendency to overlap with regard to their time evolution. This behavior has been verified through microscopic examination of the progressively eroded surface of Specimen *G3* and can be directly related to the form of the weight-loss data recorded in Fig 6.

The condition of the glass beads was checked microscopically after they collided with the specimens in the erosion tests. No fragmentation of the beads was found, and very few fractures could be found on the bead surfaces.

## Discussion

The erosion mechanisms operative on flat surfaces of fused silica glass specimens impacted by 70- and 290-$\mu$m glass beads have been established through detailed microscopic investigations of progressively eroded surfaces. The following patterns emerge.

The basic element for the initiation of erosion damage in glass specimens is the ring fracture. The diameter of the ring and the geometry of the conical fracture surface extending into the bulk of glass plates impacted by glass beads are dependent on the radius and impact velocity of the glass beads as well as the material properties of the colliding bodies. For the range of conditions used in this program the conical fracture surfaces are typically 5 to 10 $\mu$m deep and on the order of 25 $\mu$m in diameter at the

surface of the glass plate for the 70-$\mu$m beads. The 290-$\mu$m beads produce fracture surfaces which are 50 to 90 $\mu$m deep and approximately 65 $\mu$m in diameter at the surface of the glass plate.

Subsequent impacts in the vicinity of the shallow-fracture frustrums produced by the 70-$\mu$m beads initiate chipping of material from the surface on a very fine scale. Microscopic observations of the time evolution of the eroded surface indicate that once a ring fracture occurs it is the nucleation site for the removal of material. The eroded areas grow preferentially around a ring fracture by fine-scale chipping of material due to intersecting ring fractures. This process continues to remove material from the surface layer and exposes a highly fractured and irregular subsurface from which material is removed by chipping of small pieces with each impact.

In the case of the 290-$\mu$m beads another impact in the vicinity of a deep conical fracture surface is generally not sufficient to cause material removal but contributes instead to a more severely fractured subsurface. Additional impacts in this region produce a predictable pattern of subsurface fractures at depths which still allow a substantial layer of overlying material to remain intact. It is only after a number of impacts have occurred in the vicinity of the initial ring fracture that removal of the material exterior to the developing distribution of conical frustrums takes place. The material contained within the frustrums formed by the conical fracture surfaces is more resistant to erosive attack than the highly fractured interstitial regions; therefore, material removal from the interstitial volumes takes place at a higher rate than during the ring fracture development phase. The interstitial material is removed, leaving a dense distribution of solid frustrums protruding from the bulk specimen. The impacting beads chip small pieces of material from these frustrums at a slower rate than in the interstitial material removal stage. As the frustrums erode, more surface area is susceptible to bead impacts. Chipping of the highly fractured and irregular surface of the bulk material takes place at a uniform rate and constitutes the final phase of the erosion process.

The microscopic observations of the erosion process associated with the two bead sizes used in the erosion tests indicate that the depth of the cone fracture surface determines whether a single impact in the vicinity of a preexisting ring fracture will result in material removal or whether a number of impacts are required before material removal is initiated. The form of the nucleation process for material removal is therefore dependent on the radius and velocity of the impacting glass bead; however, the general erosion process remains unchanged over the range of bead sizes and impact velocities used in this research.

With this understanding of the microscopic erosion mechanisms con-

tributing to material removal as a function of exposure time, it is necessary to translate the qualitative data into quantitative terms. As a first step toward this objective, the applicability of the Hertz-Huber theory is ascertained.

The equivalent static load, radius of the contact area, and duration of impact can be calculated from the Hertzian theory of impact using the velocities for the erosion test conditions specified in Table 2 and the mechanical properties in Table 1[*1*]. The results of these computations are listed in Table 3.

The results in Table 3 indicate that the radii of the glass beads are on the order of four times the maximum contact radius for each impact condition. The magnitude of this ratio may cast some doubt on the satisfaction of the basic assumptions of the Hertzian analysis. Assuming the Hertzian approach is valid, the calculated duration of contact (on the order of $10^{-7}$ seconds) indicates that a dilatational wave in fused silica will travel a maximum of 0.25 cm from the initial point of contact during this time interval. The shear and Rayleigh waves will have traveled only 0.15 cm. On the basis of these distances in relation to the dimensions of the maximum contact area and bead size, the quasi-static loading requirements for the treatment of impact phenomena can also be questioned. According to calculations of the dynamic contact stress at the boundary of the area of contact, provided by Tsai[*7*], it is seen that the radial tensile stress component is essentially equal to the Hertzian radial stress for a maximum radius of contact less than 0.25 mm independent of the duration of contact. This would imply that the Hertzian approach may be valid for the test conditions which are of interest in particulate erosion studies. The experi-

TABLE 3—*Hertzian impact parameters for fused silica.*

| | Equivalent Static Load, $P$(N) | Radius of Contact Circle, $a(\mu m)$ | Duration of Contact, $T$(s) |
|---|---|---|---|
| 70-$\mu$m Glass Beads | | | |
| 61.0 m/s | 0.965 | 8.9 | $1.19 \times 10^{-7}$ |
| 91.5 m/s | 1.59 | 10.5 | $1.10 \times 10^{-7}$ |
| 290-$\mu$m Glass Beads | | | |
| 61.0 m/s | 16.0 | 36.3 | $4.76 \times 10^{-7}$ |
| 91.5 m/s | 26.4 | 43.0 | $4.40 \times 10^{-7}$ |

mental observations of ring fracture formation are used to determine the applicability of the Hertzian analysis.

The average diameter for the inner ring fracture for Specimen *G2* was found to be 67 $\mu$m, while it was 64 $\mu$m for Specimen *G3*. The Hertzian theory predicts that the diameter of the contact area for Specimens *G2* and *G3* should be 72.5 and 86 $\mu$m, respectively. A very high probability was found for the occurrence of multiple ring fractures with the outer ring diameters exceeding the calculated values. The comparison between theory and experiment is reasonable. The stress generated at an intermediate stage of the compression phase of the impact is sufficient to initiate ring fractures, but the magnitude of the load continues to act along with the expansion of the contact area. Additional ring fractures are produced as a larger area reaches the critical stress level. The process stops when the maximum contact area is reached where it is still possible for a crack to develop just outside this region before the magnitude of the load begins to subside. The static experiment of Sheldon and Finnie[*4*] for the variation of the center of approach of a 1/8-in. (3.175 mm) steel ball on a glass plate indicates that the Hertzian expression for the distance of approach of the two bodies deviates from the experimental value by only 25 percent when the applied load is more than 120 times the load for the initial ring fracture. It thus appears that cracked material will transmit load. Sheldon and Finnie state that this is due to the fact that the stresses in the contact region are primarily compressive. The ring fractures formed on the surface of Specimen *G1* at 61 m/s are only single rings with an estimated average diameter of 23 $\mu$m, which compares favorably with the Hertzian prediction of 17.8 $\mu$m.

The measurements of the ring fracture diameters would tend to support the Hertzian evaluation of the contact stresses for the erosion test conditions used in this research. The Hertzian expression for the contact stresses will therefore be used to construct an appropriate fracture criterion for the small bead sizes used in the experimental program. This task will be considered in future work.

## Conclusions

Microscopic examination of the erosion of fused silica by repetitive collisions with 70- and 290-$\mu$m glass beads at moderate impact velocities confirms that material is removed through a process of pit nucleation and growth, which is the basis for a recently developed statistical model for characterizing this form of erosion behavior[*1*]. The operative erosion mechanisms in fused silica over a range of impact conditions have been identified on the basis of a series of controlled experiments employing the

AFML-Bell rotating-arm facility. The quantitative evaluation of ring fracture formation in these tests supports the preliminary observation that the Hertz-Huber theory of impact is applicable to the impact conditions on a scale appropriate to solid-particle erosion by spherical bodies.

*Acknowledgment*

This research was supported by the Air Force Materials Laboratory under Contract No. F33615-71-C-1528.

## References

[1] Adler, W. F. and Sha, G. T., "Analytical Modeling of Subsonic Particle Erosion," AFML-TR-72-144, Air Force Materials Laboratory, July 1972.
[2] Adler, W. F., "Analytical Modeling of Liquid and Solid Particle Erosion," AFML-TR-73-174, Air Force Materials Laboratory, Sept. 1973.
[3] Bitter, J. G. A., *Wear*, Vol. 6, 1963, pp. 5–21 and 169–186.
[4] Sheldon, G. L. and Finnie, I., *Transactions*, American Society of Mechanical Engineers, *Journal of Engineering for Industry*, Vol. 88B, 1966, pp. 393–400.
[5] Head, W. J. and Harr, M. E., *Wear*, Vol. 15, 1970, pp. 1–46.
[6] Sheldon, G. L., *Transactions*, American Society of Mechanical Engineers, *Journal of Basic Engineering*, Vol. 92D, 1970, pp. 619–626.
[7] Tsai, Y. M., *International Journal of Solids and Structures*, Vol. 7, 1971, pp. 543–558.

# DISCUSSION

*A. F. Conn*[1]—The talk by Dr. Adler represents a well-planned and expertly presented approach toward what must eventually be the answer to a complete explanation of the response of materials to a raindrop impact. In his oral presentation he suggested that he was not going to side either with Dr. William Morris (formerly of Bell Aerospace) or with me with regard to the discussion of whether a uniaxial strain or a uniaxial stress description is the correct one to use in trying to describe rain erosion phenomenon. On the contrary, Dr. Adler has stated, and I could not agree more, that the phenomenon is an extremely complex spherical wave propagation situation. It was also nice to hear Dr. Adler reinforce what we have been trying to emphasize, namely, the importance of using dynamic properties when studying rain erosion, particularly for the highly elastomeric, extremely rate-dependent materials, and the impossibility of ever making any sense out of the problem if one tries to use the statically measured responses of such materials.

Let me emphasize that I do not claim that the waves generated by a drop impact are simple bar waves, and of course I am aware of their spherical nature. However, the results of our research, as described most recently in our paper in this volume,[2] indicate that one may make many useful engineering correlations with the rain erosion response of these materials by using the results of such uniaxial stress testing. However, the complete solution of this problem, as Dr. Adler has so well described it, must be the result of the eventual understanding of the full spherical wave problem. This paper by Dr. Adler, and the clear indication he has given of the usefulness and limits of Dr. Peterson's paper,[3] are valuable contributions to the rain erosion literature.

[1] Principal research scientist and head, Materials Sciences Division, HYDRONAUTICS, Incorporated, Laurel, Md. 20810.

[2] Conn, A. F. and Rudy, S. L., this volume, pp. 239–269.

[3] Peterson, F. B., "Some Considerations of Material Response Due to Liquid-Solid Impact," American Society of Mechanical Engineers' Winter Annual Meeting, Nov. 1972, Paper No. 72-WA/FE-27.

*A. Begelinger* [1] *and A. W. J. de Gee* [1]

# A New Method for Testing Brake Lining Materials

**REFERENCE:** Begelinger, A. and de Gee, A. W. J., "A New Method for Testing Brake Lining Materials," *Erosion, Wear, and Interfaces with Corrosion, ASTM STP 567*, American Society for Testing and Materials, 1974, pp. 316–335.

**ABSTRACT:** A new method for testing brake lining materials in the laboratory is described. This method is essentially isothermal by nature, thus avoiding the usual problems associated with differences between the heat-transfer characteristics of brake assemblies in road vehicles and those of laboratory test rigs. As an example of application of the method, friction-time-temperature curves of five different brake lining materials are presented and discussed in terms of time- and temperature-depending transformations in the composition of the lining materials.

The quality of the materials is described by the following properties: temperature range in which glazing effects occur; temperature range in which carbonization effects occur; steady-state value of the coefficient of friction; wear (decrease in thickness) of the lining; and sensitivity of the lining material to moisture.

**KEY WORDS:** brake linings, test method, pin and ring machine, erosion, induction heating, isothermal conditions, temperature, friction, wear, evaluation, tests

The quality of brake lining materials depends on a number of factors that relate to safety, endurance, and air pollution. However, it is of primary importance that the coefficient of friction between a brake lining and the mating drum or disk should be high and constant.

Brake linings, composed on the basis of organic compounds (resins and synthetic rubbers), have a relatively poor capacity for energy adsorption. In case of high-duty application (emergency stop) they "fade" easily, that is, they suffer a fall in friction at elevated surface temperature. This fading

[1] Senior research associate and head of department, Tribology Department, Metal Research Institute TNO, Apeldoorn, The Netherlands.

effect is associated with decomposition and evaporation of the organic compounds. Evaporation effects may generate gas pressure at the interface between the lining and mating surface. This may provide aerodynamic gas lubrication, with the result that, temporarily, friction is lowered dramatically. Cooling down of brakes which suffer from fading effects may lead to the phenomenon known as "delayed fade." This is associated with the fact that decomposition and partial evaporation of the organic compounds at a transient high temperature may—upon cooling down—result in the formation of a glassy or "glazed" surface with relatively low friction.

After initial fading effects, prolonged use at high temperature may lead to an appreciable increase in friction, sometimes to values above those found with a new lining. This phenomenon, currently known as "over-recovery," is also associated with transformations in the composition of the organic material (usually carbonization). Actually, over-recovery is a particularly dangerous type of friction instability, because automotive brakes are normally designed to show fading effects at elevated temperature so that, as the temperature rises, more of the braking effort will be shifted to the cooler wheels[*1*].[2]

The foregoing considerations lead to the requirement that a good lining material should have a thermal stability, high enough to survive brief periods of high-duty application (emergency stops) without giving problems in a later stage of operation. Obviously, a good lining should preserve its desirable friction characteristics, not only at elevated temperatures, but also under atmospheric conditions that deviate from "normal." In this respect insensitivity to moisture is an important quality criterion.

A next and obvious requirement is that the wear rates of both the lining material and the mating metal of drum or disk should be low. Finally, wear debris, formed during use, should not be toxic. In this respect, attention should be paid to the fact that certain crystallographic forms of asbestos, the usual filler material for organic brake materials, may be dangerous upon inhalation[*2,3*].

The purpose of the research program which forms the basis for this paper was to design a rapid testing method for screening new brake lining materials developed in industry. In the course of this program some 25 lining materials were characterized with respect to coefficient of friction, wear, thermal stability, reaction to intermediate exposure to moisture and production of deleterious waste products. After designing a test method and screening the lining materials, the two best linings were selected for

[2] The italic numbers in brackets refer to the list of references appended to this paper.

field trials. Both were found to be perfectly suited for the practical application at hand.

The present paper serves the purpose of making the new testing method more widely known. For this reason, characteristic results of friction and wear testing of five materials (for the present purpose presented as materials A, B, C, D, and E) are shown and discussed in detail.

## Method

In establishing friction and wear characteristics of materials, it must always be realized that the properties of the friction system may change considerably during use as a result of thermally induced transformations in the surface zone. While this statement holds for any combination of materials, it is extremely important in the case of brake lining materials, in particular because of two reasons:

1. Brake lining materials operate under conditions of dry friction; in order to function adequately, the friction coefficient between lining material and mating material must be high (that is, usually between 0.3 and 0.5), which means that considerable frictional heating occurs.

2. Many brake lining materials are composed on the basis of organic materials (resins and synthetic rubbers); this makes these materials particularly sensitive to thermal deterioration effects.

Because of this, it is generally recognized[*4–6*] that the determination and (in testing) the simulation of the temperatures reached at the friction surface during brake applications form one of the fundamental problems in studies devoted to the braking of vehicles. The main factors that determine the surface temperatures attained during braking are the rate of deceleration and the duration of braking, the road speeds at each brake application, the dimensions and physical properties of the drums or disks and linings, the frequency of the brake applications, and the degree of air cooling from finning and wheels. Obviously, these factors each play a different part in the different kinds of braking likely to be encountered; namely, continuous brake applications to bring the vehicle to rest and intermittent braking to control vehicle speed in traffic or when traveling downhill. Consequently, in each kind of braking assembly as well as in each kind of braking procedure, different temperatures may occur.

These considerations have lead to the widespread practice of testing brake lining materials in their natural habitat, that is, in actual vehicle applications[*7,8*]. Although, admittedly, a road test in a vehicle should form the final step in any brake lining development program, the *exclusive* use of vehicle testing in developing new brake lining materials is undoubtedly cumbersome[*9*]. Thus, there has always been a tendency toward

development of cheap, reliable methods for the preselection of potential brake lining materials in the laboratory[*1*,*5*,*6*,*9–11*].

The different laboratory methods so far developed have one thing in common; namely, they are essentially *nonisothermal.* This means that although additional external heating is sometimes applied the interface temperature is determined primarily by the generation of frictional heat. This creates a problem, because it is difficult to measure or accurately calculate such friction-induced interface temperatures. Usually attempts to solve this problem are by simulating as much as possible the heat conductivity properties of the vehicle system in the laboratory test rig, or by performing tests at constant torque.

In the present case, the aforementioned difficulty was overcome by using an essentially isothermal test method. In this method, a small specimen, machined from the lining material to be tested, is pressed for a brief period of time (for example, 5 s) against the curved surface of a metal ring, machined from drum or disk material. Figure 1 shows the essential elements of the apparatus. Figure 2 shows four lining specimen-ring combinations, tested at different temperatures.

Increase in temperature as a result of friction is virtually avoided by choosing a low speed of rotation (for example, 0.1 m/s), and "thermal

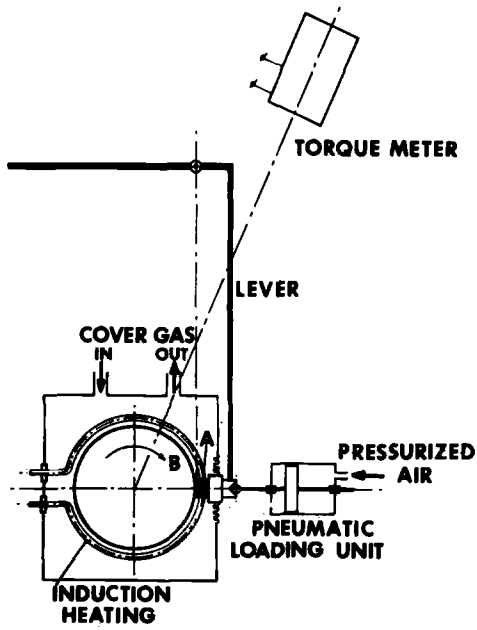


FIG. 1—*Essential elements of test apparatus.*

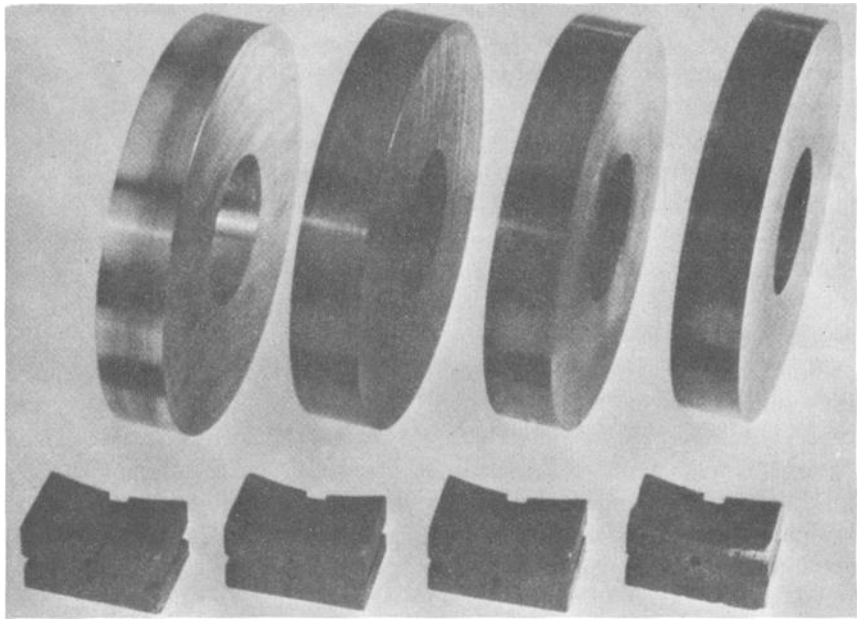

FIG. 2—*Four lining specimen-ring combinations, tested at different temperatures.*

loading" of the surface zone of the lining specimen is obtained by heating up the ring to the desired experimental temperature, prior to contact with the specimen. This is done by induction heating.

The pneumatic loading system is designed in such a way that the load can be built up from zero to the test value (for example, 200 N) in less than 0.2 s.

After termination of the first contact period, the load is removed, the lining specimen is moved backwards, and a heat shield is inserted between the ring and the lining specimen. After reconditioning the lining specimen (cooling down to room temperature, adjustment of humidity conditions, etc.,) the foregoing procedure is repeated as many times as is considered necessary (that is, usually until friction has attained a steady-state value).

In this manner significant information on the behavior of friction as a function of time (number of contact periods) can be obtained. The relation between friction and temperature can be established by performing tests at different ring temperatures. If transition phenomena are observed, the transition temperature, or the transition temperature range, can be determined accurately by performing additional experiments at intermediate temperature intervals.

The wear behavior of the lining material can be characterized by measuring the decrease in thickness of the lining specimen with a dial gage after each contact period or after a prearranged number of contact periods. Since, usually, the number of contact periods in one test run is limited to about 30 (the coefficient of friction then having attained its stationary value), the total testing time in one test run is usually limited to about 150 s. In such a short time, the amount of wear is necessarily very limited (that is, on the order of 1 to 10 $\mu$m). As this is about the lower limit at which dial gage measurements can still be performed with an acceptable degree of accuracy, control experiments are usually performed. In these control experiments a lining specimen is brought into contact with a preheated ring for an extended period of time, and wear is determined, for example, after 8 h continuous running.

In designing the aforementioned method it has been assumed that the condition of the upper surface zone of the lining specimen—rather than its outer surface—determines the frictional behavior of the system. As the contact between the lining specimen and the ring is of an intimate nature, the outer surface of the lining specimen acquires a temperature, $T_s$, which is nearly equal to the ring temperature immediately upon contact between the lining specimen and the ring. $T_s$ is kept constant throughout the entire contact period by induction heating of the ring. In the Appendix it is shown that the temperature of the lining specimen at a depth of 10 $\mu$m below the contact surface becomes equal to 0.99 $T_s$ in about 600 $\mu$s. As the total amount of wear of the lining material during this time period is only about $1.10^{-4}\mu$m, the statement that the method is essentially isothermal by nature seems fully justified.

It should be emphasized that the method represents a form of "accelerated testing," because of the fact that in actual brake applications it may take a considerable number of subsequent brake applications before the frictional interface acquires a temperature of, for instance, 300°C (572°F). This effect is not to be confused with the effects observed—and dreaded—in typical "overload tests," in which accelerated testing is realized by overloading the lining material mechanically.

In a preliminary experiment, performed at 25°C (77°F) ring temperature, it was verified whether, at a relative speed of 0.1 m/s and a normal load of 200 N, frictional heating had indeed a negligible influence on the temperature of the lining material. To that purpose, a thermal couple with a diameter of 0.5 mm was inserted in the lining specimen at 0.5 mm distance from the friction interface. It was found that the temperature rise, built up during 15 min continuous running under the foregoing experimental conditions, was only 3°C. On the basis of this result it was decided

that the increase in interface temperature as a result of frictional heating during each 5 s contact period could be neglected.

## Materials

The present tests were performed with rings machined from SAE D-3 steel. This material was chosen because of its high thermal stability and its resistance against surface oxidation. Obviously, the choice of ring material may have some influence on the friction and wear behavior of the friction assembly. Probably, such influence will be particularly pronounced in the case of a sintered metal lining material. Obviously, in technical applications of the present test method, other ring materials (for example, cast iron) may be used. The steel rings were finished by turning to a surface roughness of $2 \pm 0.2$ $\mu$m ($80 \pm 8$ $\mu$in.) rms.

The lining specimens were machined from five different materials. Materials A through D were moulded asbestos-filled composites, bonded with resin and synthetic rubber and containing metallic and ceramic particles. They differed with respect to asbestos/binder ratio, chemical composition of the organic compounds, average size of the asbestos filaments, and composition and size of the metal and ceramic particles. Material E was an iron-based sinter metal.

By machining prior to use, the contact surfaces of the lining specimens were adapted carefully to the radius of curvature of the steel rings.

## Experimental Procedure

In the present test series, experiments were performed in dry air [relative humidity <1 percent at 25°C (77°F)] at temperature levels of 25, 100, 200, 300, 400, and 500°C (77, 212, 392, 572, 752, and 932°F). Each individual test run was performed as follows. Prior to testing, the specimen assembly was conditioned to the surrounding atmosphere for 30 min. After termination of the conditioning period, the first "braking procedure" was performed by pressing the lining specimen against the rotating ring under a normal load of 200 N for a time period of 5 s. The speed of rotation of the ring was 0.1 m/s and the normal pressure was equal to $10^6$ N/m$^2$. After termination of the first contact period, the lining specimen was moved backwards, the heat shield was inserted between the rotating ring and—for ring temperatures of 100°C (212°F) and higher—the lining specimen was allowed to cool down to room temperature. In order to accelerate the cooling procedure, cool dry air was blown onto the lining specimen. At 100°C (212°F) the cooling periods lasted 1.5 min, at 500°C (932°F) they lasted 4 min.

In each of the test runs, the foregoing procedure (that is, 5 s contact period, followed by a cooling period) was performed 30 times. Thus, the integrated contact time was 150 s.

In additional experiments, the influence of moisture on the performance characteristics of the lining Materials A through E was determined. To that purpose the lining specimens were soaked in distilled water, prior to test, subsequent testing being performed at 25°C (77°F) ring temperature. In between subsequent contact periods, additional distilled water was applied to the surface of the friction material with a soft wet brush.

All experiments were performed in triplicate.

## Results

### *Friction Curves*

Friction records obtained during the first four contact periods of an experiment performed with Material A at 200°C (392°F) are shown in Fig. 3. The figure shows that, during each of the individual contact periods, only minor variations in friction occurred. This behavior is characteristic for all materials at all testing temperatures. Thus, the frictional behavior of the different lining materials in each individual contact period could be characterized by an average coefficient of friction $\bar{f}_i$. Analysis of the results of triplicate experiments showed that the spread in triplicate $\bar{f}_i$ values was usually low. Actually, the highest spread observed [that is, with Material A at 500°C (932°F)] amounted to 15 percent of the total average value $\bar{f}$. Thus the total average friction values were used for further data processing. Figure 4 shows $\bar{f}$ as a function of the number of contact periods N for Material A, tested at 25, 100, 200, 300, 400 and 500°C (77, 212, 392, 572, 752, and 932°F). For reasons of simplicity, only the data points corresponding to the 1st, 5th, 10th, 15th, 20th, 25th, and 30th contact period are shown, different markings indicating different temperature levels. Figure 4 shows that, from 100°C (212°F) on, the average coefficients of friction, measured during the first ten contact periods, decreased steadily with increasing ring temperature. This decrease in friction was probably due to transformations in and (partial) decomposition of the organic compounds. At 200°C (392°F) and higher the first contact between the friction material and the preheated ring was accompanied by the evolution of organic vapors. At ring temperatures of 300°C (572°F) and higher, the surface of the lining material readily acquired a glazed appearance.

At approximately the 10th contact period, the coefficient of friction measured at 500°C (932°F) ring temperature began to increase again.

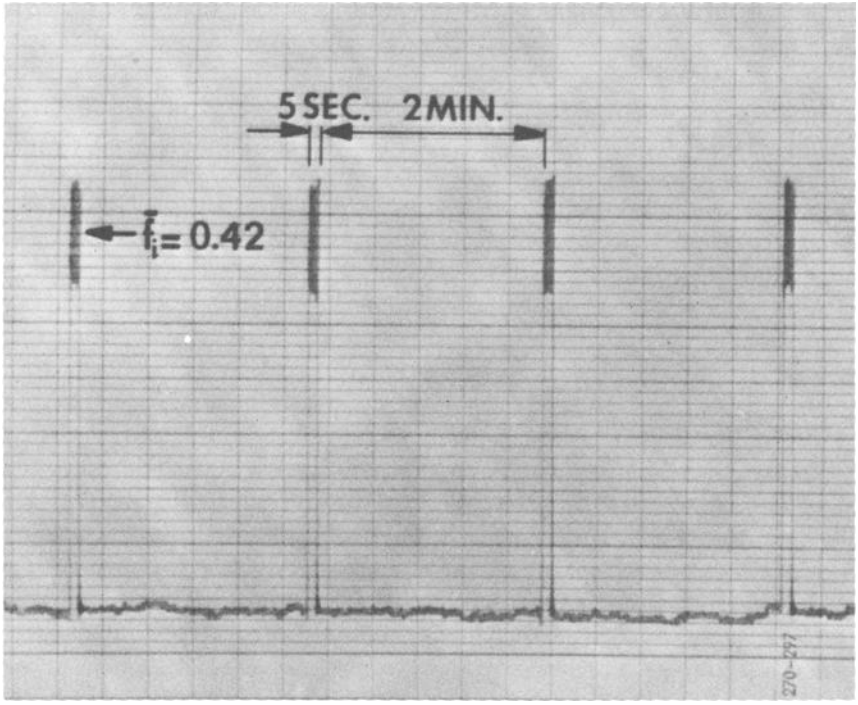


FIG. 3—*Friction-time records obtained during the first four contact periods of an experiment performed with Material A at 200°C(392°F). Duration of each contact period: 5 s; speed: 0.1 m/s; load: 200 N; atmosphere: dry air.*

Inspection of the contact surfaces of the friction material after termination of each of the individual contact periods shows that this increase in friction was accompanied by—and probably due to—local carbonization of the surface. Also at 400°C (752°F) ring temperature, the friction surfaces showed signs of beginning carbonization when inspected after termination of the entire test run.

The $\bar{f}/N$ curve obtained with Material A in moistened condition at 25°C (77°F) shows that the friction behavior of this material was only slightly affected by moisture.

Friction curves obtained with Material B are shown in Fig. 5. It turns out that these $\bar{f}/N$ curves bear a close resemblance to the curves obtained with Material A, be it that in this case a discontinuous drop in friction occurred between 200 and 300°C (392 and 572°F). Apparently, with Material B serious decomposition of the organic compounds started at a temperature between 200 and 300°C (392 and 572°F). The increase

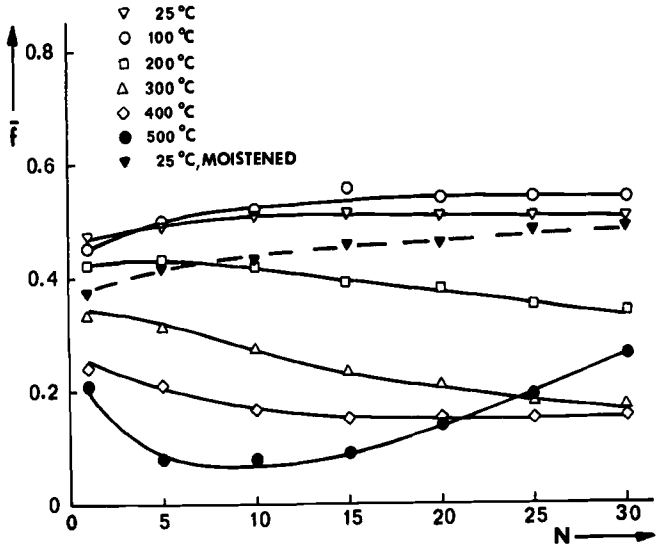


FIG. 4—*Coefficient of friction ($\bar{f}$) as a function of number of contact periods (N) for Material A at ring temperatures of 25, 100, 200, 300, 400 and 500°C (77, 212, 392, 572, 752, and 932°F). Duration of each contact period: 5 s; speed: 0.1 m/s; load: 200 N; atmosphere: dry air.*

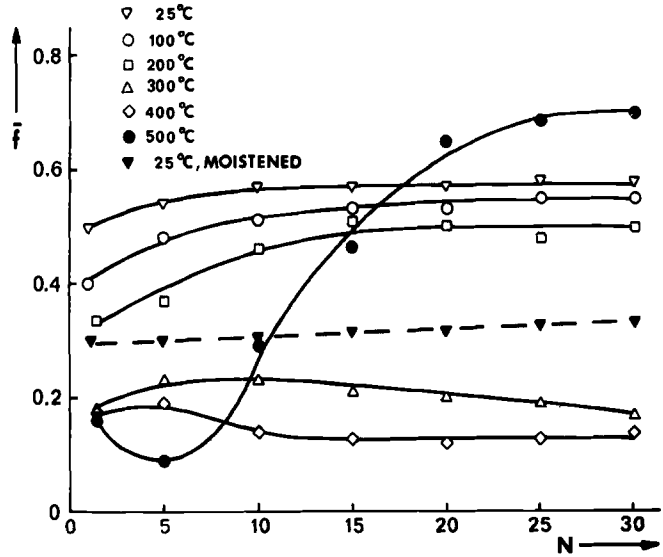


FIG. 5—*Coefficient of friction ($\bar{f}$) as a function of number of contact periods (N) for Material B at ring temperatures of 25, 100, 200, 300, 400 and 500°C (77, 212, 392, 572, 752, and 932°F). Duration of each contact period: 5 s; speed: 0.1 m/s; load: 200 N; atmosphere: dry air.*

in friction, observed at 500°C (932°F) ring temperature, was more pronounced than with Material A. Accordingly, the contact surfaces of the lining specimens tested at 500°C (932°F) were found to have carbonized completely after termination of the 30th contact period. This is illustrated by Fig. 6, which shows the condition of the contact surfaces of the lining specimens after termination of the test runs at 100, 200, 300, 400 and 500°C (212, 392, 572, 752, and 932°F), respectively. Figure 6 shows that, after testing at 100 and 200°C (212 and 392°F), the appearance of the contact surfaces of the lining specimens closely resembled that of a new specimen.

After performing tests at 300 and 400°C (572 and 752°F) ring temperature, however, the contact surfaces were found to have acquired a metallic luster, indicating that a considerable amount of "glazing" had occurred! After testing at 500°C (932°F), finally, large parts of the test surface were found to have acquired a dull black, nonreflecting appearance, indicating total carbonization.

The $\bar{f}/N$ curve obtained with Material B in moistened condition at 25°C (77°F) shows that this material was seriously affected by moisture, although the coefficient of friction of the moistened material was still rather high ($\bar{f} = 0.34$).

Next, Fig. 7 shows $\bar{f}/N$ curves for Material C. This material is characterized by an initial decrease in friction at increasing temperature, in the temperature range from 100 to 300°C (212 to 572°F). At 400 and 500°C (752 and 932°F), however, a "recovery" in friction value occurred from the very start of the test runs on.

Visual inspection of the contact surfaces after each individual contact period showed that this was due to extensive carbonization, occurring already during the first contact period.

The $\bar{f}/N$ curve obtained with Material C in moistened condition shows that this material was extremely sensitive to moisture.

Figure 8 shows $\bar{f}/N$ curves for Material D. This material showed surprisingly constant friction behavior at temperatures of 25, 100, 200, and 300°C (77, 212, 392, and 572°F). At 400 and 500°C (752 and 932°F), however, severe glazing as well as carbonization took place. The friction behavior of Material D at 25°C (77°F) was not much affected by moisture.

Finally, Fig. 9 shows $\bar{f}/N$ curves obtained with Material E. This material does not contain organic compounds, thus glazing and carbonization effects were not found. As was to be expected with a metallic material, friction was a rather complex function of temperature and running time, probably because of the occurrence of temperature- and time-depending adhesion and oxidation effects. Initially (that is, at the first contact period), an

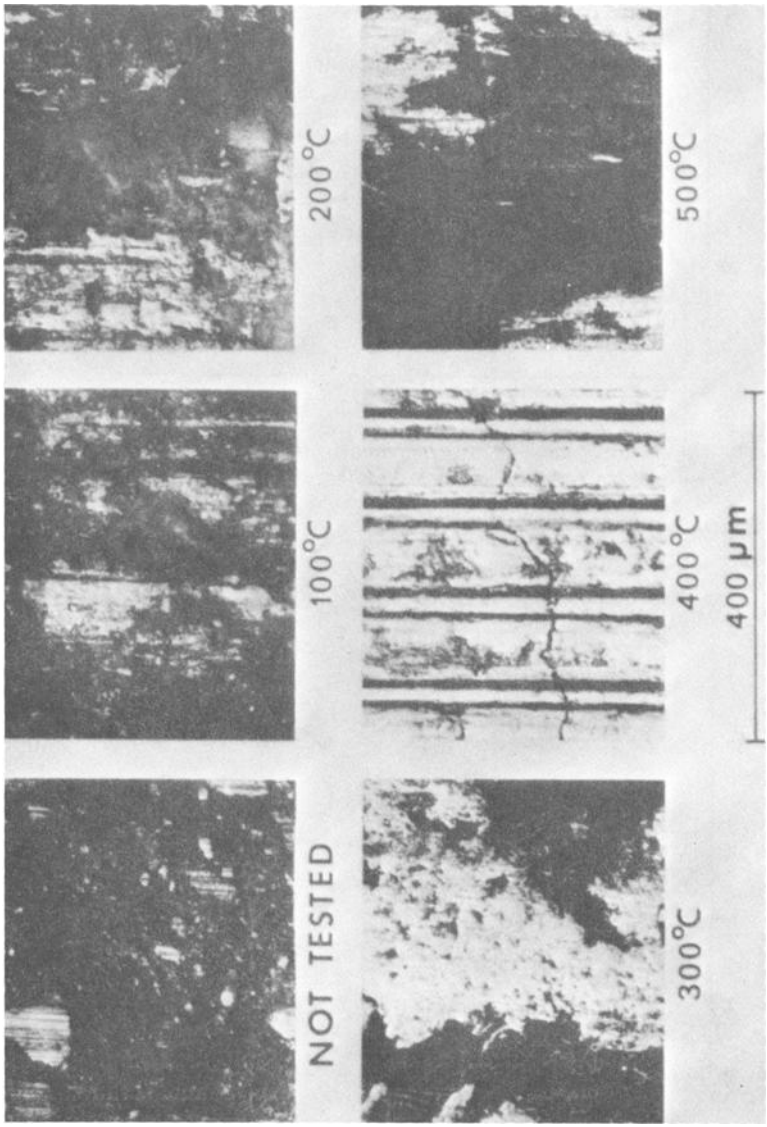


FIG. 6—*Condition of contact surfaces of lining specimens of Material B not tested and after termination of test runs at 100, 200, 300, 400 and 500°C (212, 392, 572, 752, and 932°F).*

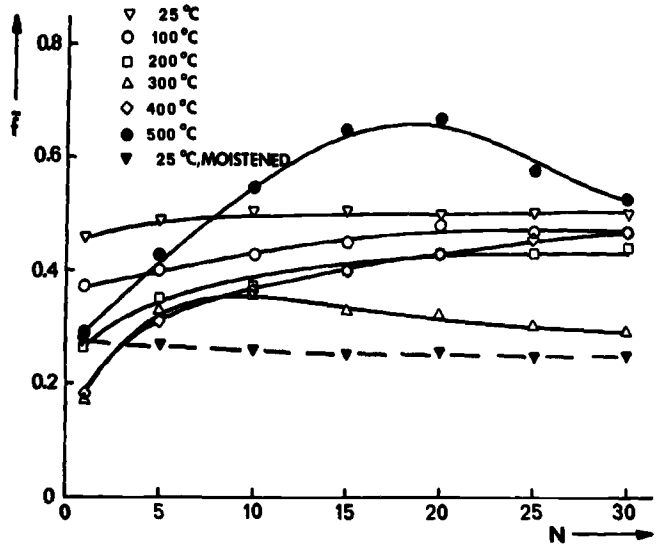


FIG. 7—*Coefficient of friction* ($\bar{f}$) *as a function of number of contact periods (N) for Material C at ring temperatures of 25, 100, 200, 300, 400 and 500°C (77, 212, 392, 572, 752, and 932 °F). Duration of each contact period: 5 s; speed: 0.1 m/s; load: 200 N; atmosphere: dry air.*

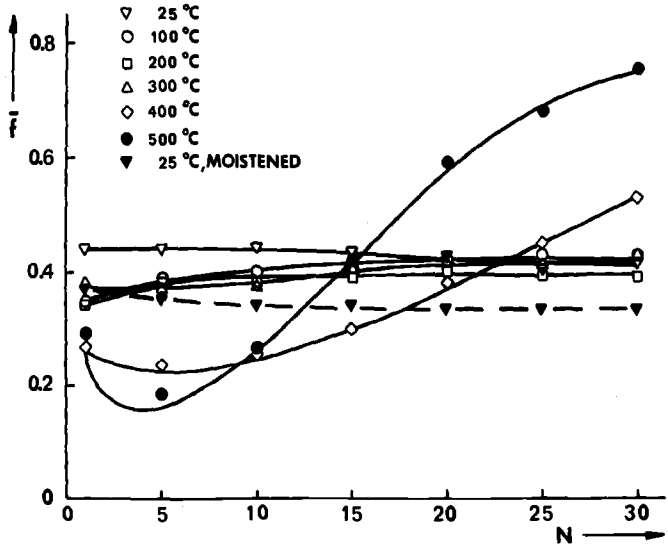


FIG. 8—*Coefficient of friction* ($\bar{f}$) *as a function of number of contact periods (N) for Material D at ring temperatures of 25, 100, 200, 300, 400 and 500°C (77, 212, 392, 572, 752, and 932 °F). Duration of each contact period: 5 s; speed: 0.1 m/s; load: 200 N; atmosphere: dry air.*

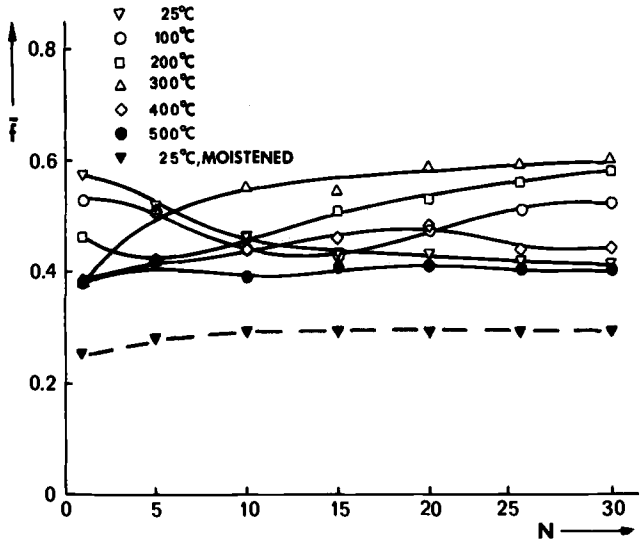


FIG. 9—*Coefficient of friction ($\bar{f}$) as a function of number of contact periods (N) for Material E at ring temperatures of 25, 100, 200, 300, 400 and 500°C (77, 212, 392, 572, 752, and 932 °F). Duration of each contact period: 5 s; speed: 0.1 m/s; load: 200 N; atmosphere: dry air.*

increase in temperature from 25 to 300°C (77 to 572°F) caused a gradual decrease in friction from about $\bar{f} = 0.58$ to $\bar{f} = 0.38$. A further increase in temperature, however, did not result in a further decrease in friction. At 25°C (77°F) friction decreased steadily with increasing number of contact periods to a steady-state value of $\bar{f} = 0.42$. At 100°C (212°F) friction made some erratic excursions with increasing number of contact periods, but acquired a $N_{30}$ value of $\bar{f} = 0.52$, that is, nearly equal to the starting value of $\bar{f} = 0.54$. At 200 and 300°C (392 and 572°F), a definite trend toward increasing friction with increasing number of contact periods was observed. At 400 and 500°C (752 and 932°F), finally, the coefficient of friction remained nearly constant during the entire test run.

Obviously, the scope of this paper does not permit a detailed analysis of the aforementioned phenomena. For the time being it should suffice to conclude that Material E continues to function as a good friction material until temperatures of 500°C (932°F) or higher. However, the $\bar{f}/N$ curve obtained for Material E in moistened condition at 25°C (77°F) shows that it was surprisingly sensitive to the presence of moisture.

The severe decrease in friction at elevated temperatures that was observed with Materials A, B, C, and D is a typical example of "delayed fade." Catastrophic fading by aerodynamic gas lubrication effects could

not be observed in the present tests, presumably because the ring rotated very slowly. It is to be expected, however, that materials which were showing severe delayed-fading effects in the present tests may suffer from gas lubrication effects upon high-speed application in practice.

The increase in friction which followed the initial decrease at 500°C (932°F), clearly corresponded to the practical phenomenon known as over-recovery. Thus, in this case, over-recovery was due to carbonization effects.

### *Wear Measurements*

Results of wear measurements, performed after termination of 30 contact periods at 25, 100, 200, 300, 400, and 500°C (77, 212, 392, 572, 752, and 932°F), respectively, are given in Table 1. Results of wear measurements after 8 h continuous running at 200°C (392°F) are given in Column 7 of the same table.

Table 1 shows that after 30 contact periods (total running time 150 s) the total amount of wear of Materials A, B, D, and E was very small, even after testing at 500°C (932°F) ring temperature. Still, on the basis of these data a distinction between these four materials can be made. The sinter metal (Material E) emerges as the best material; it had suffered less than 1 $\mu$m wear after 30 contact periods at 500°C (932°F) ring temperature. The wear of Materials A, B, and D was distinctly higher at all temperatures, but particularly so at ring temperatures of 400 and 500°C (752 and 932°F). This was probably due to the occurrence of carbonization effects. Material C, finally, suffered more wear than either of the

TABLE 1—*Results of wear measurements.*

| Lining Material | $\Delta d_{N30}$[a] $\mu$m | | | | | $\Delta d_{8\,h}$[b] $\mu$m |
|---|---|---|---|---|---|---|
| | 100°C (212°F) | 200°C (392°F) | 300°C (572°F) | 400°C (752°F) | 500°C (932°F) | 200°C (392°F) |
| A | 2 | 1 | 1 | 4 | 4 | 110 |
| B | 1 | 2 | 1 | 3 | 4 | 95 |
| C | 4 | 3 | 3 | 8 | 25 | 200 |
| D | 1 | 2 | 2 | 3 | 3 | 130 |
| E | <1 | <1 | <1 | <1 | <1 | 2 |

[a] $\Delta d_{N30}$ = decrease in thickness of the lining material after 30 contact periods.
[b] $\Delta d_{8\,h}$ = decrease in thickness of the lining material after 8 h continuous running.

other materials, particularly at 500°C (932°F). These observations are corroborated by the information obtained after 8 h testing at 200°C (392°F).

## Summary and Conclusions

A summary of characteristic results is given in Table 2. In this table Column 2 contains the temperature range in which thermal decomposition effects occur and Column 3 gives the temperature ranges for carbonization. These data are based on study of the $f/N$ curves as well as on observations regarding the condition of the friction surfaces after termination of the tests.

If one considers glazing to be a dangerous and therefore intolerable phenomenon in practice, the lower limits of the temperature ranges for glazing should be taken as representing the maximum admissible temperatures for use in practice. These temperatures are given in Column 4 of Table 2. Next, Column 5 contains the average values of the steady-state friction (that is, the coefficient of friction observed during the 30th contact period) at $T = 100°C$ (212°F), and Column 6 gives the steady-state friction values obtained when testing at 25°C (77°F) with moistened materials. Finally, the wear data obtained after 8 h continuous testing at 200°C (392°F) are once more presented in Column 7 of Table 2.

From the data compiled in Table 2, the following conclusions regarding the quality of Materials A through E can be drawn:

1. The maximum admissible temperature for use of Material A is rather low (150°C) (302°F). Thus, application of Material A requires the use of a disk or drum material with good heat conductivity and, in addition, good cooling facilities. This is the more important as, at temperatures of 100°C (212°F), the coefficient of friction is rather high ($\bar{f} = 0.54$), which means that much frictional heat is dissipated upon use. Material A is remarkably insensitive to moisture.

2. When Material B is used, a higher surface temperature (200°C) (392°F) can be permitted. At 100°C (212°F), Material B has about the same high coefficient of friction as Material A, that is, $\bar{f} = 0.55$. The effect of moisture, however, is more pronounced than with Material A.

3. As far as the maximum admissible surface temperature is concerned, Material C shows no advantage over Material B. Friction with this material is generally lower than that observed with Materials A and B. This may be an advantage, if the cooling facilities of the brake assembly are relatively poor. On the other hand, when using Material C, one needs more friction surface to obtain the same braking power as one gets with Materials A and B. The carbonization temperature of Material C is distinctly lower

TABLE 2—*Summary of characteristic test results.*

| Lining Material | Temperature Range Decomposition Effects, °C | Temperature Range Carbonization Effects, °C | Max Allowable Surface Temperature, °C | $\bar{f}$[a] 100°C (212°F) | $\bar{f}$[a] 25°C(77°F) Moistened Materials | $\Delta d^{b}_{8\ h}$, 200°C (392°F) μm |
|---|---|---|---|---|---|---|
| A | 100–200[c] | ~400 | 150[c] | 0.54 | 0.48 | 110 |
| B | 200–300 | 400–500 | 200 | 0.55 | 0.34 | 95 |
| C | 200–300 | 300–400 | 200 | 0.47 | 0.25 | 200 |
| D | 300–400 | 300–400 | 300 | 0.43 | 0.23 | 130 |
| E | ... | ... | >500 | 0.52 | 0.29 | 2 |

[a] Average values of the coefficient of friction in the steady state, obtained in triplicate testing.
[b] Decrease in thickness (wear) of the lining materials after 8 h continuous running at 200°C (392°F).
[c] At 200°C (392°F) and N = 30, friction is still decreasing, the coefficient of friction, however, being still fairly high; that is $\bar{f}$ = 0.34.

than that of Materials A and B. This is a disadvantage for high-temperature use because, in practical application, carbonization effects are to be avoided at all costs. Further, Material C has a poor performance when tested in moistened condition and, finally, its wear behavior is unsatisfactory. This makes Material C a questionable choice for application in practice.

4. When compared with the other asbestos-based materials, Material D exhibits a superior behavior as far as the maximum admissible surface temperature is concerned (300°C) (572°F). The coefficient of friction obtainable with this material at 100°C (212°F), however, is much lower than that obtainable with Materials A and B. On the one hand this means safe operation, even under relatively unfavorable cooling conditions, while on the other hand one needs more friction surface to obtain the same braking power as one gets with Materials A and B. As with Material C, carbonization of Material D occurs at a lower temperature than carbonization of Materials A and B. The sensitivity toward moisture of Material D is also rather high.

5. Material E, finally, can be applied up to surface temperatures of 500°C (932°F) and higher. Wear is very low, and the coefficient of friction at 100°C (212°F) is nearly as high as observed with Materials A and B. Obviously these qualifications make the sinter metal E superior to the asbestos-based materials. In moistened condition, however, the performance of Material A is distinctly superior to that of Material E.

The foregoing conclusions show that the newly developed, isothermal test method, described in this paper, has excellent discriminating power. It can yield detailed and valuable information for designers, manufacturers, and users.

*Acknowledgments*

The authors are indebted to J. W. M. Mens for assisting in designing the equipment and to C. M. Lossie, who carefully performed the experiments.

# APPENDIX

### Calculation of Rate of Heating Up of Lining Specimens

For the present purpose the rate of heating up of the lining specimens will be characterized by the time it takes to heat up the asbestos-based lining materials at 10-$\mu$m depth below the contact surface from room temperature to a temperature that is 1 percent lower than the temperature at the contact surface ($T_s$). The shorter this time, the more favorable (that is, the more isothermal) the contact situation will be. This time, $t_{0.99}$, can be calculated as follows.

Assuming that the heat production by friction and the rate of the heat loss

by evaporation, etc. can be neglected, the change in temperature at each volume element *dxdydz* in the lining material is given by the Fourier equation

$$\frac{\partial T}{\partial t} = \kappa \left( \frac{\partial^2 T}{\partial x^2} + \frac{\partial^2 T}{\partial y^2} + \frac{\partial^2 T}{\partial z^2} \right) \tag{1}$$

in which $\kappa$ is the thermal diffusivity coefficient, equal to $K/\rho c$ ($K$ = thermal conductivity coefficient, $\rho$ = density, $c$ = specific heat).

Assuming that the heat flow in the lining specimen is primarily in the direction normal to the contact surface ($x$-direction), Eq 1 reduces to

$$\frac{\partial T}{\partial t} = \kappa \frac{\partial^2 T}{\partial x^2} \tag{1a}$$

Further, the following boundary conditions apply:

$$T = T_0 \text{ for } t = 0 \text{ and } x \geqslant 0$$
$$T = T_s \text{ for } t > 0 \text{ and } x = 0$$
$$T = T_0 \text{ for } x \to \infty$$

Solving this equation for $x = x_1$ yields

$$\frac{T_s - T_{x_1}}{T_s - T_0} = erf \frac{x_1}{2\sqrt{\kappa t}} \tag{2}$$

For the asbestos-based lining materials (most unfavorable situation), $K \approx 5.10^{-1}$ J/m s°C, $\rho \approx 2.10^3$ kg/m$^3$ and c $\approx 2.10^3$ J/kg°C. Thus, $\kappa \approx 10^{-7}$ m$^2$/s.

Applying Eq 2 for $T_s = 500$°C (932°F) (most unfavorable situation), $T_{x_1} = 495$°C (923°F), $T_0 = 25$°C (77°F), $x_1 = 10^{-5}$ m and $\kappa = 10^{-7}$ m$^2$/s yields:

$$t_{0.99} = 600\ \mu s$$

## References


[1] Starkey, W. L., Foster, T. G., and Marco, S. M., *Transactions*, American Society of Mechanical Engineers, Vol. 93, Series B, No. 4, 1971, pp. 1225–1228.

[2] Planteydt, H. T., *TNO-nieuws*, Vol. 27, No. 11, 1972, pp. 667–671.

[3] Meyer, P. B. and de Koning-Pierens, W. E., *TNO-nieuws*, Vol. 27, No. 11, 1972, pp. 661–666.

[4] Newcomb, T. P. and Spurr, R. T., *Braking of Road Vehicles*, Chapman and Hall Ltd., London, 1967, Chapter 4.

[5] Wilson, A. J., *Lucas Engineering Review*, Vol. 5, No. 4, 1972, pp. 88–95.

[6] Bäse, H., "Modellähnlichkeitsversuche an Trommel und Scheibenbremsen," *Deutsche Kraftfahrtforschung und Strassenverkehrstechnik*, Vol. 198, VDI-Verlag, Düsseldorf, Germany, 1969.

[7] *Brake System Road Test Code—Passenger Cars*, 1966 SAE Handbook, SAE J 483, Society of Automotive Engineers, p. 836.

[8] *Brake System Road Test Code—Truck and Bus*, 1966 SAE Handbook, SAE J 786, Society of Automotive Engineers, p. 838.

[9] Reinsch, E. W., "Sintered Metal Brake Linings for Automotive Applications" in *Friction and Antifriction Materials*, Vol. 4 of the series *Perspectives in Powder Metallurgy*, Plenum Press, New York-London, 1970, pp. 9–21.

[10] Newcomb, T. P. and Spurr, R. T., *Braking of Road Vehicles*, Chapman and Hall Ltd., London, 1967, Chapter 7.

[11] *Brake Lining Quality Control—Test Procedure*, 1962 SAE Handbook, SAE J 661-7a, Society of Automotive Engineers, p. 846.

# DISCUSSION

*A. F. Conn*[1]—In view of the discussions in some of the earlier papers in this symposium pertaining to the role of velocity and frictional heating on the value of the coefficient of friction, I wonder if the author would care to comment on the following question. In the tests at TNO a very low velocity was used, in order to avoid frictional heating, while a controlled external source was used to provide the elevated temperature environment. Does the author feel that this is indeed a valid simulation of the actual case wherein there is a high velocity but no external heat generation? Has this been verified experimentally, or are there theoretical bases for this assumption?

*A. Begelinger and A. W. J. de Gee (authors' closure)*—We are grateful to Dr. Conn for making his valuable comment. Actually, the proof of the pudding is in the eating; that is, only correlation with results obtained under conditions of practical application can ultimately justify acceptance of the test method for screening purposes.

Realizing this, we are now gathering such information. The data obtained thus far are certainly encouraging as they suggest that no purely mechanical velocity effects occur.

[1] Principal research scientist and head, Materials Sciences Division, HYDRONAUTICS, Incorporated, Laurel, Md. 20810.